Dynamic Stiffness and Transfer Matrix Analysis of Marine Riser Vibration

by

Yongming Cheng

Submitted to the Department of Ocean Engineering
in partial fulfillment of the requirements for the degree of

Doctor of Philosophy

at the

MASSACHUSETTS INSTITUTE OF TECHNOLOGY

January 2001
[February 2001]

Signature Redacted

Author .....
Department of Ocean Engineering
January 24, 2001

Signature Redacted

Certified by .....
J. Kim Vandiver
Professor of Ocean Engineering
Thesis Supervisor

Signature Redacted

Accepted by .....
Nicholas Patrikalakis
Kawasaki Professor of Engineering
Chairman, Department Committee on Graduate Students

Dynamic Stiffness and Transfer Matrix Analysis of Marine Riser Vibration

by

Yongming Cheng

Submitted to the Department of Ocean Engineering
on January 24, 2001, in partial fulfillment of the
requirements for the degree of
Doctor of Philosophy

Abstract

This dissertation extends the use of the dynamic stiffness and transfer matrix methods in marine riser vibration. Marine risers possess a predominant chain topology. The transfer matrix method is appropriate for the analysis of such structures. Wave transmission and reflection matrices are formulated in terms of transfer-matrix elements. The delta-matrix method is introduced to deal with numerical problems associated with very long beams and high frequencies. The general internal relationships between the transfer matrix and dynamic stiffness methods are derived and applied to the problem of a non-uniform beam with discontinuities. An implicit transfer matrix of a general non-uniform beam is derived.

The vibration analysis of non-uniform marine risers is addressed by combining the procedure of the dynamic stiffness method with the WKB theory. The WKB-based dynamic stiffness matrix is derived and the frequency-dependent shape function is expressed implicitly. The Wittrick-Williams algorithm is extended to the analysis of a general non-uniform marine riser, allowing automatic computation of natural frequencies. Marine riser models with complex boundary conditions are analyzed. The WKB-based dynamic stiffness method is improved and applied to a non-uniform beam system with discontinuities. A dynamic stiffness library is created.

Dynamic vibration absorbers and wave-absorbing terminations are investigated as a means of suppressing vibration. The optimal tuning of multiple absorbers to a non-uniform beam system under varying tension is investigated. The properties of wave-absorbing terminations of a beam system are derived.

The vibration of two concentric cylinders coupled by the annulus fluid and by periodic centralizers is modeled. The effects of coupling factors on vibration are numerically evaluated. It is shown that a properly designed inner tubular member may be used to damp the flow-induced vibration of the outer cylinder.

Thesis Supervisor: J. Kim Vandiver
Title: Professor of Ocean Engineering

Acknowledgments

First and foremost, I would like to express my deep gratitude to my supervisor, Professor J. Kim Vandiver, for his guidance and support through this research. I enjoyed our weekly meetings. His clear thinking, strong engineering sense, and rich research experience got me through the tough times. His creative work in vortex-induced vibration is well known. From him I learned how to approach a complex problem and find solutions to satisfy an engineering requirement. His endless understanding, kind encouragement and great assistance will always be appreciated.

I am also indebted to the other members of my thesis committee, Professor Eduardo Kausel, Professor Jerome H. Milgram, Professor Geir Moe (NTNU, Norway), and Dr. Leonard Imas for their time and suggestions.

I would like to thank the members of the industry consortium who supported this thesis work: Aker, BP/Amoco, Chevron, Exxon/Mobil, Petrobras, Shell, Statoil, and Texaco.

I would like to thank all members of our research group for fruitful discussions on various projects. I enjoyed our weekly group meetings.

Thanks to Mrs. Shiela McNary for her administrative assistance and the MIT writing Center for editing the draft of this thesis.

Thanks to my parents and in-law for their support and encouragement. Thanks to my son, Bohao Cheng. He helped me to forget difficulties and took me into his world. I enjoyed our discussion about how to prevent whales and sharks from eating risers. It was a big fun to play with him. Thanks to my wife, Haiyan Li. She kept me grounded through all the ups and downs. She took such good care of Bohao and me. I dedicate this thesis to her with all my love.

Contents

1 Introduction **17**

1.1 Problem Statement 17

1.2 Technical Summary of Numerical Methods 19

1.3 Overview of this thesis 21

2 Transfer Matrix Method **25**

2.1 Introduction 25

2.2 An outline of the transfer matrix method 26

2.2.1 state vector and transfer matrix 26

2.2.2 Eliminating intermediate state vectors and finding frequency determinant 28

2.2.3 Response analysis 30

2.3 Vibration analysis of a beam structure with discontinuities 31

2.4 Wave reflection and transmission in a beam structure due to discontinuities 38

2.4.1 The derivation of wave reflection and transmission matrices . . 38

2.4.2 Examples 42

2.5 Numerical difficulties and the delta-matrix 46

2.5.1 Numerical difficulties 46

2.5.2 The delta-matrix method 47

2.5.3 Examples 49

2.6 Three approximate schemes for a beam under variable tension 54

2.7 A new transfer matrix method based on symbolic operations 59

3 Dynamic Stiffness Method **65**

3.1 Introduction 65

3.2 Derivation of elemental dynamic stiffness matrix and frequency-dependent mass and stiffness matrices 66

3.2.1 Elemental dynamic stiffness matrix 66

3.2.2 Frequency-dependent mass and stiffness matrices 69

3.3 The global dynamic stiffness matrix and determination of natural frequency 72

3.3.1 The global dynamic stiffness matrix 72

3.3.2 The Determination of Natural Frequencies 73

3.3.3 An example 74

3.4 Use of the W-W algorithm to analyze a uniform beam structure . . . 75

3.5 Complex frequency analysis 77

4 WKB-Based Dynamic Stiffness Method **79**

4.1 Introduction 79

4.2 Derivation of the WKB-based dynamic stiffness matrix 80

4.3 Frequency dependent shape function 84

4.4 Natural frequencies and mode shapes 85

4.5 Numerical examples 86

4.5.1 A uniform drilling riser under linearly varying tension [1] . . . 86

4.5.2 A non-uniform riser with variable properties 89

4.6 Conclusions 92

5 The WKB-Based Dynamic Stiffness Method with the W-W Algorithm **93**

5.1 Introduction 93

5.2 Extension of the W-W algorithm to non-uniform marine risers 94

5.3 Examples of marine risers 97

5.4 Calculation of mode shapes, slopes and curvatures 99

5.4.1 Introduction 99

5.4.2 Examples 102
5.5 Marine risers with complex boundary conditions 111

6 Relationship Between Transfer Matrix and Dynamic Stiffness Methods and Its Application 120
6.1 Introduction 120
6.2 The relationship between transfer matrix and dynamic stiffness methods 121
6.2.1 Relationship between the transfer matrix and the dynamic stiffness matrix 121
6.2.2 Relationship between the two methods 124
6.3 Derivation of a transfer matrix from the WKB-based dynamic stiffness matrix 127
6.4 Dynamic stiffness method for a riser with discontinuities 129
6.5 Establishment of dynamic stiffness library 133

7 Vibration Suppression by Means of Absorbers and Wave-Absorbing Termination 137
7.1 Introduction 137
7.2 Optimum tuning of a DVA to a beam with general boundary conditions 138
7.3 Approximate solution of optimal tuning 143
7.4 A numerical example 144
7.5 Optimal tuning of multiple DVAs to a beam with general boundary conditions 149
7.5.1 Optimal solution 149
7.5.2 An example of a simply supported beam tuned by DVAs . . . 154
7.6 Optimal tuning of multiple DVAs to a non-uniform beam under varying tension 157
7.6.1 Optimal solution 157
7.6.2 Optimal tuning of DVAs to a uniform beam under constant tension 159

7.6.3 An example of a 1400-ft riser 160
7.7 Incorporation of structural damping 163
7.8 Wave-absorbing termination of a beam system 164

8 Vibration Analysis of a Coupled Fluid/ Riser System 170
8.1 Introduction 170
8.2 Free vibration of a spring connected double-beam system and optimal design of a dynamic absorbing beam 171
8.2.1 Analytical solutions 171
8.2.2 Optimal design of a dynamic absorbing beam 175
8.2.3 An example: A coupled double-axial cylinder system 177
8.3 Free vibration of a spring-coupled tensioned beam system and optimal design of a dynamic absorbing beam 181
8.3.1 Analytical solutions 181
8.3.2 Optimal design of a dynamic absorbing beam 182
8.3.3 An example: A coupled constantly tensioned beam system . . 182
8.4 Free vibration of a constantly tensioned beam system coupled by an ideal fluid and springs 184
8.4.1 Analytical solutions 184
8.4.2 An example: a constantly tensioned beam system coupled by an ideal fluid and springs 187
8.5 Theoretical formulation of a general coupled double-riser system . . . 195
8.5.1 Hydrodynamic forces of viscous fluid in between concentric cylinders 195
8.5.2 Formulation of a coupled fluid/riser system 197
8.6 Undamped and damped natural frequency analysis of a coupled system 204
8.7 Effects of coupling factors on the vibration of a coupled system 216
8.7.1 Fluid viscosity 217
8.7.2 Damping of centralizers 222
8.7.3 Rigidity of centralizers 227

8.7.4 Spacing of centralizers 232

9 Summary **235**

9.1 New contributions 235

9.2 Further work 237

A Vibration Analysis of a Riser Under Linearly Varying Tension Using FEM **239**

A.1 Derivation of geometric stiffness matrix 239

A.2 Example 241

B The frequency dependent shape function **246**

C Dynamic Stiffness Library **249**

C.1 A general non-uniform beam under variable tension 249

C.2 A uniform Bernoulli-Euler beam 252

C.3 A Beam Subjected a Constant Tension 252

C.4 Combination of a uniform beam with point mass 253

C.5 Combination of a uniform tensioned beam with point mass 254

C.6 Combination of a tensioned beam with spring-dashpot support 256

C.7 A uniform tensioned beam with an abosrber on the right end 257

C.8 Combination of a tensioned beam with concentrated mass and rotary inertia 259

C.9 Combination of a tensioned beam with concentrated mass and spring support 261

D The VIV Prediction of the Helland-Hansen riser **263**

List of Figures

2-1 A typical uniform beam section 27

2-2 A beam divided into n sections 28

2-3 The determinant of the transfer matrix versus frequency 33

2-4 The simply-supported constantly tensioned uniform beam attached by a mass-spring absorber at the midpoint 34

2-5 The determinant of the transfer matrix versus frequency 35

2-6 The first four modes of the composite system 36

2-7 The transfer mobility of the free-free pipe 37

2-8 The simply-supported constantly tensioned uniform beam attached by a mass-spring absorber at the midpoint 37

2-9 The transfer mobility of the free-free pipe with mass attachment . . . 38

2-10 The modulus of transmission coefficients 44

2-11 The reflection and transmission coefficients of $\mathbf{r}$ and $\mathbf{t}$ 45

2-12 The determinant versus frequency (Hz) 50

2-13 The determinant versus frequency (Hz) 51

2-14 The delta-matrix determinant versus frequency (Hz) 53

2-15 The approximation scheme (a) 54

2-16 The approximation scheme (b) 54

2-17 The approximation scheme (c) 55

2-18 The absolute determinant of the riser versus frequency in Hz (approximate scheme (a)) 56

2-19 The absolute determinant of the riser versus frequency in Hz (approximate scheme (b)) 56

2-20 The absolute determinant of the riser versus frequency in Hz (approximate scheme (c)) 57
2-21 The absolute determinant of the riser versus frequency in Hz (approximate scheme (a)) 58
2-22 The absolute determinant of the riser versus frequency in Hz (approximate scheme (b)) 58
2-23 The absolute determinant of the system versus frequency in Hz 64

3-1 The determinant of the dynamic stiffness matrix versus frequency . . 75

4-1 The determinant of the dynamic stiffness matrix of a 500-ft riser versus frequency 87
4-2 The first three natural mode shapes for a 500-ft riser 88
4-3 The mass density variation of the Helland riser 90
4-4 The tension variation of the Helland riser 91
4-5 The comparison of the natural frequencies with those obtained by Shear7 91
4-6 The 20th mode shape of the Helland riser 92

5-1 The comparison of the natural frequencies with those obtained by Shear7 99
5-2 The 1st mode shape, slope and curvature of the 1400-ft riser 103
5-3 The 2nd mode shape, slope and curvature of the 1400-ft riser 104
5-4 The 3rd mode shape, slope and curvature of the 1400-ft riser 104
5-5 The 4th mode shape, slope and curvature of the 1400-ft riser 105
5-6 The 5th mode shape, slope and curvature of the 1400-ft riser 105
5-7 The 6th mode shape, slope and curvature of the 1400-ft riser 106
5-8 The 7th mode shape, slope and curvature of the 1400-ft riser 106
5-9 The 13th mode shape, slope and curvature of the 1400-ft riser 107
5-10 The 1st mode shape, slope and curvature of the Helland riser 108
5-11 The 2nd mode shape, slope and curvature of the Helland riser 108
5-12 The 3rd mode shape, slope and curvature of the Helland riser 109
5-13 The 4th mode shape, slope and curvature of the Helland riser 109

5-14 The 5th mode shape, slope and curvature of the Helland riser 110
5-15 The 18th mode shape, slope and curvature of the Helland riser 110
5-16 The 20th mode shape, slope and curvature of the Helland riser 111
5-17 The determinant of the fixed-fixed 1400-ft riser versus frequency . . . 112
5-18 The determinant of the fixed-fixed 400-ft riser versus frequency 113
5-19 The absolute determinant (log10) of the fixed-fixed 400-ft riser versus frequency 113
5-20 The 1st mode shape, slope and curvature of the free-pinned beam with varying tension 115
5-21 The 5th mode shape, slope and curvature of the free-pinned beam with varying tension 115
5-22 The 1st mode shape, slope and curvature of the 1400-ft riser with rotational springs 117
5-23 The 5th mode shape, slope and curvature of the 1400-ft riser with rotational springs 117
5-24 The 1st mode shape, slope and curvature of the free-pinned beam with varying tension and rotational spring at $x = l$ 118
5-25 The 5th mode shape, slope and curvature of the free-pinned beam with varying tension and rotational spring at $x = l$ 119

6-1 A member with section changes 124
6-2 Frequency analysis of the 1400-ft riser using a new type of delta-matrix 130
6-3 Frequency analysis of the 1400-ft riser by 3 and 10 elements respectively 130
6-4 A submerged floating pipeline 131
6-5 A beam system with absorbers 132
6-6 The determinant of the system versus frequency 132

7-1 Beam with a damped dynamic vibration absorber 138
7-2 Finding roots of $p^2 - f^2 - \mu f^2 p^2 H(h,h) = 0$ for $p = \lambda_1$ 144
7-3 The relationship between p and f $(\mu = 1/5)$ 146
7-4 The relationship between p and f $(\mu = 1/5)$ 146

7-5 The frequency response curves ($\mu = 1/5$, $p = 0.6$) 147
7-6 The frequency response curves ($\mu = 1/5$, $p_0 = 0.56$) 148
7-7 The frequency response curves ($\mu = 1/5$, $p_0 = 0.56$) 148
7-8 Comparison of response curves with different tuning ($\mu = 1/5$) 149
7-9 Frequency response of a simply supported beam with 1st natural frequency tuned by one DVA ($\mu = 1/5$) 155
7-10 Frequency response of a simply supported beam with the 1st natural frequency tuned by one and two DVAs respectively 155
7-11 Frequency response of a simply supported beam with the 3rd natural frequency tuned by multiple DVAs 156
7-12 Frequency response of a uniform riser with its 1st frequency tuned by multiple DVAs 161
7-13 Frequency response of a non-uniform riser with its 1st natural frequency tuned by multiple DVAs 162
7-14 Frequency response of a non-uniform riser with its 6th natural frequency tuned by seven DVAs 162
7-15 Frequency response of a damped non-uniform riser with its 3rd natural frequency tuned by three DVAs 163
7-16 A wave absorbing termination 164
7-17 Wave reflection coefficient at the termination 169

8-1 A double-beam system coupled by springs and dampers 172
8-2 Two-degrees-of-freedom system for nth mode 176
8-3 Effects of spring stiffness on synchronous and asynchronous natural frequencies 179
8-4 Frequency response of the 15th mode due to a concentrated force . . 180
8-5 Frequency response of the 15th mode due to a concentrated force . . 184
8-6 The first four synchronous and asynchronous mode shapes (Case 1) . 188
8-7 The first four synchronous and asynchronous mode shapes (Case 2) . 190

8-8 First four synchronous and asynchronous mode shapes by the WKB-DSSM (solid line: Beam 1; dash-dot line: Beam 2) 192
8-9 First four synchronous and asynchronous mode shapes by using closed form solutions (solid line: Beam 1; dash-dot line: Beam 2) 193
8-10 The third in-phase mode shapes($r_{sp} = 10$, solid line: Beam 1; dash-dot line: Beam 2) 194
8-11 Schematic of two concentric tubes containing a viscous fluid 195
8-12 The first 8 mode shapes of the coupled system ($k^* = 1/48$, solid line: external riser; dash-dot line: internal riser) 208
8-13 The 9th to 16th mode shapes of the coupled system ($k^* = 1/48$, coupled by the fluid and springs) 209
8-14 The first 8 mode shapes of the coupled system ($k^* = 1$, solid line: external riser; dash-dot line: internal riser) 211
8-15 The 9th to 16th mode shapes of the coupled system ($k^* = 1$, coupled by the fluid and springs) 212
8-16 The first 8 mode shapes of the coupled system ($k^* = 1000$, solid line: external riser; dash-dot line: internal riser) 213
8-17 The 9th to 16th mode shapes of the coupled system ($k^* = 1000$, coupled by the fluid and springs 214
8-18 The RMS frequency response of the external riser (fluid coupled, NCOUP=2)218
8-19 The RMS frequency response of the internal riser (fluid coupled, NCOUP=2)219
8-20 The RMS frequency response of the external riser (fluid coupled, NCOUP=2)220
8-21 The RMS frequency response of the internal riser (fluid coupled, NCOUP=2)221
8-22 The RMS frequency response of the external riser (generally coupled, NCOUP=3) 223
8-23 The RMS frequency response of the internal riser (generally coupled, NCOUP=3) 224
8-24 The RMS frequency response of the external riser (generally coupled, NCOUP=3) 225

8-25 The RMS frequency response of the internal riser (generally coupled, NCOUP=3) 226
8-26 The RMS frequency response of the external riser (generally coupled, NCOUP=3) 228
8-27 The RMS frequency response of the internal riser (generally coupled, NCOUP=3) 229
8-28 The RMS frequency response of the external riser (generally coupled, NCOUP=3) 230
8-29 The RMS frequency response of the internal riser (generally coupled, NCOUP=3) 231
8-30 The RMS frequency response of the external riser (generally coupled, NCOUP=3) 233
8-31 The RMS frequency response of the external riser (generally coupled, NCOUP=3) 234

A-1 Natural frequencies of the 1400-ft riser 242
A-2 The first three mode shapes of the 1400-ft riser 243

C-1 Combination of beam with point mass 253
C-2 Combination of tensioned beam with point mass 254
C-3 Combination of tensioned beam with spring-dashpot support 256
C-4 Combination of tensioned beam with an absorber 258
C-5 Combination of tensioned beam with concentrated mass and rotary inertia 259
C-6 Combination of tensioned beam with concentrated mass and spring support 261

D-1 The displacement along the riser 265
D-2 The acceleration along the riser 266
D-3 The acceleration along the riser 266
D-4 The damage rate along the riser 267

List of Tables

2.1 Comparison of natural frequencies found by using the TMM and the analytical solutions 33

2.2 Delta-matrix lexicon 47

2.3 Comparison of natural frequencies (Hz) found by using the delta-matrix and the analytical solutions 51

2.4 Comparison of natural frequencies (Hz) found by using the delta-matrix and Shear7 52

2.5 Natural frequencies (Hz) of the composite system 64

3.1 Complex natural frequencies of a damped beam 78

4.1 Comparison of circular natural frequencies 88

5.1 Comparison of natural frequencies (Hz) 98

5.2 Natural frequencies (Hz) of the 1400-ft riser under different spring stiffness ratios 116

7.1 Frequencies of a cantilever beam with an undamped DVA ($b = l/2$, $h = l$, $\mu = 1/5$) 145

8.1 Comparison of natural frequencies f_{1n} (Hz) of synchronous vibrations 178

8.2 Comparison of natural frequencies f_{2n} (Hz) of asynchronous vibrations 178

8.3 Comparison of natural frequencies f_{1n} (Hz) of synchronous vibrations 183

8.4 Comparison of natural frequencies f_{2n} (Hz) of asynchronous vibrations 183

8.5 Comparison of natural frequencies(Hz) of asynchronous and synchronous vibrations (Case 1) 187
8.6 Comparison of natural frequencies(Hz) of asynchronous and synchronous vibrations (Case 2) 189
8.7 Comparison of natural frequencies f_{1n} (Hz) 191
8.8 Comparison of natural frequencies f_{2n} (Hz) 191
8.9 Coefficients of natural mode shapes $a_{in}(r_{sp} = 1.0)$ 193
8.10 Coefficients of natural mode shapes a_{in} $(r_{sp} = 10)$ 194
8.11 Natural frequencies (Hz) of the double-riser system coupled by only springs 206
8.12 Natural frequencies (Hz) of a coupled two-riser system 207
8.13 Natural frequencies (Hz) of a coupled two-riser system 210
8.14 Complex circular frequencies($\omega = \omega_r + i\omega_i$) of a coupled two-riser system 215

A.1 Comparison of natural frequencies (Hz) 243
A.2 Comparison of natural frequencies (Hz) 244
A.3 Comparison of natural frequencies (Hz) 244

Chapter 1

Introduction

1.1 Problem Statement

Marine structures such as production risers and deep-water pipelines are susceptible to Vortex-Induced Vibration (VIV), which results from complicated, non-linear interactions between structural motions and vortex-shedding. VIV is of great practical importance because it may cause fatigue failure.

Much research has focused on understanding the VIV phenomenon. King (1977) [2], Sarpakaya (1979) [3], and Griffin and Ramberg [4] reviewed the early studies of VIV and its applications. Vandiver (1993) [5] summarized his 17 years of experimental observations, discussed the phenomenon of long flexible cylinders, and identified the dimensionless parameters important to the prediction of VIV. Recently, Vandiver, Allen, and Li (1996) [6] investigated the occurrence of lock-in under highly sheared conditions and indicated two dimensionless parameters to predict the likelihood of the occurrence.

There is broad research work done on structural dynamic analysis and on the VIV suppression of marine risers. Kim (1983) [7] assumed that the continuous coefficients are slowly varying and used the WKB asymptotic method to analyze a slender beam. The MIT Sea Grant Program supported the studies on the dynamics of compliant risers and cable dynamics, shown respectively in the references by Patrikalakis, et al [8, 9] and Triantafyllou, et al [10]. Li (1993) [11] modeled a riser as a string system,

used the transfer matrix method to study the dynamics of strings with rigid lumps, and evaluated their effects on wave propagation. Vandiver and Li (1994) [12] developed for tension-dominated structures a device called a wave absorbing termination, which is capable of suppressing the vibration. Levesque (1997) [13] studied vibration suppression in a finite length string with constant tension using the transfer matrix method and found that a translational mass-spring-dashpot absorber works better than in-line absorbers.

There are a number of analysis programs [17], such as SHEAR7, VIVA, and Vi-CoMo, available to the industry to predict the VIV of marine risers. SHEAR7, which is widely applied, uses mode superposition of uniform string and beam models to evaluate which modes are likely to be excited, and estimates the cross-flow VIV response in steady, uniform or shear flows. The program is capable of evaluating multi-mode, non-lock-in response, as well as single-mode, lock-in response.

As offshore drilling and production proceed into deep waters, marine risers become longer and more flexible. Deepwater marine risers are very susceptible to VIV [18]. The increase in length lowers the natural frequencies and the magnitude of current required to excite the VIV. Long slender risers with complicated boundary conditions can cause numerical difficulties in dynamic analysis. A typical marine riser is a long non-uniform beam structure with discontinuities. Its variable properties include mass density, bending stiffness, and effective tension. Due to discontinuities such as buoyancy elements, the mass per unit length changes discontinuously. The dynamic behavior of such a slender system having variable properties and discontinuities is difficult to predict.

Floating production platforms require more complex riser configurations for well production or fluid injection fluids, between the subsea well-heads and the surface production facilities [19]. One type of riser assembly is made up of two concentric cylinders separated by a gap filled with viscous fluid. Centralizers are discretely and longitudinally distributed in between the two cylinders. Both predicting VIV and suppressing vibration require analysis of a coupled two-riser system, evaluation of the effects of coupling factors, and determination of the spacing of centralizers.

This thesis focuses on the dynamics of a long slender non-uniform riser structure and a coupled double-riser system. The specific objectives are as follows:

(1) to construct effective numerical approaches for a long non-uniform marine riser with discontinuities and variable properties including bending rigidity, mass per unit length, and effective tension;

(2) to explore new means such as dynamic vibration absorbers and wave-absorbing terminations to control vibration; and

(3) to formulate a coupled double-riser system and to numerically evaluate the effects of coupling factors, such as fluid viscosity and spacing of centralizers between two risers.

1.2 Technical Summary of Numerical Methods

A typical marine riser is a non-uniform beam structure with discontinuities. An analytical solution to its partial differential equation is generally not possible. We have to use a numerical technique for analyzing the dynamic behavior of a marine riser. A number of approaches can be employed to analyze marine risers, such as the Transfer Matrix Method (TMM), the Finite Element Method (FEM), the Finite Difference Method (FDM), and the Dynamic Stiffness Method (DSM). Each method has its advantages and disadvantages.

The transfer matrix method

The TMM, also known as the line-solution technique, has its origin in Germany. It is one of the most appropriate methods for the analysis of a chain-type structure because only successive multiplications are necessary to fit the elements together and intermediate conditions have no effect on the order of transfer matrix required. Hence, this method handles discontinuities very conveniently.

The line-solution methodology theoretically can be applied to appropriate structural members to solve problems involving almost any physically conceivable situations to which a line-type solution applies. However, the fact that a computer requires

calculations to be performed on the basis of a limited number of digits introduces complications into the numerical implementation of a line solution for certain classes of members, such as those members whose higher natural frequencies are to be sought and those members which include stiff spring supports. Numerical problems arise when large, almost equal numbers are subtracted. Due to the limited number of digits carried by computers, the results may be inaccurate or totally meaningless.

It has been found that the TMM works quite well for a string model but will have numerical problems for a beam structure when its length is larger and a high natural frequency analysis is desired. In this case, we have to improve the TMM to avoid the numerical problems.

The finite element method and the finite difference method

The FEM is a flexible and powerful tool which is widely used in engineering, and which in particular is employed extensively in the analysis of solids and structures. The FEM requires the division of a structural domain into many subdomains called elements. On the basis of frequency-independent shape functions, it effectively reduces a continuous model into one having finite degrees of freedom. The accuracy with which the behavior of the substitute finite degrees-of-freedom system represents that of the real structure clearly depends on the number of elements and their assumed shape functions. The FDM gives a pointwise approximation of the governing equation. The accuracy of this method depends on the number of grid points. It can give accurate results if sufficient grid points are used. Hence, both methods are effective for the analysis of lower frequencies of structures. If high natural frequencies are to be sought, a large number of degrees of freedom is required.

For a uniform beam element under linearly varying tension, we have found the stiffness matrix using the FEM, shown in Appendix A. This matrix is more efficient than that of a conventional constantly-tensioned element in analyzing a uniform riser under linearly varying tension.

The dynamic stiffness method

Historically, Kolosek first presented the idea of the DSM in the early 1940s and found an elaborate formulation of this method in 1950. This method has a great appeal

since it is based on the exact dynamic stiffness matrix derived from the free vibration analysis. The DSM performs free and forced vibration analysis within the differential equation theory of beams, thus avoiding assumed modes and lumped masses. This method enables one to analyze an infinite number of natural frequencies and modes by means of a finite number of degrees of freedom. The difference between the DSM and the FEM is that the shape function in DSM is frequency-dependent while that in the FEM is independent of frequency. The DSM is appropriate for the analysis of low frequencies as well as high frequencies.

A marine riser structure possesses a predominant chain-type topology. For risers in deep water areas, the high order natural frequencies and multiple modes are potentially excited by VIV. Hence, this thesis employs and explores the TMM and DSM for the analysis of a long slender non-uniform riser structure and a complicated coupled double-riser system.

1.3 Overview of this thesis

This thesis investigates the vibration analyses of a long slender non-uniform riser structure with discontinuities and a coupled double-riser system by improving the transfer matrix and dynamic stiffness methods, explores new means such as dynamic vibration absorbers and wave-absorbing terminations to control vibration, and evaluates the effects of coupling factors on the frequency response of a coupled dual riser system.

Chapter 1 states the topic and specific objectives of this thesis, summarizes the numerical methods which are employed for the analysis of marine risers, and presents the two methods, the TMM and DSM, to be used and explored in the thesis.

Chapter 2 discusses the transfer matrix method and its application for a beam structure. The first few sections outline the transfer matrix method and illustrate the applications with examples. In order to consider wave propagation in a beam structure with discontinuities, the chapter derives wave transmission and reflection

matrices in terms of transfer-matrix elements. The method presents numerical problems in analyzing a beam structure when the length is very large or high natural frequencies are desired. The chapter specifically introduces the delta-matrix method and illustrates the method with examples. We often approximate a non-uniform beam by a number of stepped uniform ones. This chapter investigates three approximate schemes for a beam structure under variable tension and shows their convergence rates with an example. This chapter finally presents a symbolic operation-based transfer matrix method to avoid numerical problems.

Chapter 3 introduces the dynamic stiffness matrix analysis of a uniform beam structure and discusses the analysis of complex natural frequencies. For a uniform Euler beam, the chapter derives the elemental dynamic stiffness matrix and the corresponding frequency-dependent mass and stiffness matrices. The global dynamic stiffness matrix is then assembled as in the FEM. Natural frequencies are determined by equating the frequency determinant to zero. The chapter introduces the Wittrick-Williams (W-W) algorithm, as a more reliable method for determining natural frequencies. In order to include damping effects, this chapter finds complex frequencies by means of the Muller method.

Chapter 4 investigates the vibration analysis of non-uniform marine risers by combining the DSM procedure in Chapter 3 with the WKB theory, which assumes that the coefficients in the differential equation of motion are slowly varying. The WKB-based elemental dynamic stiffness matrix is first derived and the frequency-dependent shape function is expressed implicitly. Natural frequencies are found by equating to zero the determinant of a global dynamic stiffness matrix. Two non-uniform risers appear as an illustration of the efficiency of this method.

Chapter 5 extends the W-W algorithm to the analysis of a general non-uniform marine riser and combines the algorithm with the WKB-based dynamic stiffness method described in Chapter 4. This technique allows automatic computation of natural frequencies of a non-uniform beam structure. On the basis of the WKB-based DSM, the chapter derives the formulas for calculating mode shapes, slopes and curvatures. This chapter further analyzes marine riser models with complex bound-

ary conditions.

Chapter 6 generalizes the internal relationship between the TMM and the DSM and discusses its application. Due to different sign conventions which may be used in the two methods, the chapter generalizes the relationship by introducing corresponding transformation matrices. Using this internal relationship, the chapter then derives an implicit transfer matrix of a non-uniform beam from the dynamic stiffness matrix found in Chapter 4 and shows the application by an example of a riser under linearly varying tension. Again, using the relationship, the chapter improves the WKB-based DSM for describing a non-uniform beam structure with discontinuities. Further using the relationship, this chapter establishes a dynamic stiffness library.

Chapter 7 discusses the vibration suppression of a general beam structure by means of dynamic vibration absorbers and wave-absorbing terminations. The first few sections introduce the optimal tuning of a single dynamic vibration absorber to a uniform beam. The chapter next studies optimal tuning of multiple identical dynamic absorbers to a uniform beam with general boundary conditions. The chapter next investigates optimal tuning of multiple identical absorbers to a non-uniform beam system under varying tension. Since practical structures have structural damping, the chapter discusses the effects of structural damping on the optimal tuning. Based on the research by Vandiver and Li, this chapter further extends the analysis of wave-absorbing terminations of a beam system.

Chapter 8 systematically investigates the vibration analysis of coupled beams. The first few sections discuss the coupled vibration analysis and the optimal tuning of a dynamic absorbing beam, coupled by distributed springs and dampers to a second beam. The chapter then analyzes the coupled system in which both uniform beams are under constant tension. The complexity of the coupled system is next increased by the introduction of an ideal fluid in between two beams. The effects of the fluid on natural frequencies and mode shapes are discussed. A practical composite riser structure is modeled as a generally coupled double-beam system, in which both beams are non-uniform ones under variable tension, the fluid in between the beams is viscous, and stiffness and damping from discrete centralizers are longitudinally distributed.

The chapter mathematically formulates the coupled system, numerically solves for both real and complex natural frequencies, and evaluates the effects of coupling factors on the vibration.

Chapter 9 summarizes new contributions made in this thesis and recommends further research in the future.

Chapter 2

Transfer Matrix Method

2.1 Introduction

The transfer matrix method is ideally suited to vibration analysis of a structure which has a predominant chain topology. The size of the transfer matrices is dependent on the order of the differential equations of the system. Discontinuities such as a concentrated mass and a mass-spring absorber present no difficulty since they have no effect on the order of the transfer matrices required. A marine riser is a chain-like structure and it is convenient to employ the transfer matrix method to analyze it. Li and Vandiver [11, 20] modeled a marine riser as a string system and studied the wave propagation by the transfer matrix method.

However, this method has numerical problems in solving beam-like structures when the structural length is very large or high order natural frequencies are desired [21]. Researchers have been improving the method to avoid the numerical problems [22].

The next section of this chapter briefly outlines the transfer matrix method. The third section illustrates the applications of the method with examples, solving for natural frequencies and mode shapes. The fourth section derives the wave transmission and reflection matrices in a beam structure due to discontinuities and gives illustrative examples. The fifth section discusses the numerical problems of the method in analyzing a beam structure, specifically introduces the delta-matrix method, and

illustrates the improved method with examples. The sixth section investigates three approximate schemes for a beam structure under variable tension and shows their convergence rates with an example. The final section of this chapter presents a symbolic operation-based transfer matrix method to avoid the numerical problems.

2.2 An outline of the transfer matrix method

2.2.1 state vector and transfer matrix

The state vector at a point i of an elastic system is a column vector whose components are the generalized displacements and the corresponding generalized forces at the point. For a uniform beam, the displacements are lateral displacement y and slope θ, and the corresponding forces are shear force Q and bending moment M. The state vector in this case is:

$$\mathbf{s}_i = \begin{bmatrix} y \\ \theta \\ M \\ Q \end{bmatrix}. \tag{2.1}$$

We should note that the displacements and corresponding forces in Eq. (2.1) are in positions which are symmetrical about the center of the column.

We define the transfer matrix as the matrix which relates two state vectors at different positions in an elastic system, namely:

$$\mathbf{s}_{i+1} = \mathbf{U}_i \, \mathbf{s}_i, \tag{2.2}$$

in which $\mathbf{U}_i$ is the transfer matrix and $\mathbf{s}_i$ and $\mathbf{s}_{i+1}$ are the state vectors at stations i and $i+1$, respectively. It is evident that if there are n components in the column vector, then the transfer matrix is square and of the order of n. When i and $i+1$ are the different points of a continuous system, the transfer matrix relating the state vectors at these points is known as a field matrix. The transfer matrix relating the state vectors on either side of a point is known as a point matrix.

There are a number of approaches to deriving a field matrix [21]. A uniform beam section, shown in Figure 2-1, appears as an example.

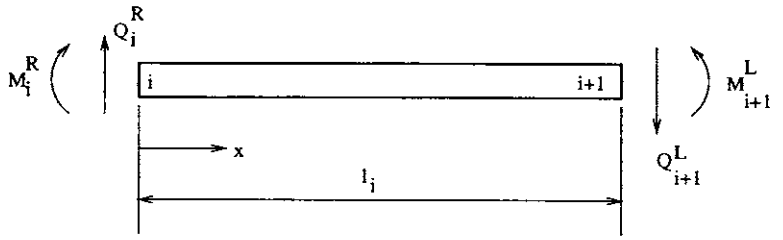

Figure 2-1: A typical uniform beam section

The differential equation of motion for a beam is:

$$EI\frac{d^4Y}{dx^4} - \rho A\omega^2 Y = 0, \tag{2.3}$$

where ρA is the mass per unit length, EI is the bending stiffness, and Y is the transverse displacement amplitude. We find its transfer matrix on the basis of Eq. (2.3):

$$\mathbf{U}_i = \begin{bmatrix} S(kl_i) & \frac{1}{k}T(kl_i) & \frac{1}{EIk^2}U(kl_i) & \frac{1}{EIk^3}V(kl_i) \\ kV(kl_i) & S(kl_i) & \frac{1}{EIk}T(kl_i) & \frac{1}{EIk^2}U(kl_i) \\ EIk^2U(kl_i) & EIkV(kl_i) & S(kl_i) & \frac{1}{k}T(kl_i) \\ EIk^3T(kl_i) & EIk^2U(kl_i) & kV(kl_i) & S(kl_i) \end{bmatrix}, \tag{2.4}$$

in which $k^4 = \frac{\rho A\omega^2}{EI}$ and the frequency-dependent functions are:

$$\begin{aligned} S(kl_i) &= \frac{1}{2}[\cosh(kl_i) + \cos(kl_i)]; \\ T(kl_i) &= \frac{1}{2}[\sinh(kl_i) + \sin(kl_i)]; \\ U(kl_i) &= \frac{1}{2}[\cosh(kl_i) - \cos(kl_i)]; \\ V(kl_i) &= \frac{1}{2}[\sinh(kl_i) - \sin(kl_i)]. \end{aligned}$$

A point matrix relating the left and right state vectors at a discontinuity can be

constructed by considering dynamic equilibrium of the point.

2.2.2 Eliminating intermediate state vectors and finding frequency determinant

Elimination of intermediate state vectors

Taking a uniform beam as an example, we divide the beam into n sections without lumping the masses at the station points, as shown in Figure 2-2.

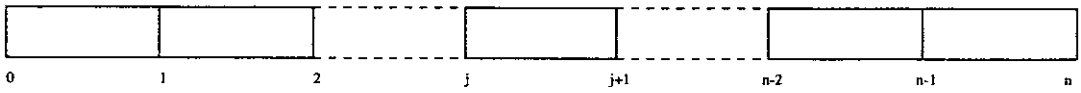

Figure 2-2: A beam divided into n sections

Equation (2.4) shows the transfer matrix of a uniform beam. The following matrix relations exist between adjacent state vectors:

$$\begin{aligned} \mathbf{s}_1^L &= \mathbf{U}_1\mathbf{s}_0; \\ \mathbf{s}_2^L &= \mathbf{U}_2\mathbf{s}_1^R; \\ &\vdots \\ \mathbf{s}_{n-1}^L &= \mathbf{U}_{n-1}\mathbf{s}_{n-2}^R; \\ \mathbf{s}_n &= \mathbf{U}_n\mathbf{s}_{n-1}^R. \end{aligned} \tag{2.5}$$

Noting that $\mathbf{s}_i^L = \mathbf{s}_i^R$ $(i = 1, 2, \cdots n-1)$ in this case, we obtain from the last two equations in (2.5):

$$\mathbf{s}_n = \mathbf{U}_n\,\mathbf{U}_{n-1}\mathbf{s}_{n-2}^R. \tag{2.6}$$

We continue this procedure until obtaining the relation between the state vectors at the two ends of the beam:

$$\mathbf{s}_n = \mathbf{U}_n\,\mathbf{U}_{n-1}\cdots\mathbf{U}_2\,\mathbf{U}_1 \equiv \mathbf{U}\,\mathbf{s}_0, \tag{2.7}$$

where **U** is the overall transfer matrix formed by taking the products of all the intermediate transfer matrices in the order indicated. In this manner all the intermediate state vectors have been eliminated.

Frequency determinant

Equation (2.7) is expanded as:

$$\begin{bmatrix} y \\ \theta \\ M \\ Q \end{bmatrix}_n = \begin{bmatrix} u_{11} & u_{12} & u_{13} & u_{14} \\ u_{21} & u_{22} & u_{23} & u_{24} \\ u_{31} & u_{32} & u_{33} & u_{34} \\ u_{41} & u_{42} & u_{43} & u_{44} \end{bmatrix} \begin{bmatrix} y \\ \theta \\ M \\ Q \end{bmatrix}_0 . \tag{2.8}$$

The frequency determinant is formulated by applying the boundary conditions to Eq. (2.8). For a simply-supported beam, the boundary conditions are:

$$y_0 = 0, \quad M_0 = 0, \quad y_n = 0, \quad M_n = 0. \tag{2.9}$$

Substituting Eq. (2.9) into (2.8) leads to:

$$\begin{aligned} u_{12}\,\theta_0 + u_{14}\,Q_0 &= 0, \\ u_{32}\,\theta_0 + u_{34}\,Q_0 &= 0. \end{aligned} \tag{2.10}$$

For a nontrivial solution of Eq. (2.10), the determinant of the coefficients must be zero, namely:

$$\begin{vmatrix} u_{12} & u_{14} \\ u_{32} & u_{34} \end{vmatrix} = 0. \tag{2.11}$$

Since the elements u_{ik}, $(i, k = 1, \cdots, 4)$ are known functions of the circular frequency ω, this frequency determinant serves to calculate the natural frequencies of the beam structure.

For other boundary conditions the frequency equation will require that other sub-determinants of the overall transfer matrix **U** vanish. For example, for a beam clamped at station 0 and free at station n, we find the frequency equation by following

the same procedure:

$$\begin{vmatrix} u_{33} & u_{34} \\ u_{43} & u_{44} \end{vmatrix} = 0. \tag{2.12}$$

Once the natural frequencies are known, we set equal to one one of the state components corresponding to the final frequency determinant. The other state component is found by means of one of the final equations such as Eq. (2.10). It then follows that the corresponding state variables at all stations can be determined. Hence, we obtain the mode shape in this procedure.

2.2.3 Response analysis

In order to find steady-state forced vibrations, we add an extra column to the transfer matrix Eq. (2.4) to include forcing terms. The extended state vector and transfer matrix are:

$$\bar{\mathbf{s}}_i = \begin{bmatrix} y \\ \theta \\ M \\ Q \\ 1 \end{bmatrix}, \tag{2.13}$$

$$\bar{\mathbf{U}} = \begin{bmatrix} u_{11} & u_{12} & u_{13} & u_{14} & 0 \\ u_{21} & u_{22} & u_{23} & u_{24} & 0 \\ u_{31} & u_{32} & u_{33} & u_{34} & f_m \\ u_{41} & u_{42} & u_{43} & u_{44} & f_q \\ 0 & 0 & 0 & 0 & 1 \end{bmatrix}, \tag{2.14}$$

where f_m and f_q are external moment and force, respectively.

For example, the extended point matrix of a concentrated mass m_i, on which a

harmonic force $p(t) = p_0 e^{i\omega t}$ acts, is:

$$\bar{\mathbf{U}}_i = \begin{bmatrix} 1 & 0 & 0 & 0 & 0 \\ 0 & 1 & 0 & 0 & 0 \\ 0 & 0 & 1 & 0 & 0 \\ \omega^2 m_i & 0 & 0 & 1 & p_0 \\ 0 & 0 & 0 & 0 & 1 \end{bmatrix}. \tag{2.15}$$

As in the undamped case, the relation between the state vectors at the boundaries 0 and n of the system is achieved by the multiplication of the extended transfer matrices. The unknown initial parameters at the boundaries are first solved. Hence the state vector at each node can be obtained as previously.

2.3 Vibration analysis of a beam structure with discontinuities

In order to solve natural frequencies and mode shapes, we first find field matrices of continuous sections and point matrices at discontinuities. For a uniform beam section under constant tension, we derive its transfer matrix from the differential equation of motion, as shown in the example of Section 2.7. The transfer matrix is also available in [21]. However, we need to note the differences in the sign convention. The point matrix describing the mass-spring-dashpot absorber is found as follows:

$$\mathbf{U}_c = \begin{bmatrix} 1 & 0 & 0 & 0 \\ 0 & 1 & 0 & 0 \\ 0 & 0 & 1 & 0 \\ \frac{m\omega^2(k+i\omega c)}{k-m\omega^2+i\omega c} & 0 & 0 & 1 \end{bmatrix}, \tag{2.16}$$

where m is the mass of the absorber, k is the spring stiffness, and c is the damping of the absorber.

With the field and point matrices, we calculate the overall transfer matrix and

then find the frequency determinant by means of the boundary conditions. We determine the natural frequencies by plotting the determinant versus frequency. Once natural frequencies are found, the corresponding mode shapes are calculated by following the procedure in Section 2.2.

Since the field and point matrices are available, we can easily obtain the corresponding extended matrices by including the terms of external exciting forces. Following the procedure in Section 2.2.3, we solve for the state vector at each node and hence find the steady-state response.

The following examples illustrate the vibration analysis of a beam structure with discontinuities by means of the transfer matrix method.

(1) A simply-supported uniform beam under constant tension

A simply-supported uniform beam first appears as an illustration. The beam's specification is as follows:

Length $l = 50.8$ m;

Mass per unit length $\rho A = 78.0$ kg/m;

Bending rigidity $EI = \frac{4\rho Al}{\pi}\ Nm^2$; and

Tension $T = 10000$ N.

The analytical solutions of natural frequencies are:

$$\omega_n = \frac{n^2\pi^2}{l^2}\sqrt{\frac{EI}{\rho A}}\sqrt{1+\frac{Tl^2}{n^2\pi^2 EI}}, \quad (n = 1, 2, ...). \tag{2.17}$$

Figure 2-3 shows the determinant of the transfer matrix of the beam versus frequency. The troughs correspond to the natural frequencies. Table (2.1) indicates the first seven natural frequencies found by means of the TMM and Eq. (2.17). This table demonstrates that the TMM is accurate in finding the natural frequencies.

The mode shapes can be found numerically and compared to the analytical solution which is known to be $\phi_n(x) = \sin(\frac{n\pi x}{l})$. The mode shapes are normalized to have maximum amplitude 1.0.

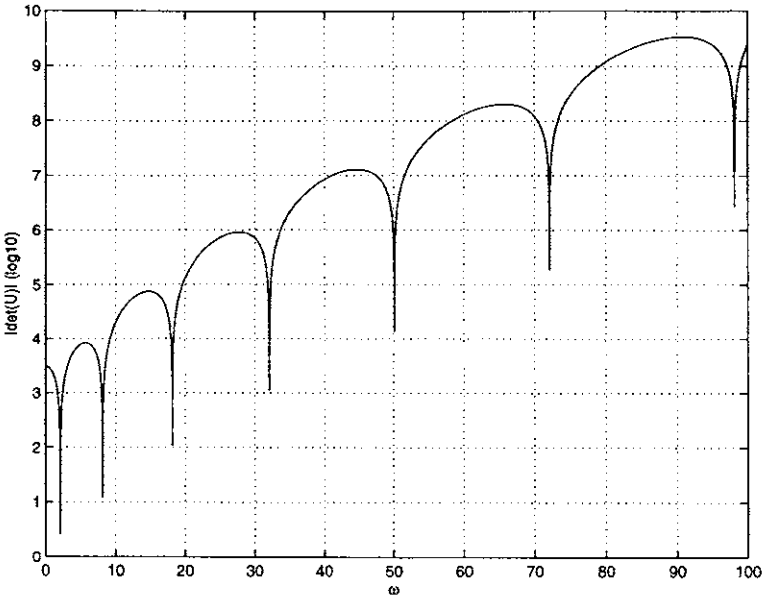

Figure 2-3: The determinant of the transfer matrix versus frequency

order	by TMM	by Eq. (2.17)
1	2.12	2.12
2	8.12	8.12
3	18.12	18.12
4	32.12	32.12
5	50.12	50.12
6	72.12	72.12
7	98.13	98.12

Table 2.1: Comparison of natural frequencies found by using the TMM and the analytical solutions

(2) A simply-supported and constantly tensioned uniform beam optimally tuned by an absorber

We attach an undamped mass-spring absorber at the midpoint of the beam in **(1)**, shown in Figure 2-4. The absorber is optimized to tune the first mode of the beam:

The first natural frequency: $\Omega_1 = 2.12$;

The first modal mass of the beam: $m_b = \rho A l/2$;

Natural frequency of absorber: $\omega_a^2 = k/m$;

Absorber mass ratio: $\mu = m/m_b = 0.01$; and

Optimal frequency ratio [25]: $f = \omega_a/\Omega_1 = 1/(1+\mu) = 0.9091$.

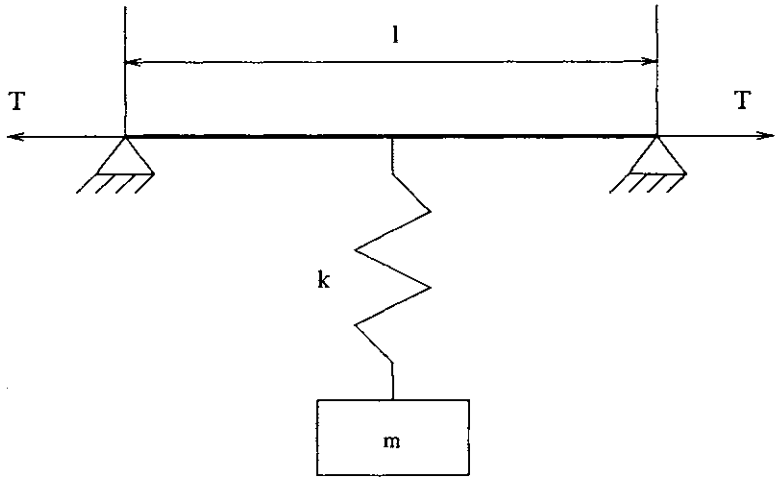

Figure 2-4: The simply-supported constantly tensioned uniform beam attached by a mass-spring absorber at the midpoint

We evenly discretize the beam into two segments so that each segment has the same transfer matrix. The undamped point matrix describing the discontinuity due to the absorber is obtained from Eq. (2.15) by setting $c = 0$. The overall transfer matrix is the product of all the field and point matrices. We then find the natural frequencies by plotting the corresponding undamped frequency determinant. Figure 2-5 shows the determinant versus circular frequency. The first eight natural frequencies are found by inspecting those coinciding with the troughs: 1.72, 2.36, 8.12, 18.14, 32.12, 50.12, 72.12, and 98.12.

Comparing the results with those obtained in (**1**), we find that the absorber causes the first natural frequency to split into two but has little influence on higher order natural frequencies. Figure 2-6 shows the first four mode shapes and indicates that the first two mode shapes corresponding to the first two natural frequencies are similar. The mode shapes as drawn do not show the position of the absorber which is in phase with the beam for the lowest frequency and out of phase for the second frequency.

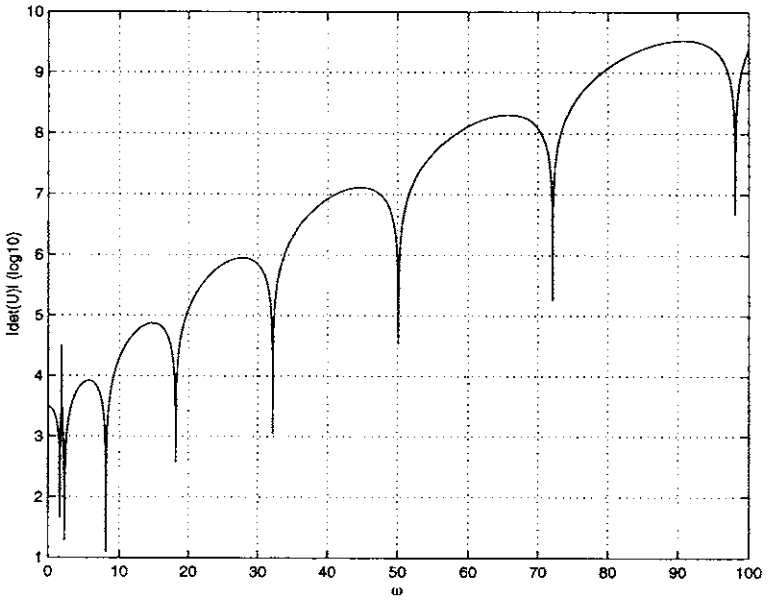

Figure 2-5: The determinant of the transfer matrix versus frequency

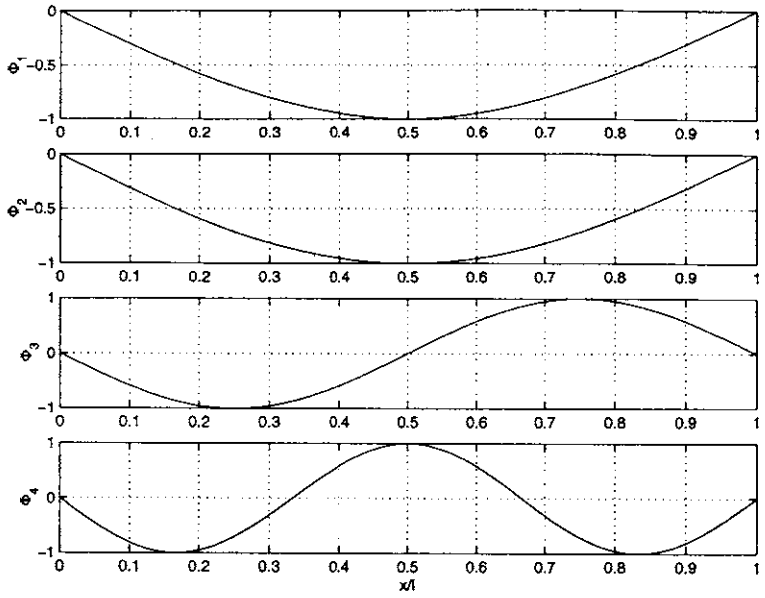

Figure 2-6: The first four modes of the composite system

(3) Steady-state response of a free-free pipe structure

Case (a): A uniform free-free pipe

The parameters of the pipe are as follows:

Length: $l = 6.10\,m$;

Outer diameter: $d_o = 0.0230\,m$;

Inside diameter: $d_i = 0.0206\,m$;

Bending rigidity: $EI = 1.0284 \times 10^3\ N.m^2$; and

Amplitude of the exciting force at the left end: $p_o = 1000\,N$.

Figure 2-7 shows the transfer mobility (α_{RL}) versus frequency. The mobility (α_{RL}) is the harmonic velocity at R due to a unit exciting force at L. We calculate the velocity amplitude of the right end due to the unit harmonic exciting force at the left end. The peaks correspond to the natural frequencies. The first elastic natural frequency found from this figure is 3.84 while the analytical solution is 3.83. Other natural frequencies are all close to those analytical values.

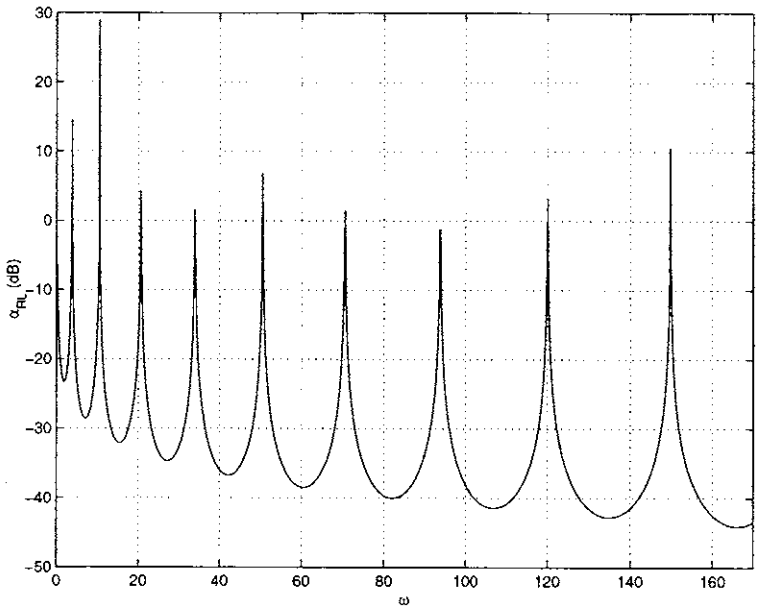

Figure 2-7: The transfer mobility of the free-free pipe

Case (b): A uniform free-free pipe with mass attachment at midpoint

On the basis of the free-free pipe in **(a)**, we attach a concentrated mass (m=1.40 kg) at the midpoint, shown in Figure 2-8. Figure 2-9 shows the transfer mobility (α_{RL}) versus frequency. The result in **(a)** is also included for comparison.

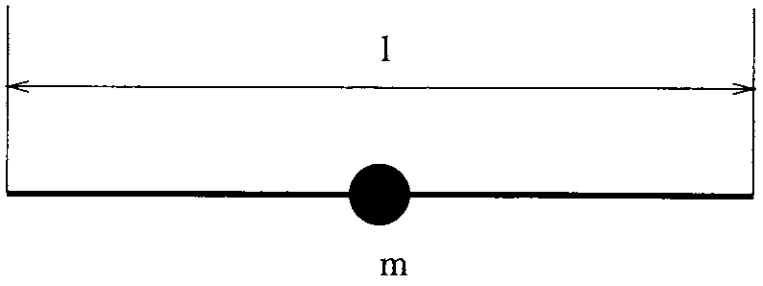

Figure 2-8: The simply-supported constantly tensioned uniform beam attached by a mass-spring absorber at the midpoint

For a free-free beam, the midpoint is a node of even elastic modes. Hence, for the even elastic modes, the mass attachment has no influence. Figure 2-9 indicates that

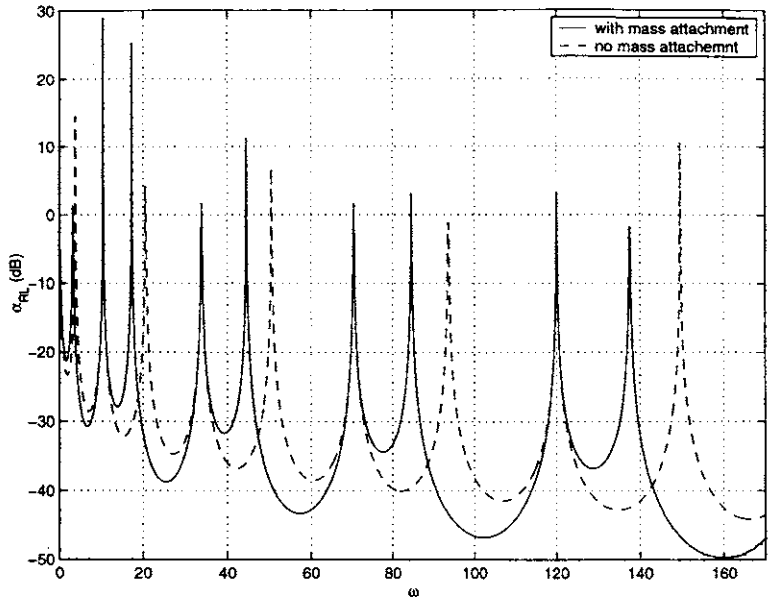

Figure 2-9: The transfer mobility of the free-free pipe with mass attachment

the natural frequencies of the even elastic modes are identical and that the mobility peaks coincide at the frequencies. For odd elastic modes, the midpoint is not a node. The mass attachment influences the old elastic modes, and it increases inertia of the system. Thus Figure 2-9 shows that the natural frequencies of the odd elastic modes are lower than in the case without the mass attachment.

2.4 Wave reflection and transmission in a beam structure due to discontinuities

2.4.1 The derivation of wave reflection and transmission matrices

The equation of motion of a uniform beam under constant tension is:

$$EI\frac{d^4y}{dx^4} - T\frac{d^2y}{dx^2} + \rho A\frac{d^2y}{dt^2} = 0, \tag{2.18}$$

where $y(x,t)$ is the displacement of the beam, EI is the flexural rigidity, ρA is mass per unit length of the beam, and T is the tension. The shear force Q and bending moment M are:

$$Q = EI\,\partial^3 y/\partial x^3 - T\,\partial y/\partial x, \qquad M = EI\,\partial^2 y/\partial x^2. \tag{2.19}$$

Assuming $y(x,t) = e^{i(kx-i\omega t)}$, and substituting it into Eq. (2.18) results in the following dispersion relation:

$$EI\,k^4 + T\,k^2 - \rho A\omega^2 = 0, \tag{2.20}$$

where the propagating wavenumber k_1 and evanescent wavenumber k_2 are:

$$\begin{aligned} k_1 &= \pm\sqrt{-\frac{1}{2}(\frac{T}{EI})^2 + \sqrt{\frac{1}{4}(\frac{T}{EI})^4 + \frac{\rho A\omega^2}{EI}}}, \\ k_2 &= \pm i\sqrt{\frac{1}{2}(\frac{T}{EI})^2 + \sqrt{\frac{1}{4}(\frac{T}{EI})^4 + \frac{\rho A\omega^2}{EI}}}. \end{aligned} \tag{2.21}$$

The solution to Eq. (2.18) can be written as the sum of four flexural wave components:

$$y(x,t) = (a^+ e^{-ik_1 x} + a^- e^{ik_1 x} + a_N^+ e^{-k_2 x} + a_N^- e^{k_2 x})e^{i\omega t}, \tag{2.22}$$

where the amplitude a may be complex. The a^+ and a^- represent respectively positive-going and negative-going propagating waves and the a_N^+ and a_N^- are positive- and negative-going attenuating waves which decay exponentially.

As in [26], we group the wave amplitudes into 2×1 vectors of positive-going waves $\mathbf{a}^+$ and negative-going waves $\mathbf{a}^-$:

$$\begin{aligned} \mathbf{a}^+ &= \begin{pmatrix} a^+ \\ a_N^+ \end{pmatrix}, \\ \mathbf{a}^- &= \begin{pmatrix} a^- \\ a_N^- \end{pmatrix}. \end{aligned} \tag{2.23}$$

With Eq. (2.22), we calculate the derivatives of $y(x,t)$ and suppress the time-dependent term of $e^{i\omega t}$:

$$\begin{aligned}
\frac{\partial y}{\partial x} &= -ik_1 a^+ e^{-ik_1 x} + ik_1 a^- e^{ik_1 x} - k_2 a_N^+ e^{-k_2 x} + k_2 a_N^- e^{k_2 x};\\
\frac{\partial^2 y}{\partial x^2} &= -k_1^2 a^+ e^{-ik_1 x} - k_1^2 a^- e^{ik_1 x} + k_2^2 a_N^+ e^{-k_2 x} + k_2^2 a_N^- e^{k_2 x};\\
\frac{\partial^3 y}{\partial x^3} &= ik_1^3 a^+ e^{-ik_1 x} - ik_1^3 a^- e^{ik_1 x} - k_2^3 a_N^+ e^{-k_2 x} + k_2^3 a_N^- e^{k_2 x}. \qquad (2.24)
\end{aligned}$$

The bending moment M and shear force Q are expressed in terms of wave amplitudes by means of Eq. (2.19):

$$\begin{aligned}
M &= EI(-k_1^2 a^+ e^{-ik_1 x} - k_1^2 a^- e^{ik_1 x} + k_2^2 a_N^+ e^{-k_2 x} + k_2^2 a_N^- e^{k_2 x});\\
Q &= i(EIk_1^3 + k_1 T)a^+ e^{-ik_1 x} - i(EIk_1^3 + k_1 T)a^- e^{ik_1 x}\\
&\quad -(EIk_2^3 - k_2 T)a_N^+ e^{-k_2 x} + (EIk_2^3 - k_2 T)a_N^- e^{k_2 x}. \qquad (2.25)
\end{aligned}$$

The state vector on the left of a discontinuity is written in terms of the wave amplitudes:

$$\mathrm{s} = \begin{pmatrix} y \\ \partial y/\partial x \\ M \\ Q \end{pmatrix} =$$

$$\begin{bmatrix} 1 & 1 & 1 & 1 \\ -ik_1 & -k_2 & ik_1 & k_2 \\ -EIk_1^2 & EIk_2^2 & -EIk_1^2 & EIk_2^2 \\ i(EIk_1^3 + k_1 T) & -(EIk_2^3 - k_2 T) & -i(EIk_1^3 + k_1 T) & (EIk_2^3 - k_2 T) \end{bmatrix} \begin{pmatrix} a^+ \\ a_N^+ \\ a^- \\ a_N^- \end{pmatrix}. \qquad (2.26)$$

Equation (2.26) is rewritten in the following abbreviated form:

$$\mathbf{s}_L = \mathbf{R}_L\, \mathbf{a}_L. \qquad (2.27)$$

The wave amplitudes $\mathbf{a}_L$ are formulated as:

$$\mathbf{a}_L = \mathbf{R}_L^{-1}\,\mathbf{s}_L. \tag{2.28}$$

Likewise, the wave amplitudes on the right side of the discontinuity are written as:

$$\mathbf{a}_R = \mathbf{R}_R^{-1}\,\mathbf{s}_R. \tag{2.29}$$

Using the TMM, we establish the relation between the state vectors on both sides of a discontinuity:

$$\mathbf{s}_R = \mathbf{u}\,\mathbf{s}_L. \tag{2.30}$$

Equations (2.27) to (2.30) lead to:

$$\mathbf{a}_R = (\mathbf{R}_R^{-1}\,\mathbf{u}\,\mathbf{R}_L)\mathbf{a}_L \equiv \mathbf{w}\mathbf{a}_L, \tag{2.31}$$

where $\mathbf{w} = \mathbf{R}_R^{-1}\,\mathbf{u}\,\mathbf{R}_L$.

A set of positive-going waves $\mathbf{a}_L^+$ is incident upon a discontinuity and gives rise to the transmitted $\mathbf{a}_R^+$ and reflected $\mathbf{a}_L^-$. The relations among the waves are defined as follows:

$$\begin{aligned} \mathbf{a}_R^+ &= \mathbf{t}\,\mathbf{a}_L^+, \\ \mathbf{a}_L^- &= \mathbf{r}\,\mathbf{a}_L^+, \end{aligned} \tag{2.32}$$

where $\mathbf{t}$ and $\mathbf{r}$ are the transmission and reflection matrices, respectively.

With Eqs. (2.32), we write Eq. (2.31) in the partitioned matrix form:

$$\mathbf{a}_R = \begin{pmatrix} \mathbf{a}_R^+ \\ \mathbf{a}_R^- \end{pmatrix} = \begin{bmatrix} \mathbf{w}_{11} & \mathbf{w}_{12} \\ \mathbf{w}_{21} & \mathbf{w}_{22} \end{bmatrix} \begin{pmatrix} \mathbf{a}_L^+ \\ \mathbf{r}\mathbf{a}_L^+ \end{pmatrix}. \tag{2.33}$$

Expanding Eqs. (2.33) results in:

$$\begin{aligned} \mathbf{a}_R^+ &= (\mathbf{w}_{11} + \mathbf{w}_{12}\mathbf{r})\,\mathbf{a}_L^+, \\ \mathbf{a}_R^- &= (\mathbf{w}_{21} + \mathbf{w}_{22}\mathbf{r})\,\mathbf{a}_L^+. \end{aligned} \tag{2.34}$$

Comparing the first equation in Eqs. (2.34) with the first one in Eqs. (2.32) leads to:

$$\mathbf{t} = \mathbf{w}_{11} + \mathbf{w}_{12}\mathbf{r}. \tag{2.35}$$

Noting that the incident waves are $\mathbf{a}_L$, we have $\mathbf{a}_R^- = \mathbf{0}$. Since the wave amplitudes $\mathbf{a}_L^+$ are arbitrary, the second equation in Eqs. (2.34) leads to:

$$\mathbf{r} = -\mathbf{w}_{22}^{-1}\,\mathbf{w}_{21}. \tag{2.36}$$

Substituting Eq. (2.36) into Eq. (2.35) results in:

$$\mathbf{t} = \mathbf{w}_{11} - \mathbf{w}_{12}\mathbf{w}_{22}^{-1}\mathbf{w}_{21}. \tag{2.37}$$

Hence, the reflection and transmission matrices are expressed in terms of elements of the transfer matrix.

2.4.2 Examples

(1) On boundaries of a simply-supported beam

As a special case, we consider wave reflection at boundaries of a simply-supported beam. The boundary conditions are: $y = 0$ and $M = 0$.

Substituting the boundary conditions into Eq. (2.26) leads to:

$$\begin{bmatrix} 1 & 1 \\ -EIk_1^2 & EIk_2^2 \end{bmatrix} \begin{pmatrix} a^+ \\ a_N^+ \end{pmatrix} + \begin{bmatrix} 1 & 1 \\ -EIk_1^2 & EIk_2^2 \end{bmatrix} \begin{pmatrix} a^- \\ a_N^- \end{pmatrix} = \begin{pmatrix} 0 \\ 0 \end{pmatrix} \tag{2.38}$$

With the definition of the reflection matrix $\mathbf{r}$ in Eqs. (2.32), Eqs. (2.38) are further written as:

$$\{\begin{bmatrix} 1 & 1 \\ -EIk_1^2 & EIk_2^2 \end{bmatrix} + \begin{bmatrix} 1 & 1 \\ -EIk_1^2 & EIk_2^2 \end{bmatrix} \mathbf{r}\} \begin{pmatrix} a^+ \\ a_N^+ \end{pmatrix} = \begin{pmatrix} 0 \\ 0 \end{pmatrix}. \tag{2.39}$$

Since the a^+ and a_N^+ are arbitrary, we then have:

$$\begin{bmatrix} 1 & 1 \\ -EIk_1^2 & EIk_2^2 \end{bmatrix} + \begin{bmatrix} 1 & 1 \\ -EIk_1^2 & EIk_2^2 \end{bmatrix} \mathbf{r} = \begin{pmatrix} 0 \\ 0 \end{pmatrix}. \tag{2.40}$$

At the simply-supported boundaries, $\mathbf{r}$ reduces to:

$$\mathbf{r} = \begin{bmatrix} -1 & 0 \\ 0 & -1 \end{bmatrix}. \tag{2.41}$$

This result is the same as that obtained in [26]. The elements in the first column of r are the familiar reflection coefficients for incident propagating waves.

(2) At the attachment point of a mass-spring absorber

For a constantly-tensioned uniform beam with a mass-spring absorber, we consider wave reflection and transmission at the attachment point. The specification of the composite system is:

Length of the beam: $l = 592.53$ m;

Bending rigidity: $EI = 2.8219 \times 10^7\ N.m^2$;

Mass per unit length: $\rho A = 169.21$ kg;

Tension: $T = 3.1442 \times 10^5$ N;

Mass ratio (absorber mass/beam modal mass of first mode): $\mu = 1/20$;

Natural frequency of absorber: $\omega_a^2 = k_{ab}/m_{ab}$;

The first circular natural frequency of the beam: $\Omega_1 = 0.2288$; and

Optimal frequency ratio: $f = \omega_a/\Omega_1 = 1/(1+\mu) = 0.9524$.

Figure 2-10 shows the transmission coefficients versus frequency. This figure indicates

that at the optimal frequency ratio f, the incident propagating wave is totally reflected ($t_{11} \approx 0$ at the point).

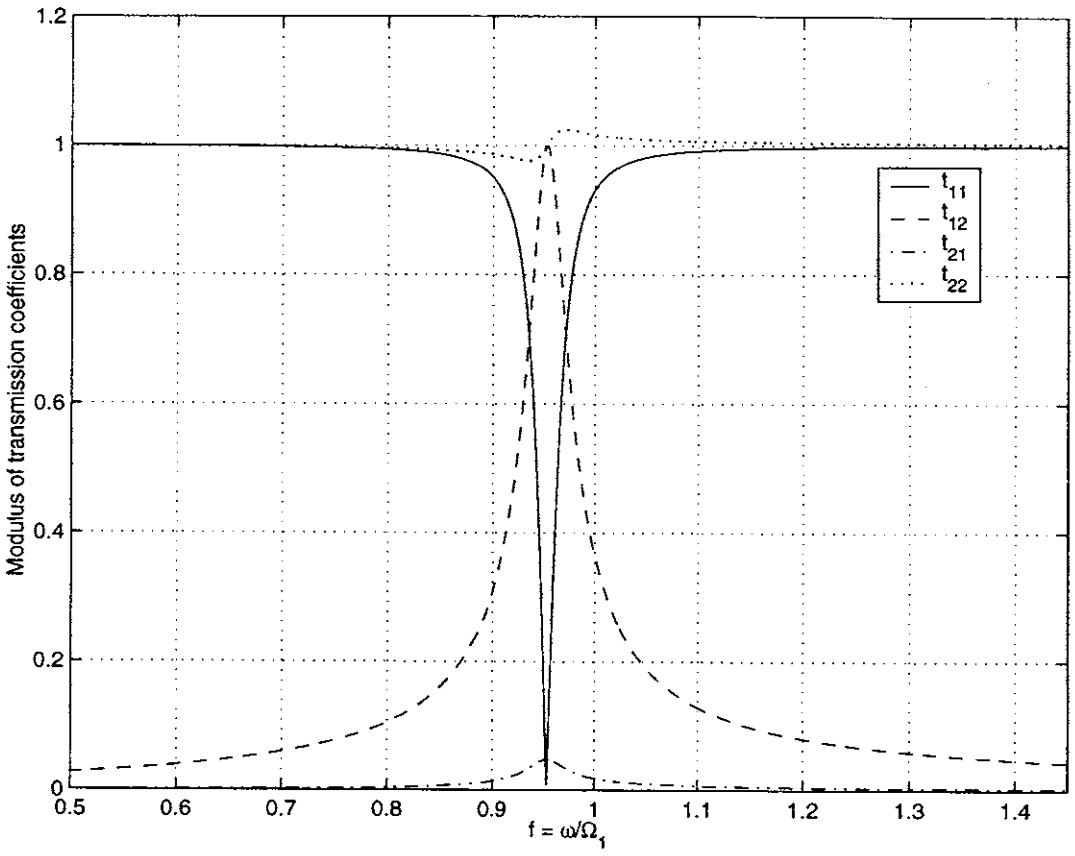

Figure 2-10: The modulus of transmission coefficients

(3) A change in the section

We now discuss wave reflection and transmission due to a change in a beam section. The left side of the beam has the same properties as in Example (**2**). The right side of the beam has similar properties except that $EI_r = 2EI$.

Figure 2-11 demonstrates the reflection and transmission coefficients for the section change of the beam. This figure indicates that due to the impedance mismatching, incident waves give rise to reflected and transmitted waves at the discontinuity. The reflection and transmission wave amplitudes are found by calculating $[\mathbf{r}]\{\mathbf{a}_{in}\}$ and $[\mathbf{t}]\{\mathbf{a}_{in}\}$, respectively. The elements in the first column of $\mathbf{r}$ and $\mathbf{t}$ are the wave amplitudes due to a unit propagating wave while the elements in the second column correspond to those due to a unit evanescent wave.

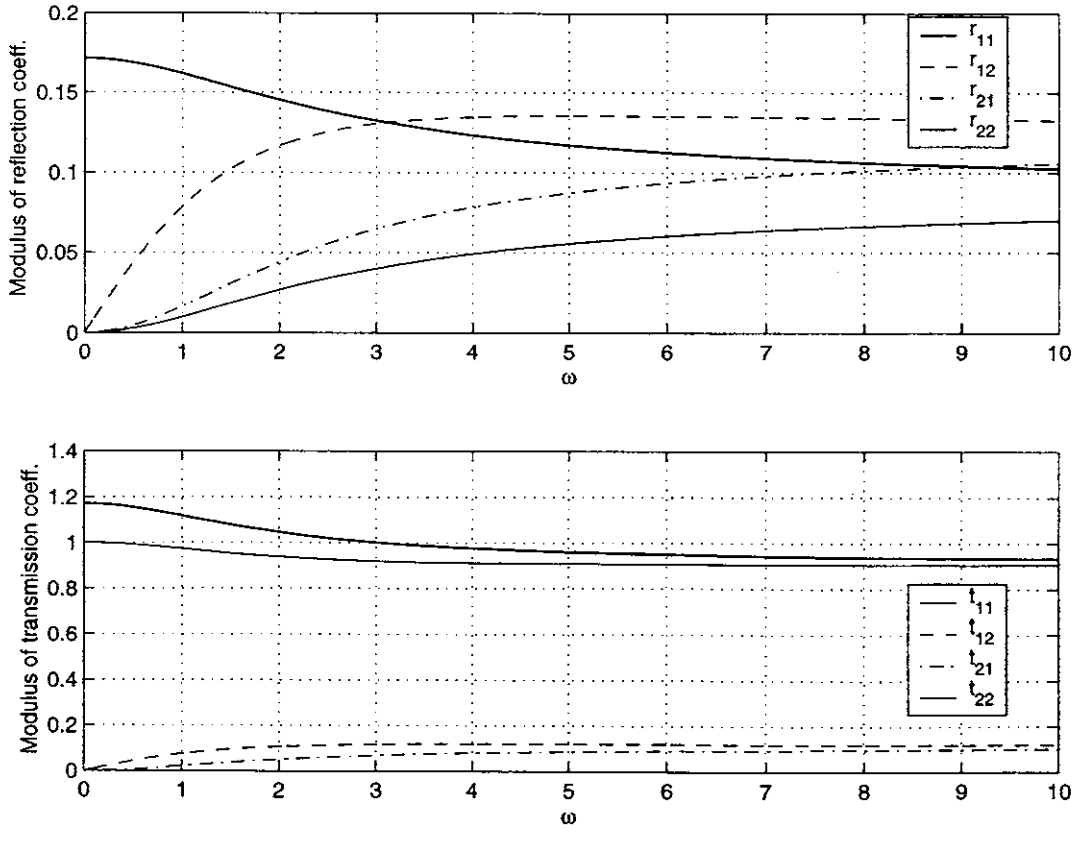

Figure 2-11: The reflection and transmission coefficients of $\mathbf{r}$ and $\mathbf{t}$

2.5 Numerical difficulties and the delta-matrix

2.5.1 Numerical difficulties

Although from the theoretical standpoint all problems in the transfer matrix method have been solved, this method has a special place among other matrix methods. Numerical difficulties prevent wide applications of the method ([21],[22]) .

In order to demonstrate the numerical difficulties with the ordinary transfer matrix method, we consider a simply-supported uniform beam. Equation (2.4) shows the transfer matrix of the beam. Equation (2.11) depicts the frequency equation, which can be specifically written as:

$$\begin{vmatrix} \frac{1}{2k}[\sinh(kl)+\sin(kl)] & \frac{1}{2EIk^3}[\sinh(kl)-\sin(kl)] \\ \frac{EIk}{2}[\sinh(kl)-\sin(kl)] & \frac{1}{2k}[\sinh(kl)+\sin(kl)] \end{vmatrix} =$$
$$\frac{1}{4k^2}\{[\sinh(kl)+\sin(kl)]^2-[\sinh(kl)-\sin(kl)]^2\}=0. \tag{2.42}$$

Expanding the left hand side of Eq. (2.42) leads to:

$$\frac{1}{4k^2}(4\sinh(kl)\sin(kl)=0. \tag{2.43}$$

The natural frequencies are the solutions to $\sin(kl)=0$. The solutions are:

$$kl=n\pi. \tag{2.44}$$

Since $k=(\frac{\rho A\omega^2}{EI})^{\frac{1}{4}}$, the natural frequencies are:

$$\omega_n^2=\frac{EI}{\rho A}(\frac{n\pi}{l})^4, \quad (n=1,\,2,\,\cdots). \tag{2.45}$$

It is obvious that $\sin(kl)$ is responsible for the solutions to Eq. (2.42). However, in the transfer-matrix analysis the elements of the determinant of Eq. (2.42) are numerical so that the contributions of the $\sin(kl)$ terms cannot be isolated. Hence, the influence of $\sin(kl)$ can be swamped by $\sinh(kl)$ as soon as (kl) is much larger

than 1 and insufficient digits are carried out in the computation.

2.5.2 The delta-matrix method

There are quite a number of schemes to avoid numerical difficulties in the transfer matrix method, such as the delta-matrix method [21], the successive reduction method by detachment of spring constants[22] and the Riccati transfer matrix method [27]. However, none of these improvements is really perfect. The delta-matrix method is not an elimination technique but an expansion technique to produce the super-matrix from the transfer matrix. Compared with other approaches, this method is better. However, this procedure has the following two disadvantages:

(1) since it is a determinant operation only, it is impossible to obtain mode shapes after finding the natural frequencies;

(2) It will most probably be limited to fourth order problems due to the enormous increase in the number of elements when cases of higher order have to be dealt with.

A delta matrix $\mathbf{U}^{\Delta}$ is a square matrix formed from a corresponding transfer matrix $\mathbf{U}$ in such a way that each element corresponds to a 2×2 sub-determinant in the transfer matrix. There exist 36 sub-determinants in a 4×4 transfer matrix. Hence, the delta-matrix has 36 elements and is of order 6×6. The transformation is accomplished through the use of the following lexicon which identifies the number of the row and column in the delta-matrix with the corresponding pairs of rows and columns in the transfer matrix. If we express respectively the transfer matrix $\mathbf{U}$ and

row or column in delta-matrix	1	2	3	4	5	6
row or column pair in transfer matrix	1, 2	1, 3	1, 4	2, 3	2, 4	3, 4

Table 2.2: Delta-matrix lexicon

the corresponding delta-matrix $\mathbf{U}^{\Delta}$ as:

$$\mathbf{U} = \begin{bmatrix} u_{11} & u_{12} & u_{13} & u_{14} \\ u_{21} & u_{22} & u_{23} & u_{24} \\ u_{31} & u_{32} & u_{33} & u_{34} \\ u_{41} & u_{42} & u_{43} & u_{44} \end{bmatrix}, \tag{2.46}$$

$$\mathbf{U}^{\Delta} = \begin{bmatrix} u_{11}^{\Delta} & u_{12}^{\Delta} & u_{13}^{\Delta} & u_{14}^{\Delta} & u_{15}^{\Delta} & u_{16}^{\Delta} \\ u_{21}^{\Delta} & u_{22}^{\Delta} & u_{23}^{\Delta} & u_{24}^{\Delta} & u_{25}^{\Delta} & u_{26}^{\Delta} \\ u_{31}^{\Delta} & u_{32}^{\Delta} & u_{33}^{\Delta} & u_{34}^{\Delta} & u_{35}^{\Delta} & u_{36}^{\Delta} \\ u_{41}^{\Delta} & u_{42}^{\Delta} & u_{43}^{\Delta} & u_{44}^{\Delta} & u_{45}^{\Delta} & u_{46}^{\Delta} \\ u_{51}^{\Delta} & u_{52}^{\Delta} & u_{53}^{\Delta} & u_{54}^{\Delta} & u_{55}^{\Delta} & u_{56}^{\Delta} \\ u_{61}^{\Delta} & u_{62}^{\Delta} & u_{63}^{\Delta} & u_{64}^{\Delta} & u_{65}^{\Delta} & u_{66}^{\Delta} \end{bmatrix}, \tag{2.47}$$

we may then illustrate the use of the lexicon by the following examples:

$$u_{11}^{\Delta} = \begin{bmatrix} u_{11} & u_{12} \\ u_{21} & u_{22} \end{bmatrix}, \tag{2.48}$$

$$u_{24}^{\Delta} = \begin{bmatrix} u_{12} & u_{13} \\ u_{32} & u_{33} \end{bmatrix}, \tag{2.49}$$

$$u_{36}^{\Delta} = \begin{bmatrix} u_{13} & u_{14} \\ u_{43} & u_{44} \end{bmatrix}. \tag{2.50}$$

In the delta-matrix technique, a delta-matrix corresponding to each transfer matrix in Eq. (2.7) is constructed according to the above transformation. The product of these delta-matrices is then taken and must be equal to the delta-matrix corresponding to the product matrix $\mathbf{U}$. This is fortunately true [21, 23], and the rule is that if

$$\mathbf{U}_n \, \mathbf{U}_{n-1} \cdots \mathbf{U}_2 \, \mathbf{U}_1 = \mathbf{U}$$

then

$$\mathbf{U}_n^{\triangle}\,\mathbf{U}_{n-1}^{\triangle}\cdots\mathbf{U}_2^{\triangle}\,\mathbf{U}_1^{\triangle} = \mathbf{U}^{\triangle}. \tag{2.51}$$

Boundary Conditions

If the transfer matrix relating the state vectors at the two ends is U, the frequency determinant for a beam built-in at both ends is:

$$\begin{vmatrix} u_{13} & u_{14} \\ u_{23} & u_{24} \end{vmatrix} = 0,$$

or $U_{16}^{\triangle} = 0$. Similarly, the condition for a simply-supported beam is:

$$\begin{vmatrix} u_{12} & u_{14} \\ u_{32} & u_{34} \end{vmatrix} = 0,$$

or $U_{25}^{\triangle} = 0$.

All possible boundary conditions and the corresponding frequency sub-determinants can be found from a table in [21].

2.5.3 Examples

(1) A uniform riser under constant tension

A uniform riser first appears as an illustration of the delta-matrix method. The data of the riser are as follows:

Length of the riser: $l = 1400 \times 0.3048 = 426.72\,m$;

Bending rigidity: $EI = 3.5793 \times 10^7\,N.m^2$;

Mass per unit length: $\rho A = 357.0832\,kg/m$; and

Constant tension: $T = 2.27 \times 10^5\,N$.

We first employ the conventional transfer matrix method to solve for natural frequencies by plotting the frequency determinant. Figure 2-12 shows the determinant versus frequency in Hz. Due to the word length (double precision) with which a

computer calculates, the TMM is totally useless in finding natural frequencies. The roots in the figure are false values generated by numerical problems. It means that in this case we cannot find any frequency by means of the conventional transfer matrix method. We have to use the improved TMMs to analyze this example.

We regard the whole riser as one section, first finding the transfer matrix and

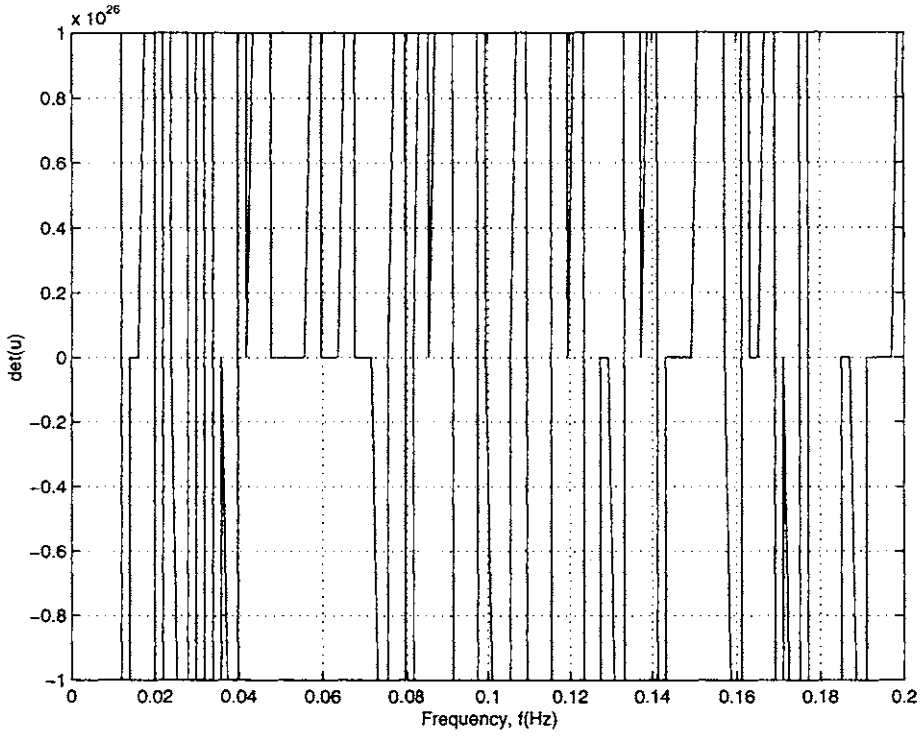

Figure 2-12: The determinant versus frequency (Hz)

then transforming it into the delta-matrix. Figure 2-13 shows the determinant corresponding to the delta-matrix versus frequency in Hz. The downward sharp peaks correspond to the natural frequencies. Table 2.3 indicates the natural frequencies found by means of the delta-matrix method. The analytical results from Eq. (2.17) are also included for comparison. Compared with the analytical solutions, the natural frequencies obtained by means of the delta-matrix method are accurate.

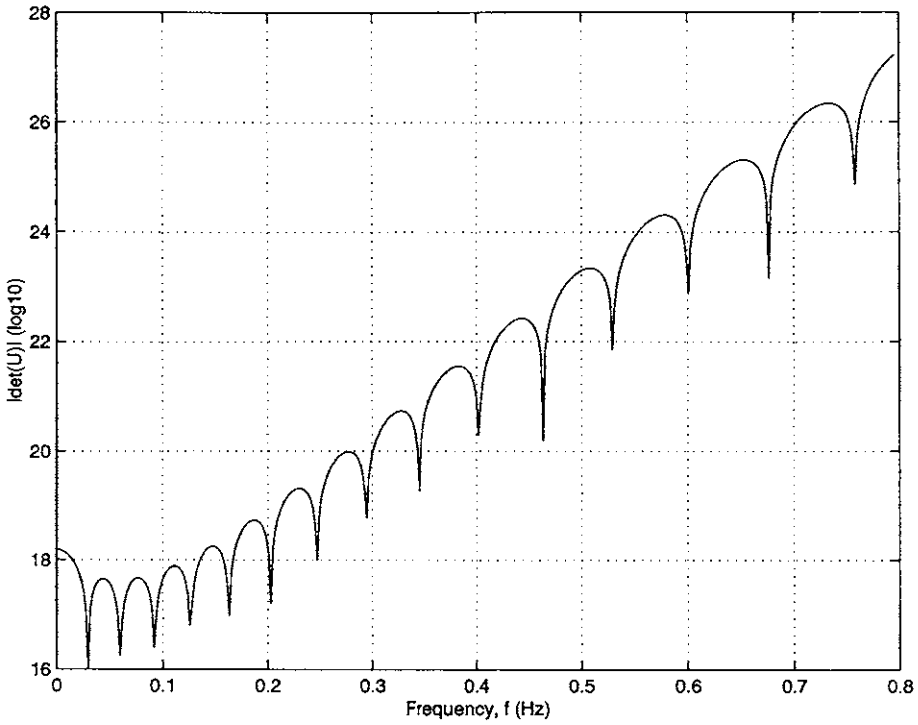

Figure 2-13: The determinant versus frequency (Hz)

order	delta-matrix	analytical solutions
1	0.030	0.0297
2	0.0597	0.0601
3	0.0915	0.0920
4	0.1273	0.1260
5	0.1630	0.1627
6	0.2029	0.2027
7	0.2467	0.2463
8	0.2944	0.2940
9	0.3462	0.3459
10	0.4018	0.4023
11	0.4613	0.4635
12	0.5292	0.5295
13	0.6008	0.6005
14	0.6764	0.6765
15	0.7560	0.7576

Table 2.3: Comparison of natural frequencies (Hz) found by using the delta-matrix and the analytical solutions

(2) A uniform riser under linearly varying tension

We now further analyze a uniform riser under linearly varying tension. The riser has similar properties except the tension, specified as follows:

Minimum tension at the bottom: $T_0 = 222410$ N; and

Linearly varying factor: $\alpha = 1.6819 \times 10^3$ N/m.

We divide the riser into 20 equally-sized sections. For each section, the tension is at its average value. Figure 2-14 shows the absolute determinant corresponding the overall delta-matrix versus frequency. The troughs coincide with the natural frequencies. Table 2.4 indicates the first 13 natural frequencies in Hz found by plotting the determinant. Using 200 elements, we calculate the natural frequencies by means of Shear7, and include the results in the table for comparison. The table demonstrates that the natural frequencies obtained by means of the delta-matrix method are quite close to those found by using Shear7, which employs a WKB solution found by Kim [7].

order	by delta-matrix	by Shear7
1	0.0458	0.0447
2	0.0905	0.0902
3	0.1373	0.1370
4	0.1860	0.1857
5	0.2367	0.2368
6	0.2905	0.2904
7	0.3472	0.3470
8	0.4078	0.4067
9	0.4715	0.4699
10	0.5401	0.5367
11	0.6117	0.6073
12	0.6883	0.6819
13	0.7690	0.7607

Table 2.4: Comparison of natural frequencies (Hz) found by using the delta-matrix and Shear7

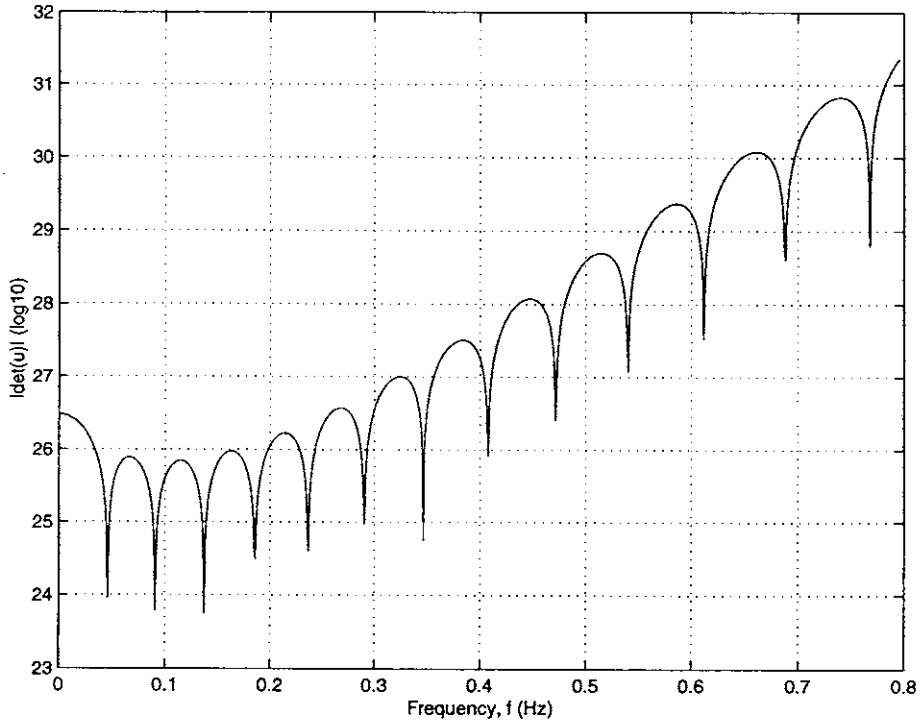

Figure 2-14: The delta-matrix determinant versus frequency (Hz)

2.6 Three approximate schemes for a beam under variable tension

A non-uniform beam under variable tension is approximated by a number of homogeneous beams under constant tension, which can be solved analytically. As the number of the stepped beams increases, the results converge on the exact solution of the original beam.

There are three approximate schemes for a beam under variable tension to generate stepped uniform beams under constant tension, as depicted in Figures 2-15 to 2-17. We assume that each section is under tension at the left node in (**a**) and at the right node in (**b**). In (**c**), average tension is chosen for each section.

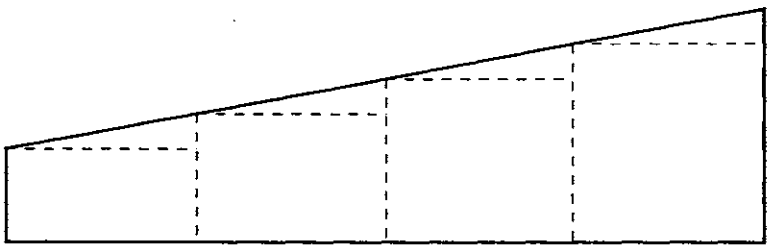

Figure 2-15: The approximation scheme (a)

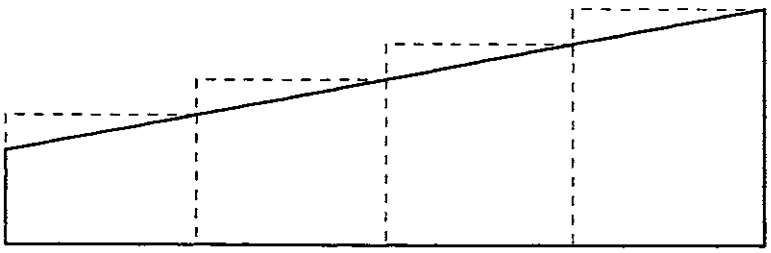

Figure 2-16: The approximation scheme (b)

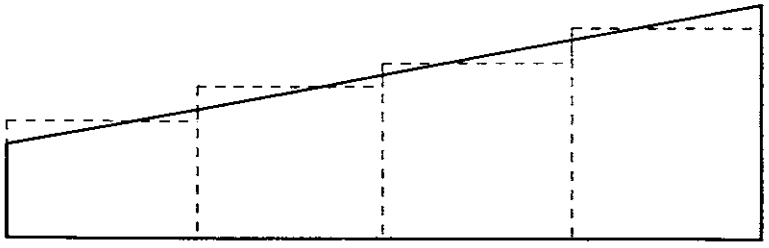

Figure 2-17: The approximation scheme (c)

We employ the uniform riser under linearly varying tension in Section 2.5.3 as an example to illustrate the three schemes and to compare their convergences. Under the schemes, we employ the delta-matrix method to solve for the natural frequencies of the riser.

Figures 2-18 to 2-20 show the absolute determinant versus frequency in Hz in Schemes (**a**), (**b**) and (**c**), respectively. In order to observe the convergences, these figures plot the results under different numbers (N) of the stepped beams. The troughs coincide with the natural frequencies.

Figure 2-18 shows that if the riser is approximated by Scheme (**a**), and as the number of stepped beams increases, the natural frequencies approach the exact values from below; namely, the troughs shift to the right. When $N = 80$ the first few natural frequencies converge while the high order natural frequencies do not converge.

Figure 2-19 shows that if the riser is approximated by Scheme (**b**), and as the number of stepped beams increases, the natural frequencies approach the exact values from above; that is, the troughs shift to the left. When $N = 80$, we observe similar trend of convergence to that in Figure 2-18.

Figure 2-20 shows that if the riser is approximated by Scheme (**c**), the rate of convergence improves significantly. When $N = 40$, all the first 13 natural frequencies converge upon the exact values.

In order to obtain all the exact values of the first 13 natural frequencies, we need to employ a much high number of stepped beams by using the approximate schemes (**a**) and (**b**), demonstrated in Figures 2-21 and 2-22.

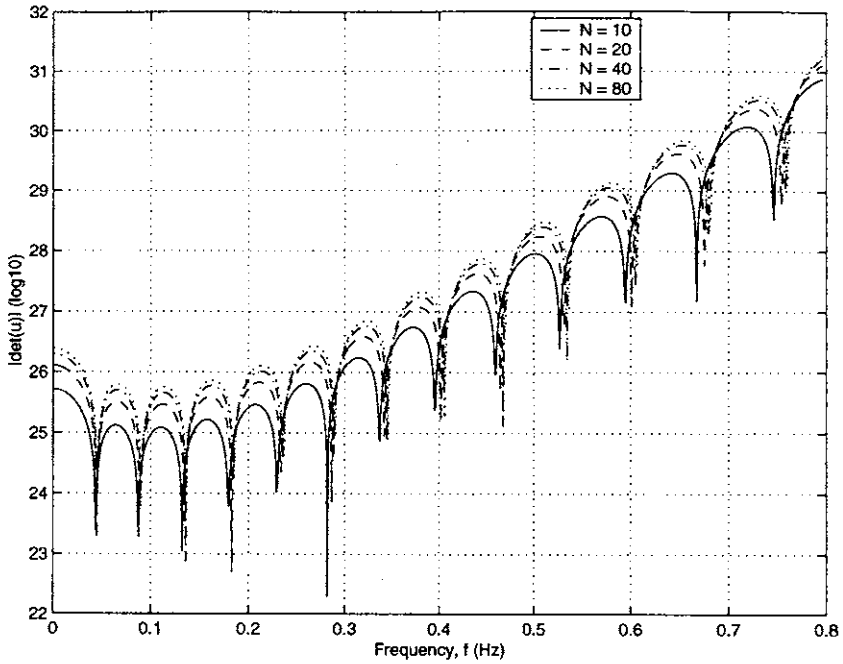

Figure 2-18: The absolute determinant of the riser versus frequency in Hz (approximate scheme (a))

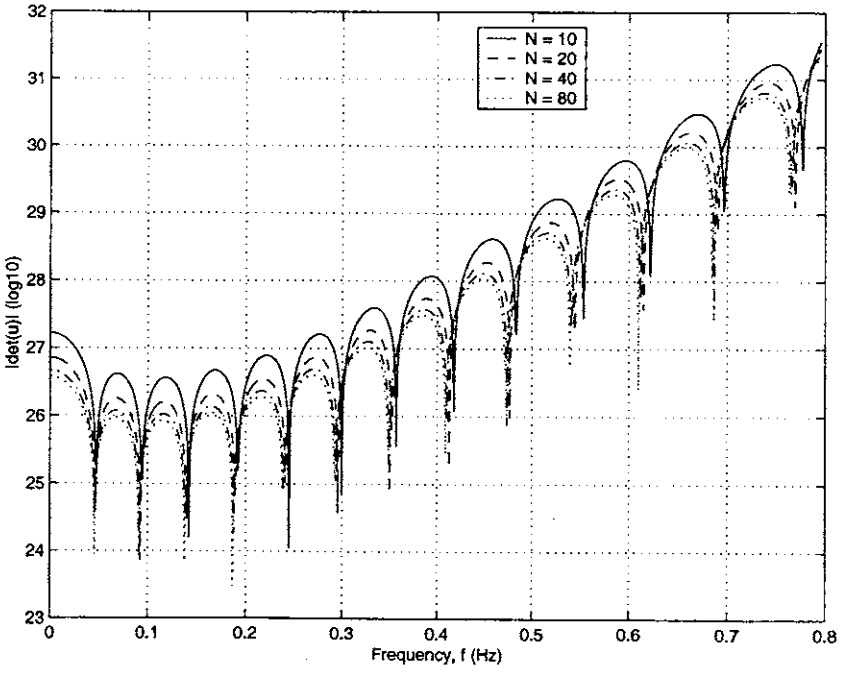

Figure 2-19: The absolute determinant of the riser versus frequency in Hz (approximate scheme (b))

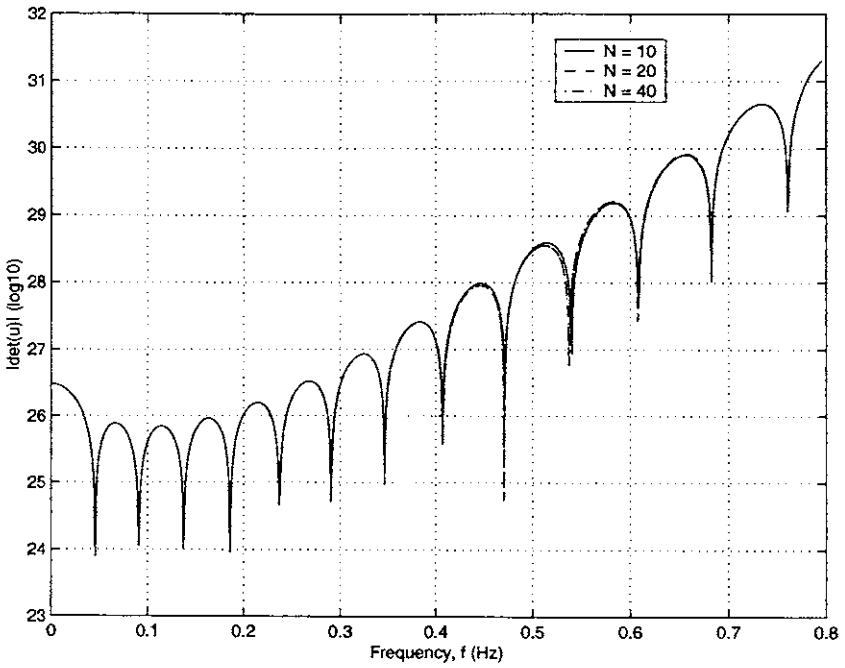

Figure 2-20: The absolute determinant of the riser versus frequency in Hz (approximate scheme (c))

In all three approximate schemes, with sufficient numbers of stepped beams, all thirteen natural frequencies converge on the exact values depicted in Tables 2.4 and 5.1. Hence, if the riser is approximated by scheme (c), the rate of convergence of the natural frequencies is the fastest.

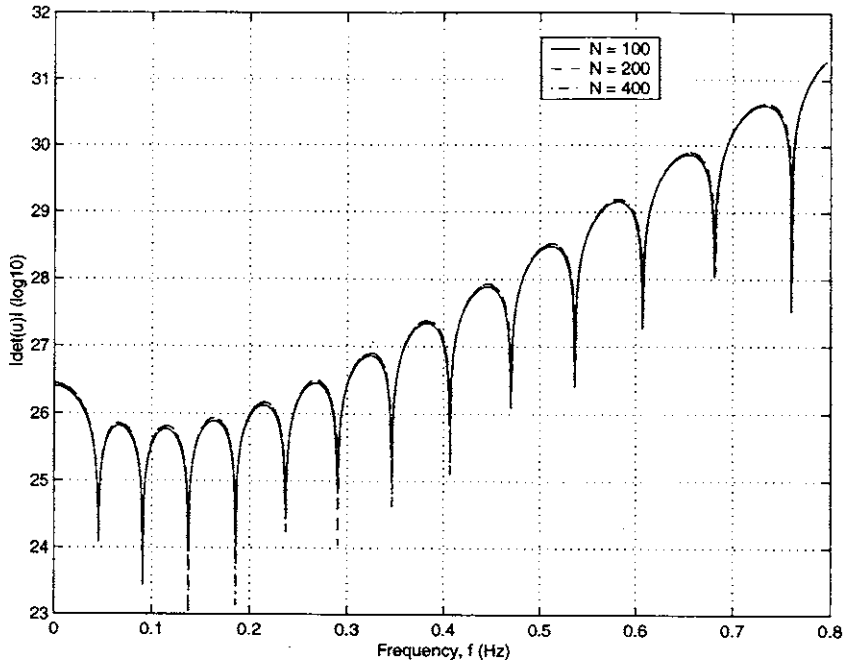

Figure 2-21: The absolute determinant of the riser versus frequency in Hz (approximate scheme (a))

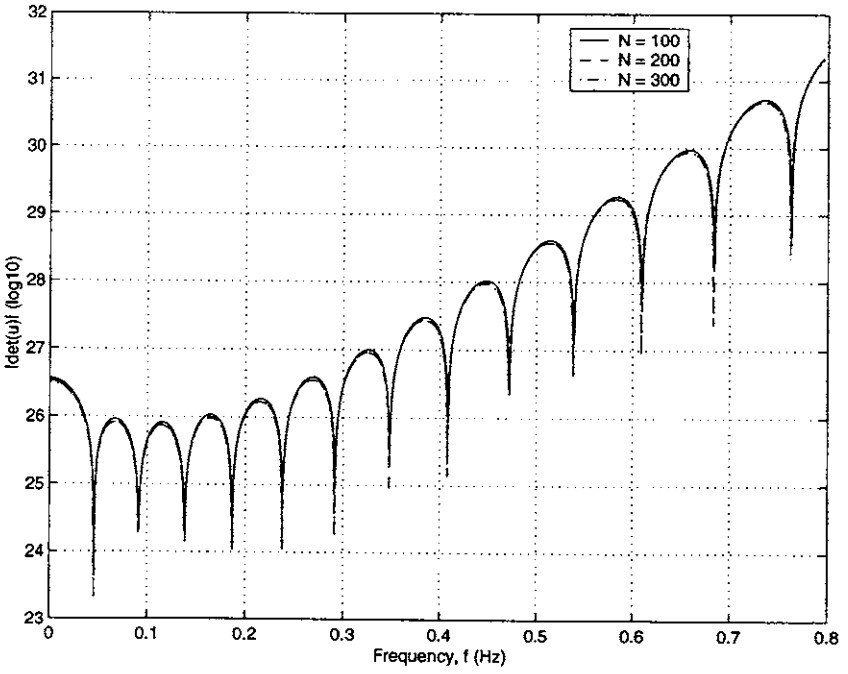

Figure 2-22: The absolute determinant of the riser versus frequency in Hz (approximate scheme (b))

2.7 A new transfer matrix method based on symbolic operations

Using the transfer matrix method, we establish an overall transfer matrix relating to state vectors at boundaries. Considering boundary conditions leads to a frequency equation in the form of a 2×2 determinant. The numerical difficulty originates from numerically calculating the frequency determinant when it is equal to the difference between large and almost equal numbers and the number of decimal digits necessary exceeds the capacity of most high-speed digital computers.

For a simply-supported beam, we can extract the harmonic terms and analytically find the natural frequencies without any numerical problem by expanding the 2×2 determinant and simplifying the expressions. For a complex system, the frequency equation is complicated, and furthermore it will be cumbersome to extract the roots. In this case, it is advisable to replace algebraic by numerical computation, which may cause numerical problems. In order to overcome the numerical problems, Section 2.5 discusses the delta-matrix method.

However, a number of software programs such as Maple and Mathematica can do much more complicated algebraic operations. Hence, we present a new transfer matrix method based on symbolic operations. With these programs, we first do symbolic calculations for obtaining an overall transfer matrix, then expand the frequency equation in terms of a 2×2 determinant and simplify the expressions, and finally numerically solve the simplified equation. With this technique, we can avoid the numerical problems.

The following two examples appear as an illustration:

(1) A simply-supported uniform beam under constant tension

Section 2.4.1 shows that the wave solution of a uniform beam under constant tension can be written as:

$$y(x,t) = [c_1 \sin(\lambda_1 x) + c_2 \cos(\lambda_1 x) + c_3 \sinh(\lambda_2 x) + c_4 \cosh(\lambda_2 x)]e^{i\omega t}, \qquad (2.52)$$

where λ_1 and λ_2 are:

$$\begin{aligned}\lambda_1 &= \sqrt{-\frac{1}{2}(\frac{T}{EI})^2 + \sqrt{\frac{1}{4}(\frac{T}{EI})^4 + \frac{\rho A\omega^2}{EI}}},\\ \lambda_2 &= \sqrt{\frac{1}{2}(\frac{T}{EI})^2 + \sqrt{\frac{1}{4}(\frac{T}{EI})^4 + \frac{\rho A\omega^2}{EI}}}.\end{aligned} \tag{2.53}$$

With Eq. (2.52), we calculate the derivatives of $y(x,t)$ and suppress the time-dependent term of $e^{i\omega t}$:

$$\begin{aligned}\frac{\partial y}{\partial x} &= c_1\lambda_1\cos(\lambda_1 x) - c_2\lambda_1\sin(\lambda_1 x) + c_3\lambda_2\cosh(\lambda_2 x) + c_4\lambda_2\sinh(\lambda_2 x);\\ \frac{\partial^2 y}{\partial x^2} &= -c_1\lambda_1^2\sin(\lambda_1 x) - c_2\lambda_1^2\cos(\lambda_1 x) + c_3\lambda_2^2\sinh(\lambda_2 x) + c_4\lambda_2^2\cosh(\lambda_2 x);\\ \frac{\partial^3 y}{\partial x^3} &= -c_1\lambda_1^3\cos(\lambda_1 x) + c_2\lambda_1^3\sin(\lambda_1 x) + c_3\lambda_2^3\cosh(\lambda_2 x) + c_4\lambda_2^3\sinh(\lambda_2 x)\end{aligned} \tag{2.54}$$

Substituting the derivatives of y into Eqs. (2.19) leads to:

$$\begin{aligned}M &= EI\left[-c_1\lambda_1^2\sin(\lambda_1 x) - c_2\lambda_1^2\cos(\lambda_1 x) + c_3\lambda_2^2\sinh(\lambda_2 x) + c_4\lambda_2^2\cosh(\lambda_2 x)\right],\\ Q &= EI\left[-c_1\lambda_1^3\cos(\lambda_1 x) + c_2\lambda_1^3\sin(\lambda_1 x) + c_3\lambda_2^3\cosh(\lambda_2 x) + c_4\lambda_2^3\sinh(\lambda_2 x)\right]\\ &\quad -T\left[c_1\lambda_1\cos(\lambda_1 x) - c_2\lambda_1\sin(\lambda_1 x) + c_3\lambda_2\cosh(\lambda_2 x) + c_4\lambda_2\sinh(\lambda_2 x)\right]\\ &= -c_1(EI\lambda_1^3 + T\lambda_1)\cos(\lambda_1 x) + c_2(EI\lambda_1^3 + T\lambda_1)\sin(\lambda_1 x)\\ &\quad +c_3(EI\lambda_2^3 - T\lambda_2)\cosh(\lambda_2 x) + c_4(EI\lambda_2^3 - T\lambda_2)\sinh(\lambda_2 x).\end{aligned} \tag{2.55}$$

At $x = L$, the state vector is:

$$\mathrm{s}_{i+1} = \begin{pmatrix} y\\ \theta\\ M\\ Q\end{pmatrix}_{x=L} =$$

$$\begin{bmatrix} \sin(\lambda_1 L) & \cos(\lambda_1 L) & \sinh(\lambda_2 L) & \cosh(\lambda_2 L) \\ \lambda_1 \cos(\lambda_1 L) & -\lambda_1 \sin(\lambda_1 L) & \lambda_2 \cosh(\lambda_2 L) & \lambda_2 \sinh(\lambda_2 L) \\ -EI\lambda_1^2 \sin(\lambda_1 L) & -EI\lambda_1^2 \cos(\lambda_1 L) & EI\lambda_2^2 \sinh(\lambda_2 L) & EI\lambda_2^2 \cosh(\lambda_2 L) \\ -\alpha \cos(\lambda_1 L) & \alpha \sin(\lambda_1 L) & \beta \cosh(\lambda_2 L) & \beta \sinh(\lambda_2 L) \end{bmatrix} \begin{pmatrix} c_1 \\ c_2 \\ c_3 \\ c_4 \end{pmatrix}, \tag{2.56}$$

where $\alpha = (EI\lambda_1^3 + T\lambda_1)$ and $\beta = (EI\lambda_2^3 - T\lambda_2)$.

Equation (2.56) is rewritten in the following abbreviated form:

$$\mathbf{s}_{i+1} = \mathbf{A}\,\mathbf{C}. \tag{2.57}$$

Likewise, we obtain the state vector at $x = 0$:

$$\mathbf{s}_i = \begin{pmatrix} y \\ \theta \\ M \\ Q \end{pmatrix}_{x=0} = \begin{bmatrix} 0 & 1 & 0 & 1 \\ \lambda_1 & 0 & \lambda_2 & 0 \\ 0 & -EI\lambda_1^2 & 0 & EI\lambda_2^2 \\ -(EI\lambda_1^3 + T\lambda_1) & 0 & (EI\lambda_2^3 - T\lambda_2) & 0 \end{bmatrix} \begin{pmatrix} c_1 \\ c_2 \\ c_3 \\ c_4 \end{pmatrix}. \tag{2.58}$$

Equation (2.58) is rewritten in the following abbreviated form:

$$\mathbf{s}_i = \mathbf{B}\,\mathbf{C}. \tag{2.59}$$

We have: $\mathbf{C} = \mathbf{B}^{-1}\,\mathbf{s}_i$ from Eq. (2.59). Substituting this result into Eq. (2.57) leads to:

$$\mathbf{s}_{i+1} = \mathbf{u}_i\,\mathbf{s}_i, \tag{2.60}$$

where $\mathbf{u}$ is the transfer matrix relating to the state vectors of $\mathbf{s}_i$ and $\mathbf{s}_{i+1}$, $\mathbf{u}_i = \mathbf{A}\,\mathbf{B}^{-1}$.

We divide a uniform beam under constant tension into two equally-sized sections. The overall transfer matrix is then $\mathbf{u} = \mathbf{u}_2\,\mathbf{u}_1 = \mathbf{u}_1^2$, and the corresponding frequency equation is indicated in Eq. (2.11).

As depicted in the first example in Section 2.5.3, there are numerical problems in

directly numerically solving the beam structure for natural frequencies. When the beam is much longer or high natural frequencies are needed, we have to resort to the improved transfer matrix method such as the delta-matrix method.

We now solve this problem by means of the transfer matrix method based on symbolic operations. We employ Maple VI to calculate all the algebraic operations stated above, first calculating the elemental transfer matrix and then the overall transfer matrix, and finally finding the frequency equation in the 2×2 matrix and simplifying the final expression. We obtain the simplified frequency equation by means of Maple VI:

$$4\frac{\cosh(\lambda_2 L)\sinh(\lambda_2 L)\sin(\lambda_1 L)\cos(\lambda_1 L)}{\lambda_1\lambda_2} = 0. \tag{2.61}$$

If the whole length of the beam is l, then $L = l/2$. Equation (2.61) is written as:

$$\frac{\sinh(\lambda_2 l)\sin(\lambda_1 l)}{\lambda_1\lambda_2} = 0. \tag{2.62}$$

Thus $\sin(\lambda_1 l) = 0$, and the roots are:

$$\lambda_{1n} l \;=\; n\pi. \tag{2.63}$$

Substituting Eq. (2.53) into Eq. (2.62) results in the analytical solutions of the natural frequencies, shown in Eq. (2.17).

(2) A constantly tensioned uniform beam with an absorber at the midpoint

We now analyze a constantly-tensioned uniform beam with a mass-spring absorber by means of the symbolic operation-based transfer matrix method. The undamped transfer matrix of a mass-spring absorber, $\mathbf{u}_a$, is obtained from Eq. (2.16) by setting $c = 0$. The transfer matrix of the beam section on either side of the absorber, $\mathbf{u}_1$ and $\mathbf{u}_2$, is derived in **(1)**. The overall transfer matrix is: $\mathbf{u} = \mathbf{u}_2\,\mathbf{u}_a\,\mathbf{u}_1 = \mathbf{u}_1\,\mathbf{u}_a\,\mathbf{u}_1$.

Following the same procedure as in **(1)**, we find the following frequency equation

of the composite system by means of Maple VI:

$$
\begin{aligned}
&2\sin(\lambda_1 L)\sinh(\lambda_2 L) \\
&(2\omega^2 m{\lambda_1}^3\cosh(\lambda_2 L)EJ\,\lambda_2\cos(\lambda_1 L) - \omega^2 m\cos(\lambda_1 L)\sinh(\lambda_2 L)\lambda_1 k \\
&+2\omega^2 m\lambda_1 EJ\,{\lambda_2}^3\cosh(\lambda_2 L)\cos(\lambda_1 L) + \omega^2 m\cosh(\lambda_2 L)\sin(\lambda_1 L)\lambda_2 k - \\
&2{\lambda_1}^3\cosh(\lambda_2 L)EJ\,\lambda_2 k\cos(\lambda_1 L) - 2\lambda_1 EJ\,{\lambda_2}^3\cosh(\lambda_2 L)k\cos(\lambda_1 L)) \\
&/[{\lambda_2}^2 EJ\,{\lambda_1}^2(-k+m\omega^2)({\lambda_2}^2+{\lambda_1}^2)] = 0, \qquad (2.64)
\end{aligned}
$$

where the m and k are the absorber mass and stiffness, respectively. We can find the roots by plotting the left hand side of Eq. (2.64) versus frequency.

We attach a mass-spring absorber at the midpoint of the uniform riser under constant tension discussed in Section 2.5.3. The parameters of the absorber are specified as follows:

The first natural frequency of the beam: $\Omega_1 = 2 \times \pi \times 0.0297 = 0.1866$;

Modal mass of the beam: $m_b = \rho Al/2 = 7.6187 \times 10^4$ kg;

Mass ratio of the absorber: $\mu = m/m_b = 1/10$;

Frequency of the absorber: $\omega_a = \sqrt{k/m}$; and

Optimal frequency ratio: $f = \omega_a/\Omega_1 = 1/(1+\mu)$.

The absorber is optimally tuned to the first mode of the uniform beam. Again, as depicted in Section 2.5.3, there are numerical problems in analyzing this system by means of the conventional transfer matrix method.

Figure 2-23 shows the absolute value of the left hand side of Eq. (2.64) versus frequency in Hz. The troughs coincide with the natural frequencies of the composite system. Table 2.5 indicates the first 16 natural frequencies. The first 15 natural frequencies of the beam, shown in Table 2.4, are also included for comparison. This table demonstrates that the absorber has high influence around the frequency to which it is tuned while it has little influence on other natural frequencies. In addition, the absorber causes an additional natural frequency. There are two frequencies distributed around the first natural frequency of the beam itself ($f_1 = 0.0297Hz$), one lower than f_1 and the other higher than f_1.

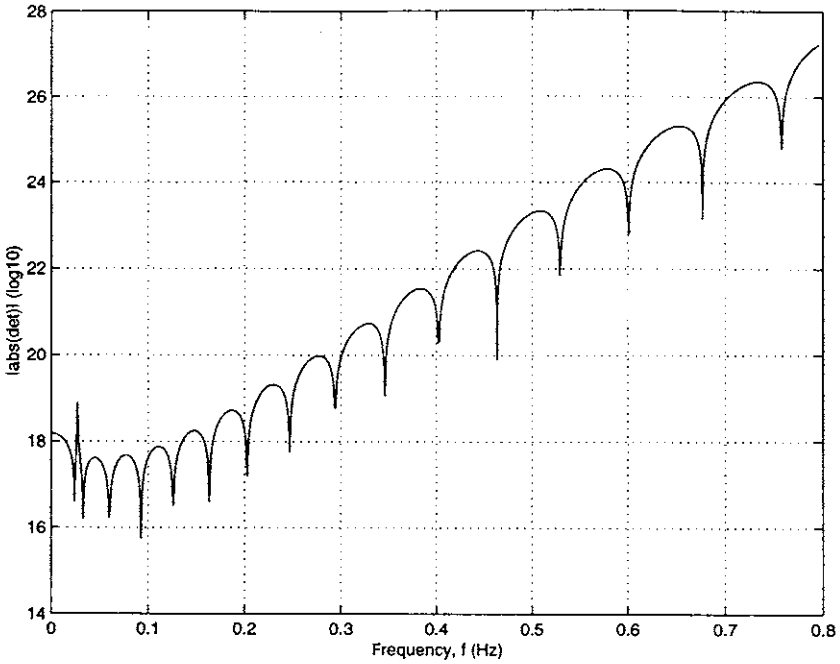

Figure 2-23: The absolute determinant of the system versus frequency in Hz

order	with absorber	no absorber	order
1	0.0239		
2	0.0328	0.0297	1
3	0.0597	0.0601	2
4	0.0925	0.0920	3
5	0.1263	0.1260	4
6	0.1631	0.1627	5
7	0.2029	0.2027	6
8	0.2467	0.2463	7
9	0.2944	0.2940	8
10	0.3462	0.3459	9
11	0.4019	0.4023	10
12	0.4635	0.4635	11
13	0.5292	0.5295	12
14	0.6008	0.6005	13
15	0.6764	0.6765	14
16	0.7580	0.7576	15

Table 2.5: Natural frequencies (Hz) of the composite system

Chapter 3

Dynamic Stiffness Method

3.1 Introduction

Historically, Kolosek first presented the idea of Dynamic Stiffness Method (DSM) in the early 1940s, and gave an elaborate formulation of this method in 1950. Since then the DSM has been widely used in the vibration analysis of beam structures. Improvements on calculating natural frequencies have been made by the Williams and Wittrick (W-W) algorithm [28] and Simpson's Newtonian iteration method [29].

The DSM has a great appeal for an exact dynamic analysis of a uniform beam structure, as it is based on the exact dynamic stiffness matrix derived from the free vibration analysis. The DSM performs free and forced vibration analysis within the differential equation theory of beams, thus avoiding assumed modes and lumped masses. This method enables one to analyze an infinite number of natural frequencies and modes by means of a finite number of degrees of freedom.

The next section of this chapter introduces the derivation of the elemental dynamic stiffness matrix of a uniform Euler beam, and then shows the frequency-dependent mass and stiffness matrices based on the theorem developed by Richards and Leung [30]. The third section discusses the assembly procedure for obtaining a global dynamic stiffness matrix, and determining natural frequencies. The third section then illustrates the DSM with an example. The fourth section introduces the W-W algorithm. Finally, this chapter discusses complex frequency analysis.

3.2 Derivation of elemental dynamic stiffness matrix and frequency-dependent mass and stiffness matrices

3.2.1 Elemental dynamic stiffness matrix

The equation describing undamped bending vibration is:

$$EI\partial^4 y/\partial x^4 + \rho A \partial^4 y/\partial t^4 = 0, \tag{3.1}$$

where EI is bending rigidity, ρA is mass per unit length, and y is lateral displacement.

Assuming $y = \bar{v} \sin \omega t$, and substituting it into Eq. (3.1), generates:

$$\frac{d^4 \bar{v}}{dx^4} - \lambda^4 \bar{v} = 0, \tag{3.2}$$

where $\lambda^4 \equiv \frac{\rho A \omega^2}{EI}$.

The general solution to Eq. (3.2) and its first three derivatives are:

$$\begin{aligned}
\bar{v} &= B_1 \sin \lambda x + B_2 \cos \lambda x + B_3 \sinh \lambda x + B_4 \cosh \lambda x; \\
\bar{v}' &= \lambda B_1 \cos \lambda x - \lambda B_2 \sin \lambda x + \lambda B_3 \cosh \lambda x + \lambda B_4 \sinh \lambda x; \\
\bar{v}'' &= -\lambda^2 B_1 \sin \lambda x - \lambda^2 B_2 \cos \lambda x + \lambda^2 B_3 \sinh \lambda x + \lambda^2 B_4 \cosh \lambda x; \\
\bar{v}''' &= -\lambda^3 B_1 \cos \lambda x + \lambda^3 B_2 \sin \lambda x + \lambda^3 B_3 \cosh \lambda x + \lambda^3 B_4 \sinh \lambda x.
\end{aligned} \tag{3.3}$$

The geometric boundary conditions for a simply supported beam are as follows:

$$\text{at } x = 0, \quad \bar{v} = v_{1y}, \quad \frac{d\bar{v}}{dx} = \theta_1; \tag{3.4}$$

$$\text{at } x = l, \quad \bar{v} = v_{2y}, \quad \frac{d\bar{v}}{dx} = \theta_2. \tag{3.5}$$

Equations (3.4) and (3.5) lead to:

$$\begin{pmatrix} v_{1y} \\ \theta_1 \\ v_{2y} \\ \theta_2 \end{pmatrix} = \begin{bmatrix} 0 & 1 & 0 & 1 \\ \lambda & 0 & \lambda & 0 \\ \sin\lambda l & \cos\lambda l & \sinh\lambda l & \cosh\lambda l \\ \lambda\cos\lambda l & -\lambda\sin\lambda l & \lambda\cosh\lambda l & \lambda\sinh\lambda l \end{bmatrix} \begin{pmatrix} B_1 \\ B_2 \\ B_3 \\ B_4 \end{pmatrix}. \tag{3.6}$$

Finally, with one symbol to represent each matrix in Eq. (3.6), it is written in abbreviated form as:

$$\mathbf{V_F} = \mathbf{CB}. \tag{3.7}$$

The nodal forces represented by the first three derivatives of Eq. (3.3) can be expressed in terms of B_i. The force boundary conditions for a beam element can be written as:

$$m_1 = -EI\frac{d^2\bar{v}}{dx^2}\,|_{x=0}, \quad s_{1y} = EI\frac{d^3\bar{v}}{dx^3}\,|_{x=0}; \tag{3.8}$$

$$m_2 = EI\frac{d^2\bar{v}}{dx^2}\,|_{x=l}, \quad s_{2y} = -EI\frac{d^3\bar{v}}{dx^3}\,|_{x=l}\,. \tag{3.9}$$

The nodal forces at two ends of a beam element are written by means of the expressions in Eqs. (3.8),(3.9), and (3.3), as follows:

$$\begin{pmatrix} s_{1y} \\ m_1 \\ s_{2y} \\ m_2 \end{pmatrix} = EI \begin{bmatrix} -\lambda^3 & 0 & \lambda^3 & 0 \\ 0 & \lambda^2 & 0 & -\lambda^2 \\ \lambda^3\cos\lambda l & -\lambda^3\sin\lambda l & -\lambda^3\cosh\lambda l & -\lambda^3\sinh\lambda l \\ -\lambda^2\sin\lambda l & -\lambda^2\cos\lambda l & \lambda^2\sinh\lambda l & \lambda^2\cosh\lambda l \end{bmatrix} \begin{pmatrix} B_1 \\ B_2 \\ B_3 \\ B_4 \end{pmatrix}. \tag{3.10}$$

Similarly, with one symbol to represent each matrix in the equation above, it can be written as:

$$\mathbf{F} = \mathbf{WB}. \tag{3.11}$$

It is obvious that the vector $\mathbf{B}$ can be evaluated in terms of the nodal displacements by inverting Eq. (3.7):

$$\mathbf{B} = \mathbf{C}^{-1}\mathbf{V_F}. \tag{3.12}$$

Hence, substituting Eq. (3.12) into Eq. (3.11) leads to:

$$\mathbf{F} = \mathbf{WC}^{-1}\mathbf{V_F}. \tag{3.13}$$

The matrix product, $\mathbf{WC}^{-1}$ in Eq. (3.13), represents the dynamic stiffness matrix of a beam element by definition, because it expresses the relationship between the nodal forces and the nodal displacements; that is,

$$\mathbf{K}(\lambda) = \mathbf{WC}^{-1}. \tag{3.14}$$

It is important to note that this stiffness matrix is a function of the frequency parameter λ because both $\mathbf{W}$ and $\mathbf{C}$ depend on λ.

Using Maple V to carry out the symbolic operations of the inversion and multiplication in Eq. (3.14), the dynamic stiffness matrix of a uniform beam element is found to be:

$$\mathbf{D} = \frac{EI}{l^3}\begin{bmatrix} F_6 & -F_4 l & F_5 & F_3 l \\ -F_4 l & F_2 l^2 & -F_3 l & F_1 l^2 \\ F_5 & -F_3 l & F_6 & F_4 l \\ F_3 l & F_1 l^2 & F_4 l & F_2 l^2 \end{bmatrix}, \tag{3.15}$$

where the frequency functions F_i $(i = 1 - - 6)$ are defined by:

$F_1 = -\lambda(\sinh\lambda - \sin\lambda)/\delta;$

$F_2 = -\lambda(\cosh\lambda\sin\lambda - \sinh\lambda\cos\lambda)/\delta;$

$F_3 = -\lambda^2(\cosh\lambda - \cos\lambda)/\delta;$

$F_4 = \lambda^2(\sinh\lambda\sin\lambda)/\delta;$

$F_5 = \lambda^3(\sinh\lambda + \sin\lambda)/\delta$;

$F_6 = -\lambda^3(\cosh\lambda\sin\lambda + \sinh\lambda\cos\lambda)/\delta$; and

$\delta = \cosh\lambda\cos\lambda - 1$.

3.2.2 Frequency-dependent mass and stiffness matrices

A theorem by Richards and Leung [30] allows ready determination of $[M]$ and $[K]$, which are frequency-dependent. The theorem states that:

$$[M(\omega)] = -\frac{\partial[D(\omega)]}{\partial\omega^2}. \tag{3.16}$$

Noting that:

$$\frac{dF_i}{d\omega^2} = \frac{dF_i}{d\lambda}\frac{d\lambda}{d\omega^2}; \tag{3.17}$$

$$\frac{d\lambda}{d\omega^2} = \frac{\lambda}{4\omega^2} \tag{3.18}$$

and defining $G_i = \frac{rdF_i}{dr}\frac{1}{4r^4}$, we obtain the following equation by using Eqs. (3.17) and (3.18) and the definition of λ:

$$\frac{EI}{l^3}\frac{dF_i}{d\omega^2} = G_i\rho Al. \tag{3.19}$$

Then the fundamental $[M(\omega)]$ can be written as:

$$[M(\omega)] = \rho Al\begin{bmatrix} G_6 & -G_4l & G_5 & G_3l \\ -G_4l & G_2l^2 & -G_3l & G_1l^2 \\ G_5 & -G_3l & G_6 & G_4l \\ G_3l & G_1l^2 & G_4l & G_2l^2 \end{bmatrix}. \tag{3.20}$$

Maple is first used to derive $\frac{dF_i}{d\lambda}$, prove some identities, and then simplify the form. Finally the functions G_i are written as:

$G_1 = (F_1F_2 - F_1 - F_3)/4\lambda^4$

$G_2 = (F_1^2 - F_2)/4\lambda^4$;

$G_3 = -(F_1F_4 + 2F_3)/4\lambda^4;$

$G_4 = -(F_1F_3 + 2F_4)/4\lambda^4;$

$G_5 = (F_3F_4 - 3F_5)/4\lambda^4;$

$G_6 = (F_3^2 - 3F_6)/4\lambda^4.$

Then $[K(\omega)]$ will be given by:

$$[K(\omega)] = [D(\omega)] + \omega^2[M(\omega)]. \tag{3.21}$$

We can further prove that if $\lambda = 0$, then the frequency-dependent matrices $[M(\omega)]$ and $[K(\omega)]$ degenerate into conventional mass and stiffness matrices as in the finite element method.

In the neighborhood of $\lambda = 0$, the functions F_i and G_i are of the 0/0 type. Using Maple V, we expand the F_i and G_i as polynomials of λ:

$$\begin{aligned} F_1 &= 2 + \frac{1}{140}\lambda^4 + \frac{1097}{69854400}\lambda^8 + \frac{899}{28252224000}\lambda^{12} \\ &\quad + \frac{5220181117}{81958386400450560000}\lambda^{16} + \frac{276451037}{2172065878267084800000}\lambda^{20} \\ &\quad + O(\lambda^{22}) \end{aligned} \tag{3.22}$$

$$\begin{aligned} F_2 &= 4 - \frac{1}{105}\lambda^4 - \frac{71}{4365900}\lambda^8 - \frac{127}{3972969000}\lambda^{12} \\ &\quad - \frac{20403571}{320149946876760000}\lambda^{16} - \frac{65608307}{5154414144715836000 00}\lambda^{20} \\ &\quad + O(\lambda^{22}) \end{aligned} \tag{3.23}$$

$$\begin{aligned} F_3 &= 6 + \frac{13}{420}\lambda^4 + \frac{1681}{23284800}\lambda^8 + \frac{112631}{762810048000}\lambda^{12} \\ &\quad + \frac{41460911}{140099805812736000}\lambda^{16} + \frac{85141179649}{14394872956879134720 0000}\lambda^{20} \\ &\quad + O(\lambda^{22}) \end{aligned} \tag{3.24}$$

$$\begin{aligned} F_4 &= -6 + \frac{11}{210}\lambda^4 + \frac{223}{2910600}\lambda^8 + \frac{3547}{23837814000}\lambda^{12} \\ &\quad + \frac{4215149}{14228886527856000}\lambda^{16} + \frac{166313573}{2811498624390456000 00}\lambda^{20} \\ &\quad + O(\lambda^{22}) \end{aligned} \tag{3.25}$$

$$F_5 = -12 - \frac{9}{70}\lambda^4 - \frac{1279}{3880800}\lambda^8 - \frac{5801}{8475667200}\lambda^{12}$$

$$-\frac{417329273}{303549579260928000}\lambda^{16}-\frac{80596657487}{29322889356605644800000}\lambda^{20}$$
$$+O(\lambda^{22}) \tag{3.26}$$

$$F_6 = 12-\frac{13}{35}\lambda^4-\frac{59}{161700}\lambda^8-\frac{551}{794593800}\lambda^{12}$$
$$-\frac{753689}{547264866456000}\lambda^{16}-\frac{52483633}{19090422758206800000}\lambda^{20}$$
$$+O(\lambda^{22}) \tag{3.27}$$

$$G_1 = -\frac{1}{140}-\frac{1097}{34927200}\lambda^4-\frac{899}{9417408000}\lambda^8$$
$$-\frac{5220181117}{20489596600112640000}\lambda^{12}+O(\lambda^{16}) \tag{3.28}$$

$$G_2 = \frac{1}{105}+\frac{71}{2182950}\lambda^4+\frac{127}{1324323000}\lambda^8$$
$$+\frac{20403571}{80037486719190000}\lambda^{12}+O(\lambda^{16}) \tag{3.29}$$

$$G_3 = -\frac{13}{420}-\frac{1681}{11642400}\lambda^4-\frac{112631}{254270016000}\lambda^8$$
$$-\frac{41460911}{35024951453184000}\lambda^{12}+O(\lambda^{16}) \tag{3.30}$$

$$G_4 = -\frac{11}{210}-\frac{223}{1455300}\lambda^4-\frac{3547}{7945938000}\lambda^8$$
$$-\frac{4215149}{3557221631964000}\lambda^{12}+O(\lambda^{16}) \tag{3.31}$$

$$G_5 = \frac{9}{70}+\frac{1279}{1940400}\lambda^4+\frac{5801}{2825222400}\lambda^8$$
$$+\frac{417329273}{75887394815232000}\lambda^{12}+O(\lambda^{16}) \tag{3.32}$$

$$G_6 = \frac{13}{35}+\frac{59}{80850}\lambda^4+\frac{551}{264864600}\lambda^8$$
$$+\frac{753689}{136816216614000}\lambda^{12}+O(\lambda^{16}). \tag{3.33}$$

If the constant terms in Eqs. (3.22) to (3.33) are substituted into Eqs. (3.15), (3.20), and (3.21), then the frequency-dependent fundamental matrices $[M(\omega)]$ and $[K(\omega)]$ will degenerate into consistent mass and static stiffness matrices, again, as in the finite element method.

3.3 The global dynamic stiffness matrix and determination of natural frequency

3.3.1 The global dynamic stiffness matrix

In the previous section, we showed the dynamic direct-stiffness matrix and frequency-dependent mass and stiffness matrices of a uniform beam element. This section obtains system matrices and solves for natural frequencies and mode shapes.

In general, it is more convenient to formulate the elemental dynamic stiffness matrix with respect to local coordinates, which may differ from element to element; and therefore, such element matrices should be transformed so that they are all referred to a global coordinate system. Assemblage is then carried out by satisfying the dual conditions of geometric compatibility and force equilibrium at the common nodes.

Transformation matrices are usually derived as the relationship between the two sets of displacements or the two sets of forces in local and global coordinate systems. The nodal displacements $\mathbf{u}_e$ in local coordinates can be related to the nodal displacements $\bar{\mathbf{u}}_e$ in global coordinates by:

$$[u_e] = [T_e][\bar{u}_e]. \tag{3.34}$$

The transformed dynamic stiffness matrix (now in global coordinates) is:

$$[\bar{k}_e] = [T_e]^T[k_e][T_e]. \tag{3.35}$$

There are one-to-one correspondences between the elemental nodal displacement components $\bar{\mathbf{u}}_e$ in global coordinates, and system displacements $\mathbf{u}$:

$$[\bar{u}_e] = [C_e][u], \tag{3.36}$$

in which $[C_e]$ is a rectangular matrix consisting of ones when there are correspondences, and zeros when there is no correspondence. Using Eq. (3.36), the $n_e \times n_e$

element matrix $\bar{k}_e$ can be transformed into an $n \times n$ matrix $[k_e]$,

$$[k_e] = [C_e]^T[\bar{k}_e][C_e], \tag{3.37}$$

where n_e and n are the numbers of the degrees of freedom of the element and system matrices, respectively.

All element matrices are now of the same order n, and the direct summations yield the system dynamic stiffness matrix:

$$[K] = \sum[k_e]. \tag{3.38}$$

Finally, the restraint conditions are imposed so that the global dynamic stiffness matrix is modified. Natural frequencies will be obtained from the following equation:

$$\mathbf{KU} = \mathbf{0}, \tag{3.39}$$

where $\mathbf{K}$ is the global dynamic stiffness matrix whose elements are functions of vibration frequency, and $\mathbf{U}$ is the vector of the amplitudes of sinusoidally varying nodal displacements.

3.3.2 The Determination of Natural Frequencies

The determinant $|\mathbf{K}|$ of the global dynamic stiffness matrix is a transcendental function of the frequency of vibration, becoming infinite at certain values of the frequency, and possessing an infinite number of roots to equation $|\mathbf{K}| = 0$.

Several features of the solution to Eq. (3.39) are important [31]:

(a) $|\mathbf{K}| = 0$, $\mathbf{U} \neq \mathbf{0}$ is one set of solutions.

(b) $|\mathbf{K}| = \infty$, $\mathbf{U} = \mathbf{0}$ is not necessarily a trivial set of solutions; but it sometimes corresponds to a mode shape whose nodes correspond to the nodes of a beam structure.

It was suggested previously that Gauss elimination is seldom used directly for vibration analysis. However, it does play an indirect role successfully when used to-

gether with the Sturm sequence. The latter is very important in solving eigenvalue problem in FEM [32].

3.3.3 An example

A simply supported beam was used to model a pipe in our lab. Its data are as follows:
length $L = 5.6906\,m$ ($= 18.67\,ft$);
bending stiffness $EI = 8.66 \times 10^3\,N\,m^2$; and
mass per unit length $\rho A = 1.8320$ kg/m.
The first 12 circular natural frequencies ω_n were found by means of an analytical formula for a simply supported beam:
0.0210×10^3, 0.0838×10^3, 0.1886×10^3, 0.3353×10^3, 0.5239×10^3, 0.7544×10^3, 1.0268×10^3, 1.3411×10^3, 1.6973×10^3, 2.0955×10^3, 2.5355×10^3, 3.0174×10^3.

The beam was evenly discretized into four beam elements. A Matlab code (dstiff1.m) was developed for the vibration analysis. Figure 3-1 shows the determinant of the global dynamic stiffness matrix versus different ranges of circular frequency. The troughs correspond to natural frequencies, the values of which are close to the exact ones. This figure also indicates that the determinants of the dynamic stiffness matrix at two circular frequencies are infinite. Compared to the analytical results of natural frequency, these frequencies are both associated with modes in which all the joint displacements are zero.

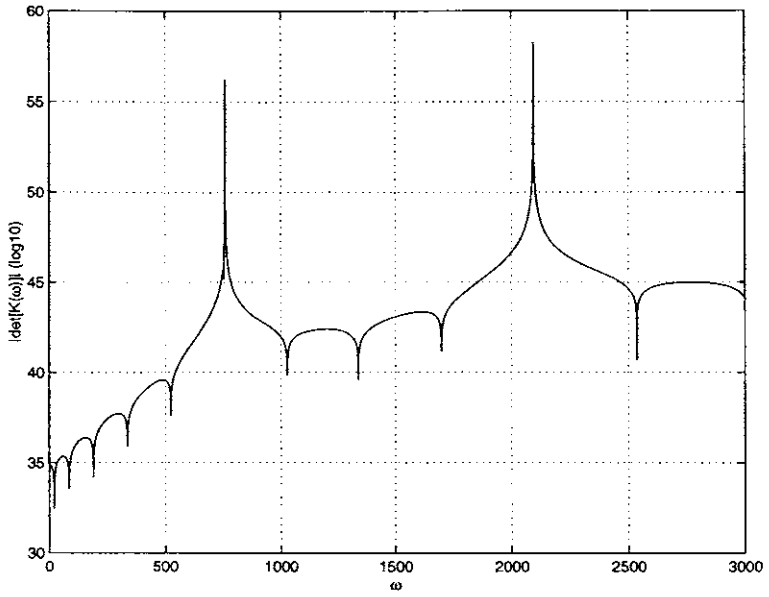

Figure 3-1: The determinant of the dynamic stiffness matrix versus frequency

3.4 Use of the W-W algorithm to analyze a uniform beam structure

A real structure, assembled from elements possessing distributed parameters, has an infinite number of degrees of freedom and an infinite number of natural frequencies. Unlike in a lump-mass model, the determinant $|\mathbf{K}|$ of the global dynamic stiffness matrix in Eq. (3.39) is a transcendental function of the frequency of vibration, becoming infinite at certain frequency values, and possessing an infinite number of roots to the equation $|\mathbf{K}| = \mathbf{0}$. In addition, it cannot be discounted that solutions to Eq. (3.39) of the form $\mathbf{U} = \mathbf{0}$ might also be relevant and nontrivial. It is possible to envisage mode shapes in which all nodal displacements are zero.

Converging on the natural frequencies of a structure having a uniform distribution of mass presents a number of problems. Several natural frequencies may be close together or coincident, while others may correspond to $\mathbf{U} = \mathbf{0}$. Also, as $|\mathbf{K}|$ is now highly irregular function of ω, any trial and error method, which involves computing $|\mathbf{K}|$ and observing when it vanishes, may miss roots. The Wittrick-Williams algo-

rithm provides a foolproof basis for the automatic computation of any and all natural frequencies for a uniform beam structure. This algorithm[28, 33] states that:

$$J = J_0 + s\{\mathbf{K}\}, \tag{3.40}$$

where J represents the number of natural frequencies of a structure exceeded by some trial frequency, ω^*, and $s\{\mathbf{K}\}$ is the sign count of the matrix. $s\{\mathbf{K}\}$ is equal to the number of negative elements on the leading diagonal of the upper (or lower) triangular matrix obtained from $\mathbf{K}$, when $\omega = \omega^*$, by the Gaussian elimination procedure. The rows of $\mathbf{K}$ are taken as pivotal in order, and suitable multiples of each pivotal row are added to all following rows, so that all elements below the pivots become zero. J_0 represents the number of natural frequencies which would still be exceeded if constraints were imposed upon the structure so as to make all the nodal displacements $\mathbf{U}$ zero. When $\mathbf{U}$ is null the structures degenerates into component members in isolation, with their ends clamped. Hence:

$$J_0 = \sum J_m, \tag{3.41}$$

in which the summation $\sum$ extends over all the members; and J_m is the number of natural frequencies between zero and the trial value of ω, for a member with its ends clamped.

From Eq. (3.15), natural frequencies of a uniform beam element with its ends clamped will occur when one or more of the elements of $\mathbf{D}$ are infinite. It is easily verified that the number of the natural frequencies lying between zero and any trial ω^* is:

$$J_m = i - \frac{1}{2}[1 - (-1)^i sign\{\delta\}]; \quad i = \text{largest integer} < \frac{\lambda}{\pi}, \tag{3.42}$$

where $sign\{\delta\}$ is 1 when δ is positive, and is -1 when δ is negative.

A simple but effective method for converging on a specified r-th natural frequency based on the result of Eq. (3.40) characterizes calculating the number of natural frequencies, J, of a structure exceeded by some trial frequency, ω^* [33]. We first try

a large value of ω and see if the corresponding J is $\geq r$. If it is, ω is an upper bound, ω_u, on the natural frequency. If not, we will double ω repetitively until an upper bound is obtained. An initial lower bound, ω_l, is zero. Every time a value of ω is tried, it will always give a new value for either ω_l or ω_u, depending upon whether J is less than r or not (except in the unlikely event of ω being exactly equal to the natural frequency). New values of ω are obtained from the equation:

$$\omega = \frac{1}{2}(\omega_l + \omega_u), \tag{3.43}$$

and the method can be made to converge to any specified accuracy.

For the beam structure in Section 3.3.3, using only one element, we employ the W-W algorithm to find the first 12 natural frequencies, which are almost identical to the analytical ones.

3.5 Complex frequency analysis

The above vibration analysis is for an undamped beam structure. If damping is involved, the determinant of the global dynamic stiffness matrix is frequency-dependent as well as complex. The complex solutions to Eq. (3.39) can be determined by using an iterative root-searching technique. The frequency solution is written as:

$$\omega = \omega_r + i\omega_i, \tag{3.44}$$

where the real part ω_r represents the damped frequency and the imaginary part ω_i represents the exponential decay factor.

The frequency equation of a beam structure can be obtained by setting the determinant of the global dynamic stiffness matrix equal to zero:

$$|\mathbf{K}(\omega)| = 0. \tag{3.45}$$

Frequently, $|\mathbf{K}(\omega)|$ is known implicitly; namely, a rule for evaluating $|\mathbf{K}(\omega)|$ is known, but its explicit form is unknown. There are a number of iterative methods to solve Eq. (3.45), such as the bisection method, the secant method and Newton's method. Some methods are not very satisfactory when all the zeros of a function are required or when good initial approximations are not available. The Muller method [34] is iterative, converges almost quadratically in the vicinity of a root, does not require the evaluation of the derivative of the function, and obtains both real and complex roots even when these roots are not simple. It is a successive iteration toward each particular root by finding the nearer root of a quadratic whose curve passes through the last three points.

Once the complex frequency is found, the nodal displacements can be found by Gauss elimination to the free vibration equation; the corresponding complex mode shape is determined by means of the frequency-dependent shape function.

An example: A simply-supported beam

Taking the beam model in Section 3.3.3 as an illustration and assuming that the structural damping is 0.01, then the bending stiffness is: $EI = 8.66 \times 10^3(1 + 0.01\,i)\,N\,m^2$.

We find the complex natural frequencies by means of the Muller method. The undamped natural frequencies are employed as initial guesses, which the method requires. Table 3.1 shows the first five complex circular natural frequencies and includes the undamped solutions for comparison. This table indicates that for the lightly damped beam structure, the damped natural frequencies are close to the undamped ones.

Order	undamped	damped
1	20.95	20.95+0.1047 i
2	83.82	83.82+0.4192 i
3	188.59	188.59+0.9423 i
4	335.27	335.28+1.6758 i
5	523.86	523.87+2.6180 i

Table 3.1: Complex natural frequencies of a damped beam

Chapter 4

WKB-Based Dynamic Stiffness Method

4.1 Introduction

Marine risers are widely used in the offshore industry for a variety of purposes, such as deep water drilling, export and production. Slender marine risers are often subject to Vortex-Induced Vibration (VIV), and therefore require accurate dynamic modeling for prediction of natural frequencies, mode shapes and fatigue damage rate. A typical marine riser tends to have a large characteristic length with rigid lumps and varying tension, flexural rigidity and mass density. The dynamic behavior of such a riser with variable properties and discontinuities is difficult to predict.

A great deal of research has focused on vibration analysis of a beam structure. For a uniform Euler beam under a constant axial load, the effect of the axial load on the natural frequencies has been found by considering the natural frequencies to be functions of a non-dimensional load parameter and boundary conditions [35]. Using the dynamic stiffness method, Howson and Williams [36] discussed the natural frequencies of Timoshenko members under constant tension. For a uniform beam under a linearly varying axial load, Laird and Fauconneau [37] discussed the upper and lower bounds of the natural frequencies. Using a power series expansion, Dareing and Huang [1] found the natural frequencies of a uniform marine drilling riser. When the

axial load is zero at one end of a beam, Huang and Dareing [38] found that the natural frequencies are functions of boundary conditions and an axial traction parameter.

A dynamic riser model is needed which is able to account for non-uniform properties such as mass density, bending rigidity and tension distribution, and discontinuities such as intermediate supports. A closed form solution to such a system is not generally possible. An approximation to the vibration analysis of such a riser may be accomplished by replacing the variable parameters with constant ones. For example, a variable axial load is often approximated by a tension that is constant over each element. However, many degrees of freedom in the approximation are required in order to obtain accurate results.

This chapter investigates the vibration analysis of marine risers by combining the dynamic stiffness method [39, 30] with the WKB theory [40], which assumes that the coefficients in the differential equation of motion are slowly varying. The WKB-based dynamic stiffness matrix is first derived and the frequency dependent shape function is expressed implicitly. Next the natural frequencies are found by equating to zero the determinant of the global dynamic stiffness matrix, which is obtained by following the procedure of the conventional finite element method. Finally, two example non-uniform risers are analyzed, and the results are compared to show the efficiency of this method.

4.2 Derivation of the WKB-based dynamic stiffness matrix

A general marine riser is a long slender beam system with variable tension distribution, bending rigidity and mass density. The mass/length changes are often discontinuous. Such a riser can be discretized into elements having continuously varying properties within the elements and allowing discontinuities to occur between elements. For each element, the WKB-based dynamic element stiffness matrix is derived by combining the dynamic direct-stiffness method [39] with the WKB approximation method

[40], which is a powerful tool for obtaining a global approximation to the solution of a linear differential equation.

The equation of motion of a riser is written as:

$$\frac{\partial^2}{\partial x^2}[EI(x)\frac{\partial^2 w}{\partial x^2}] - \frac{\partial}{\partial x}[T(x)\frac{\partial w}{\partial x}] + m(x)\frac{\partial^2 w}{\partial t^2} = f(x,t), \tag{4.1}$$

where w is the transverse displacement of riser, E is the Young's modulus of the beam material, $I(x)$ is the area moment inertia of the beam, $T(x)$ is the tension of the beam, $m(x)$ is mass of the beam per unit length, l is length of a riser element, and $f(x,t)$ is external force per unit length.

We define the following non-dimensional parameters:

$s = x/l, \qquad \tau = \omega_0 t, \qquad \omega_0 = \sqrt{\frac{E_0 I_0}{M_0 l^4}}, \qquad Y = \frac{w}{D_e}$

$P(s) = \frac{EI(ls)}{E_0 I_0}, \qquad Q(s) = \frac{T(ls)l^2}{E_0 I_0}, \qquad U(s) = \frac{m(ls)}{M_0},$

$f(s,\tau) = \frac{f(x,t)l^4}{D_e E I_0},$

where D_e is effective diameter of riser, and the subscript o represents the values at a reference cross section. Eq. (4.1) is rewritten in the following non-dimensional form:

$$\frac{\partial^2}{\partial s^2}[P(s)\frac{\partial^2 Y}{\partial s^2}] - \frac{\partial}{\partial s}[Q(s)\frac{\partial Y}{\partial s}] + U(s)\frac{\partial^2 Y}{\partial \tau^2} = f(s,\tau). \tag{4.2}$$

Letting $Y(s,\tau) = R(s)H(\tau)$, the equation for $R(s)$ is:

$$\frac{d^2}{ds^2}[P(s)\frac{d^2 R}{ds^2}] - \frac{d}{ds}[Q(s)\frac{dR}{ds}] - U(s)\Lambda^2 R = 0, \tag{4.3}$$

where $\Lambda = \frac{\omega}{\omega_0}$ is dimensionless frequency.

Assuming that $P(s)$, $Q(s)$ and $U(s)$ in Eq. (4.3) vary slowly with respect to s, compared with variations of $R(s)$, $R'(s)$ and $R''(s)$, rewrite Eq. (4.3) as

$$\varepsilon^4 P(z)\frac{d^4 R}{dz^4} + 2\varepsilon^4 P'(z)\frac{d^3 R}{dz^3} + [\varepsilon^4 P''(z) - \varepsilon^2 Q(z)]\frac{d^2 R}{dz^2} - \varepsilon^2 Q'(z)\frac{dR}{dz} - U(z)\Lambda^2 R = 0, \tag{4.4}$$

where $z \equiv \varepsilon s$, ε is a small parameter.

The formal WKB expansion is written as:

$$R(z) \sim exp[\frac{1}{\delta}\sum_{n=0}^{\infty}\delta^n S_n(z)], \qquad \delta \to 0. \tag{4.5}$$

Substituting this equation into Eq. (4.4), identifying the same order terms, truncating the series and selecting $\delta = \varepsilon$, Kim [7] found the asymptotic solution,

$$\begin{aligned} R(s) &= T_2(s)[C_1 \sin(\int_0^s h_2(\xi)d\xi) + C_2 \cos(\int_0^s h_2(\xi)d\xi)] \\ &+ T_1(s)[C_3 \sinh(\int_0^s h_1(\xi)d\xi) + C_4 \cosh(\int_0^s h_1(\xi)d\xi)], \end{aligned} \tag{4.6}$$

where, C_i $(i = 1-4)$ are constants of integration, and

$$\begin{aligned} T_1(s) &= \frac{1}{\sqrt{P}}[\frac{1}{2}(\frac{Q}{P})^3 + 2\frac{QU\Lambda^2}{P^2} + \frac{1}{2}((\frac{Q}{P})^2 + 4\frac{U\Lambda^2}{P})^{\frac{3}{2}}]^{-\frac{1}{4}}, \\ T_2(s) &= \frac{1}{\sqrt{P}}[-\frac{1}{2}(\frac{Q}{P})^3 - 2\frac{QU\Lambda^2}{P^2} + \frac{1}{2}((\frac{Q}{P})^2 + 4\frac{U\Lambda^2}{P})^{\frac{3}{2}}]^{-\frac{1}{4}}, \\ h_1(s) &= \sqrt{\frac{1}{2}\frac{Q}{P} + \frac{1}{2}\sqrt{(\frac{Q}{P})^2 + 4\frac{U\Lambda^2}{P}}}, \\ h_2(s) &= \sqrt{-\frac{1}{2}\frac{Q}{P} + \frac{1}{2}\sqrt{(\frac{Q}{P})^2 + 4\frac{U\Lambda^2}{P}}}. \end{aligned}$$

Note that: $\frac{dw}{dx} = \frac{D_e}{l}\frac{dY}{ds}$, $\frac{d^2w}{dx^2} = \frac{D_e}{l^2}\frac{d^2Y}{ds^2}$, $\frac{d^3w}{dx^3} = \frac{D_e}{l^3}\frac{d^3Y}{ds^3}$. Neglecting higher order terms, then the nodal displacement vector, $\mathbf{V}_F$, can be formulated in matrix form:

$$\begin{pmatrix} v_{1y} \\ \theta_1 \\ v_{2y} \\ \theta_2 \end{pmatrix} = D_e \begin{bmatrix} 0 & T_2(0) & 0 & T_1(0) \\ \frac{T_2(0)h_2(0)}{l} & 0 & \frac{T_1(0)h_1(0)}{l} & 0 \\ B_1T_2(1) & B_2T_2(1) & B_3T_1(1) & B_4T_1(1) \\ \frac{B_2T_2(1)h_2(1)}{l} & -\frac{B_1T_2(1)h_2(1)}{l} & \frac{B_4T_1(1)h_1(1)}{l} & \frac{B_3T_1(1)h_1(1)}{l} \end{bmatrix} \begin{pmatrix} C_1 \\ C_2 \\ C_3 \\ C_4 \end{pmatrix}. \tag{4.7}$$

Eq. (4.7) can be written in abbreviated form as

$$\mathbf{V}_F = D_e\mathbf{G}\mathbf{C}. \tag{4.8}$$

The nodal forces, $\mathbf{F}$, for an element with changing properties can be written as

$$m_1 = -EI(x)D_e\frac{d^2R}{dx^2}|_{x=0} = -\frac{EI(s)D_e}{l^2}\frac{d^2R}{ds^2}|_{s=0} = -P(s)\frac{E_0I_0D_e}{l^2}\frac{d^2R}{ds^2}|_{s=0}, \quad (4.9)$$

$$m_2 = EI(x)D_e\frac{d^2R}{dx^2}|_{x=l} = \frac{EI(s)D_e}{l^2}\frac{d^2R}{ds^2}|_{s=1} = P(s)\frac{E_0I_0D_e}{l^2}\frac{d^2R}{ds^2}|_{s=1}, \quad (4.10)$$

$$s_{1y} = -EI(x)D_e\frac{d^3R}{dx^3}|_{x=0} - T(x)D_e\frac{dR}{dx}|_{x=0} = \frac{EI(s)D_e}{l^3}\frac{d^3R}{ds^3}|_{s=0} - \frac{T(s)D_e}{l}\frac{dR}{ds}|_{s=0}, \quad (4.11)$$

$$s_{2y} = -(EI(x)D_e\frac{d^3R}{dx^3}|_{x=l} - T(x)D_e\frac{dR}{dx}|_{x=l}) = -\frac{EI(s)D_e}{l^3}\frac{d^3R}{ds^3}|_{s=1} + \frac{T(s)D_e}{l}\frac{dR}{ds}|_{s=1}. \quad (4.12)$$

Substituting for $R(s)$ from Eq. (4.6), Eqs. (4.9) to (4.12) can be written in the matrix form:

$$\mathbf{F} = D_e\mathbf{DC}, \quad (4.13)$$

where, defining: $B_1(s) = \sin\int_0^s h_2(\xi)d\xi$;

$B_2(s) = \cos\int_0^s h_2(\xi)d\xi$;

$B_3(s) = \sinh\int_0^s h_1(\xi)d\xi$; and

$B_4(s) = \cosh\int_0^s h_1(\xi)d\xi$,

the non-zero elements of the matrix $\mathbf{D}$ are:

$$\begin{aligned}
D(1,1) &= -\frac{E_0I_0}{l^3}(P(0)T_2(0)h_2^3(0) - Q(0)T_2(0)h_2(0)),\\
D(1,3) &= \frac{E_0I_0}{l^3}(P(0)T_1(0)h_1^3(0) - Q(0)T_1(0)h_1(0)),\\
D(2,2) &= \frac{P(0)E_0I_0}{l^2}T_2(0)h_2^2(0),\\
D(2,4) &= -\frac{P(0)E_0I_0}{l^2}T_1(0)h_1^2(0),\\
D(3,1) &= \frac{E_0I_0}{l^3}(P(1)T_2(1) + Q(1)T_2(1)h_2(1)),\\
D(3,2) &= -\frac{E_0I_0}{l^3}(P(1)T_2(1)h_2^3(1) + Q(1)T_2(1)h_2(1)),\\
D(3,3) &= -\frac{E_0I_0}{l^3}(P(1)T_1(1)h_1^3(1) + Q(1)T_1(1)h_1(1)),
\end{aligned}$$

$$
\begin{aligned}
D(3,4) &= -\frac{E_0 I_0 B_3}{l^3}(P(1)T_1(1)h_1^3(1) + Q(1)T_1(1)h_1(1), \\
D(4,1) &= -\frac{P(1)E_0 I_0}{l^2}B_1 T_2(1)h_2^2(1), \\
D(4,2) &= -\frac{P(1)E_0 I_0}{l^2}B_2 T_2(1)h_2^2(1), \\
D(4,3) &= \frac{P(1)E_0 I_0}{l^2}B_3 T_1(1)h_1^2(1), \\
D(4,4) &= \frac{P(1)E_0 I_0}{l^2}B_4 T_1(1)h_1^2(1).
\end{aligned}
$$

Combining Eq. (4.8) with Eq. (4.13) leads to:

$$\mathbf{F} = \mathbf{K}\mathbf{V}_F, \tag{4.14}$$

where $\mathbf{K} \equiv \mathbf{D}\mathbf{G}^{-1}$, shown in Eq. (C.1) of Appendix C, is the WKB-based dynamic element stiffness matrix, whose elements are derived by using Maple V.

4.3 Frequency dependent shape function

In order to derive the frequency dependent shape function, rewrite Eq. (4.6) as

$$\mathbf{R(s)} = \begin{bmatrix} T_2(s)\sin\int_0^s h_2(\xi)d\xi \\ T_2(s)\cos\int_0^s h_2(\xi)d\xi \\ T_1(s)\sinh\int_0^s h_1(\xi)d\xi \\ T_1(s)\cosh\int_0^s h_1(\xi)d\xi \end{bmatrix}^T \begin{pmatrix} C_1 \\ C_2 \\ C_3 \\ C_4 \end{pmatrix}. \tag{4.15}$$

Solving for $\mathbf{C}$ from Eq. (4.8) and substituting it into Eq. (4.15) results in:

$$\mathbf{R}(s) = \mathbf{\Phi}\mathbf{V}_F, \tag{4.16}$$

where $\mathbf{\Phi}$, shown in Appendix B, is the frequency dependent shape function obtained by means of Maple V.

4.4 Natural frequencies and mode shapes

With the derived local WKB-based dynamic stiffness element matrix $\mathbf{K}$ in Eq. (4.14), one can obtain the global dynamic stiffness matrix by following the procedure of the conventional finite element method [41], in which local elements are cast into global form by coordinate transformations. Then boundary conditions are imposed. Finally, the equation of motion of free vibration in the restrained global dynamic stiffness form can be written as

$$\mathbf{K}_G(\omega)\mathbf{X} = 0. \tag{4.17}$$

Natural frequencies can be found by equating to zero the determinant of the global dynamic stiffness matrix $\mathbf{K}_G$. The eigenvalues, or the natural frequencies, are obtained by plotting the figure $det[\mathbf{K}_G(\omega)]$, and finding the roots.

Once the natural frequencies are found, one can use Eq. (4.17) to solve for a specific mode shape. An effective way is to use a triangular decomposition. For a specific natural frequency, ω_n, one can use the Gauss elimination to decompose $\mathbf{K}_G(\omega_n)$ as,

$$\mathbf{K}_G(\omega_n) = [\mathbf{L}_n][\mathbf{U}_n], \tag{4.18}$$

where $[\mathbf{L}_n]$ is a lower triangular matrix and $[\mathbf{U}_n]$ is an upper triangular matrix. Then the nth eigen vector is solved from:

$$[\mathbf{U}_n]\mathbf{X}_n = \mathbf{0}, \tag{4.19}$$

where $\mathbf{X}_n \equiv [x_1, x_2, \ldots, x_n]^T$,

$$\mathbf{U}_n \equiv \begin{bmatrix} u_{1,1} & u_{1,2} & \cdots & \cdots & u_{1,n} \\ & u_{2,2} & \cdots & \cdots & u_{2,n} \\ & & \ddots & \vdots & \vdots \\ & & & u_{n-1,n-1} & u_{n-1,n} \\ & & & & u_{n,n} \end{bmatrix}.$$

Assume $x_n = 1$, the $(n-1)$th row in Eq. (4.18) gives

$$u_{n-1,n-1}x_{n-1} + u_{n-1,n} = 0, \tag{4.20}$$

then,

$$x_{n-1} = -\frac{u_{n-1,n}}{u_{n-1,n-1}}. \tag{4.21}$$

Similarly, one can obtain from the $(n-2)$ row in Eq. (4.18),

$$x_{n-2} = -\frac{u_{n-2,n-1}x_{n-1} + u_{n-2,n}}{u_{n-2,n-2}}. \tag{4.22}$$

The general recurrence relation can be written as

$$x_i = -\frac{\sum_{k=i+1}^{n} u_{i,k}x_k}{u_{i,i}}, \qquad (i = 1, \cdots, n-1). \tag{4.23}$$

Hence, mode components at element nodes are calculated from the above formulas. Then one can use Eq. (4.16) to calculate mode components for any points within an element. In this way, accurate mode shapes can be obtained.

On the basis of the above procedure, Matlab codes solving for natural frequencies and mode shapes for marine risers were developed.

4.5 Numerical examples

4.5.1 A uniform drilling riser under linearly varying tension [1]

The parameters of a simply supported riser are

Length $l = 500ft$;

Outer diameter $d_o = 24$ in.;

Thickness $t = 5/8$ in.;

Young's modulus $E = 30 \times 10^6$ lb/sq in.;

Moment of inertia $I = 3136.9in^4$;

Mass per unit length $m = 20.8$ Slugs/ft(includes mass of drilling mud and sea water);

Tension at the bottom ball joint $T_0 = 286,000$ lb;

Net weight of riser per unit length in sea water $w = 214$ lb/ft (includes 38 lb/ft for choke and kill lines);

Cross-sectional area of the riser exterior $A_e = 3.14$ sq ft.;

Cross-sectional area of the riser interior $A_i = 2.99$ sq ft.;

Density of sea water $\rho_w = 64.8$ lb/cu ft;

density of drilling mud $\rho_m = 85$ lb/cu ft.

This riser was discretized into five elements with equal length. Figure 4-1 shows the determinant of the dynamic stiffness matrix of the 500-ft riser versus frequency. Table 4-1 shows the first five natural frequencies found from Figure 4-1. In order to

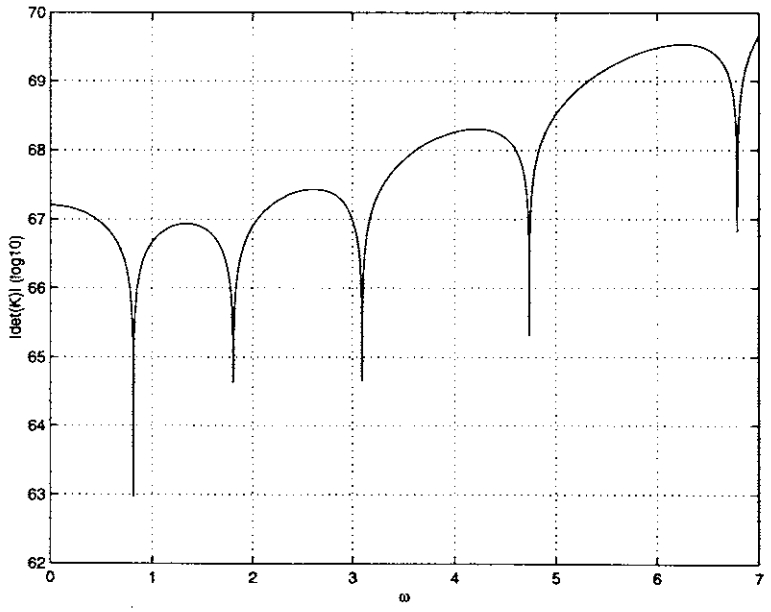

Figure 4-1: The determinant of the dynamic stiffness matrix of a 500-ft riser versus frequency

verify the results, a finite element procedure which assumed constant tension over each beam element was developed. Converged values for natural frequencies were found employing 60 elements in the FEM. The approximation result [1] previously obtained

by means of a power series expansion is also included for comparison. It is observed from Table 4-1 that the natural frequencies acquired by the WKB-based dynamic stiffness method using only five elements are accurate. Measuring the position $x(m)$ from the bottom, Figure 4-2 depicts the first three mode shapes.

Table 4-1 depicts that the natural frequencies obtained by Dareing and Huang [1] are also accurate, compared with those obtained by using the FEM and the WKB-based dynamic stiffness method. However, their finding of "points of inflection" in mode shapes is not correct.

Table 4.1: Comparison of circular natural frequencies

Order	Dareing and Huang [1]	FEM (60 elements)	WKB-DSSM (5 elements)
1	0.8150	0.8150	0.8150
2	1.8036	1.8038	1.8037
3	3.0876	3.0879	3.0875
4	4.7375	4.7377	4.7375
5	6.7890	6.7896	6.7890

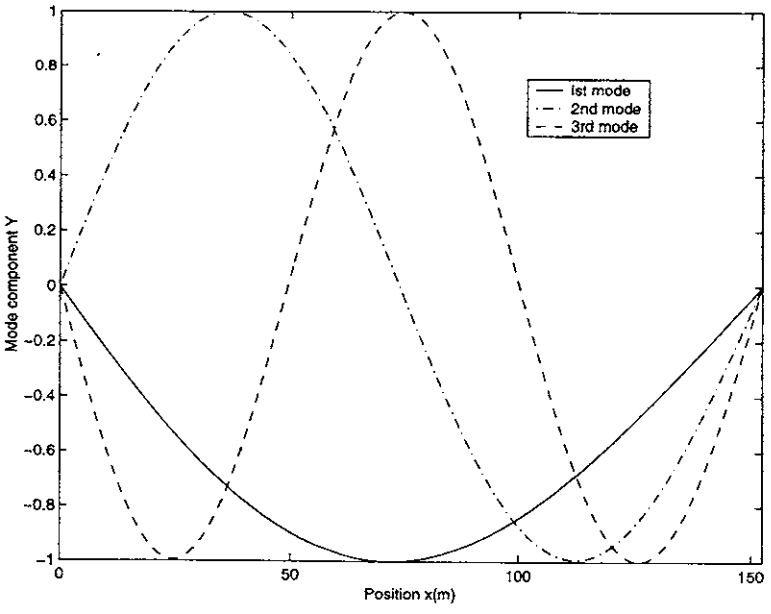

Figure 4-2: The first three natural mode shapes for a 500-ft riser

4.5.2 A non-uniform riser with variable properties

Due to attachments such as buoyancy modules, a typical marine riser is a system with variable properties including tension and mass density. The simply supported Helland-Hansen riser is one such riser, with the following specification:

Length $L = 689.29$ m;

Outer steel diameter $d_o = 21$ inches;

Inner steel diameter $d_i = 19.75$ inches;

Buoyancy diameter $d_b = 44.5$ inches.

Figures 4-3 and 4-4 show the variations of the mass density and tension at the measured points which are marked, respectively. The position is measured from the bottom. These figures demonstrate that the mass density does not change continuously, and tension does not vary linearly.

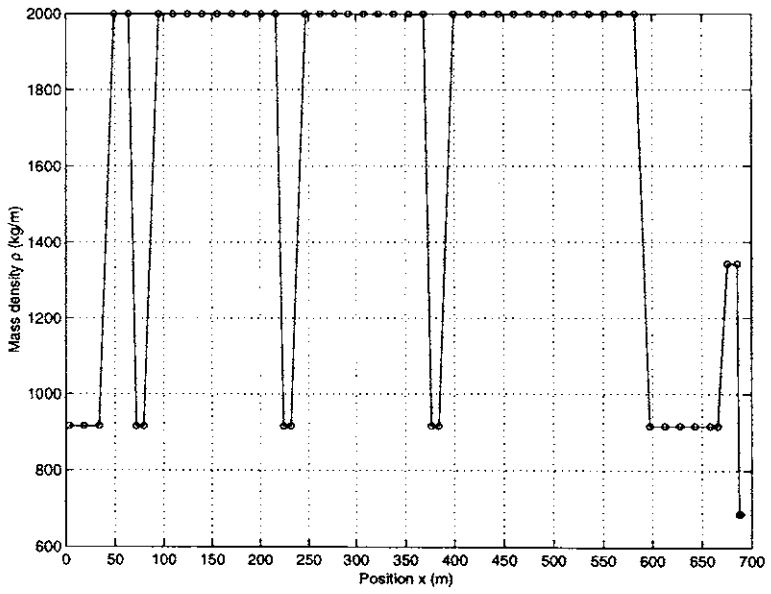

Figure 4-3: The mass density variation of the Helland-Hansen riser

There are eleven segments in Figures 4-3 and 4-4, each of which has continuous variation of mass and tension. By dividing each segment into two equally-sized elements, we used 22 elements to do the WKB-based dynamic stiffness matrix analysis. Figure 4-5 shows the first 20 natural frequencies found by means of plotting the determinant. The approximate results using Shear7, which assumed the riser to be an equivalent uniform beam with linearly varying tension, are included for comparison. The Shear7 results are accurate for lower order natural frequencies.

Figure 4-6 depicts the 20th mode shape, which is of interest. The locations of the antinodes are not evenly spaced. Therefore, the mode differs from trigonometric ones.

It is found that 282 elements are needed for the standard finite element method to obtain a good 20th mode shape and a converged natural frequency of 0.6952 Hz. This is close to 0.6955 Hz by the WKB-based dynamic stiffness method with only 11 elements. Very few elements are necessary if they are chosen wisely. Within each element, properties must vary slowly so as to satisfy the WKB assumptions. Discontinuities should occur at the junctions of elements. In this example, the mass/length changes abruptly ten times requiring a total of eleven elements to adequately model the system.

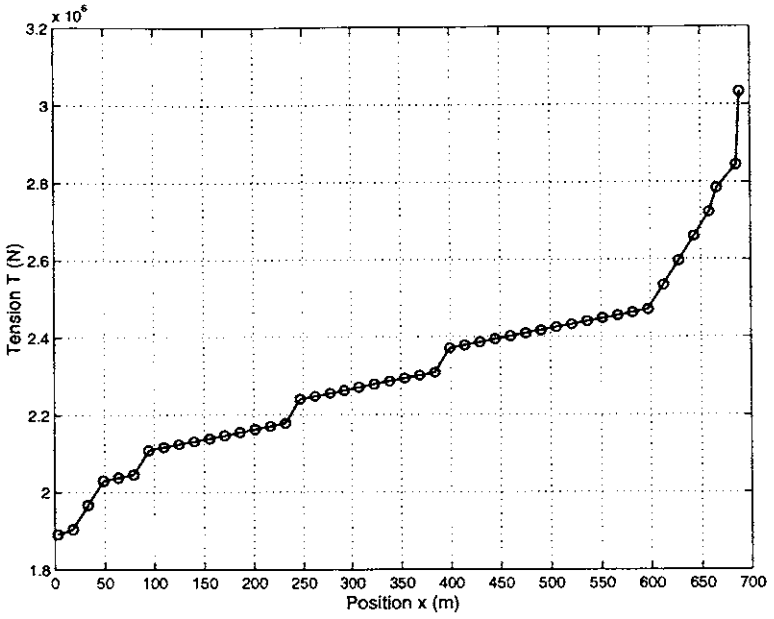

Figure 4-4: The tension variation of the Helland-Hansen riser

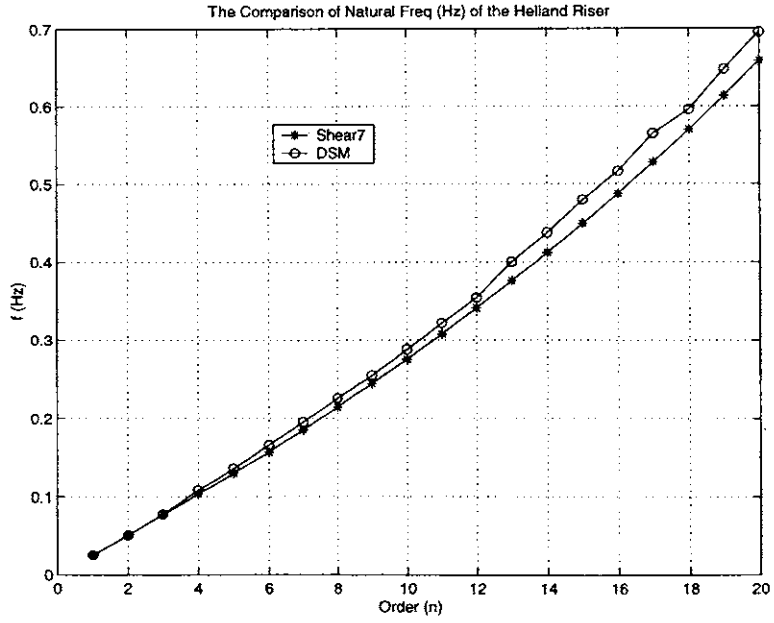

Figure 4-5: The comparison of the natural frequencies with those obtained by Shear7

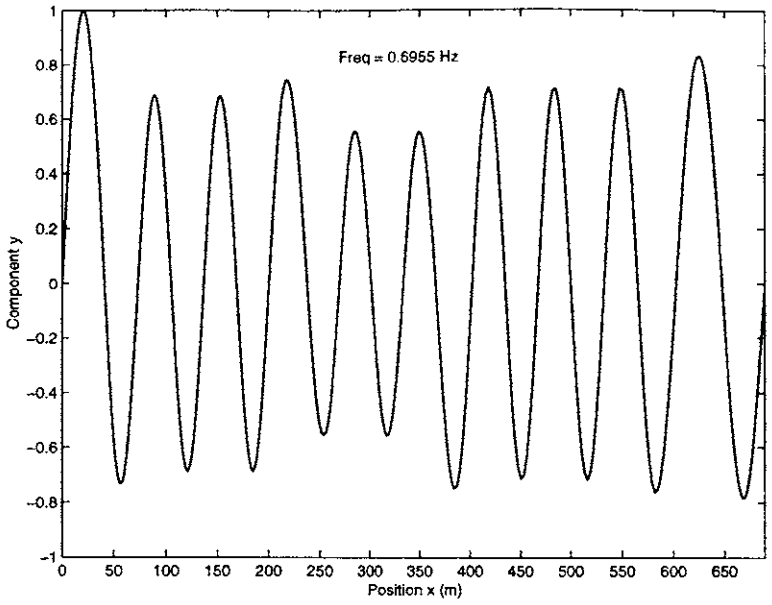

Figure 4-6: The 20th mode shape of the Helland-Hansen riser

4.6 Conclusions

Knowing natural frequencies and mode shapes is important in the prediction of the VIV of marine risers. The WKB-based dynamic stiffness method has been introduced to analyze non-uniform marine risers on the assumption that the properties are slowly varying within elements. When compared with a conventional finite element method, the present method demonstrates some advantages, such as eliminating spatial discretization error and finding accurate natural frequencies by means of a limited number of elements.

In determination of natural frequencies from Eq. (4.17), it is noted that $\mathbf{X} = \mathbf{0}$ is not necessarily a trivial set of solutions but corresponds, sometimes, to a mode shape whose nodes are nodes of the FEM. To find natural frequencies, an infallible search algorithm is available for structural analysis where element properties are uniform [31]. In the future this method will be used to extend the algorithm to the frequency analysis of marine risers whose element properties are non-uniform.

Chapter 5

The WKB-Based Dynamic Stiffness Method with the W-W Algorithm

5.1 Introduction

Chapter 4 presented the derivation of the WKB-based dynamic stiffness matrix method for a general non-uniform riser. The natural frequencies are obtained from:

$$\mathbf{K}(\omega)\,\mathbf{X} = \mathbf{0}, \tag{5.1}$$

where $\mathbf{K}$ is the global dynamic stiffness matrix whose elements are, in general, transcendental functions of circular frequency ω, and $\mathbf{X}$ is the vector of nodal displacements.

In Chapter 4, we found the roots to Eq. (5.1) using the determinant plotting method. However, solutions in the form of $\det \mathbf{K}(\omega) = \infty$ and $\mathbf{X} = \mathbf{0}$ might also be relevant and nontrivial. It does not mean that all frequencies making $\mathbf{K}(\omega) = \infty$ are eigen-frequencies. If fewer elements are used, the determinant may change sign by passing through zero as well as via infinity. In order to avoid numerical problems, the determinant plotting method requires the use of more elements.

For a uniform beam member, Wittrick and Williams [28] presented an automatic computation of natural frequencies. For a tapered beam whose section properties vary regularly, Banerjee and Williams [42] gave a procedure to calculate natural frequencies. This procedure, however, requires a preliminary step of finding the natural frequencies of clamped-clamped tapered members.

A typical marine riser is a slender system having non-uniform properties including mass per unit length, bending rigidity, and tension. The second section of this chapter extends the Wittrick-Williams (W-W) algorithm to a general non-uniform marine riser, and combines the algorithm with the WKB-based dynamic stiffness method. The third section illustrates this technique with examples to automatically compute natural frequencies. Using the WKB method, the fourth section derives the formulas for calculating mode shapes, slopes and curvatures. Finally, this chapter analyzes the marine risers with complex boundary conditions.

5.2 Extension of the W-W algorithm to non-uniform marine risers

Based on a theorem due to Lord Rayleigh, the W-W algorithm [28] states that:

$$\mathbf{J} = \mathbf{J}_0 + s\{\mathbf{K}\}, \tag{5.2}$$

where $\mathbf{J}$ represents the number of natural frequencies of a structure exceeded by a trial frequency, ω^*, $\mathbf{J}_0$ represents the number of natural frequencies which would still be exceeded if constraints were imposed upon the structure so as to make all nodal displacements $\mathbf{X}$ zero, and $s\{\mathbf{K}\}$ is the sign count of the matrix $\mathbf{K}$. $s\{\mathbf{K}\}$ is defined in [28], and is equal to the number of negative elements on the leading diagonal of the upper triangular matrix obtained from $\mathbf{K}$, when $\omega = \omega^*$, by the Gaussian elimination procedure, which is discussed in Chapter 3.

Chapter 4 derives the WKB-based dynamic stiffness matrix of a non-uniform riser

member. The global dynamic stiffness matrix $\mathbf{K}$ is obtained by assembling all the contributions from elements. Clearly $s\{\mathbf{K}\}$ is easily computed by the Gaussian elimination procedure without row interchanges. The key in the extension of the W-W algorithm to vibration analysis of a general riser is the computation of J_0.
J_0 can be found from

$$\mathbf{J}_0 = \sum J_m, \tag{5.3}$$

where J_m is the number of natural frequencies of a component member, with its ends clamped, which have been exceeded by ω^*, and the summation extends over all the component members.

For a general marine riser, Eq. (4.5) in Chapter 4 expresses the non-dimensional asymptotic solution of vibration amplitude, $R(s)$. The boundary conditions for a clamped-clamped riser member are:

$$R(0) = R'(0) = R(1) = R'(1). \tag{5.4}$$

The boundary conditions in Eqs. (5.4) result in the following characteristic equation:

$$\begin{vmatrix} 0 & T_2(0) & 0 & T_1(0) \\ T_2(0)\,h_2(0) & 0 & T_1(0)\,h_1(0) & 0 \\ T_2(1)\,B_1 & T_2(1)\,B_2 & T_1(1)\,B_3 & T_1(1)\,B_4 \\ T_2(1)\,B_2\,h_2(1) & -T_2(1)\,B_1\,h_2(1) & T_1(1)\,B_4\,h_1(1) & T_1(1)\,B_3\,h_1(1) \end{vmatrix} = 0. \tag{5.5}$$

We know from Chapter 4 that the functions in Eq. (5.5), $T_1(s)$, $T_2(s)$, $h_1(s)$, and $h_2(s)$, are highly dependent on the circular frequency ω, and B_i $(i = 1, 2, 3, 4)$ are implicit functions of ω. Hence it is not simple to directly find the closed-form component of J_m arising from Eq. (5.5). However, we can indirectly find J_m by analyzing the corresponding simply-supported beam system; namely, the boundary conditions of a riser element are first assumed to be pinned-pinned rather than clamped-clamped.

For a pinned-pinned riser element, the WKB method [7] leads to the following frequency equation:

$$\int_0^L \sqrt{-\frac{1}{2}\frac{T(x)}{EI(x)} + \frac{1}{2}\sqrt{(\frac{T(x)}{EI(x)})^2 + 4\frac{m(x)\omega_{Pn}^2}{EI(x)}}}dx = n\pi, \tag{5.6}$$

where the subscript P on ω_{Pn} indicates "pinned" boundary conditions, and L is a riser element length. Hence, the number of natural frequencies of a simply-supported riser element exceeded by the trial ω^* is J_c, which is defined as:

$$\text{the highest integer} < \frac{\int_0^L \sqrt{-\frac{1}{2}\frac{T(x)}{EI(x)} + \frac{1}{2}\sqrt{(\frac{T(x)}{EI(x)})^2 + 4\frac{m(x)\omega^{*2}}{EI(x)}}}dx}{\pi}. \tag{5.7}$$

With a pinned-pinned riser element treated as a complete structure, for which the dynamic stiffness matrix is $\mathbf{B}$, Eq. (5.2) then gives

$$J_c = J_m + s\{\mathbf{B}\}. \tag{5.8}$$

Then

$$J_m = J_c - s\{\mathbf{B}\}, \tag{5.9}$$

where $s\{\mathbf{B}\}$ is the sign count of the matrix $\mathbf{B}$.

Although its explicit form is not readily found, the WKB-based dynamic stiffness matrix, $\mathbf{B}$, of a simply-supported riser element is symbolically written as:

$$\mathbf{B} = \begin{bmatrix} b_{11} & b_{12} \\ b_{21} & b_{22} \end{bmatrix}. \tag{5.10}$$

Due to the symmetry of $\mathbf{B}$, $b_{12} = b_{21}$. The leading principal minors of $\mathbf{B}$ are: b_{11} and $b_{11}b_{22} - b_{12}^2$.

It is known that the number of negative characteristic values, $s\{\mathbf{B}\}$, of $\mathbf{B}$ is equal to the number of changes of sign between consecutive members of the Sturm sequence:

$$\{1, \quad b_{11}, \quad b_{11}b_{22} - b_{12}^2\}. \tag{5.11}$$

It can readily be shown that:

$$s\{\mathbf{B}\} = \frac{1}{2}[2 - \mathrm{sgn}(b_{11}) - \mathrm{sgn}(\frac{b_{11}b_{22} - b_{12}^2}{b_{11}})], \tag{5.12}$$

where $\mathrm{sgn}(b_{11})$ and $\mathrm{sgn}(\frac{b_{11}b_{22}-b_{12}^2}{b_{11}})$ are $+1$ or -1 depending on the signs of b_{11} and $\frac{b_{11}b_{22}-b_{12}^2}{b_{11}}$, respectively.

Substituting Eq. (5.12) into Eq. (5.9) results in:

$$J_m = J_c - \frac{1}{2}[2 - \mathrm{sgn}(b_{11}) - \mathrm{sgn}(\frac{b_{11}b_{22} - b_{12}^2}{b_{11}})]. \tag{5.13}$$

Hence, J_0 is obtained by using Eq. (5.3). As a result, J for a general riser is found from Eq. (5.2) when $\omega = \omega^*$. Thus a computer convergence routine can be written which adjusts ω^* systematically to certainly converge upon any specified natural frequency of a riser. The W-W algorithm is therefore extended to the analysis of a general non-uniform beam member, and combined with WKB-based dynamic stiffness matrix method.

5.3 Examples of marine risers

We developed the computational codes of the WKB-based dynamic stiffness method with the W-W algorithm. This new method allows us to use the minimum number of elements to accurately analyze a non-uniform riser with variable properties and discontinuities. The advantage of this approach is particularly evident for calculating higher order natural frequencies.

The first example is a uniform beam under linearly varying tension. The second example is a typical riser with variable properties. For both examples, the results found by Shear7 are also included for comparison. The comparison depicts the accuracy and efficiency of this method.

Example 1 A marine riser under linearly varying tension

A simply supported riser appears as an example with specification as follows:

Length $l = 1400$ ft;

Young's modulus $E = 29000$ Ksi;

Moment of inertia $I = 0.02074\,\text{ft}^4$;

Total mass per unit length including added mass effects $m = 7.45789$ Slugs/ft;

Minimum tension $T_0 = 50000.0$ Pounds;

Linearly varying tension factor $\alpha = 115.25$ lb/ft.

Using only one element to analyze this riser, Table-1 shows the first 13 natural frequencies . The results obtained by Shear7 using 200 and 1000 segments, respectively, are also included for comparison. The Shear7 solution is a WKB solution with linearly varying tension and constant structural properties. Table 5.1 demonstrates that the natural frequencies found by means of the W-W algorithm are accurate.

Order	shear7(200)	shear7(1000)	W-W
1	0.0447	0.0448	0.0448
2	0.0902	0.0903	0.0903
3	0.1370	0.1372	0.1373
4	0.1857	0.1860	0.1861
5	0.2368	0.2371	0.2371
6	0.2904	0.2908	0.2909
7	0.3470	0.3474	0.3475
8	0.4067	0.4072	0.4073
9	0.4699	0.4704	0.4705
10	0.5367	0.5372	0.5373
11	0.6073	0.6079	0.6080
12	0.6819	0.6825	0.6827
13	0.7607	0.7614	0.7615

Table 5.1: Comparison of natural frequencies (Hz)

Example 2 The Helland riser with variable properties

The Helland riser appears as the second example, the parameters of which are specified in Chapter 4. Figures 4-2 and 4-3 demonstrate the variations of the mass density and tension, respectively.

We find the natural frequencies and the mode shapes by using only 11 elements,

each of which has continuous variation of mass distribution and effective tension. Figure 5-1 shows the first 20 natural frequencies. We also include for comparison the approximate results by means of Shear7, which simply assumes constant average mass density and linearly varying tension for the whole riser.

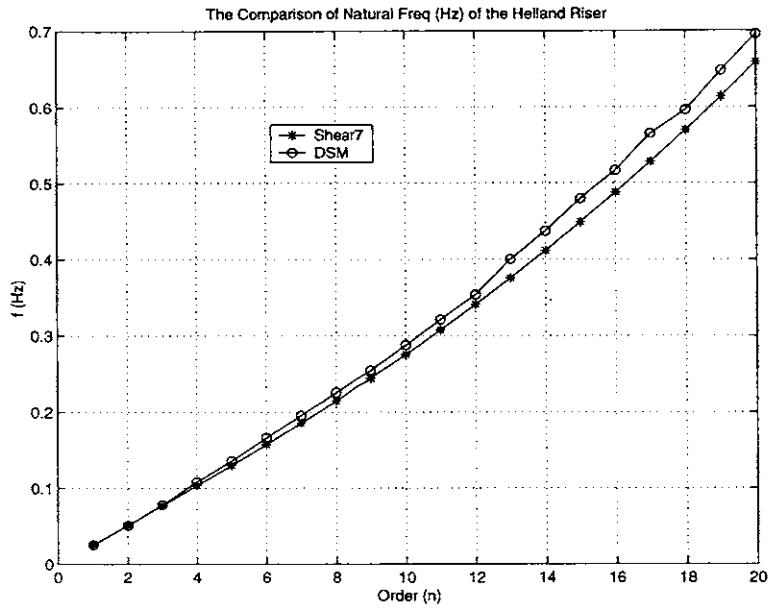

Figure 5-1: The comparison of the natural frequencies with those obtained by Shear7

5.4 Calculation of mode shapes, slopes and curvatures

5.4.1 Introduction

Mode shapes, slopes and curvatures are useful in the prediction of vortex-induced vibration of a riser. Once natural frequencies of marine risers are found by means of the WKB-Based dynamic stiffness method in connection with the W-W algorithm, mode shapes, mode slopes and mode curvatures can be derived from the frequency dependent shape function. Equation (4.5) in Chapter 4 is written as:

$$\mathbf{R(s)} = \begin{bmatrix} T_2(s)\sin\int_0^s h_2(\xi)d\xi \\ T_2(s)\cos\int_0^s h_2(\xi)d\xi \\ T_1(s)\sinh\int_0^s h_1(\xi)d\xi \\ T_1(s)\cosh\int_0^s h_1(\xi)d\xi \end{bmatrix}^T \begin{pmatrix} C_1 \\ C_2 \\ C_3 \\ C_4 \end{pmatrix}, \tag{5.14}$$

where the column vector $\mathbf{C} = G^{-1}V_F$.

$$R(s) = \Phi V_F, \tag{5.15}$$

where Φ, shown in Chapter 4, is the frequency dependent shape function obtained by means of Maple V.

With natural frequencies, mode components at nodes are found by using triangular decomposition of the global dynamic stiffness matrix, discussed in Chapter 4. Mode components at any point within an element is obtained with Eq. (5.15).

Formulas for calculating mode slope and curvature are derived from Eq. (5.14). Mode slope is formulated as:

$$\mathbf{R}'\mathbf{(s)} = \begin{bmatrix} T_2'(s)\sin\int_0^s h_2(\xi)d\xi + T_2(s)h_2(s)\cos\int_0^s h_2(\xi)d\xi \\ T_2'(s)\cos\int_0^s h_2(\xi)d\xi - T_2(s)h_2(s)\sin\int_0^s h_2(\xi)d\xi \\ T_1'(s)\sinh\int_0^s h_1(\xi)d\xi + T_1(s)h_1(s)\cosh\int_0^s h_1(\xi)d\xi \\ T_1'(s)\cosh\int_0^s h_1(\xi)d\xi + T_1(s)h_1(s)\sinh\int_0^s h_1(\xi)d\xi \end{bmatrix}^T \begin{pmatrix} C_1 \\ C_2 \\ C_3 \\ C_4 \end{pmatrix}. \tag{5.16}$$

Defining $B_1(s) \equiv \sin\int_0^s h_2(\xi)d\xi$, $B_2(s) \equiv \cos\int_0^s h_2(\xi)d\xi$, $B_3(s) \equiv \sinh\int_0^s h_1(\xi)d\xi$, and $B_4(s) \equiv \cosh\int_0^s h_1(\xi)d\xi$, Eq.(5.16) is rewritten as:

$$\mathbf{R}'\mathbf{(s)} = \begin{bmatrix} T_2'(s)B_1(s) + T_2(s)B_1'(s) \\ T_2'(s)B_2(s) + T_2(s)B_2'(s) \\ T_1'(s)B_3(s) + T_1(s)B_3'(s) \\ T_1'(s)B_4(s) + T_1(s)B_4'(s) \end{bmatrix}^T \begin{pmatrix} C_1 \\ C_2 \\ C_3 \\ C_4 \end{pmatrix}. \tag{5.17}$$

Similarly, mode curvature is obtained as:

$$\mathbf{R}''(\mathbf{s}) = \begin{bmatrix} T_2''(s)B_1(s) + 2T_2'(s)B_1'(s) + T_2(s)B_1''(s) \\ T_2''(s)B_2(s) + 2T_2'(s)B_2'(s) + T_2(s)B_2''(s) \\ T_1''(s)B_3(s) + 2T_1'(s)B_3'(s) + T_1(s)B_3''(s) \\ T_1''(s)B_4(s) + 2T_1'(s)B_4'(s) + T_1(s)B_4''(s) \end{bmatrix}^T \begin{pmatrix} C_1 \\ C_2 \\ C_3 \\ C_4 \end{pmatrix}. \tag{5.18}$$

Using $\mathbf{C} = G^{-1}V_F$, Eqs. (5.17) and (5.18) are further written as:

$$\mathbf{R}'(\mathbf{s}) = \begin{bmatrix} T_2'(s)B_1(s) + T_2(s)B_1'(s) \\ T_2'(s)B_2(s) + T_2(s)B_2'(s) \\ T_1'(s)B_3(s) + T_1(s)B_3'(s) \\ T_1'(s)B_4(s) + T_1(s)B_4'(s) \end{bmatrix}^T \mathbf{G^{-1}V_F}. \tag{5.19}$$

$$\mathbf{R}''(\mathbf{s}) = \begin{bmatrix} T_2''(s)B_1(s) + 2T_2'(s)B_1'(s) + T_2(s)B_1''(s) \\ T_2''(s)B_2(s) + 2T_2'(s)B_2'(s) + T_2(s)B_2''(s) \\ T_1''(s)B_3(s) + 2T_1'(s)B_3'(s) + T_1(s)B_3''(s) \\ T_1''(s)B_4(s) + 2T_1'(s)B_4'(s) + T_1(s)B_4''(s) \end{bmatrix}^T \mathbf{G^{-1}V_F}. \tag{5.20}$$

The final step is to find formulations of basic operators in Eqs. (5.19) and (5.20). Neglecting high order small terms, we formulate each basic operator as follows:

$B_1(s) = \sin \int_0^s h_2(\xi)d\xi$;

$B_1'(s) = B_2(s)h_2(s)$; and

$B_1''(s) = h_2'(s)B_2(s) - h_2^2(s)B_1(s)$.

$B_2(s) = \cos \int_0^s h_2(\xi)d\xi$;

$B_2'(s) = -B_1(s)h_2(s)$; and

$B_2''(s) = -h_2'(s)B_1(s) - h_2^2(s)B_2(s)$.

$B_3(s) = \sinh \int_0^s h_1(\xi)d\xi$;

$B_3'(s) = B_4(s)h_1(s)$; and

$B_3''(s) = h_1'(s)B_4(s) + h_1^2(s)B_3(s)$.

$B_4(s) = \cosh \int_0^s h_1(\xi)d\xi$;
$B_4'(s) = B_3(s)h_1(s)$; and
$B_4''(s) = h_1'(s)B_3(s) + h_1^2(s)B_4(s)$.

$T_1(s) = \frac{1}{\sqrt{P}}[\frac{1}{2}(\frac{Q}{P})^3 + 2\frac{QU\Lambda^2}{P^2} + \frac{1}{2}((\frac{Q}{P})^2 + 4\frac{U\Lambda^2}{P})^{\frac{3}{2}}]^{-\frac{1}{4}}$;
$T_2(s) = \frac{1}{\sqrt{P}}[-\frac{1}{2}(\frac{Q}{P})^3 - 2\frac{QU\Lambda^2}{P^2} + \frac{1}{2}((\frac{Q}{P})^2 + 4\frac{U\Lambda^2}{P})^{\frac{3}{2}}]^{-\frac{1}{4}}$;
$h_1(s) = \sqrt{\frac{1}{2}\frac{Q}{P} + \frac{1}{2}\sqrt{(\frac{Q}{P})^2 + 4\frac{U\Lambda^2}{P}}}$; and
$h_2(s) = \sqrt{-\frac{1}{2}\frac{Q}{P} + \frac{1}{2}\sqrt{(\frac{Q}{P})^2 + 4\frac{U\Lambda^2}{P}}}$.

It is very tedious to derive $T_1'(s)$, $T_1''(s)$, $T_2'(s)$ and $T_2''(s)$. The details of the derivation are not given here. However, as in Shear7, these derivatives can be neglected. Our numerical experiments have shown that the difference between final results calculated by keeping or neglecting the terms associated with the derivatives is very small.

5.4.2 Examples

Example 1 A 1400-ft riser under linearly varying tension

This riser is specified in Example 1 of Section 5.3. It is a uniform beam under linearly varying tension. We analyzed this example for a particular current profile by Shear7 and found that the 6th, 7th and 13th modes were dominant. Figures 5-2 to 5-9 depict the mode shapes, slopes and curvatures of the first to 7th and 13th modes. The nth mode shape of a pinned-pinned beam with varying tension is [43]:

$$Y_n(x) = sin[\int_0^x \sqrt{-\frac{1}{2}\frac{T(s)}{EI(s)} + \frac{1}{2}\sqrt{[\frac{T(s)}{EI(s)}]^2 + 4\frac{m(s)\omega_n^2}{EI(s)}}}\, ds], \qquad (5.21)$$

where x is the spatial location. On the basis of this equation, Shear7 finds the approximate solutions to mode slopes and curvatures by neglecting higher terms. We include the results by means of the formulas in Shear7 for comparison. Figures 5-2

to 5-9 indicate that the formulations in Section 5.4 are correct.

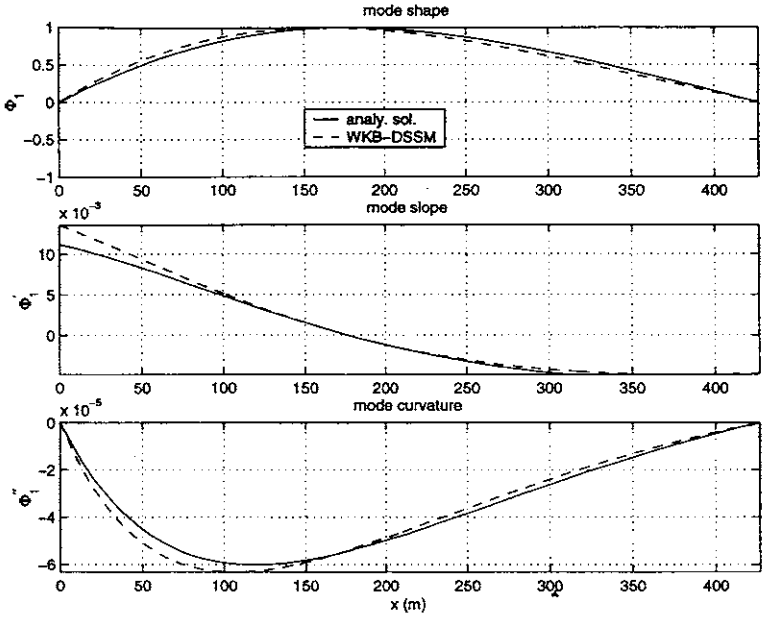

Figure 5-2: The 1st mode shape, slope and curvature of the 1400-ft riser

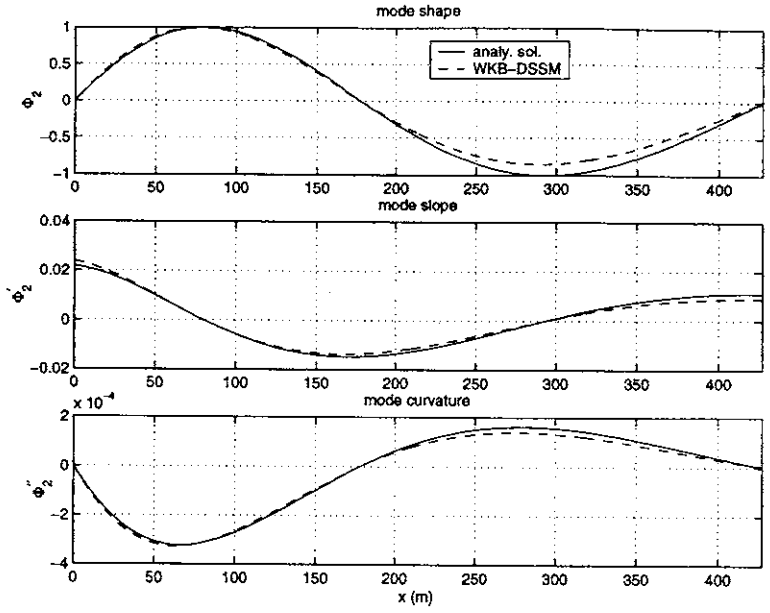

Figure 5-3: The 2nd mode shape, slope and curvature of the 1400-ft riser

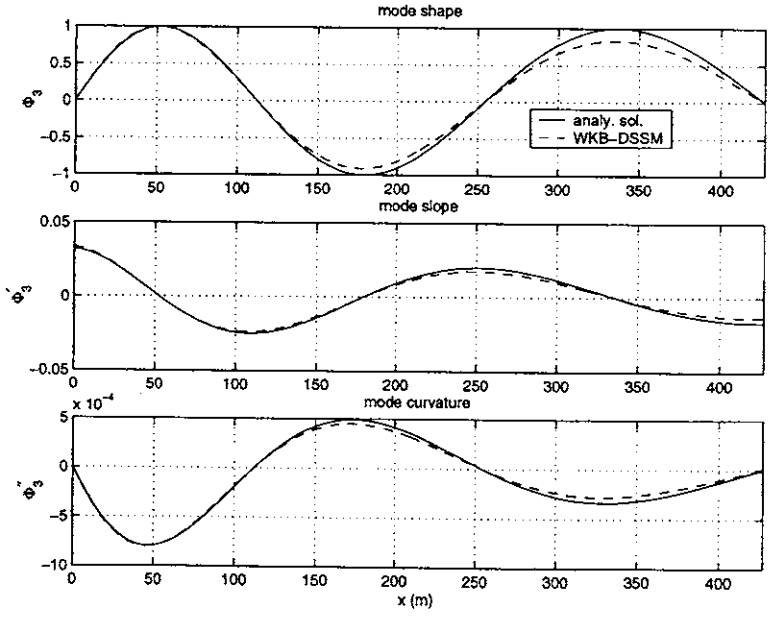

Figure 5-4: The 3rd mode shape, slope and curvature of the 1400-ft riser

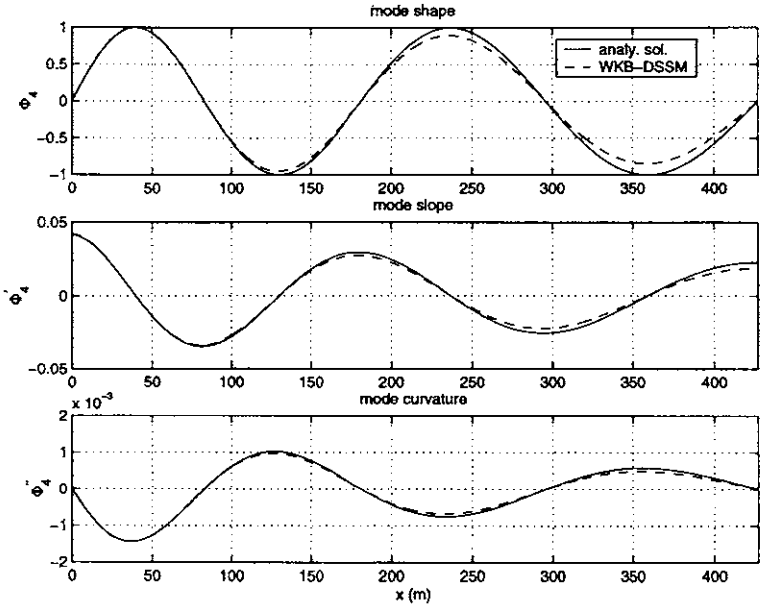

Figure 5-5: The 4th mode shape, slope and curvature of the 1400-ft riser

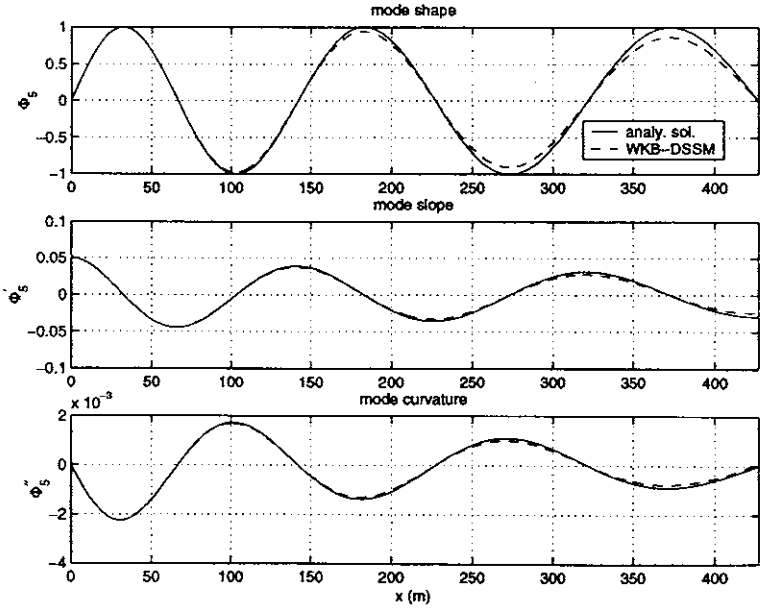

Figure 5-6: The 5th mode shape, slope and curvature of the 1400-ft riser

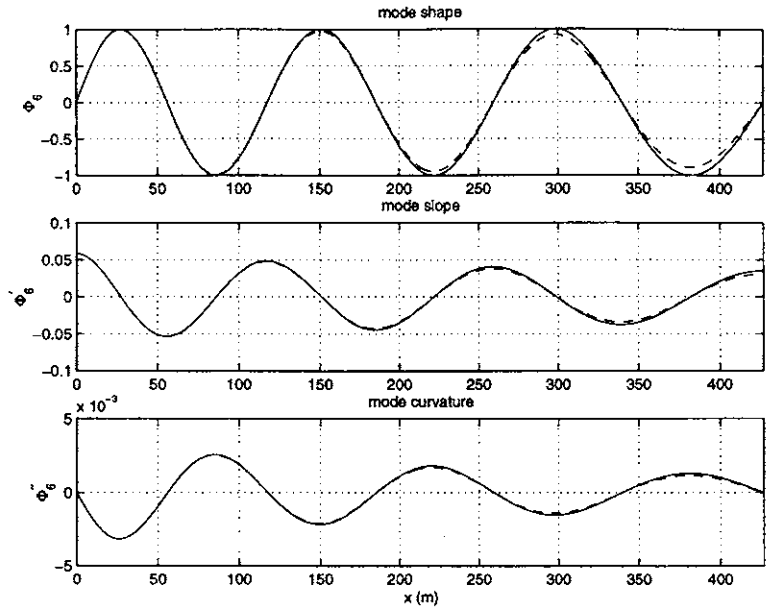

Figure 5-7: The 6th mode shape, slope and curvature of the 1400-ft riser

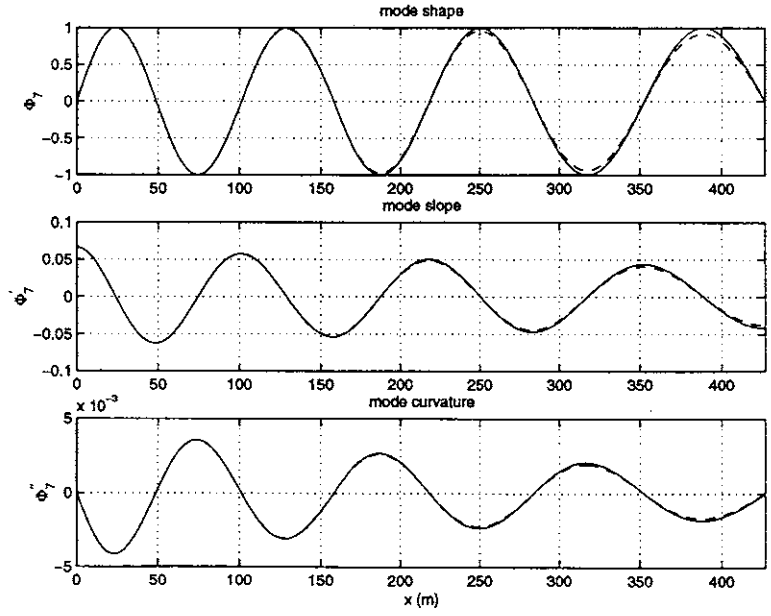

Figure 5-8: The 7th mode shape, slope and curvature of the 1400-ft riser

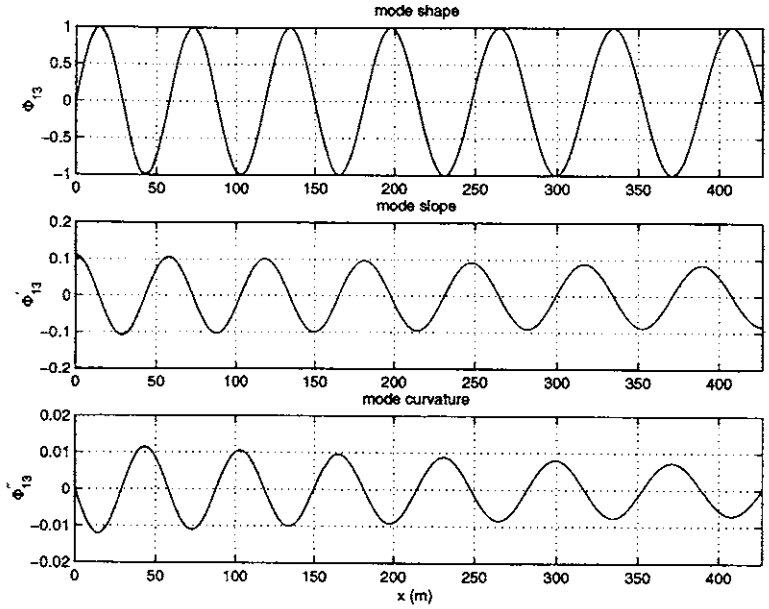

Figure 5-9: The 13th mode shape, slope and curvature of the 1400-ft riser

Example 2 The Helland-Hansen riser with variable properties

The Helland riser re-appears as an example to illustrate calculations of mode shapes, slopes and curvatures, as discussed in Section 5.4.1.

Figures 5-10 to 5-16 indicate the mode shapes, slopes and curvatures of the 1st to 5th, 18th and 20th mode, respectively. These figures demonstrate that the curvature of lower modes is sensitive to the discontinuities of the riser.

We normalize the mode shapes such that they have a maximum displacement equal to 1, as required by Shear7 program. The results of natural frequencies, mode shapes, mode slopes, and mode curvatures are exported from the WKB-based DSM model to the built-for-purpose vortex induced vibration prediction program, Shear7. Appendix D shows the VIV results by Shear7 (version 3.0) for a particular current profile and indicates for comparison the results by the approximation used in Section 4.5.2.

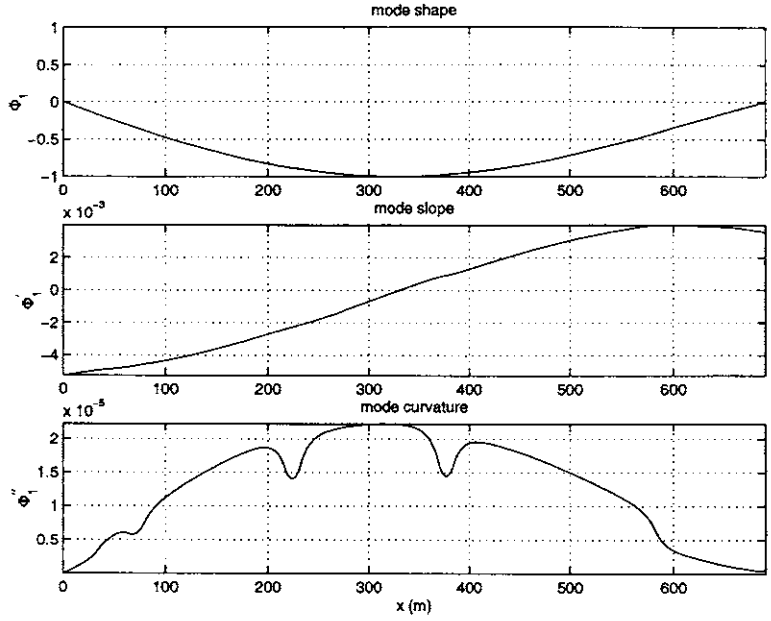

Figure 5-10: The 1st mode shape, slope and curvature of the Helland riser

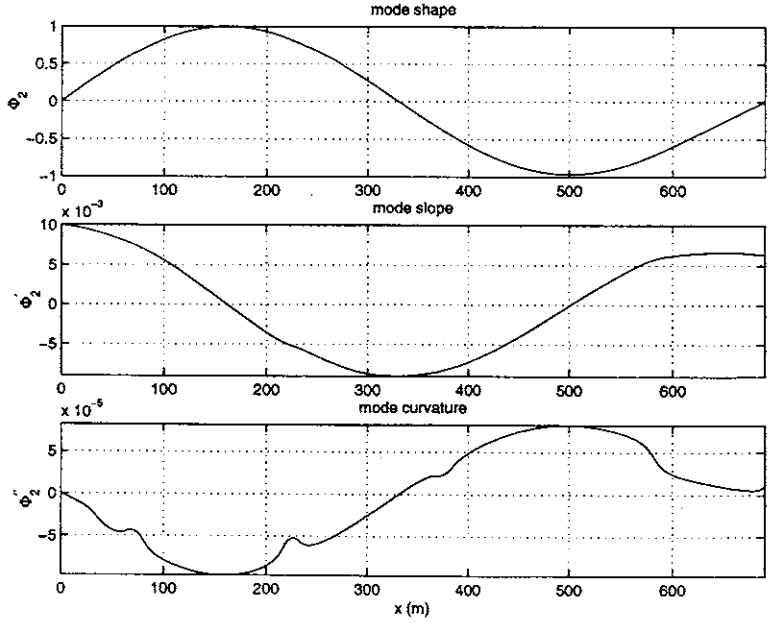

Figure 5-11: The 2nd mode shape, slope and curvature of the Helland riser

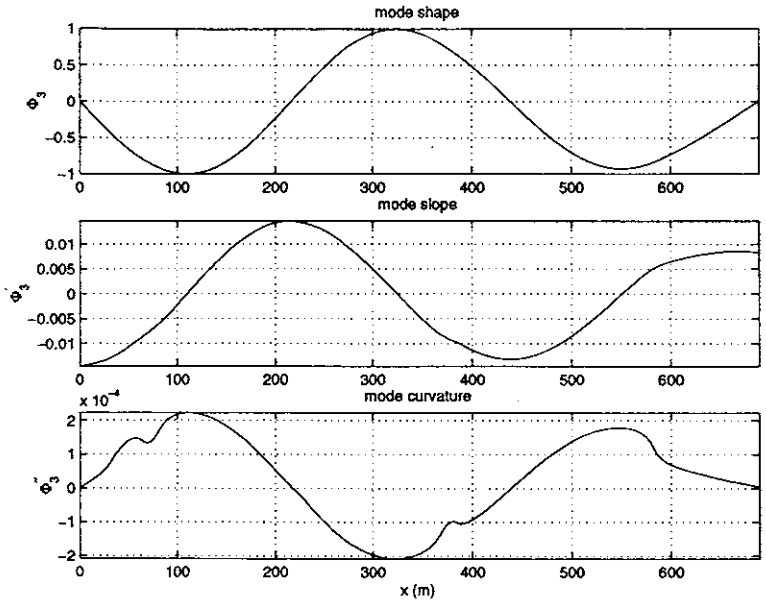

Figure 5-12: The 3rd mode shape, slope and curvature of the Helland riser

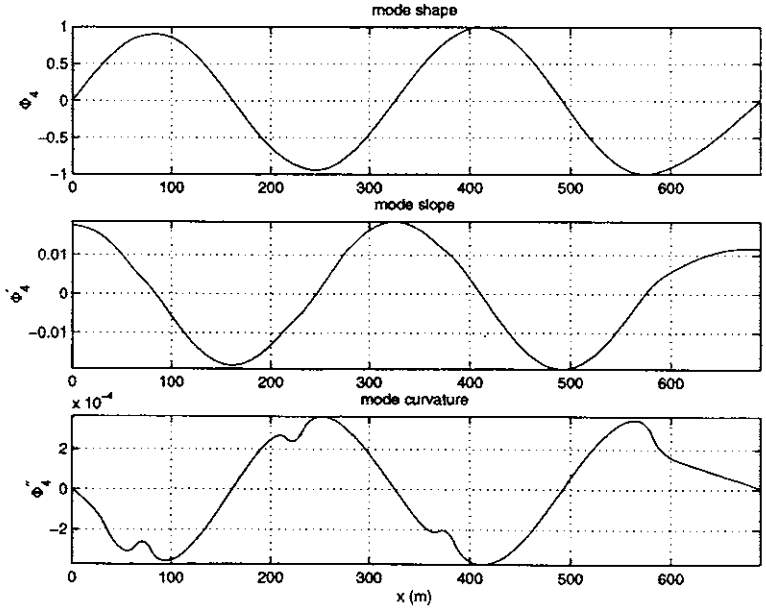

Figure 5-13: The 4th mode shape, slope and curvature of the Helland riser

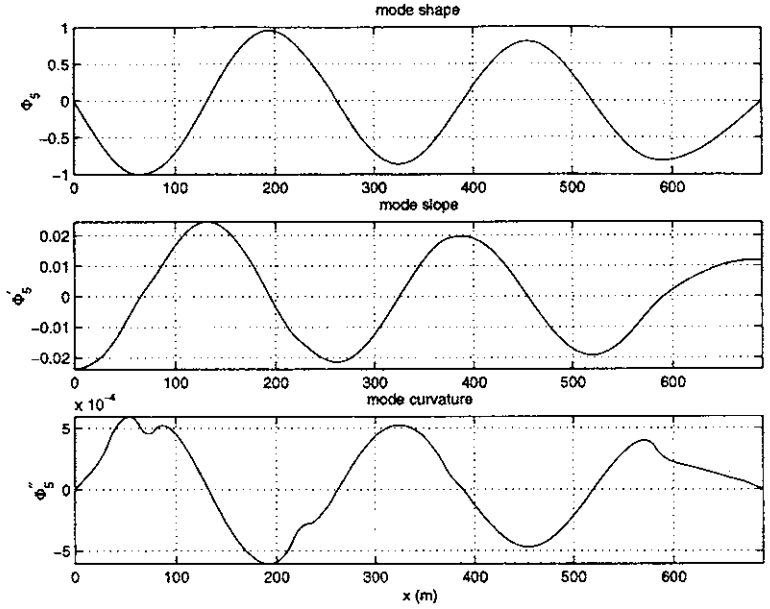

Figure 5-14: The 5th mode shape, slope and curvature of the Helland riser

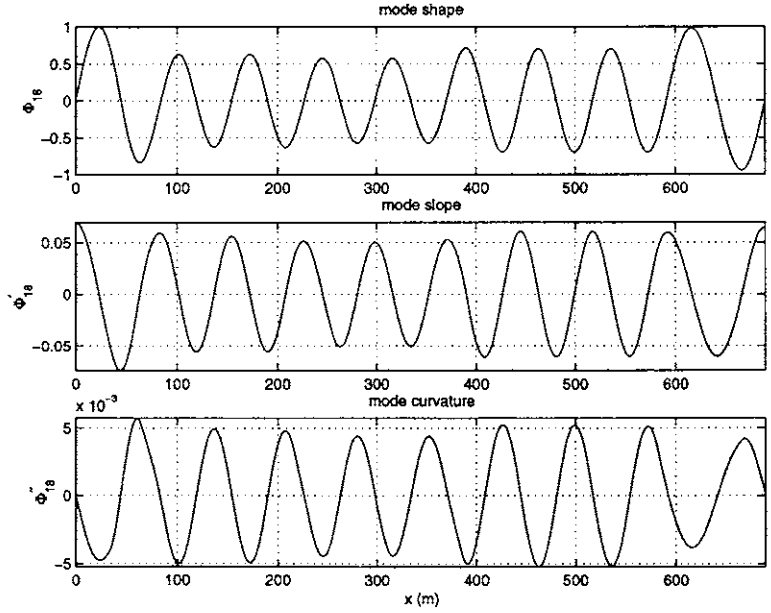

Figure 5-15: The 18th mode shape, slope and curvature of the Helland riser

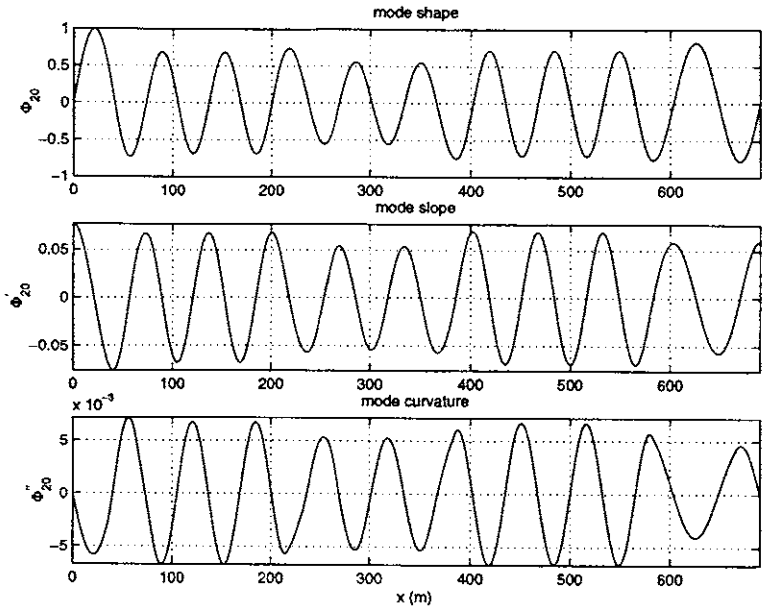

Figure 5-16: The 20th mode shape, slope and curvature of the Helland riser

5.5 Marine risers with complex boundary conditions

The WKB method is an efficient tool for analysis of a marine riser with pinned-pinned boundary conditions. For a simply supported riser, the natural frequencies are obtained numerically from an implicit integral characteristic equation, and the mode shapes are explicitly written as a simple harmonic function. However, for a riser with other boundary conditions, numerical problems appear when its length is very large or high natural frequencies are involved.

We illustrate this point with the 1400-ft riser, which is analyzed in Sections 5.3 and 5.4. The pinned-pinned boundary conditions are now assumed to be clamped-clamped. Eq. (5.5) shows the characteristic equation. It should be noted that the frequency equation obtained by Kim [7] is not correct: the element at 4×1 should be $T_2(1)B_2h_2(1)$ rather than $T_2(1)B_1h_2(1)$. The natural frequencies, in principle, can be found by means of the determinant-plotting method.

We found that the maximum determinant was even greater than 1.0×10^{51}, which is

far beyond the number a computer can handle. Figure 5-17 shows the determinant of the riser versus frequency. The frequencies corresponding to zeros of the determinant in this figure are not real eigen-frequencies. They give false roots due to numerical problems, which is similar to what we found in Chapter 2.

If the riser length is reduced, for example, to 400 ft, there is no numerical

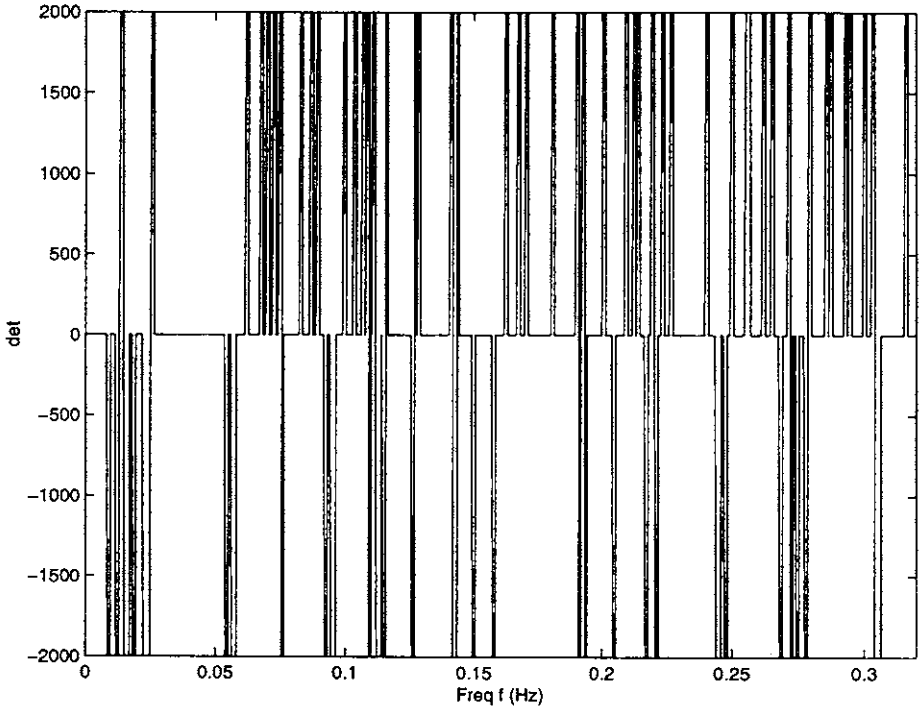

Figure 5-17: The determinant of the fixed-fixed 1400-ft riser versus frequency

problem in calculation of the first five natural frequencies. Figure 5-18 shows the determinant of the 400-ft riser versus frequency. The first five natural frequencies found from this figure are close to the exact ones: 0.1547, 0.3366, 0.5654, 0.8507, 0.1197 (Hz). Figure 5-19 demonstrates the absolute determinant of the fixed-fixed 400-ft riser versus a large range of frequency. This figure indicates that even for this short riser, there exist numerical problems for calculating high natural frequencies from the characteristic equation.

However, using the WKB-based dynamic stiffness method with the W-W algo-

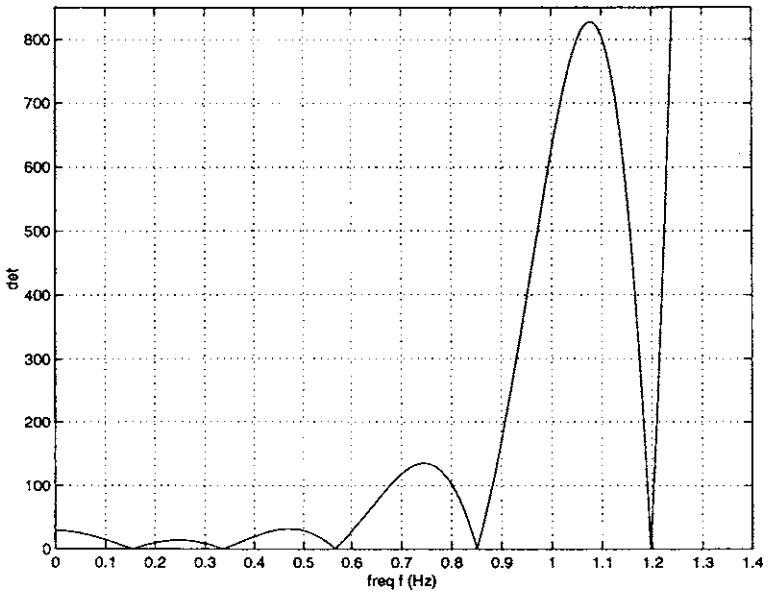

Figure 5-18: The determinant of the fixed-fixed 400-ft riser versus frequency

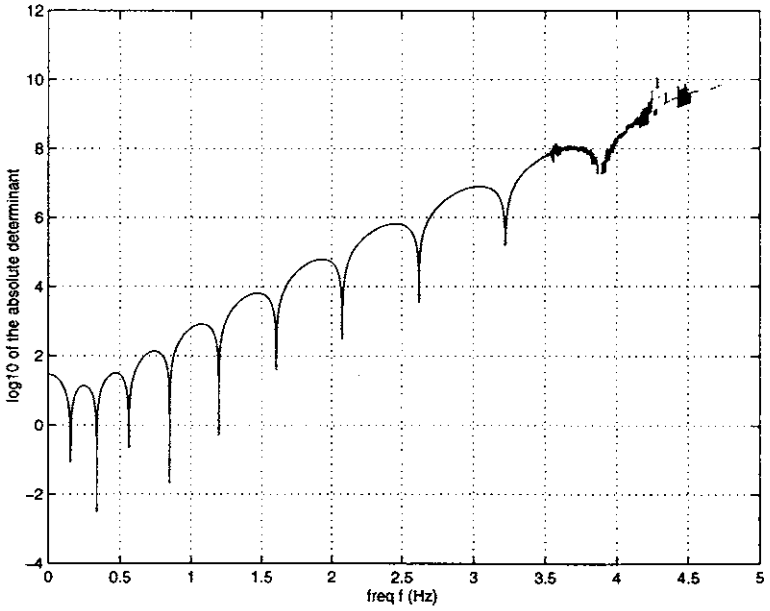

Figure 5-19: The absolute determinant (log10) of the fixed-fixed 400-ft riser versus frequency

rithm, we accurately find high natural frequencies. The first 20 natural frequencies in Hz are obtained as follows:

0.0474, 0.0954, 0.1446, 0.1955, 0.2486, 0.3043, 0.3630, 0.4249, 0.4903, 0.5594, 0.6324, 0.7094, 0.7908, 0.8764, 0.9664, 1.0614, 1.1609, 1.2652, 1.3744, 1.4886.

Taking the 1400-ft riser as an example, we further analyze several structural models used in Shear7. Using the WKB-based DSSM with the W-W algorithm, we solve for natural frequencies and the corresponding mode shapes, slopes and curvatures. Having analyzed previously a pinned-pinned beam with varying tension, we now discuss other structural models.

(1) Free-pinned beam with varying tension

The first ten natural frequencies in Hz are found by means of the WKB-based DSSM with the W-W algorithm:

0.02235, 0.06732, 0.11314, 0.16045, 0.20988, 0.26192, 0.31690, 0.37508, 0.41198, 0.50183.

Testing with different numbers of elements, we found the result was independent of the discretization.

Based on Section 5.4, Figures 5-20 and 5-21 show the mode shapes, slopes, and curvatures of the first and fifth modes. Since the boundary condition is free-pinned, the mode shapes vanish at the right end, and the curvatures are zero at both ends.

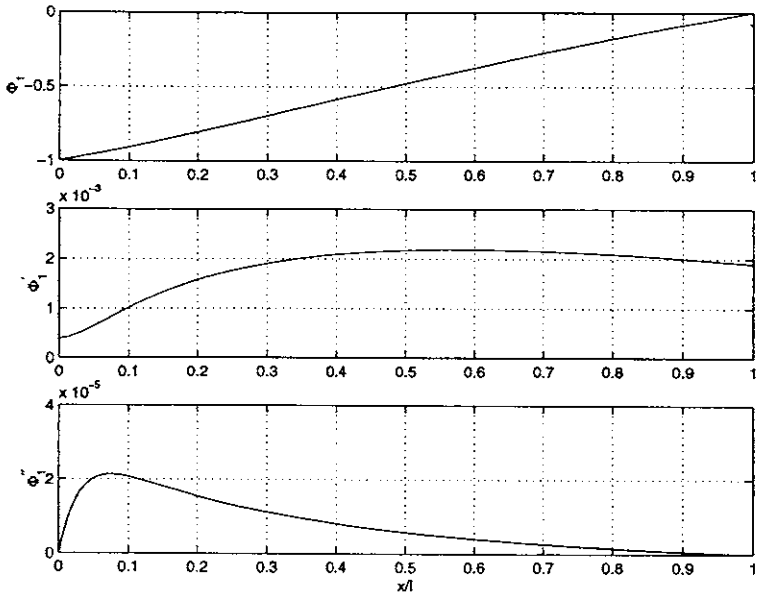

Figure 5-20: The 1st mode shape, slope and curvature of the free-pinned beam with varying tension

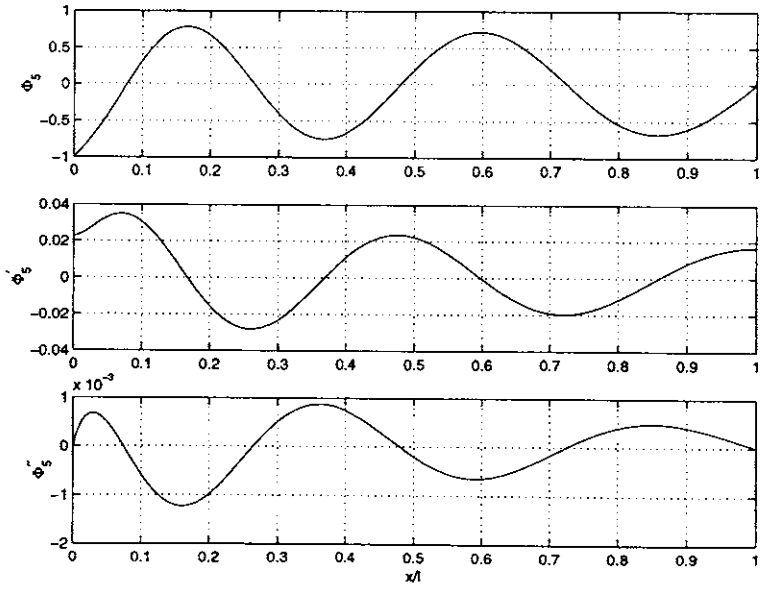

Figure 5-21: The 5th mode shape, slope and curvature of the free-pinned beam with varying tension

(2) Pinned-pinned beam with varying tension and rotational springs at both ends

The rotational stiffness ratio is defined as:

$$r = \frac{k}{EI/l},$$

where k is rotational spring stiffness, l is the riser length, and EI is bending rigidity. Setting stiffness ratio $r = 100$, we obtained the first ten natural frequencies in Hz: 0.04665, 0.09388, 0.14227, 0.19237, 0.24464, 0.29949, 0.35728, 0.41813, 0.49753, 0.55036. Figures 5-22 and 5-23 show the mode shapes, slopes and curvatures of the first and fifth modes. Since both ends have rotational springs, the modes vanish at both ends, but the curvatures at both ends are not zero.

In addition, Table 5.2 indicates the first five natural frequencies under different spring stiffness ratios. When $r = 0$, the riser is a simply-supported model, the natural frequencies of which are found in Section 5.3. When $r = 1.0 \times 10^4$ or 1.0×10^{10}, the riser boundary condition is close to clamped-clamped. When $r = 1.0 \times 10^{10}$, the natural frequencies are same as those obtained previously. Hence we verified the results of the riser when it is clamped-clamped.

r	**1**	**2**	**3**	**4**	**5**
0	0.0448	0.0903	0.1373	0.1861	0.2371
1.0×10^2	0.0467	0.0939	0.1423	0.1924	0.2446
1.0×10^4	0.0474	0.0954	0.1446	0.1954	0.2485
1.0×10^{10}	0.0474	0.0954	0.1446	0.1955	0.2486

Table 5.2: Natural frequencies (Hz) of the 1400-ft riser under different spring stiffness ratios

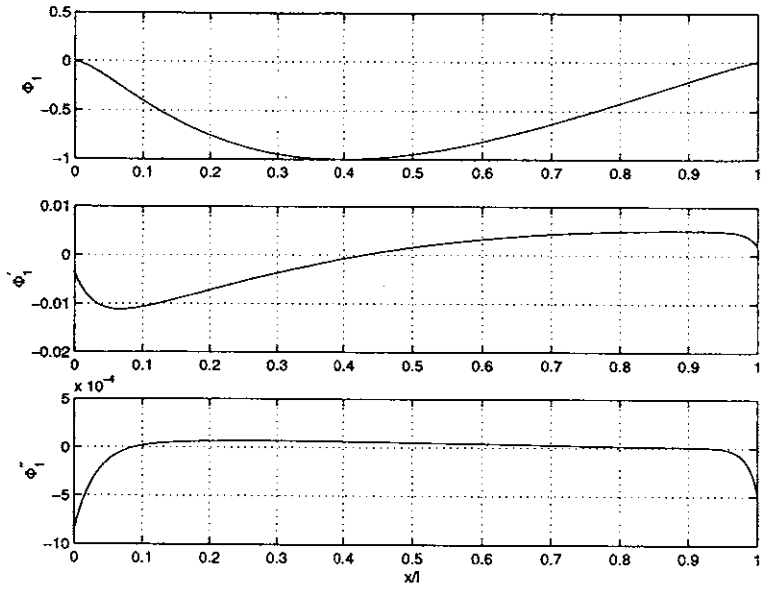

Figure 5-22: The 1st mode shape, slope and curvature of the 1400-ft riser with rotational springs

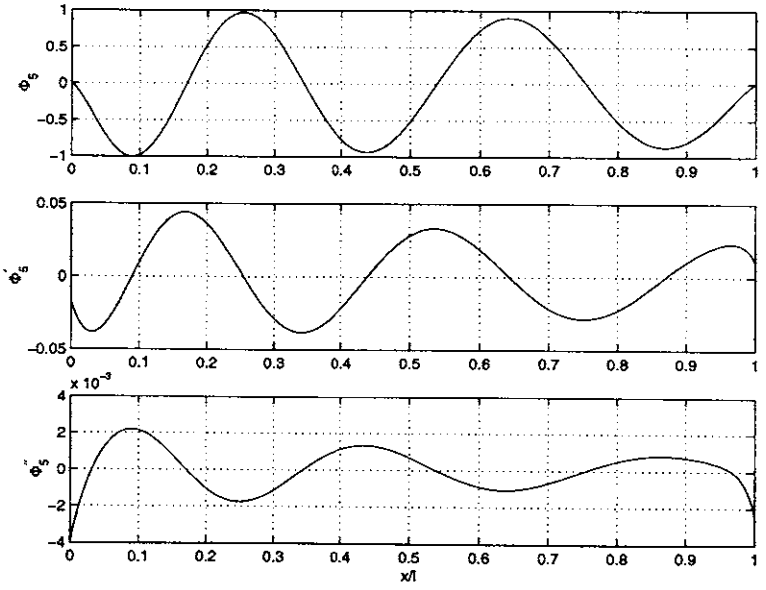

Figure 5-23: The 5th mode shape, slope and curvature of the 1400-ft riser with rotational springs

(3) Free-pinned beam with varying tension and rotational spring at $x = l$

Setting the spring stiffness ratio $r = 100$, we found its first ten natural frequencies in Hz:

0.02250, 0.06775, 0.11386, 0.16145, 0.21113, 0.26339, 0.31857, 0.37694, 0.43874, 0.50414.

Figures 5-24 and 5-25 show the mode shapes, slopes and curvatures of the first and fifth modes. In this case, mode components at the right end are zero, and the curvatures at the left end are zero while those at the right end are not zero.

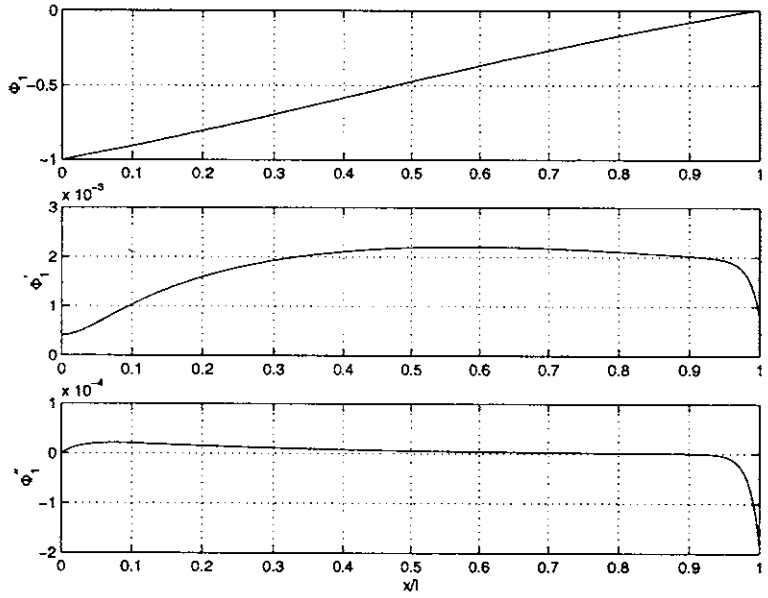

Figure 5-24: The 1st mode shape, slope and curvature of the free-pinned beam with varying tension and rotational spring at $x = l$

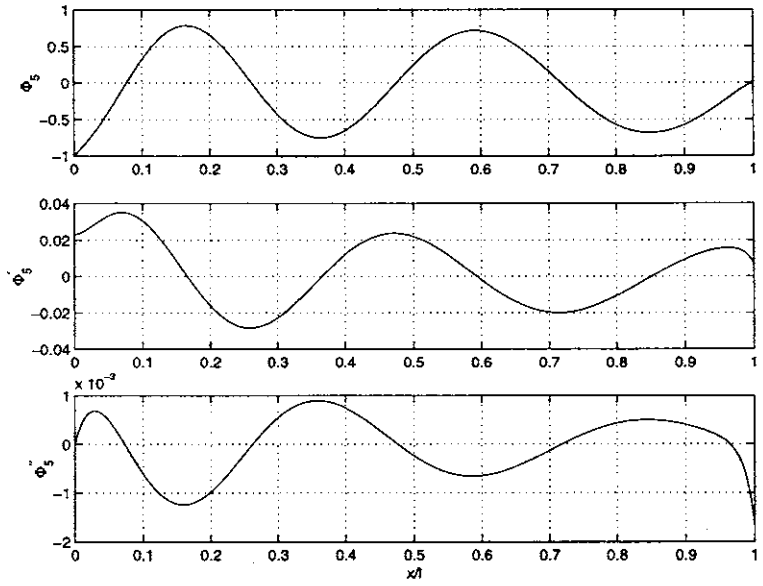

Figure 5-25: The 5th mode shape, slope and curvature of the free-pinned beam with varying tension and rotational spring at $x = l$

Chapter 6

Relationship Between Transfer Matrix and Dynamic Stiffness Methods and Its Application

6.1 Introduction

Matrix methods of structural analysis have come more and more into practice. Among those matrix methods, the transfer matrix method holds a special position. Uhrig [22] showed that under a particular sign convention the transfer matrix method can be transformed into either the displacement method or force method in structural analysis. Using the same sign convention for transfer matrix and stiffness matrix, Pestel [21] derived transfer matrix from stiffness matrix; Pilkey [44] found the relation between transfer matrix and stiffness matrix. However, the sign conventions between the transfer matrix method and the stiffness method are often different. Li [11] noted the difference in sign conventions and derived the transfer matrix from the stiffness matrix for a second-order subsystem.

This chapter first generalizes the relationship between the Transfer Matrix Method (TMM) and the Dynamic Stiffness Method (DSM) by introducing the corresponding transformation matrices due to different sign conventions. The next section of this

chapter discusses the derivation of an implicit transfer matrix from the dynamic stiffness matrix found in Chapter 4, and shows an example of a riser under linearly varying tension by means of fewer transfer matrices. The fourth section extends the WKB-based dynamic stiffness method to a general riser with discontinuities. The final section employs the relationship between the two methods to establish a dynamic stiffness library.

6.2 The relationship between transfer matrix and dynamic stiffness methods

6.2.1 Relationship between the transfer matrix and the dynamic stiffness matrix

We first derive a dynamic stiffness matrix from a transfer matrix.

The transfer of state variables from station i to station $i+1$, across segment i, for a member with n (even) state variables is written as:

$$\mathbf{s}_{i+1} = \mathbf{U}_i \mathbf{s}_i + \mathbf{F}_i, \tag{6.1}$$

where $\mathbf{s}$ is an $n \times 1$ matrix of state variables, $\mathbf{U}$ is an $n \times n$ transfer matrix, and $\mathbf{F}$ is an $n \times 1$ matrix of loading functions. Eq. (6.1) can be partitioned as:

$$\begin{bmatrix} \mathbf{d}_{i+1} \\ \mathbf{p}_{i+1} \end{bmatrix} = \begin{bmatrix} \mathbf{U}_{11} & \mathbf{U}_{12} \\ \mathbf{U}_{21} & \mathbf{U}_{22} \end{bmatrix}_i \begin{bmatrix} \mathbf{d}_i \\ \mathbf{p}_i \end{bmatrix} + \begin{bmatrix} \mathbf{F}_d \\ \mathbf{F}_p \end{bmatrix}_i, \tag{6.2}$$

where $\mathbf{d}$ contains the $n/2$ displacement variables and $\mathbf{p}$ contains the corresponding $n/2$ force variables. The $\mathbf{U}_{ij}$ $(i, j = 1, 2)$ are $(n/2) \times (n/2)$ submatrices. $\mathbf{F}_d$ is an $(n/2) \times 1$ submatrix of loading function terms corresponding to the $\mathbf{d}$ state variables and $\mathbf{F}_p$ contains the forcing terms for the $\mathbf{p}$ state variables. For convenience, the subscript i to $\mathbf{U}$ and $\mathbf{F}$ is omitted in the following derivations.

Expanding Eq. (6.2) results in:

$$\mathbf{d}_{i+1} = \mathbf{U}_{11}\mathbf{d}_i + \mathbf{U}_{12}\mathbf{p}_i + \mathbf{F}_d, \tag{6.3}$$

$$\mathbf{p}_{i+1} = \mathbf{U}_{21}\mathbf{d}_i + \mathbf{U}_{22}\mathbf{p}_i + \mathbf{F}_p. \tag{6.4}$$

Eq. (6.3) reduces to:

$$\mathbf{p}_i = -\mathbf{U}_{12}^{-1}\mathbf{U}_{11}\mathbf{d}_i + \mathbf{U}_{12}^{-1}\mathbf{d}_{i+1} - \mathbf{U}_{12}^{-1}\mathbf{F}_d. \tag{6.5}$$

Substituting Eq. (6.5) into Eq. (6.4) yields:

$$\mathbf{p}_{i+1} = (\mathbf{U}_{21} - \mathbf{U}_{22}\mathbf{U}_{12}^{-1}\mathbf{U}_{11})\mathbf{d}_i + \mathbf{U}_{22}\mathbf{U}_{12}^{-1}\mathbf{d}_{i+1} + \mathbf{F}_p - \mathbf{U}_{22}\mathbf{U}_{12}^{-1}\mathbf{F}_d. \tag{6.6}$$

Eqs. (6.5) and (6.6) are rewritten in matrix form:

$$\begin{pmatrix} \mathbf{p}_i \\ \mathbf{p}_{i+1} \end{pmatrix} = \begin{bmatrix} -\mathbf{U}_{12}^{-1}\mathbf{U}_{11} & \mathbf{U}_{12}^{-1} \\ \mathbf{U}_{21} - \mathbf{U}_{22}\mathbf{U}_{12}^{-1}\mathbf{U}_{11} & \mathbf{U}_{22}\mathbf{U}_{12}^{-1} \end{bmatrix} \begin{pmatrix} \mathbf{d}_i \\ \mathbf{d}_{i+1} \end{pmatrix} + \begin{bmatrix} -\mathbf{U}_{12}^{-1} & 0 \\ -\mathbf{U}_{22}\mathbf{U}_{12}^{-1} & 1 \end{bmatrix} \begin{pmatrix} \mathbf{F}_d \\ \mathbf{F}_p \end{pmatrix}. \tag{6.7}$$

In local coordinate system of the DSM, the nodal force vector is:

$$\bar{\mathbf{P}} = \begin{pmatrix} \bar{\mathbf{p}}_i \\ \bar{\mathbf{p}}_{i+1} \end{pmatrix} = \mathbf{L}_p \begin{pmatrix} \mathbf{p}_i \\ \mathbf{p}_{i+1} \end{pmatrix}, \tag{6.8}$$

where $\mathbf{L}_p$ is the transformation matrix between a nodal force vector in the DSM and a force state vector in the TMM.

Substituting Eq. (6.7) into (6.8) gives:

$$\bar{\mathbf{P}} = \mathbf{L}_p \begin{bmatrix} -\mathbf{U}_{12}^{-1}\mathbf{U}_{11} & \mathbf{U}_{12}^{-1} \\ \mathbf{U}_{21} - \mathbf{U}_{22}\mathbf{U}_{12}^{-1}\mathbf{U}_{11} & \mathbf{U}_{22}\mathbf{U}_{12}^{-1} \end{bmatrix} \begin{pmatrix} \mathbf{d}_i \\ \mathbf{d}_{i+1} \end{pmatrix} + \mathbf{L}_p \begin{bmatrix} -\mathbf{U}_{12}^{-1} & 0 \\ -\mathbf{U}_{22}\mathbf{U}_{12}^{-1} & 1 \end{bmatrix} \begin{pmatrix} \mathbf{F}_d \\ \mathbf{F}_p \end{pmatrix}. \tag{6.9}$$

The matrix $\mathbf{L}_p$ can be diagonally partitioned as:

$$\mathbf{L}_p = \begin{bmatrix} \mathbf{L}_{p1} & 0 \\ 0 & \mathbf{L}_{p2} \end{bmatrix}. \tag{6.10}$$

Likewise, the nodal displacement vector in the DSM is expressed as:

$$\mathbf{X}_e = \begin{pmatrix} \bar{\mathbf{d}}_i \\ \bar{\mathbf{d}}_{i+1} \end{pmatrix} = \mathbf{L}_d \begin{pmatrix} \mathbf{d}_i \\ \mathbf{d}_{i+1} \end{pmatrix}, \tag{6.11}$$

where $\mathbf{L}_d$ is the transformation matrix between the nodal displacement vector in the DSM and the displacement state vector in the TMM, and can also be diagonally partitioned as:

$$\mathbf{L}_d = \begin{bmatrix} \mathbf{L}_{d1} & 0 \\ 0 & \mathbf{L}_{d2} \end{bmatrix}. \tag{6.12}$$

Substituting Eqs. (6.10) to (6.12) into (6.9) results in:

$$\mathbf{K}_e \mathbf{X}_e = \mathbf{F}_e, \tag{6.13}$$

where the dynamic stiffness matrix, $\mathbf{K}_e$ is :

$$\mathbf{K}_e = \begin{bmatrix} -\mathbf{L}_{p1}\mathbf{U}_{12}^{-1}\mathbf{U}_{11}\mathbf{L}_{d1}^{-1} & \mathbf{L}_{p1}\mathbf{U}_{12}^{-1}\mathbf{L}_{d2}^{-1} \\ \mathbf{L}_{p2}(\mathbf{U}_{21} - \mathbf{U}_{22}\mathbf{U}_{12}^{-1}\mathbf{U}_{11})\mathbf{L}_{d1}^{-1} & \mathbf{L}_{p2}\mathbf{U}_{22}\mathbf{U}_{12}^{-1}\mathbf{L}_{d2}^{-1} \end{bmatrix}, \tag{6.14}$$

the force $\mathbf{F}_e$ is:

$$\mathbf{F}_e = \begin{pmatrix} \mathbf{L}_{p1}\mathbf{p}_i \\ \mathbf{L}_{p2}\mathbf{p}_{i+1} \end{pmatrix} + \begin{bmatrix} \mathbf{L}_{p1}\mathbf{U}_{12}^{-1} & 0 \\ \mathbf{L}_{p2}\mathbf{U}_{22}\mathbf{U}_{12}^{-1} & -\mathbf{L}_{p2} \end{bmatrix} \begin{pmatrix} \mathbf{F}_d \\ \mathbf{F}_p \end{pmatrix}. \tag{6.15}$$

Following the same procedure, we find the transfer matrix in terms of the submatrices of the dynamic stiffness matrix $\mathbf{K}_e$:

$$\mathbf{U} = \begin{bmatrix} -\mathbf{L}_{d2}^{-1}\mathbf{K}_{e12}^{-1}\mathbf{K}_{e11}\mathbf{L}_{d1} & \mathbf{L}_{d2}^{-1}\mathbf{K}_{e12}^{-1}\mathbf{L}_{p1} \\ \mathbf{L}_{p2}^{-1}(\mathbf{K}_{e21} - \mathbf{K}_{e22}\mathbf{K}_{e12}^{-1}\mathbf{K}_{e11})\mathbf{L}_{d1} & \mathbf{L}_{p2}^{-1}\mathbf{K}_{e22}\mathbf{K}_{e12}^{-1}\mathbf{L}_{p1} \end{bmatrix}. \tag{6.16}$$

Eqs. (6.14) and (6.16) establish the general relationship between the transfer matrix and the dynamic stiffness matrix.

6.2.2 Relationship between the two methods

(1) Transfer matrix method as a means of elimination

Transfer matrix method is a means of elimination of intermediate state vectors. Although from the theoretical standpoint all problems in this method had been solved, numerical difficulties prevented its wide practical application [44]. There are numerous suggestions for overcoming the computational difficulties, which are discussed in Chapter 2. An effective technique, which runs counter to the idea of the TMM, is based on the classical elimination process, the Gauss elimination [44, 22].

The state vector for a member with changes in field (Figure 6-1) is written for each section as:

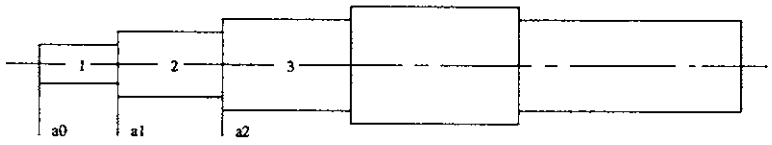

Figure 6-1: A member with section changes

$$\begin{aligned} \mathbf{s}_1 &= \mathbf{u}_1\mathbf{s}_0 + \mathbf{F}_1 \\ \mathbf{s}_2 &= \mathbf{u}_2\mathbf{s}_1 + \mathbf{F}_2 \\ &\cdots \\ \mathbf{s}_n &= \mathbf{u}_n\mathbf{s}_{n-1} + \mathbf{F}_n, \end{aligned} \tag{6.17}$$

where $\mathbf{u}_j = \mathbf{u}_j(a_j, a_{j-1})$.

Eq. (6.17) is rearranged as follows:

$$\begin{aligned}
\mathbf{u}_1\mathbf{s}_0 - \mathbf{s}_1 &= -\mathbf{F}_1 \\
\mathbf{u}_2\mathbf{s}_1 - \mathbf{s}_2 &= -\mathbf{F}_2 \\
\cdots &= \cdots \\
\mathbf{u}_n\mathbf{s}_{n-1} - \mathbf{s}_n &= -\mathbf{F}_n.
\end{aligned} \tag{6.18}$$

The structure of Eqs. (6.18) suggests the simple technique of eliminating all the intermediate unknowns $\mathbf{s}_1$, $\mathbf{s}_2$, $\cdots$, used in the TMM. All the state vectors $\mathbf{s}_i$ can be expressed in terms of $\mathbf{s}_0$:

$$\begin{aligned}
\mathbf{s}_j &= (\mathbf{u}_j\mathbf{u}_{j-1}\cdots\mathbf{u}_2\mathbf{u}_1)\mathbf{s}_0 + \bar{\mathbf{F}}_j \\
&= \mathbf{u}(a_j, a_0)\mathbf{s}_0 + \bar{\mathbf{F}}_j,
\end{aligned} \tag{6.19}$$

where $\mathbf{u}(a_j, a_0)$ is a transfer matrix from section a_0 to a_j.

Use of a classical elimination technique, such as the Gauss process [45], will overcome the numerical difficulties inherent in the transfer matrix solution in Eq. (6.19). The member is divided into segments of such length that they can be represented by transfer matrices without numerical complications. Then Gauss elimination can be employed to transform the coefficient matrix into an upper and a lower triangular matrix, and thus it solves the problem [44, 22].

It should be noted that the coefficient matrix in Eq. (6.18) is not symmetric, thus not convenient for decomposing into triangular matrices. In the following, we will transform the Eqs. (6.18) into the form of the direct dynamic stiffness matrix method.

(2) Dynamic stiffness matrix method

It has been verified that the field transfer matrix relation for one element in Eq. (6.1) can be transformed into Eq. (6.13), which for convenience is rewritten as:

$$\begin{bmatrix} k_{11} & k_{12} \\ k_{21} & k_{22} \end{bmatrix} \begin{bmatrix} d_i \\ d_{i+1} \end{bmatrix} = \begin{bmatrix} f_i \\ f_{i+1} \end{bmatrix}. \tag{6.20}$$

If we do similar operations for each row in Eqs. (6.18), then the Eqs. (6.18) can be transformed in to the following form:

$$\begin{bmatrix} k_{11}^1 & k_{12}^1 & & \\ k_{21}^1 & k_{22}^1 & & \\ & k_{11}^2 & k_{12}^2 & \\ & k_{21}^2 & k_{22}^2 & \\ & & \vdots & \vdots \end{bmatrix} \begin{bmatrix} d_1^1 \\ d_2^1 \\ d_1^2 \\ d_2^2 \\ \vdots \end{bmatrix} = \begin{bmatrix} f_1^1 \\ f_2^1 \\ f_1^2 \\ f_2^2 \\ \vdots \end{bmatrix}, \tag{6.21}$$

where the superscripts refer to the number of elements, and elements not shown are zeros.

Noting $d_2^{i-1} = d_1^i$, the geometric continuity leads to:

$$\begin{bmatrix} \vdots \\ d_1^{i-1} \\ d_2^{i-1} \\ d_1^i \\ d_2^i \\ \vdots \end{bmatrix} = \begin{bmatrix} \vdots & I & & & \\ & & I & & \\ & & I & & \\ & & & I & \\ & & & I & \\ & & & & I \quad \vdots \end{bmatrix} \begin{bmatrix} \vdots \\ d_{i-1} \\ d_i \\ d_{i+1} \\ \vdots \end{bmatrix}, \tag{6.22}$$

where I is a unit matrix, and elements not shown are zero submatrices. Eqs. (6.22) can be written in the abbreviated form:

$$d = LX, \tag{6.23}$$

where d is a super-vector containing the component displacements of all elements, L is the the index matrix.

Substituting Eq. (6.23) into Eq. (6.21) and pre-multiplying by L^T yields:

$$\mathbf{KX} = \mathbf{F}, \tag{6.24}$$

where the global stiffness matrix $\mathbf{K}$ and force vector $\mathbf{F}$ are:

$$\mathbf{K} = L^T \begin{bmatrix} k_{11}^1 & k_{12}^1 & & \\ k_{21}^1 & k_{22}^1 & & \\ & k_{11}^2 & k_{12}^2 & \\ & k_{21}^2 & k_{22}^2 & \\ & & \vdots & \vdots \end{bmatrix} L, \tag{6.25}$$

$$\mathbf{F} = L^T \begin{bmatrix} f_1^1 \\ f_2^1 \\ f_1^2 \\ f_2^2 \\ \vdots \end{bmatrix}. \tag{6.26}$$

It can be shown that the elements in Eq. (6.23) $k(i,i) = k_{22}^{i-1} + k_{11}^i$, $k(i,i+1) = k_{12}^i$.

Equations (6.24) to (6.26) are the formulations of the dynamic stiffness matrix method, the global stiffness matrix is symmetric, i.e., $\mathbf{K}^T = \mathbf{K}$.

6.3 Derivation of a transfer matrix from the WKB-based dynamic stiffness matrix

In the local coordinate system of the DSM, defined in Chapter 4, the nodal force vector is:

$$\mathbf{P} = \begin{pmatrix} \bar{p}_i \\ \bar{p}_{i+1} \end{pmatrix} = \begin{bmatrix} s_{1y} \\ m_1 \\ s_{2y} \\ m_2 \end{bmatrix} = L_F \begin{bmatrix} Q_i \\ M_i \\ Q_{i+1} \\ M_{i+1} \end{bmatrix}, \tag{6.27}$$

where L_F is the matrix relating nodal forces in an element reference to the corresponding state force components defined in Chapter 2. L_F for a beam then is:

$$L_F = \begin{bmatrix} 1 & 0 & 0 & 0 \\ 0 & -1 & 0 & 0 \\ 0 & 0 & -1 & 0 \\ 0 & 0 & 0 & 1 \end{bmatrix}.$$

In order to relate state vectors in the TMM, the following transformation is used:

$$\begin{pmatrix} Q_i \\ M_i \\ Q_{i+1} \\ M_{i+1} \end{pmatrix} = L_r \begin{pmatrix} M_i \\ Q_i \\ M_{i+1} \\ Q_{i+1} \end{pmatrix}, \tag{6.28}$$

where L_r is:

$$L_r = \begin{bmatrix} 0 & 1 & 0 & 0 \\ 1 & 0 & 0 & 0 \\ 0 & 0 & 0 & 1 \\ 0 & 0 & 1 & 0 \end{bmatrix}.$$

Hence the transformation matrix $\mathbf{L}_p$ defined in Eq. (6.8) is:

$$\mathbf{L}_p = L_F L_r$$

$$= \begin{bmatrix} 0 & 1 & 0 & 0 \\ -1 & 0 & 0 & 0 \\ 0 & 0 & 0 & -1 \\ 0 & 0 & 1 & 0 \end{bmatrix}.$$

The transformation matrix $\mathbf{L}_d$ defined in Eq. (6.11) is a 4×4 identity matrix.

Chapter 4 has found the WKB-based dynamic stiffness matrix of a general non-uniform riser under linearly varying tension. With the transformation matrices $\mathbf{L}_p$ and $\mathbf{L}_d$, the corresponding transfer matrix is obtained implicitly by means of Eq. (6.16). In order to avoid the numerical problems, we transform this transfer matrix into a delta-matrix, discussed in Chapter 2.

The 1400-ft riser in Chapter 5 is employed here as illustration. Figure 6-2 shows the determinant of the delta-matrix versus frequency (Hz) by discretizing 3 equally sized segments. The troughs correspond to the natural frequencies. The first thirteen frequencies in Hz are obtained by zooming in around the peaks:
0.0448, 0.0905, 0.1370, 0.1860, 0.2370, 0.2904, 0.4068, 0.4705, 0.5372, 0.6076, 0.6824, 0.7618.
They are quite close to those obtained in the example of Chapter 5. Figure 6-3 further depicts the accuracy of this new type of delta matrix. This figure indicates that only a few transfer delta-matrices are required to solve for natural frequencies with good accuracy.

6.4 Dynamic stiffness method for a riser with discontinuities

A typical marine riser is a general non-uniform beam system with discontinuities. Chapter 4 derives the WKB-based element dynamic stiffness matrix of a non-uniform beam structure. Chapter 2 indicates that as a means of elimination of intermediate state vectors, the transfer matrix method is a convenient approach to handle discontinuities. Using the relationship between transfer matrix and dynamic stiffness

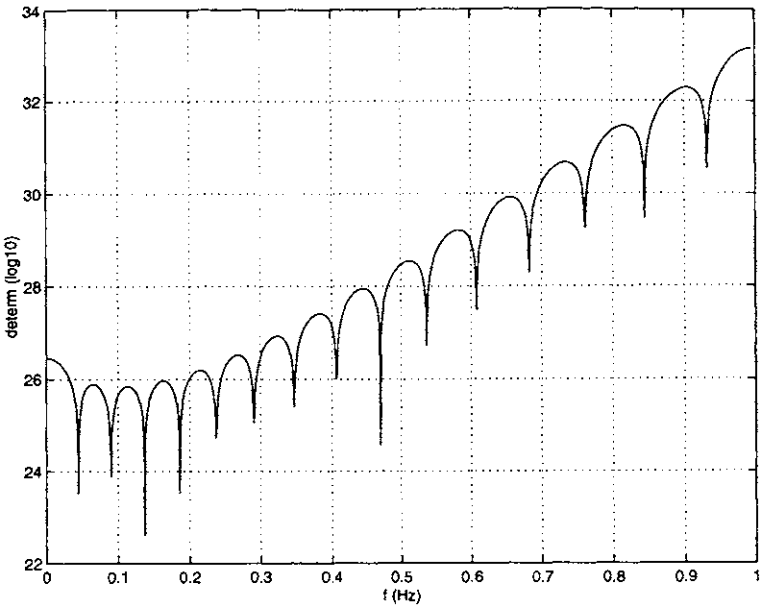

Figure 6-2: Frequency analysis of the 1400-ft riser using a new type of delta-matrix

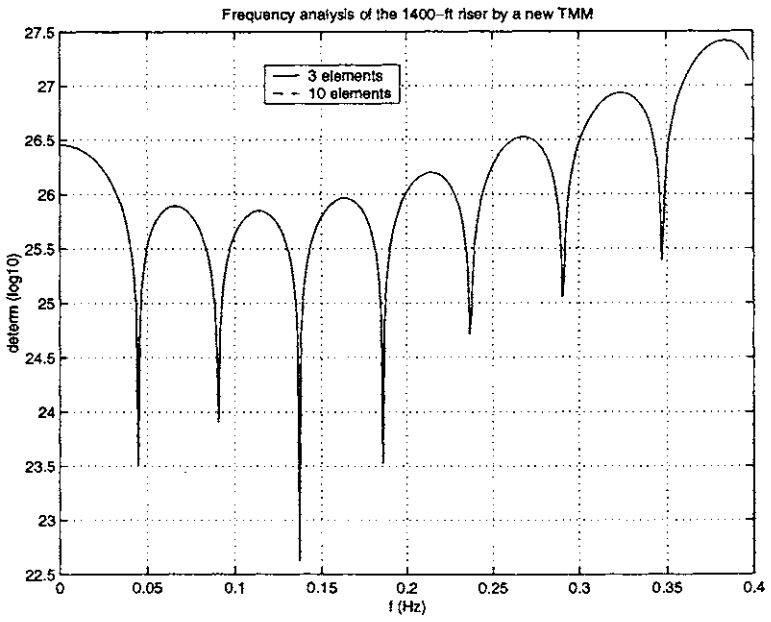

Figure 6-3: Frequency analysis of the 1400-ft riser by 3 and 10 elements respectively

matrix, we first obtain an overall transfer matrix for a substructure, then find the corresponding dynamic stiffness matrix from the transfer matrix. Hence in this way we extend the WKB-based DSM to a general riser with discontinuities. In some cases, we can also extend the W-W algorithm to the analysis of natural frequencies of such a system.

In addition, the internal degrees of freedom of each substructure are not employed in this technique. Therefore the order of the model is greatly reduced by means of the combination of transfer and dynamic stiffness matrices. For example, a type of submerged floating pipeline in deep water has a large number of discrete buoyancy modules and one vertical tether at each mooring point, as shown in Figure 6-4. Using this technique, we first obtain the overall transfer matrix for each span segment along which a large number of discrete buoyancy modules are distributed, and then find the corresponding dynamic stiffness matrix. The part within each span here is regarded as a substructure or "super-element".

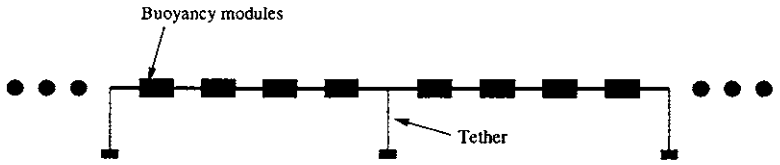

Figure 6-4: A submerged floating pipeline

A constantly tensioned beam system with evenly distributed dynamic absorbers, as shown in Figure 6-5, is used here as an example, whose specifications are as follows:
length $l = 609.6$ m;
elastic modulus $E = 2.0 \times 10^{11}\ N/m^2$;
outside diameter $OD = 0.3397$ m;
inside diameter $ID = 0.3204$ m;
moment of inertia $I = 1.3642 \times 10^{-4}\ m^4$;
mass per unit length $\rho A = 78.57$ kg/m;
constant tension $T = 1.39 \times 10^5$ N;
number of absorbers $N_{abs} = 19$;

mass of absorber $m = 0.2\rho Al/(N_{abs} = 25.21$kg; and

stiffness of absorber $k = 46.24$ N/m.

The 19 absorbers are evenly distributed along the simply supported beam. The

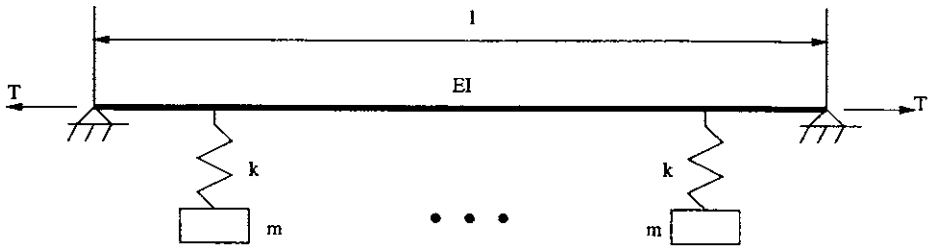

Figure 6-5: A beam system with absorbers

"super-element" here is a constantly tensioned uniform beam with a mass-spring absorber on its right end. Its dynamic stiffness matrix is derived in the next section. Figure 6-6 shows the determinant of the system versus frequency. The troughs correspond to the natural frequencies. The first five natural frequencies in Hz are: 0.0345, 0.070, 0.105, 0.142, 0.181.

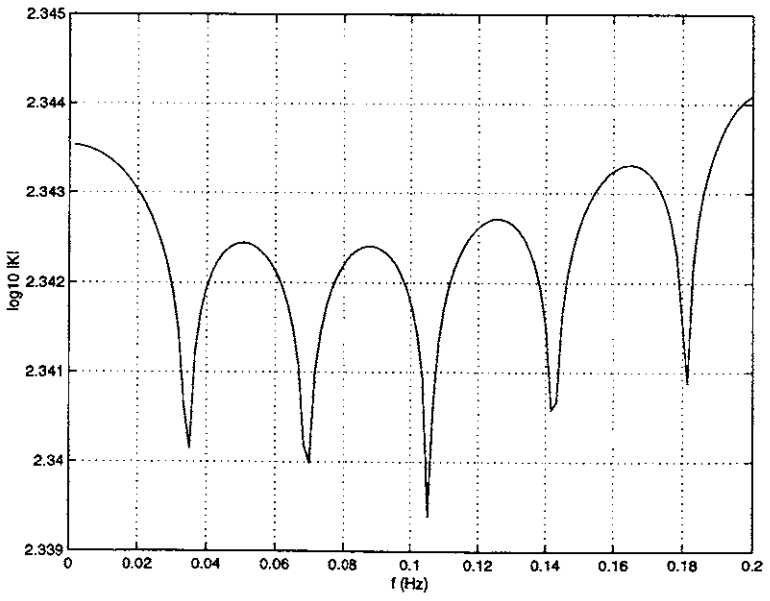

Figure 6-6: The determinant of the system versus frequency

6.5 Establishment of dynamic stiffness library

The combination of transfer and dynamic stiffness matrices encouraged us to establish a dynamic stiffness library. Pestel and Leckie [21] gave a catalogue of transfer matrices. Using the general relationship in Section 6.2, we can transform it into that of the corresponding dynamic stiffness matrices in a sign convention we define. For a member with discontinuities, we first find its overall transfer matrix, and then transform this matrix into the dynamic stiffness one. The following two examples illustrate this technique.

(1) A uniform Bernoulli-Euler beam

Chapter 2 shows that its transfer matrix U whose elements are:

$$
\begin{aligned}
\mathbf{U}(1,1) &= 1/2\,\cosh(kl) + 1/2\,\cos(kl);\\
\mathbf{U}(1,2) &= \frac{1/2\,\sinh(kl) + 1/2\,\sin(kl)}{k};\\
\mathbf{U}(1,3) &= \frac{1/2\,\cosh(kl) - 1/2\,\cos(kl)}{EI\,k^2};\\
\mathbf{U}(1,4) &= \frac{1/2\,\sinh(kl) - 1/2\,\sin(kl)}{EI\,k^3};\\
\mathbf{U}(2,1) &= k\,(1/2\sinh(kl) - 1/2\sin(kl))\,;\\
\mathbf{U}(2,2) &= 1/2\,\cosh(kl) + 1/2\,\cos(kl);\\
\mathbf{U}(2,3) &= \frac{1/2\,\sinh(kl) + 1/2\,\sin(kl)}{EI\,k};\\
\mathbf{U}(2,4) &= \frac{1/2\,\cosh(kl) - 1/2\,\cos(kl)}{EI\,k^2};\\
\mathbf{U}(3,1) &= k^2EI\ (1/2\,\cosh(kl) - 1/2\,\cos(kl))\,;\\
\mathbf{U}(3,2) &= kEI\ (1/2\,\sinh(kl) - 1/2\,\sin(kl))\,;\\
\mathbf{U}(3,3) &= 1/2\,\cosh(kl) + 1/2\,\cos(kl);\\
\mathbf{U}(3.4) &= \frac{1/2\,\sinh(kl) + 1/2\,\sin(kl)}{k};\\
\mathbf{U}(4,1) &= k^3EI\ (1/2\,\sinh(kl) + 1/2\,\sin(kl))\,;\\
\mathbf{U}(4,2) &= k^2EI\ (1/2\,\cosh(kl) - 1/2\,\cos(kl))\,;\\
\mathbf{U}(4,3) &= k\,(1/2\,\sinh(kl) - 1/2\,\sin(kl))\,;
\end{aligned}
$$

$$\mathbf{U}(4,4) \;=\; 1/2\,\cosh(kl) + 1/2\,\cos(kl). \tag{6.29}$$

The transformation matrices of $\mathbf{L}_p$ and $\mathbf{L}_d$ are indicated in Section 6.3. With Eq. (6.14), we find the corresponding dynamic stiffness matrix, $\mathbf{k}$, by means of Maple. The dynamic stiffness matrix is symmetric, which is also verified by using Maple. The upper triangular elements of $\mathbf{k}$ are:

$$\begin{aligned}
\mathbf{k}(1,1) &= -\frac{EI\,k^3\,(\cos(kl)\sinh(kl)+\cosh(kl)\sin(kl))}{\cosh(kl)\cos(kl)-1};\\
\mathbf{k}(1,2) &= -\frac{EI\,k^2\sinh(kl)\sin(kl)}{\cosh(kl)\cos(kl)-1};\\
\mathbf{k}(1,3) &= \frac{EI\,k^3\,(\sinh(kl)+\sin(kl))}{\cosh(kl)\cos(kl)-1};\\
\mathbf{k}(1,4) &= \frac{EI\,k^2\,(-\cosh(kl)+\cos(kl))}{\cosh(kl)\cos(kl)-1};\\
\mathbf{k}(2,2) &= -\frac{kEI(\cosh(kl)\sin(kl)-\sinh(kl)\cos(kl))}{\cosh(kl)\cos(kl)-1};\\
\mathbf{k}(2,3) &= -\frac{EI\,k^2\,(-\cosh(kl)+\cos(kl))}{\cosh(kl)\cos(kl)-1};\\
\mathbf{k}(2,4) &= -\frac{EI\,k\,(\sinh(kl)-\sin(kl))}{\cosh(kl)\cos(kl)-1};\\
\mathbf{k}(3,3) &= -\frac{EI\,k^3\,(\cos(kl)\sinh(kl)+\cosh(kl)\sin(kl))}{\cosh(kl)\cos(kl)-1};\\
\mathbf{k}(3,4) &= \frac{EI\,k^2\sinh(kl)\sin(kl)}{\cosh(kl)\cos(kl)-1};\\
\mathbf{k}(4,4) &= \frac{EI\,k\,(-\cosh(kl)\sin(kl)+\cos(kl)\sinh(kl))}{\cosh(kl)\cos(kl)-1}.
\end{aligned} \tag{6.30}$$

This dynamic stiffness matrix $\mathbf{k}$ is identical to that expressed by Richards and Leung [30]. Hence this example justifies the technique of deriving a dynamic stiffness matrix by means of the relationship between transfer and dynamic stiffness matrices.

(2) A uniform tensioned beam with a mass-spring-dashpot absorber on its right end

The example in Section 6.4 uses the dynamic stiffness matrix of this subsystem. Chap-

ter 2 shows the transfer matrix U_1 of a uniform tensioned beam, whose elements are:

$$
\begin{aligned}
U_1(1,1) &= \frac{\cos(\lambda_1 l)\lambda_2{}^2}{\lambda_2{}^2+\lambda_1{}^2}+\frac{\cosh(\lambda_2 l)\lambda_1{}^2}{\lambda_2{}^2+\lambda_1{}^2};\\
U_1(1,2) &= -\frac{\sin(\lambda_1 l)\left(-EI\,\lambda_2{}^2+T\right)}{EI\left(\lambda_2{}^2+\lambda_1{}^2\right)\lambda_1}+\frac{\sinh(\lambda_2 l)\left(EI\,\lambda_1{}^2+T\right)}{EI\left(\lambda_2{}^2+\lambda_1{}^2\right)\lambda_2};\\
U_1(1,3) &= -\frac{\cos(\lambda_1 l)}{EI\left(\lambda_2{}^2+\lambda_1{}^2\right)}+\frac{\cosh(\lambda_2 l)}{EI\left(\lambda_2{}^2+\lambda_1{}^2\right)};\\
U_1(1,4) &= -\frac{\sin(\lambda_1 l)}{EI\left(\lambda_2{}^2+\lambda_1{}^2\right)\lambda_1}+\frac{\sinh(\lambda_2 l)}{EI\left(\lambda_2{}^2+\lambda_1{}^2\right)\lambda_2};\\
U_1(2,1) &= -\frac{\lambda_1\sin(\lambda_1 l)\lambda_2{}^2}{\lambda_2{}^2+\lambda_1{}^2}+\frac{\lambda_2\sinh(\lambda_2 l)\lambda_1{}^2}{\lambda_2{}^2+\lambda_1{}^2};\\
U_1(2,2) &= -\frac{\cos(\lambda_1 l)\left(-EI\,\lambda_2{}^2+T\right)}{EI\left(\lambda_2{}^2+\lambda_1{}^2\right)}+\frac{\cosh(\lambda_2 l)\left(EI\,\lambda_1{}^2+T\right)}{EI\left(\lambda_2{}^2+\lambda_1{}^2\right)};\\
U_1(2,3) &= \frac{\lambda_1\sin(\lambda_1 l)}{EI\left(\lambda_2{}^2+\lambda_1{}^2\right)}+\frac{\lambda_2\sinh(\lambda_2 l)}{EI\left(\lambda_2{}^2+\lambda_1{}^2\right)};\\
U_1(2,4) &= -\frac{\cos(\lambda_1 l)}{EI\left(\lambda_2{}^2+\lambda_1{}^2\right)}+\frac{\cosh(\lambda_2 l)}{EI\left(\lambda_2{}^2+\lambda_1{}^2\right)};\\
U_1(3,1) &= -\frac{EI\,\lambda_1{}^2\cos(\lambda_1 l)\lambda_2{}^2}{\lambda_2{}^2+\lambda_1{}^2}+\frac{EI\,\lambda_2{}^2\cosh(\lambda_2 l)\lambda_1{}^2}{\lambda_2{}^2+\lambda_1{}^2};\\
U_1(3,2) &= \frac{\lambda_1\sin(\lambda_1 l)\left(-EI\,\lambda_2{}^2+T\right)}{\lambda_2{}^2+\lambda_1{}^2}+\frac{\lambda_2\sinh(\lambda_2 l)\left(EI\,\lambda_1{}^2+T\right)}{\lambda_2{}^2+\lambda_1{}^2};\\
U_1(3,3) &= \frac{\lambda_1{}^2\cos(\lambda_1 l)}{\lambda_2{}^2+\lambda_1{}^2}+\frac{\lambda_2{}^2\cosh(\lambda_2 l)}{\lambda_2{}^2+\lambda_1{}^2};\\
U_1(3,4) &= \frac{\lambda_1\sin(\lambda_1 l)}{\lambda_2{}^2+\lambda_1{}^2}+\frac{\lambda_2\sinh(\lambda_2 l)}{\lambda_2{}^2+\lambda_1{}^2};\\
U_1(4,1) &= \frac{\left(EI\,\lambda_1{}^2+T\right)\lambda_1\sin(\lambda_1 l)\lambda_2{}^2}{\lambda_2{}^2+\lambda_1{}^2}+\frac{\left(EI\,\lambda_2{}^2-T\right)\lambda_2\sinh(\lambda_2 l)\lambda_1{}^2}{\lambda_2{}^2+\lambda_1{}^2};\\
U_1(4,2) &= -\frac{\left(-EI\,\lambda_1{}^2-T\right)\cos(\lambda_1 l)\left(-EI\,\lambda_2{}^2+T\right)}{EI\left(\lambda_2{}^2+\lambda_1{}^2\right)}\\
&\quad+\frac{\left(EI\,\lambda_2{}^2-T\right)\cosh(\lambda_2 l)\left(EI\,\lambda_1{}^2+T\right)}{EI\left(\lambda_2{}^2+\lambda_1{}^2\right)};\\
U_1(4,3) &= -\frac{\left(EI\,\lambda_1{}^2+T\right)\lambda_1\sin(\lambda_1 l)}{EI\left(\lambda_2{}^2+\lambda_1{}^2\right)}+\frac{\left(EI\,\lambda_2{}^2-T\right)\lambda_2\sinh(\lambda_2 l)}{EI\left(\lambda_2{}^2+\lambda_1{}^2\right)};
\end{aligned}
$$

$$U_1(4,4) = -\frac{\left(-EI\,{\lambda_1}^2 - T\right)\cos(\lambda_1 l)}{EI\left({\lambda_2}^2 + {\lambda_1}^2\right)} + \frac{\left(EI\,{\lambda_2}^2 - T\right)\cosh(\lambda_2 l)}{EI\left({\lambda_2}^2 + {\lambda_1}^2\right)}, \tag{6.31}$$

where the λ_1 and λ_2 are:

$$\lambda_1 = \sqrt{-\frac{1}{2}\frac{T}{EI} + \sqrt{\frac{1}{4}(\frac{T}{EI})^2 + \omega^2\frac{\rho A}{EI}}},$$
$$\lambda_2 = \sqrt{\frac{1}{2}\frac{T}{EI} + \sqrt{\frac{1}{4}(\frac{T}{EI})^2 + \omega^2\frac{\rho A}{EI}}}.$$

The transfer matrix U_2 of a mass-spring-dashpot absorber is:

$$U_2 = \begin{bmatrix} 1 & 0 & 0 & 0 \\ 0 & 1 & 0 & 0 \\ 0 & 0 & 1 & 0 \\ \frac{m\omega^2(k+j\omega c)}{k-m\omega^2+j\omega c} & 0 & 0 & 1 \end{bmatrix}, \tag{6.32}$$

where m is mass of absorber, m is spring stiffness, and c is damping of absorber.

The transfer matrix $\mathbf{U}$ for the subsystem is:

$$\mathbf{U} = U_2 U_1. \tag{6.33}$$

With the transfer matrix $\mathbf{U}$, the corresponding dynamic stiffness matrix $\mathbf{k}$, shown in Appendix C, is found by means of Maple.

Appendix C shows the dynamic stiffness library of the super-elements in a general marine riser system. Dynamic stiffness matrices for other members can be similarly derived.

Chapter 7

Vibration Suppression by Means of Absorbers and Wave-Absorbing Termination

7.1 Introduction

A Dynamic Vibration Absorber (DVA) has wide application in reducing undesirable vibration of structures. It originated from the Fraham's 1909 invention. Ormondroyd and Den Hartog [25] first analyzed the DVA. Brook [46] completed the analysis when he found optimal solutions for a viscously damped absorber. However, their analyses had considered only the application of a lumped parameter absorber to a lumped main system. Young [47] was the first to apply an absorber to a beam. Using a single mode approximation, Jacquot [47] found approximate tuning of a DVA to a uniform beam with regular boundary conditions.

The second section of this chapter introduces optimal tuning of a DVA to a beam. The third section finds an approximate optimal solution. The next section employs an example as an illustration. The fifth section studies optimal tuning of multiple identical DVAs to a beam with general boundary conditions. In order to describe the characteristic of non-uniformity of a marine riser, the sixth section investigates

optimal tuning of multiple identical DVAs to a non-uniform beam under varying tension. The seventh section discusses the incorporation of structural damping. On the basis of the research by Vandiver and Li [48], the final section derives a wave-absorbing termination for a beam system.

7.2 Optimum tuning of a DVA to a beam with general boundary conditions

The main idea here is that for a composite system including a beam and a DVA, shown in Figure 7-1, we use a mode of the beam rather than a mode of the composite system, to analyze and optimize parameters of a DVA.

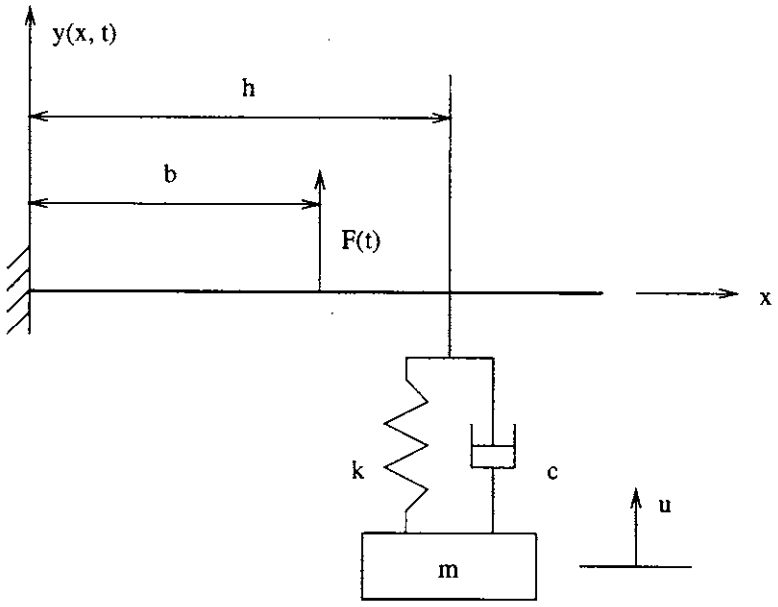

Figure 7-1: Beam with a damped dynamic vibration absorber

It is well known that the characteristic functions, $\phi_n(x), (n = 1, 2, ..., \infty)$, for a beam constitute an orthogonal set, which satisfies the following relations:

$$\int_0^l \phi_r \phi_s dx = 0, \quad (r \neq s),$$

$$
\begin{aligned}
\int_0^l \phi_r^2 dx &= l, \quad (r=s), \\
\int_0^l \frac{d^2\phi_r}{dx^2}\frac{d^2\phi_s}{dx^2} dx &= 0, \quad (r \neq s), \\
\int_0^l (\frac{d^2\phi_r}{dx^2})^2 dx &= \beta_r^4 l, \quad (r=s),
\end{aligned} \tag{7.1}
$$

where l is the length of the beam and $\beta_n^4 = m\omega_n^2/EIl$, in which m is the total mass of the beam, ω_n is the natural frequency of the beam, and EI is the bending stiffness.

Let $y(x,t)$ be the deflection of the beam, $z = y(h,t)$ be the deflection of the beam at the point of attachment of a DVA, and u be the absolute displacement of the absorber mass. Then y can be written in terms of characteristic functions $\phi_n(x)$:

$$
y = \sum_{n=1}^{\infty} q_n \phi_n(x), \tag{7.2}
$$

where q_n and the displacement coordinate u are considered to be the generalized coordinates for the composite system.

Using Eq. (7.2), one can formulate the kinetic energy T, the elastic strain energy potential V, and the dissipation function D for this problem.

$$
\begin{aligned}
T &= (m/2l)\int_0^l \dot{y}^2 dx + M\dot{u}^2/2 \\
&= (m/2)\sum_{n=1}^{\infty} \dot{q}_n^2 + M\dot{u}^2/2, \\
V &= (EI/2)\int_0^l (\frac{\partial^2 y}{\partial x^2})^2 dx + k(u-z)^2/2, \\
D &= (c/2)(\dot{u}-\dot{z})^2 \\
&= (c/2)[\dot{u} - \sum_{n=1}^{\infty} \dot{q}_n \phi_n(h)]^2,
\end{aligned} \tag{7.3}
$$

where M is the mass of absorber, c is the viscous damping of the absorber, and k is the spring constant of the absorber.

We take the periodic force $F(t)$ which acts at $x = b$ in the complex form, $F(t) = Pe^{i\omega t}$. Then the generalized force, Q_n, corresponding to the coordinate q_n is:

$$
Q_n = \phi_n(b) P e^{i\omega t}. \tag{7.4}
$$

Lagrange's equations of motion have the following form:

$$\frac{d}{dt}(\frac{\partial T}{\partial \dot{q}_n}) - \frac{\partial T}{\partial q_n} + \frac{\partial V}{\partial q_n} + \frac{\partial D}{\partial \dot{q}_n} = Q_n. \tag{7.5}$$

Substituting Eqs. (7.3) and (7.4) into (7.5) results in the following equations by means of Eq. (7.1):

$$\begin{aligned} m\ddot{q}_n + m\omega_n^2 q_n - k\phi_n(h)[u - \sum_{r=1}^{\infty} q_r\phi_r(h)] - c\phi_n(h)[\dot{u} - \sum_{r=1}^{\infty} \dot{q}_r\phi_r(h)] &= \phi_n(b)Pe^{i\omega t}, \\ M\ddot{u} + k[u - \sum_{r=1}^{\infty} q_r\phi_r(h)] + c[\dot{u} - \sum_{r=1}^{\infty} \dot{q}_r\phi_r(h)] &= 0. \end{aligned} \tag{7.6}$$

To find the steady state solution, we assume that:

$$q_n = A_n e^{i\omega t}, \qquad u = u_0 e^{i\omega t}, \tag{7.7}$$

and substitute them into Eqs. (7.6), thus obtaining the following:

$$\begin{aligned} m(\omega_n^2 - \omega^2)A_n - \phi_n(h)M\omega^2 u_0 &= \phi_n(b)P, \\ (k - M\omega^2 + ic\omega)u_0 &= (k + ic\omega)\sum_{n=1}^{\infty} A_n\phi_n(h). \end{aligned} \tag{7.8}$$

The first equation in Eqs. (7.8) represents an infinite set of equations corresponding to $n = 1, 2, 3, \ldots$. Multiplying each equation in the set by $\phi_n(h)$ and then adding the entire set leads to:

$$\begin{aligned} \sum_{n=1}^{\infty} A_n\phi_n(h) &= \frac{M\omega^2 u_0}{m}\sum_{n=1}^{\infty}\frac{\phi_n^2(h)}{\omega_n^2 - \omega^2} + \frac{P}{m}\sum_{n=1}^{\infty}\frac{\phi_n(b)\phi_n(h)}{\omega_n^2 - \omega^2} \\ &= \frac{M\omega^2 u_0}{m\omega_1^2}H(h,h) + \frac{P}{m\omega_1^2}H(b,h), \end{aligned} \tag{7.9}$$

where $H(h,h)$ and $H(b,h)$ are obtained by substituting $x = b$ in the following expressions:

$$H(h,x) = \sum_{n=1}^{\infty}\frac{\phi_n(h)\phi_n(x)}{\lambda_n^2 - f^2},$$

$$H(b,x) = \sum_{n=1}^{\infty} \frac{\phi_n(b)\phi_n(x)}{\lambda_n^2 - f^2}, \tag{7.10}$$

where $\lambda_n = \omega_n/\omega_1$ is the ratio of the n-th natural frequency of the beam to its first natural frequency, and $f = \omega/\omega_1$ is the ratio of exciting force frequency to first natural frequency of beam.

Solving for u_0 by the second equation in (7.8) and (7.9) and then substituting into the first equation in (7.8), we find:

$$A_n = \frac{P}{m(\omega_n^2 - \omega^2)}[\phi_n(b) + \frac{\phi_n(h)H(b,h)}{\frac{m}{M}\frac{\omega_1^2}{\omega^2}(\frac{k-M\omega^2+ic\omega}{k+ic\omega}) - H(h,h)}]. \tag{7.11}$$

The steady state deflection of the beam is:

$$y = e^{i\omega t}\sum_{n=1}^{\infty} A_n\phi_n(x). \tag{7.12}$$

We define the following dimensionless parameters:
mass ratio of absorber, $\mu = M/m$;
dimensionless deflection curve of the beam, $w(x) = y(x,t)\,(\frac{m\omega_1^2}{Pe^{i\omega t}})$;
the ratio of frequency of absorber to the first frequency of beam, $p = \sqrt{\frac{k}{M\omega_1^2}}$;
ratio of viscous damping to critical damping, $\zeta = \frac{c}{c_c}$, $c_c = 2\sqrt{kM}$.

Hence the dimensionless deflection, $w(x)$, is found from Eqs. 7.11 and 7.12:

$$w(x) = H(b,x) + \frac{H(b,h)H(h,x)(1+i2\zeta\frac{f}{p})}{\frac{1}{\mu}(\frac{1}{f^2} - \frac{1}{p^2}) - H(h,h)) + i2\zeta\frac{f}{p}(\frac{1}{\mu f^2} - H(h,h))}. \tag{7.13}$$

Eq. (7.13) is the principal equation to determine the behavior of the system. Based on this equation, the following two cases are discussed:

(1) The undamped vibration absorber

Equation (7.13) reduces to:

$$w(x) = H(b,x) + \frac{H(b,h)H(h,x)}{\frac{1}{\mu}(\frac{1}{f^2} - \frac{1}{p^2}) - H(h,h))}. \tag{7.14}$$

Then the deflection at $x = h$ is:

$$w(h) = \frac{(p^2 - f^2)H(b,h)}{p^2 - f^2 - \mu f^2 p^2 H(h,h)}. \tag{7.15}$$

It is noted that the deflection at $x = h$ vanishes when $f = p$. The undamped natural frequencies of the composite system are obtained by solving the following equation:

$$p^2 - f^2 - \mu f^2 p^2 H(h,h) = 0. \tag{7.16}$$

(2) The damped vibration absorber

Replacing $x = h$ into Eq. (7.13), one can obtain the deflection at the point where the absorber is attached:

$$w(h) = \frac{H(b,h)(1 - f^2/p^2 + i2\zeta f/p)}{(1 - f^2/p^2 - \mu f^2 H(h,h)) + i2\zeta f/p(1 - \mu f^2 H(h,h))}. \tag{7.17}$$

As in the case of a two-degree-of-freedom system, there are two "fixed points" of frequencies at which vibration amplitudes are independent of the damping. The two "fixed points" of frequencies, f_1 and f_2, are solved from the following equation [47]:

$$p^2 = \frac{f^2}{2}[\frac{2 - \mu f^2 H(h,h)}{1 - \mu f^2 H(h,h)}]. \tag{7.18}$$

For any pair of frequencies f_1 and f_2, one can find the corresponding amplitudes through Eq. (7.13) assuming ζ is, for simplicity, infinite:

$$[w(h)]_{f_1,f_2} = [\frac{H(b,h)}{1 - \mu f^2 H(h,h)}]_{f_1,f_2}. \tag{7.19}$$

By trial and error, one can find optimal absorber tuning which makes equal the amplitudes at the fixed points.

7.3 Approximate solution of optimal tuning

Assuming that a dynamic vibration absorber is tuned to a frequency at or near the n-th natural frequency of a beam itself, i.e., $p \approx \lambda_n$, and neglecting the contribution of all other modes, $H(b,h)$ and $H(h,h)$ are approximated as:

$$\begin{aligned} H(b,h) &\approx \frac{\phi_n(b)\phi_n(h)}{\lambda_n^2 - f^2}, \\ H(h,h) &\approx \frac{\phi_n(h)^2}{\lambda_n^2 - f^2}. \end{aligned} \tag{7.20}$$

Equation (7.17) reduces to:

$$w(h) = \frac{\phi_n(b)\phi_n(h)(p^2 - f^2 + i2\zeta fp)}{(p^2 - f^2)(\lambda_n^2 - f^2) - \mu f^2 p^2 \phi_n^2(h) + i2\zeta fp(\lambda_n^2 - f^2 - \mu f^2 \phi_n^2(h))}. \tag{7.21}$$

The modulus of $w(h)$ is then written as:

$$|w(h)| = \phi_n(b)\phi_n(h)\sqrt{\frac{(2\zeta fp)^2 + (p^2 - f^2)^2}{(2\zeta fp)^2(\lambda_n^2 - f^2 - \mu f^2\phi_n^2(h))^2 + [\mu f^2 p^2 \phi_n^2(h) - (\lambda_n^2 - f^2)(p^2 - f^2)]^2}}. \tag{7.22}$$

A convenient way to find the optimal solution to Eq. (7.22) is to use the analogy between this equation and the expression by Den Hartog [25] in a two-degree-of-freedom system. The optimal tuning is found by means of the analogy:

$$p_0/\lambda_n = \frac{1}{1 + \mu\phi_n^2(h)}, \tag{7.23}$$

$$(\zeta_0 p_0/\lambda_n)^2 = \frac{3\mu\phi_n^2(h)}{8(1 + \mu\phi_n^2(h))^3}, \tag{7.24}$$

where p_0 and ζ_0 are optimal tuning values.

Based on Eqs. (7.23) and (7.24), ζ_0 is written as:

$$\zeta_0^2 = \frac{3\mu\phi_n^2(h)}{8(1 + \mu\phi_n^2(h))}. \tag{7.25}$$

Equations (7.23) and (7.25) are approximate optimal solutions for a DVA tuned to a beam.

7.4 A numerical example

A cantilever beam with a dynamic vibration absorber at the free end, shown in Figure 7-1, appears as an example. A pipe in our lab is used as an illustration, with the following specifications:

pipe length $l = 5.69\ m$, (18.67 ft);

mass per unit length $\rho a = 1.8320$ kg/m;

bending stiffness $EI = 8.66 \times 10^3\ N.m^2$, (obtained by testing);

the first circular natural frequency of beam $\omega_1 = 7.4641$ rad/s;

distance of absorber to left end of beam $h = l$;

distance of exciting force to left end of beam $b = l/2$; and

absorber mass ratio $\mu = 1/5$.

(1) Natural frequencies of the composite system

One can find natural frequencies of the composite system by solving Eq. (7.16). Since $H(h,h)$ is a nonlinear function of f, Eq. (7.16) cannot be solved analytically. The resonant frequencies of the composite system are found by plotting the left hand side of Eq. (7.16) as a function of f and by finding the roots. Figure 7-2 shows the first two resonant frequencies for $p = \lambda_1$.

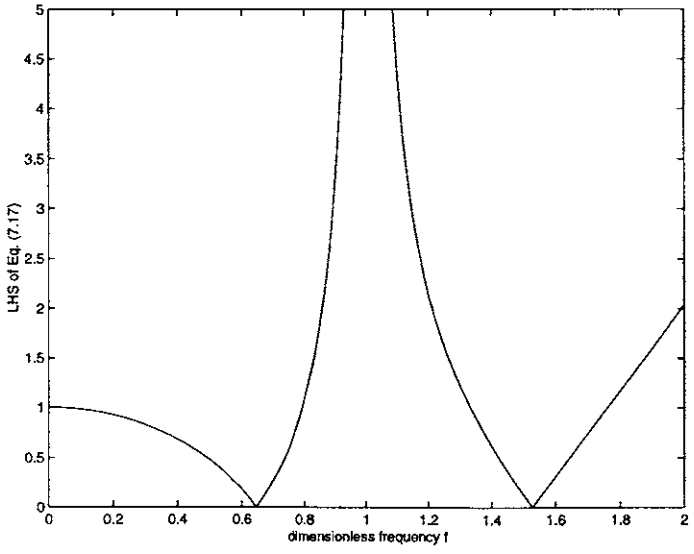

Figure 7-2: Finding roots of $p^2 - f^2 - \mu f^2 p^2 H(h,h) = 0$ for $p = \lambda_1$

Table 7.1 depicts the natural frequencies of the composite system for different tunings and indicates that a DVA causes an additional natural frequency. When $p = \lambda_1$, the natural frequencies are shown in the second column of Table 7.1. In this case, the first frequency $f_1 = 0.65$ is lower than λ_1 and the second frequency $f_2 = 1.54$ is higher than λ_1, while the higher frequencies of the system are nearly the same as for the cantilever beam without a DVA. Calculations are also carried out for the DVA tuned to the second and third frequencies of the beam, respectively, and the same trend is observed as for $p = \lambda_1$. The results in the first rows of Table 7.1 are similar to in [47]. This table also indicates that the DVA results in a great effect on the natural frequency distribution of the system around the frequency to which the DVA is tuned.

no DVA	$p = \lambda_1$	$p = \lambda_2$	$p = \lambda_3$
1.000	0.65	0.74	0.74
6.267	1.54	4.81	5.14
17.550	6.34	10.10	14.61
34.393	17.61	18.70	26.95
56.848	34.40	34.88	40.35
84.925	56.58	57.20	59.58
	85.00	85.00	86.65

Table 7.1: Frequencies of a cantilever beam with an undamped DVA ($b = l/2$, $h = l$, $\mu = 1/5$)

(2) Optimal tuning

With Eq. (7.18), one can numerically find frequencies at two "fixed points" by plotting the right hand side for a given value of p, shown in Figure 7-3. This figure indicates that there are two f-values around the frequency to be tuned for a given p-value. Figure 7-4 depicts the curve around $\lambda_1 = 1$. Given $p = 0.6$, the two "fixed points"obtained from Figure 7-4 are $f_1 \approx 0.55$ and$f_2 \approx 0.95$.

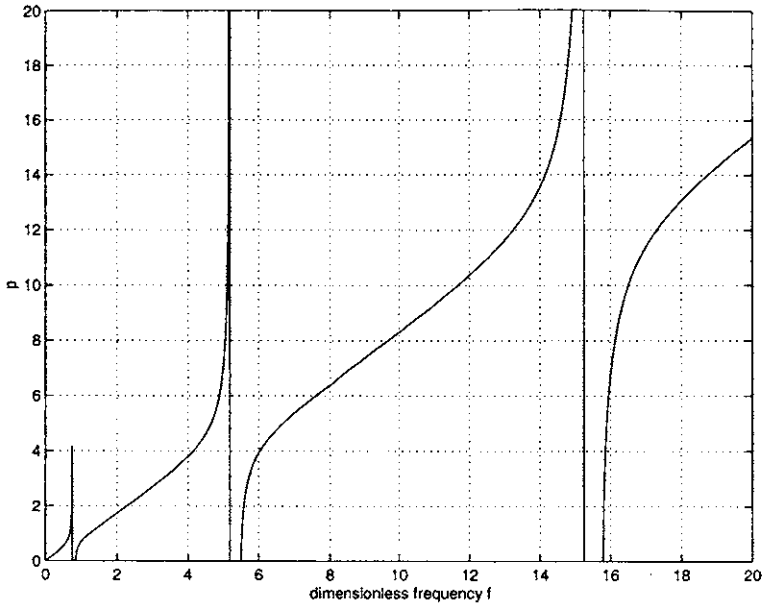

Figure 7-3: The relationship between p and f ($\mu = 1/5$)

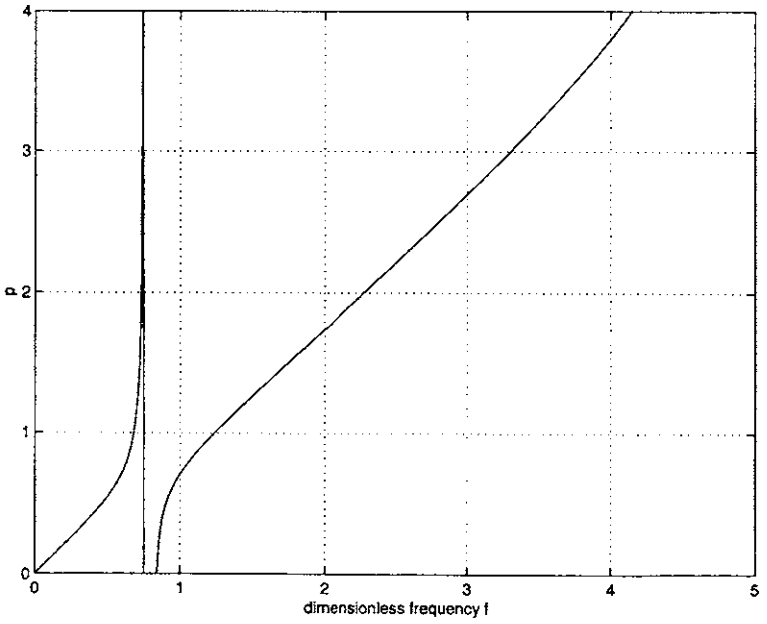

Figure 7-4: The relationship between p and f ($\mu = 1/5$)

In order to further verify that there exist these two "fixed points", set $p = 0.6$, $\zeta = 0.0, 0.1, 100, 0.4$ respectively, and calculate their responses by Eq. (7.17), shown in Figure 7-5. This figure shows two fixed points, P and Q, which correspond to f_1, f_2, respectively.

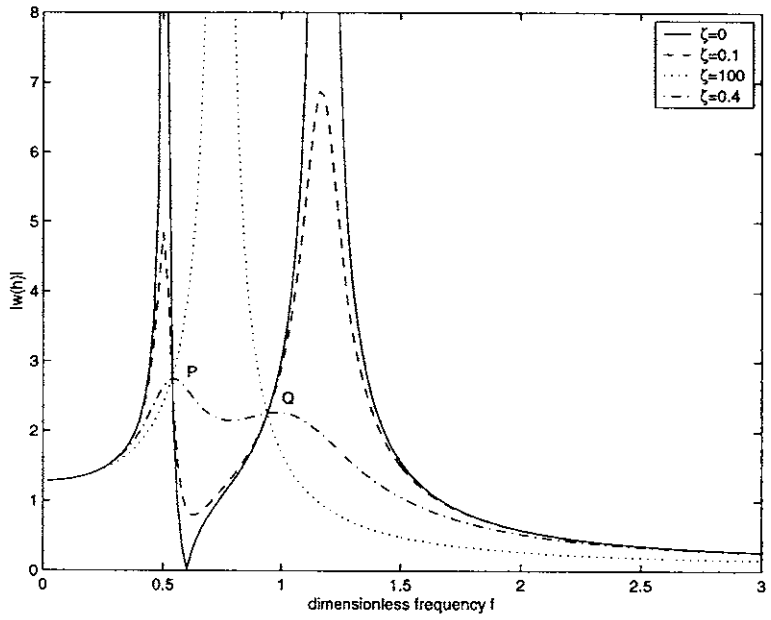

Figure 7-5: The frequency response curves ($\mu = 1/5$, $p = 0.6$)

One can find the amplitudes at such a pair of frequencies f_1 and f_2 by means of Eq. (7.19). The optimal value p_0 is obtained by adjusting p-value and observing the change of the two peaks so that they are equal. It is found by trial and error that optimal tuning occurs for p=0.56, and that the fixed points are at $f_1 \approx 0.50$ and $f_2 \approx 0.93$. The corresponding amplitudes are 2.392 and 2.409, respectively. These results are slightly different from those obtained by Young [47].

By a proper choice of ζ, the curve is adjusted to pass with a horizontal tangent through one of the two fixed points. Figure 7-6 shows that $\zeta = 0.45$ is close to the optimal one. Figure 7-7 indicates that the optimal damping ratio $\zeta \approx 0.432$.

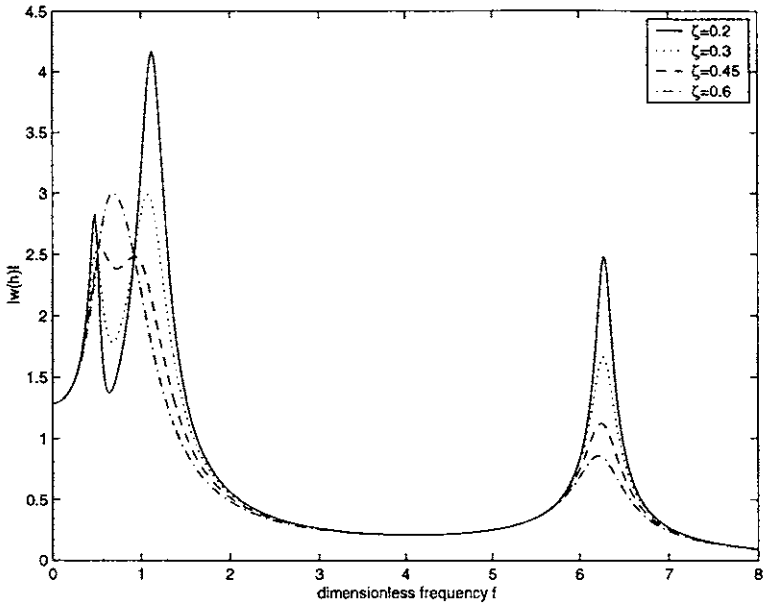

Figure 7-6: The frequency response curves ($\mu = 1/5$, $p_0 = 0.56$)

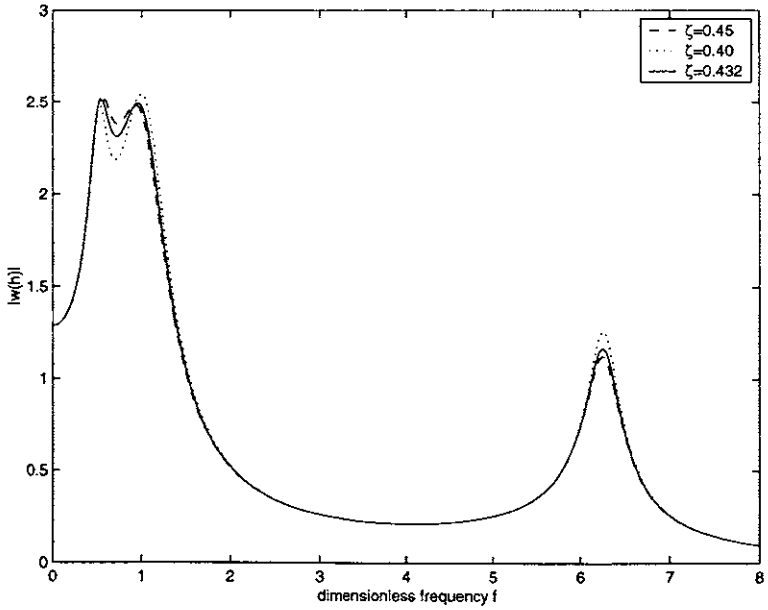

Figure 7-7: The frequency response curves ($\mu = 1/5$, $p_0 = 0.56$)

(3) Approximate optimal tuning

The approximate optimal tuning is found by means of the formulas (7.23) to (7.25). Figure 7-8 demonstrates that the difference between the response curve by the solution obtained in **(2)** and that by approximate solution is small.

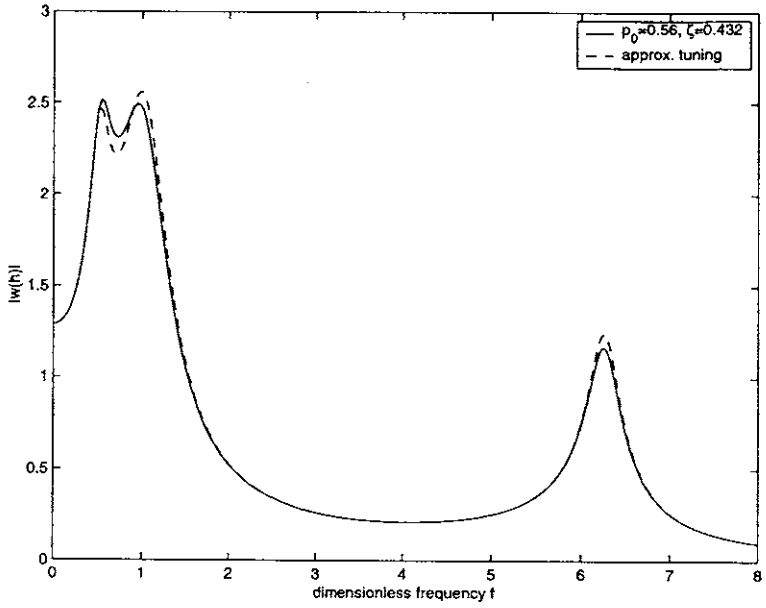

Figure 7-8: Comparison of response curves with different tuning ($\mu = 1/5$)

7.5 Optimal tuning of multiple DVAs to a beam with general boundary conditions

7.5.1 Optimal solution

For a composite system of a beam with multiple identical dynamic vibration absorbers, a mode of the beam rather than that of the composite system is employed to find optimal tuning. Let $y(x,t)$ be the deflection of a beam, $z_i = y(a_i,t)$ be the deflection of the beam at the points where DVAs are attached, and $u_i(t)$ be the absolute coordinate of a DVA mass. Assume that k-th mode dominates a beam's vibration,

then y is written in terms of the beam mode $\phi_k(x)$:

$$y = q_k(t)\phi_k(x). \tag{7.26}$$

Using Eq. (7.26), we formulate the kinetic energy T , the elastic strain energy potential V, and the virtual work δw, and then derive the governing equation of motion by using the Lagrange's equation:

$$\frac{d}{dt}(\frac{\partial L}{\partial \dot{q}_n}) - \frac{\partial L}{\partial q_n} = \tilde{Q}_n, \qquad (n = 1, 2), \tag{7.27}$$

where $L = T - V$, q_n is a general coordinate of the composite system, $\tilde{Q}_n$ is the corresponding general force.

$$\begin{aligned} T &= \frac{1}{2}\sum_{i=1}^{N} m\dot{u}_i^2 + \frac{1}{2}\rho A\int_0^l \dot{y}^2 dx, \\ V &= \frac{1}{2}\sum_{i=1}^{N} k(y(a_i) - u_i)^2 + \frac{1}{2}EI\int_0^l (\frac{d^2y}{dx^2})^2 dx, \\ \delta w &= \int_0^l f(x)\delta y dx e^{j\omega t}, \end{aligned} \tag{7.28}$$

where N is the total number of absorbers, m is mass of a DVA, and k is stiffness of a DVA, and ρA is mass of the beam per unit length.

Substitution of Eq. (7.26) into Eq. (7.28) gives:

$$\begin{aligned} T &= \frac{1}{2}\sum_{i}^{N} m\dot{u}_i^2 + \frac{1}{2}\rho A\dot{q}_k^2\int_0^l \phi_k^2 dx, \\ V &= \frac{1}{2}\sum_{i=1}^{N}(q_k\phi_k(a_i) - u_i)^2 + \frac{1}{2}EIq_k^2\int_0^l (\frac{d^2\phi_k}{dx^2})^2 dx, \\ \delta w &= \delta q_k\int_0^l f(x)\phi_k(x)dx e^{j\omega t}. \end{aligned} \tag{7.29}$$

Since $f(x)$ is specified for an exciting force spatial distribution, δw can be rewritten as:

$$\delta w = \delta q_k \epsilon_f e^{j\omega t}, \tag{7.30}$$

where $\epsilon_f = \int_0^l f(x)q_k(x)dx$.

With Eqs. (7.28) and (7.29), we have by means of the orthogonality of characteristic functions, shown in Eq. (7.1):

$$\begin{aligned}
L &= \frac{1}{2}\sum_{i=1}^{N} m\dot{u}_i^2 + \frac{1}{2}\rho A\dot{q}_k^2\int_0^l \phi_k^2 dx - \frac{1}{2}\sum_{i=1}^{N} k(q_k\phi_k(a_i) - u_i)^2 - \frac{1}{2}EIq_k^2\int_0^l (\frac{d^2\phi_k}{dx^2})^2 dx, \\
\frac{\partial L}{\partial \dot{q}_k} &= \rho Al\dot{q}_k, \\
\frac{d}{dt}(\frac{\partial L}{\partial \dot{q}_k}) &= \rho Al\ddot{q}_k, \\
\frac{\partial L}{\partial q_k} &= -k\sum_{i=1}^{N}(q_k\phi_k(a_i) - u_i)\phi_k(a_i) - EI\beta_k^4 lq_k, \\
&= -k(\sum_{i=1}^{N}\phi_k^2(a_i))q_k + k\sum_{i=1}^{N}\phi_k(a_i)u_i - EI\beta_k^4 lq_k, \\
\frac{\partial L}{\partial \dot{u}_n} &= m\dot{u}_n, \\
\frac{d}{dt}(\frac{\partial L}{\partial \dot{u}_n}) &= m\ddot{u}_n, \\
\frac{\partial L}{\partial u_n} &= k(q_k\phi_k(a_i) - u_n), \qquad (n = 1, 2, ..., N).
\end{aligned} \tag{7.31}$$

Substituting Eqs. (7.31) into Eqs. (7.27) results in:

$$\rho Al\ddot{q}_k + (k\sum_{i=1}^{N}\phi_k^2(a_i) + EI\beta_k^4 l)q_k - k\sum_{i=1}^{N}\phi_k(a_i)u_i = \epsilon_f e^{j\omega t}, \tag{7.32}$$

$$m\ddot{u}_n - k\phi_k(a_n)q_k + ku_n = 0, \quad (n = 1, 2, ..., N) \tag{7.33}$$

Assuming $\begin{pmatrix} q_k \\ u_n \end{pmatrix} = \begin{pmatrix} Q_k \\ U_n \end{pmatrix} e^{j\omega t}$, and substituting into Eqs. (7.32) and (7.33) generate:

$$(k\sum_{i=1}^{N}\phi_k^2(a_i) + EI\beta_k^4 l - \omega^2\rho Al)Q_k - k\sum_{i=1}^{N}\phi_k(a_i)U_i = \epsilon_f, \tag{7.34}$$

$$-k\phi_k(a_n)Q_k + (k - m\omega^2)U_n = 0. \tag{7.35}$$

Eq. (7.35) gives the expression of U_n in terms of Q_k:

$$U_n = \frac{k\phi_k(a_n)}{k - m\omega^2} Q_k. \tag{7.36}$$

Multiplying Eq. (7.36) by $\phi_k(a_n)$ results in:

$$\phi_k(a_n) U_n = \frac{k\phi_k^2(a_n)}{k - m\omega^2} Q_k. \tag{7.37}$$

Adding all the terms in Eq. (7.37) for n from 1 to N, we obtain the following result:

$$\sum_{i=1}^{N} \phi_k(a_i) U_i = \frac{kQ_k}{k - m\omega^2} \sum_{i=1}^{N} \phi_k^2(a_i). \tag{7.38}$$

Substituting Eq. (7.38) into Eq. (7.34) results in:

$$(k \sum_{i=1}^{N} \phi_k^2(a_i) + EI\beta_k^4 l - \omega^2 \rho A l) Q_k - \frac{k^2 Q_k}{k - m\omega^2} \sum_{i=1}^{N} \phi_k^2(a_i) = \epsilon_f. \tag{7.39}$$

Eq. (7.39) further reduces to:

$$\begin{aligned} Q_k(\omega) &= \frac{\epsilon_f (k - m\omega^2)}{\rho A l m \omega^4 - \omega^2 (\rho A l k + mk \sum_{i=1}^{N} \phi_k^2(a_i) + mEI\beta_k^4 l) + kEI\beta_k^4 l} \\ &= \frac{\epsilon_f (k/m - \omega^2)}{\rho A l \omega^4 - \omega^2 (\rho A l k/m + k \sum_{i=1}^{N} \phi_k^2(a_i) + EI\beta_k^4 l) + EI\beta_k^4 lk/m} \end{aligned} \tag{7.40}$$

In order to generalize the analysis, we define the following dimensionless quantities:
dimensionless frequency $\lambda = \frac{\omega}{\beta_k^2} \sqrt{\frac{\rho A}{EI}}$;
tuning ratio $T^2 = (\frac{k}{m})(\frac{\rho A}{EI\beta_k^4})$;
mass ratio of a DVA $\mu = \frac{m}{\rho A l}$.

With these dimensionless parameters, Eq. (7.40) is simplified as:

$$Q_k(\omega) = \frac{\epsilon_f}{EI\beta_k^4 l} \{ \frac{T^2 - \lambda^2}{\lambda^4 - \lambda^2 [1 + T^2 (1 + \mu \sum_{i=1}^{N} \phi_k^2(a_i))] + T^2} \}. \tag{7.41}$$

The frequency response of any point on a beam in terms of the dimensionless parameters is then:

$$y(x,\lambda) = \frac{\epsilon_f \phi_k(x)}{EI\beta_k^4 l}\{\frac{T^2-\lambda^2}{\lambda^4 - \lambda^2[1+T^2(1+\mu\sum_{i=1}^{N}\phi_k^2(a_i))]+T^2}\}. \tag{7.42}$$

For viscous damping in DVAs, it can be easily accomplished by replacing T^2 with a corresponding complex frequency-dependent quantity, namely:

$$T^2 \to T^2 + j2\zeta\lambda T, \tag{7.43}$$

where ζ is the damping ratio of a DVA defined in the usual sense, i.e., $\zeta = c/2\sqrt{km}$.

It is interesting to note that the approximate frequency response function in Eq. (7.42) is the same form as that considered by Brock [46] with the exception that the mass ratio μ is replaced by $\mu\sum_{i=1}^{N}\phi_k^2(a_i)$. Hence the results given in [46] are directly applied to this problem. In this case the optimal tuning ratio is:

$$T_0 = \frac{1}{1+\mu\sum_{i=1}^{N}\phi_k^2(a_i)}. \tag{7.44}$$

The frequencies at "fixed points" are:

$$\lambda_{1,2}^2 = T_0[1 \pm \sqrt{\frac{\mu\sum_{i=1}^{N}\phi_k^2(a_i)}{2+\mu\sum_{i=1}^{N}\phi_k^2(a_i)}}]. \tag{7.45}$$

The dimensionless frequency response is defined as:

$$H(\lambda) = \frac{y(x,\lambda)EI\beta_k^4 l}{\epsilon_f \phi_k(x)}. \tag{7.46}$$

The square of the magnitude of the frequency response at the fixed points is then:

$$H^2(\lambda_{1,2}) = \frac{2+\mu\sum_{i=1}^{N}\phi_k^2(a_i)}{\mu\sum_{i=1}^{N}\phi_k^2(a_i)}. \tag{7.47}$$

Substituting Eq. (7.43) into (7.42) yields the square of the frequency response function with viscous damping:

$$H^2(\lambda) = \frac{(T^2 - \lambda^2) + (2\zeta T\lambda)^2}{\{\lambda^4 - \lambda^2[1 + T^2(1 + \mu \sum \phi_k^2(a_i))] + T^2\}^2 + (2\zeta T)^2\{\lambda - \lambda^3[1 + \mu \sum \phi_k^2(a_i)]\}^2}. \tag{7.48}$$

With the similarity of this expression to that by Brock [46], the optimal damping can be written as:

$$\zeta_0^2 = \frac{3\mu \sum_{i=1}^{N} \phi_k^2(a_i)}{8[1 + \mu \sum_{i=1}^{N} \phi_k^2(a_i)]}. \tag{7.49}$$

7.5.2 An example of a simply supported beam tuned by DVAs

The beam in Section 7.4 is now assumed to be simply supported. Identical DVAs are assumed to be evenly distributed. The total mass ratio of DVAs in this example is kept constant, namely, $N\mu = 0.20$.

(1) Assuming that one DVA at the midpoint is tuned to the 1st natural frequency of the beam, the optimal solution by Eqs. (7.44) and (7.49) is: $T_0 = 0.7143$, and $\zeta_0 = 0.3273$.

Figure 7-9 shows the frequency response of the beam with one DVA tuned optimally and un-optimally. This figure indicates that the vibration around dimensionless frequency $\lambda = 1$ is reduced when the DVA at the midpoint is optimally tuned.

Figure 7-10 depicts that the frequency response of the beam with the 1st frequency tuned by one and two DVAs, respectively. In the first case, the DVA is at the midpoint of the beam and corresponds to the antinode of the 1st mode. In the second case, the DVAs are evenly distributed along the beam; namely, one DVA is at one third and the other is at two thirds of the length. Hence, in this case one DVA is more effective than two DVAs.

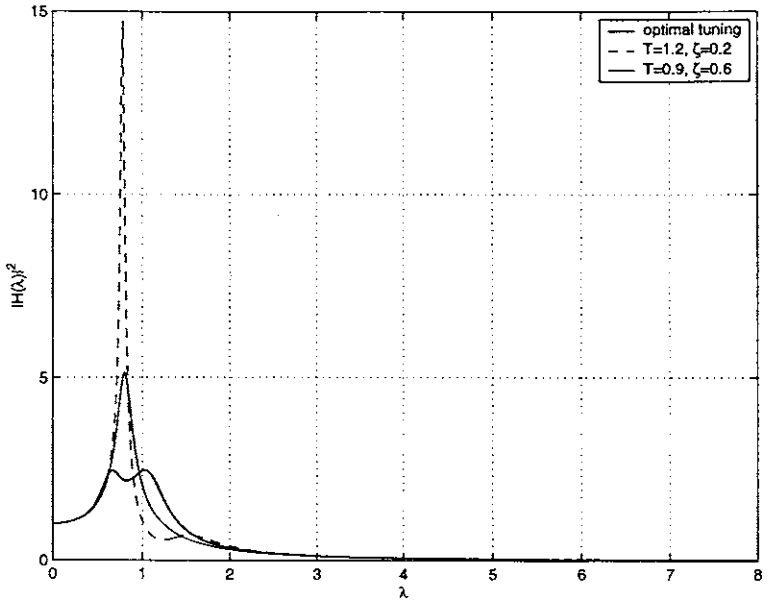

Figure 7-9: Frequency response of a simply supported beam with 1st natural frequency tuned by one DVA ($\mu = 1/5$)

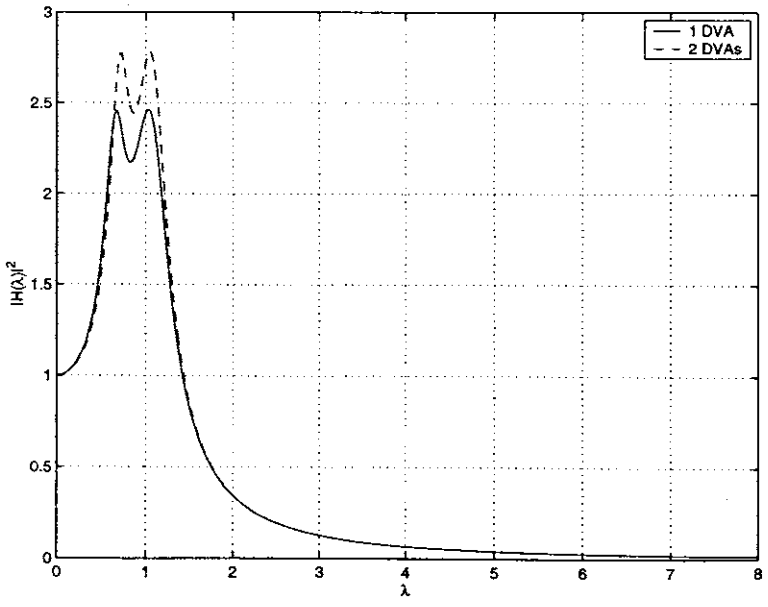

Figure 7-10: Frequency response of a simply supported beam with the 1st natural frequency tuned by one and two DVAs respectively

(2) Assuming that DVAs are designed to optimally tune the 3rd natural frequency, we calculate the frequency response by means of Eq. (7.48). Figure 7-11 shows that the frequency response of the beam optimally tuned by two, three and six DVAs, respectively. All the DVAs are evenly distributed, as in (1). In the first case, DVAs are at the nodes of the 3rd mode shape, thus are useless, and the corresponding response peak is close to infinite. Compared with the other two cases, the second case is the most effective in suppressing vibration since the DVAs are at the antinodes of the 3rd mode shape. Hence, the effectiveness of DVAs depends on their location distribution.

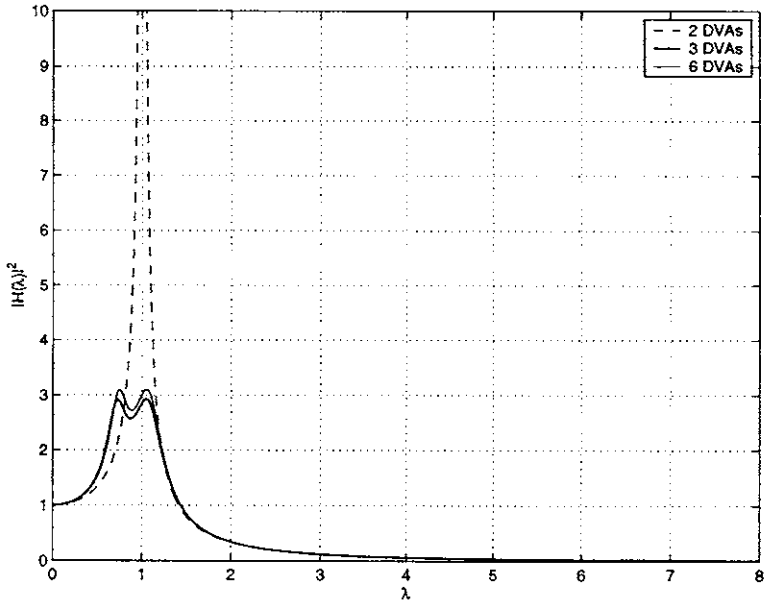

Figure 7-11: Frequency response of a simply supported beam with the 3rd natural frequency tuned by multiple DVAs

7.6 Optimal tuning of multiple DVAs to a non-uniform beam under varying tension

7.6.1 Optimal solution

In this section, optimal tuning of multiple identical dynamic vibration absorbers to a general non-uniform beam is investigated. Following the same procedure as in Section 7.5, we need to modify the terms to include the tension contribution and to generalize the expressions when applying Lagrange's equation, Eq. (7.27):

$$\begin{aligned} T &= \frac{1}{2}\sum_{i=1}^{N} m\dot{u}_i^2 + \frac{1}{2}\int_0^l \rho A(x)\dot{y}^2 dx, \\ V &= \frac{1}{2}\int_0^l [EI(x)(\frac{\partial^2 y}{\partial x^2})^2 + S(x)(\frac{\partial y}{\partial x})^2]dx + \frac{1}{2}\sum_{i=1}^{N} k(y(a_i,t) - u_i)^2, \end{aligned} \quad (7.50)$$

where $S(x)$ is the spatially varying tension.
Substituting Eq. (7.26) into (7.50) yields:

$$\begin{aligned} T &= \frac{1}{2}\sum_{i}^{N} m\dot{u}_i^2 + \frac{1}{2}\dot{q}_k^2\int_0^l \rho A(x)\phi_k^2 dx, \\ V &= \frac{1}{2}k\sum_{i=1}^{N}(q_k\phi_k(a_i) - u_i)^2 + \frac{1}{2}q_k^2\int_0^l [EI(x)(\frac{d^2\phi_k}{dx^2})^2 + S(x)(\frac{d\phi_k}{dx})^2]dx. \end{aligned} \quad (7.51)$$

Doing the algebraic operations with Eq. (7.51) gives:

$$\begin{aligned} L &= \frac{1}{2}\sum_{i}^{N} m\dot{u}_i^2 + \frac{1}{2}\dot{q}_k^2\int_0^l \rho A(x)\phi_k^2 dx \\ &\quad - \frac{1}{2}k\sum_{i=1}^{N}(q_k\phi_k(a_i) - u_i)^2 - \frac{1}{2}q_k^2\int_0^l [EI(x)(\frac{d^2\phi_k}{dx^2})^2 + S(x)(\frac{d\phi_k}{dx})^2]dx, \\ \frac{\partial L}{\partial \dot{q}_k} &= \dot{q}_k\int_0^l \rho A(x)\phi_k^2 dx, \\ \frac{d}{dt}(\frac{\partial L}{\partial \dot{q}_k}) &= \ddot{q}_k\int_0^l \rho A(x)\phi_k^2 dx, \\ \frac{\partial L}{\partial q_k} &= -k(\sum_{i=1}^{N}\phi_k^2(a_i))q_k + k\sum_{i=1}^{N}\phi_k(a_i)u_i - q_k\int_0^l [EI(x)(\frac{d^2\phi_k}{dx^2})^2 + S(x)(\frac{d\phi_k}{dx})^2]dx, \end{aligned} \quad (7.52)$$

Substituting Eq. (7.52) into Eq. (7.27) results in:

$$\ddot{q}_k \int_0^l \rho A(x)\phi_k^2 dx + \{k\sum_{i=1}^{N}\phi_k^2(a_i) \quad + \quad \int_0^l [EI(x)(\frac{d^2\phi_k}{dx^2})^2 + S(x)(\frac{d\phi_k}{dx})^2]dx\}q_k$$
$$- \quad k\sum_{i=1}^{N}\phi_k(a_i)u_i = \epsilon_f e^{j\omega t}. \tag{7.53}$$

Substituting $\begin{pmatrix} q_k \\ u_n \end{pmatrix} = \begin{pmatrix} Q_k \\ U_n \end{pmatrix} e^{j\omega t}$ into Eqs. (7.53) yields:

$$\{-\omega^2 \int_0^l \rho A(x)\phi_k^2 dx + k\sum_{i=1}^{N}\phi_k^2(a_i) \quad + \quad \int_0^l [EI(x)(\frac{d^2\phi_k}{dx^2})^2 + S(x)(\frac{d\phi_k}{dx})^2]dx)\}Q_k$$
$$- \quad k\sum_{i=1}^{N}\phi_k(a_i)U_i = \epsilon_f. \tag{7.54}$$

Then substituting Eq. (7.38) into Eq. (7.54) reduces to:

$$\{-\omega^2 \int_0^l \rho A(x)\phi_k^2 dx + k\sum_{i=1}^{N}\phi_k^2(a_i) \quad + \quad \int_0^l [EI(x)(\frac{d^2\phi_k}{dx^2})^2 + S(x)(\frac{d\phi_k}{dx})^2]dx\}Q_k$$
$$- \quad \frac{k^2 Q_k}{k - m\omega^2}\sum_{i=1}^{N}\phi_k^2(a_i) = \epsilon_f. \tag{7.55}$$

We define the following modal parameters:

modal mass $m_k = \int_0^l \rho A(x)\phi_k^2 dx$;

modal stiffness $\alpha_k = \int_0^l [EI(x)(\frac{d^2\phi_k}{dx^2})^2 + S(x)(\frac{d\phi_k}{dx})^2]dx$;

modal frequency $\omega_k^2 = \alpha_k/m_k$.

Eq. (7.55) reduces to:

$$\begin{aligned} Q_k(\omega) &= \frac{\epsilon_f(k - m\omega^2)}{mm_k\omega^4 - \omega^2(km_k + mk\sum_{i=1}^{N}\phi_k^2(a_i) + m\alpha_k) + k\alpha_k} \\ &= \frac{\epsilon_f(k/m - \omega^2)}{m_k\omega^4 - \omega^2(m_k k/m + k\sum_{i=1}^{N}\phi_k^2(a_i) + \alpha_k) + \alpha_k k/m}. \end{aligned} \tag{7.56}$$

We redefine the following two dimensionless quantities:

dimensionless frequency $\lambda = \omega/\omega_k$;

tuning ratio $T^2 = \frac{k/m}{\omega_k}$.

Eq. (7.56) then reduces to:

$$Q_k(\omega) = \frac{\epsilon_f}{\alpha_k}\{\frac{T^2 - \lambda^2}{\lambda^4 - \lambda^2[1 + T^2(1 + \mu\sum_{i=1}^{N}\phi_k^2(a_i))] + T^2}\}. \tag{7.57}$$

The expression of the frequency response function is the same as in Eq. (7.46). With the same replacement as in Eq. (7.43), we find the optimal tuning shown in Eqs. (7.44) and (7.49), namely:

$$\begin{aligned} T_0 &= \frac{1}{1 + \mu\sum_{i=1}^{N}\phi_k^2(a_i)}, \\ \zeta_0^2 &= \frac{3\mu\sum_{i=1}^{N}\phi_k^2(a_i)}{8[1 + \mu\sum_{i=1}^{N}\phi_k^2(a_i)]}. \end{aligned}$$

Noting that the beam is non-uniform and under spatially varying tension, modal parameters–including modal shapes, mass, stiffness, and natural frequencies– do not have closed-form solutions. In addition, mode slope and curvature are needed in order to obtain modal stiffness. In Chapters 4 and 5, we have investigated the vibration analysis of such a beam by the WKB-based DSM with the W-W algorithm. Hence, all the required modal parameters are found numerically using this powerful technique.

7.6.2 Optimal tuning of DVAs to a uniform beam under constant tension

As a special case, this subsection discusses optimal tuning of DVAs to a uniform beam under constant tension, in which some expressions in the above subsections are simplified. Exact solutions for the effect of an axial load on natural frequencies are available for pinned-pinned, sliding-sliding, and sliding-pinned single-span uniform beams. For other uniform beams, an approximate formula for the effect of axial load on the natural frequencies is also available [35]. The mode shapes of the pinned-pinned, sliding-sliding, and sliding-pinned beam are unaffected by an axial load. This section analyzes a simply supported beam model. Similarly, this process can provide

closed form solutions to other beam models.

The k-th natural frequency and mode shape of a simply supported beam subject to constant tension, s_0, are:

$$\begin{aligned} \omega_k &= \frac{k^2\pi^2}{l^2}\sqrt{\frac{EI}{\rho A}}\sqrt{1+\frac{s_0 l^2}{k^2\pi^2 EI}}, \\ \phi_k(x) &= \sqrt{2}\sin(\frac{k\pi x}{l}), \qquad (k=1,2,3,...). \end{aligned} \tag{7.58}$$

Then $\phi_k'(x)$ and $\phi_k''(x)$ are expressed as:

$$\begin{aligned} \phi_k'(x) &= \frac{\sqrt{2}k\pi}{l}\cos(\frac{k\pi x}{l}), \\ \phi_k''(x) &= -\frac{\sqrt{2}\pi^2 k^2}{l^2}\sin(\frac{k\pi x}{l}). \end{aligned} \tag{7.59}$$

With Eqs. (7.58) and (7.59), the k-th modal mass and stiffness are written as:

$$\begin{aligned} m_k &= \rho A l, \\ \alpha_k &= EIl(\frac{\pi k}{l})^4 + s_0 l(\frac{\pi k}{l})^2 \\ &= \rho A l \omega_k^2. \end{aligned} \tag{7.60}$$

The modal parameters, shown in Section 7.6.1, are now in the analytical form.

7.6.3 An example of a 1400-ft riser

The 1400-ft riser in the example of Chapter 4 is employed as an illustration. DVAs are again assumed to be identical and evenly distributed along the beam. The total mass ratio of DVAs is kept constant as before, $N\mu = 0.20$.

(1) Assuming that the riser is under its average tension, $T_{av} = 2.224 \times 10^5$ N, Figure 7-12 shows the frequency response curves of the beam with its first frequency, $\omega_1 = 0.1845$ rad/s, optimally tuned by one, three and five DVAs, respectively. In the case of one DVA ($T_0 = 0.7143$, $\zeta_0 = 0.3273$), the DVA is at the midpoint which corresponds to the antinode of the first mode, hence its effect is the most evident on reducing the

vibration amplitude.

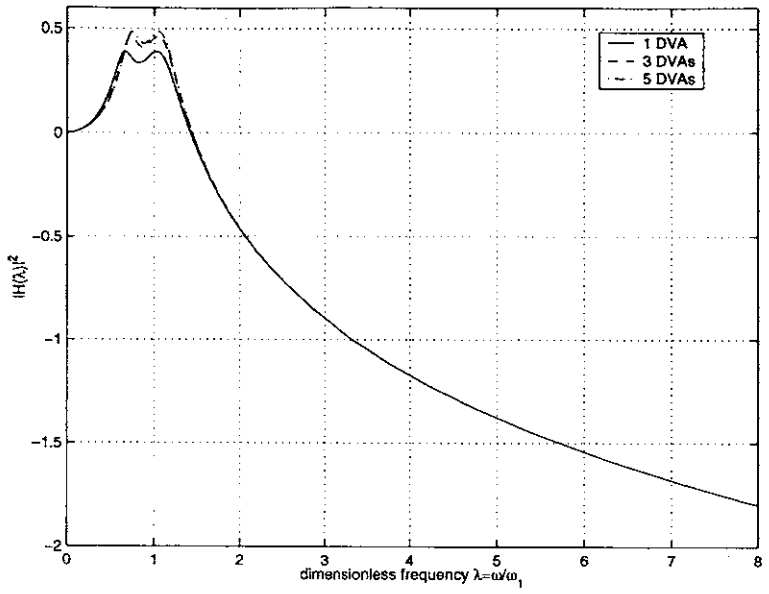

Figure 7-12: Frequency response of a uniform riser with its 1st frequency tuned by multiple DVAs

(2) Now the riser is under linearly varying tension. Figure 7-13 depicts the response of the riser under linearly varying tension with its first natural frequency, $\omega_1 = 0.2816$ rad/s, optimally tuned by one, three and then five DVAs. In the case of one DVA ($T_0 = 0.8333$, $\zeta_0 = 0.2500$), the DVA is at the midpoint, not exactly at antinode but close to the antinode of the first mode. Thus one DVA is the most effective in suppressing the vibration amplitude, compared with the other cases. Figure 7-14 further demonstrates that the frequency response of the beam with its 6th frequency ($\omega_6 = 1.8275$ rad/s) tuned by 7 DVAs optimally and un-optimally.

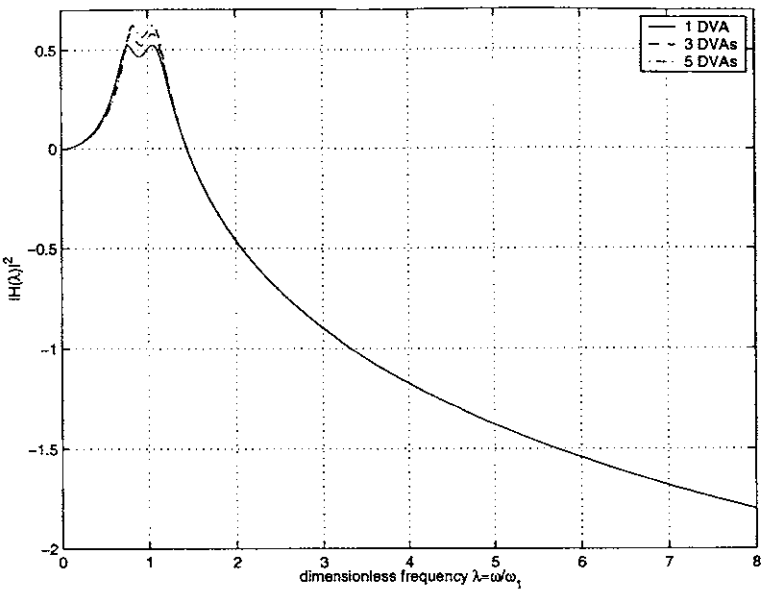

Figure 7-13: Frequency response of a non-uniform riser with its 1st natural frequency tuned by multiple DVAs

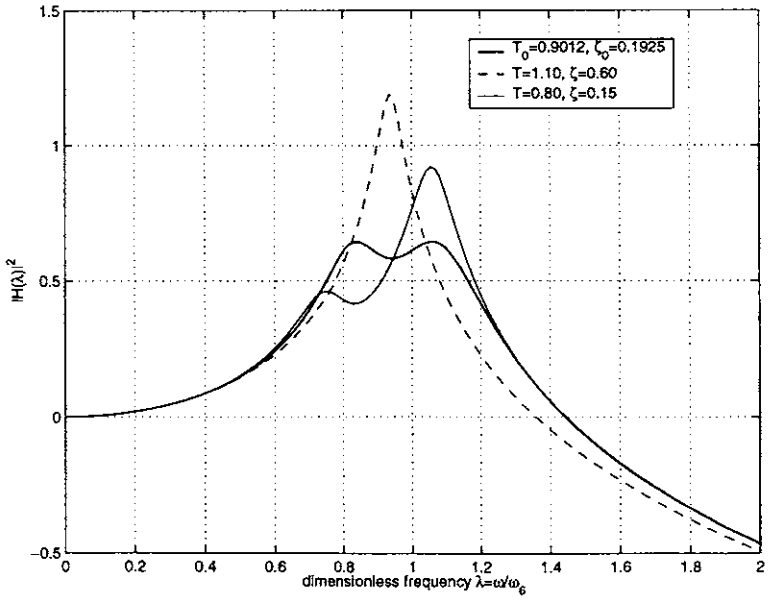

Figure 7-14: Frequency response of a non-uniform riser with its 6th natural frequency tuned by seven DVAs

7.7 Incorporation of structural damping

In the previous sections, structural damping in the beam is neglected. When the primary system has no damping, the optimization procedure is simplified by means of two "fixed points" on the family of frequency response curves. If there is primary damping, the frequency response curves do not possess any "fixed points". In the latter case, Thompson [49] found the optimal solution by means of the frequency locus method; Vandiver and Mitome [50] obtained the result through small changes around the values in an undamped case so that the double response peaks are of equal height. For a lightly damped beam system, it is practical to employ the method by Vandiver and Mitome.

The second example in Section 7.6.3 is further used as an illustration. Assuming that structural damping of the riser is: $\delta = 0.01$, Figure 7-15 shows the response curves of a damped non-uniform beam with its 3rd frequency ($\omega_3 = 0.8624$ rad/s) tuned by three evenly distributed DVAs. The optimal solution for the undamped

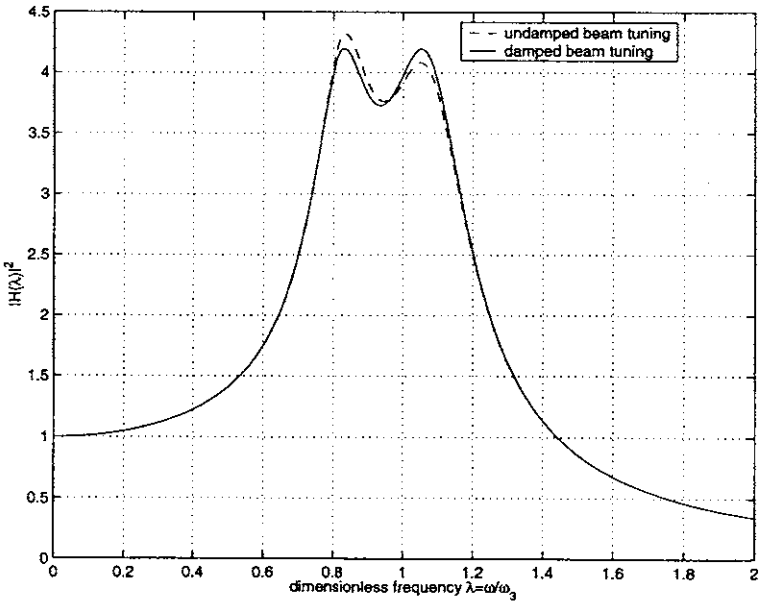

Figure 7-15: Frequency response of a damped non-uniform riser with its 3rd natural frequency tuned by three DVAs

beam is: $T_0 = 0.8975, \zeta_0 = 0.1961$. Using the values as an initial guess, the optimal

result for the damped beam is obtained through a few iterations: $T_0 = 0.8913, \zeta_0 = 0.1941$. The height difference between the two peaks is more sensitive to tuning ratio T than damping ratio ζ. Hence, it is recommended to first adjust tuning ratio so that the two peaks are roughly at the same height, then to slightly change the damping ratio, and re-adjust these values. A few iterations in this procedure will provide a much improved optimal solution.

7.8 Wave-absorbing termination of a beam system

Large amplitude flow-induced vibration of cables and risers is often associated with a phenomenon known as lock-in when a vortex shedding process is synchronized with a natural frequency. Professor Vandiver and Dr. Li [48] presented a wave absorbing termination to suppress cable vibration. The key idea is to design the boundary at the points of termination of a cable so that incident waves are absorbed rather than reflected when they hit the boundary. On the basis of their research, this section derives a wave-absorbing termination for a beam model riser, shown in Figure 7-16.

A wave traveling to the right can be expressed as:

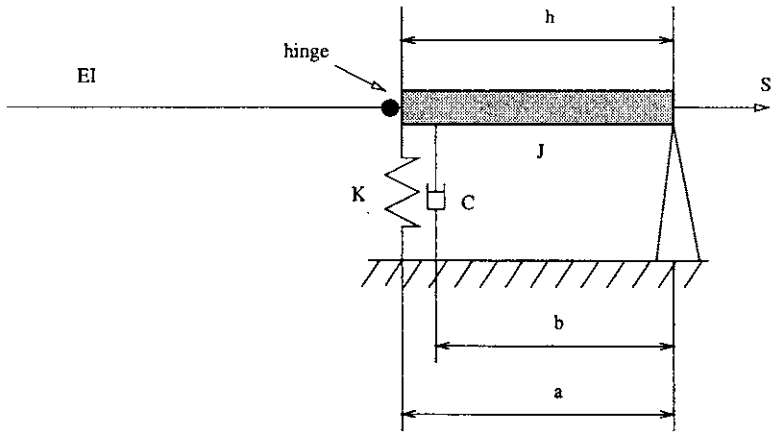

Figure 7-16: A wave absorbing termination

$$y(x,t) = (A_i e^{-ik_1 x} + A_r e^{ik_1 x} + A_r^c e^{k_2 x}) e^{i\omega t}, \tag{7.61}$$

where k_1 is a propagating wave number, and k_2 is an evanescent wave number.

Based on Eq. (7.61), the derivatives of $y(x,t)$ are written as:

$$\begin{aligned}
\frac{\partial y}{\partial x} &= -ik_1 A_i e^{-ik_1 x} + ik_1 A_r e^{ik_1 x} + k_2 A_r^c e^{k_2 x}, \\
\frac{\partial^2 y}{\partial x^2} &= -k_1^2 A_i e^{-ik_1 x} - k_1^2 A_r e^{ik_1 x} + k_2^2 A_r^c e^{k_2 x}, \\
\frac{\partial^3 y}{\partial x^3} &= ik_1^3 A_i e^{-ik_1 x} - ik_1^3 A_r e^{ik_1 x} + k_2^3 A_r^c e^{k_2 x}.
\end{aligned} \tag{7.62}$$

The boundary conditions at $x = l$ are:

$$\begin{aligned}
y(x,t)|_{x=l} &= h\theta, \\
M(x,t)|_{x=l} &= 0, \\
Q(x,t)|_{x=l} &= Q_-,
\end{aligned} \tag{7.63}$$

where $M(x,t)$ is the bending moment, $Q(x,t)$ is the shear force, and Q_- is to be determined by considering the termination device.

The equation of motion of the rigid link is found by Newton's second law:

$$J\ddot{\theta} + C\,b^2\dot{\theta} + (Ka^2 + hS)\theta - Q_- h = 0, \tag{7.64}$$

where J is the mass moment of inertia of the rigid link with respect to the right pinned end, K is the spring constant, C is the damping constant, h is distance between the riser connection point and pivot point, a is the distance from the spring connection to the pivot, b is the distance from the connection of the damper to the pivot, θ is the angle of rotation of the rigid link about the pivot, and S is constant tension to which the beam system is subject.

Based on Eq. (7.64), Q_- is expressed as:

$$Q_- = \frac{J\ddot{\theta} + C\,b^2\dot{\theta} + (Ka^2 + hS)\theta}{h}. \tag{7.65}$$

Using $Q = \frac{\partial M}{\partial x} - S\frac{\partial y}{\partial x}$, and assuming that $\theta = \bar{\theta}e^{i\omega t}$, Eqs. (7.63) and Eq. 7.65 reduce to:

$$\begin{aligned} A_i e^{-ik_1 l} + A_r e^{ik_1 l} + A_r^c e^{k_2 l} &= h\bar{\theta}, \\ -k_1^2 A_i e^{-ik_1 l} - k_1^2 A_r e^{ik_1 l} + k_2^2 A_r^c e^{k_2 l} &= 0, \\ EI(ik_1^3 A_i e^{-ik_1 l} - ik_1^3 A_r e^{ik_1 l} + k_2^3 A_r^c e^{k_2 l}) - S(-ik_1 A_i e^{-ik_1 l} + ik_1 A_r e^{ik_1 l} + k_2 e^{k_2}) &= \\ \frac{-J\omega^2 + iC\,b^2\omega + Ka^2 + hS}{h}\bar{\theta}. \end{aligned} \quad (7.66)$$

The right hand side of the third equation in Eqs. (7.66) is further written as:

$$\begin{aligned} RHS &= \frac{-J\omega^2 + iC\,b^2\omega + Ka^2 + hS}{h^2}(h\bar{\theta}) \\ &= i\omega Z_m(h\bar{\theta}), \end{aligned} \quad (7.67)$$

where the input impedance Z_m of the termination as seen at the connection point of the riser is the same as when connected to a string. As shown in [48], it is:

$$Z_m = \frac{1}{h^2}[C\,b^2 + i\frac{-Sh - Ka^2 + J\omega^2}{\omega}]. \quad (7.68)$$

Combining Eqs. (7.66) with Eq. (7.67) results in:

$$\begin{aligned} -k_1^2 e^{-ik_1 l} - k_1^2 e^{ik_1 l} r + k_2^2 e^{k_2 l} r^c &= 0, \\ (ik_1^3 EI + ik_1 S - i\omega Z_m)e^{-ik_1 l} - (ik_1^3 EI + ik_1 S + i\omega Z_m)e^{ik_1 l} r &+ \\ (k_2^3 EI - k_2 S - i\omega Z_m)e^{k_2 l} r^c &= 0, \end{aligned} \quad (7.69)$$

where the reflection coefficients for propagating and evanescent waves, r and r^c, are defined as:

$$r = \frac{A_r}{A_i}, \qquad r^c = \frac{A_r^c}{A_i}. \quad (7.70)$$

The first equation in Eqs. (7.69) gives:

$$e^{k_2 l} r^c = \frac{k_1^2}{k_2^2}(e^{-ik_1 l} + re^{ik_1 l}). \quad (7.71)$$

Substituting Eq. (7.71) into the third equation in Eqs. (7.69) reduces to:

$$r = \frac{ik_1^3EI + ik_1S - i\omega Z_m + \frac{k_1^2}{k_2^2}(k_2^3EI - k_2S - i\omega Z_m)}{ik_1^3EI + ik_1S + i\omega Z_m - \frac{k_1^2}{k_2^2}(k_2^3EI - k_2S - i\omega Z_m)} e^{-i2k_1l}. \tag{7.72}$$

As in [48], we decompose the input impedance of the device into a real part, R_m, and an imaginary part, X_m, namely:

$$Z_m = R_m + iX_m. \tag{7.73}$$

The numerator in Eq. (7.72) becomes:

$$\begin{aligned} & ik_1^3EI + ik_1S - i\omega Z_m + \frac{k_1^2}{k_2^2}(k_2^3EI - k_2S - i\omega Z_m) \\ = \; & \frac{k_1^2}{k_2^2}(k_2^3EI - k_2S) + (1 + \frac{k_1^2}{k_2^2})\omega X_m + i[k_1^3EI + k_1S - (1 + \frac{k_1^2}{k_2^2})\omega R_m] \\ \equiv \; & \alpha_r + i\alpha_i, \end{aligned} \tag{7.74}$$

where $\alpha_r = \frac{k_1^2}{k_2^2}(k_2^3EI - k_2S) + (1 + \frac{k_1^2}{k_2^2})\omega X_m$, and $\alpha_i = k_1^3EI + k_1S - (1 + \frac{k_1^2}{k_2^2})\omega R_m$.

In order to match the impedance perfectly, one needs:

$$\alpha_r = 0, \qquad \alpha_i = 0. \tag{7.75}$$

The first equation in (7.75) requires:

$$X_m = \frac{k_2S - k_2^3EI}{\Omega(1 + \frac{k_2^2}{k_1^2})|_\Omega}. \tag{7.76}$$

When the device is optimally designed, $\omega = \Omega$.

From the definition of Z_m, we have:

$$X_m = \frac{-hS - Ka^2 + J\omega^2}{\omega h^2}. \tag{7.77}$$

Equalizing the right hand sides of Eqs. (7.76) and (7.77) at $\omega = \Omega$ yields:

$$\Omega = \sqrt{\frac{Ka^2 + hS}{J} + \frac{h^2}{J(1 + k_2^2/k_1^2)}(k_2 S - k_2^3 EI)}. \tag{7.78}$$

The second equation in (7.75) requires:

$$R_m = \frac{1}{1 + k_1^2/k_2^2} \frac{k_1^3 EI + k_1 S}{\Omega}. \tag{7.79}$$

From Eq. (7.68), we have the real part of Z_m: $Re[Z_m] = \frac{C_o b^2}{h^2}$. Equating the two expressions for R_m leads to:

$$C_o = \frac{h^2}{b^2(1 + k_1^2/k_2^2)} \frac{k_1^3 EI + k_1 S}{\Omega}. \tag{7.80}$$

We define the following dimensionless parameters:

dimensionless frequency $\bar{\omega} = \frac{\omega}{\Omega}$;

wave number ratio $k = \frac{k_2}{k_1}$;

tension factor $p = \frac{S}{k_1^2 EI}$; and

impedance ratio $\bar{Z}_m = \frac{Z_m}{k_1^3 EI/\Omega}$.

The tension factor p is a parameter characterizing structural behavior and is the same as defined in SHEAR7. For a constantly tensioned uniform beam, its wave numbers are:

$$\begin{aligned} k_1 &= \sqrt{-\frac{1}{2}\frac{S}{EI} + \sqrt{\frac{1}{4}(\frac{S}{EI})^2 + \omega^2 \frac{\rho A}{EI}}} \qquad \text{(propagating wave)}, \\ k_2 &= \sqrt{\frac{1}{2}\frac{S}{EI} + \sqrt{\frac{1}{4}(\frac{S}{EI})^2 + \omega^2 \frac{\rho A}{EI}}} \qquad \text{(evanescent wave)}. \end{aligned} \tag{7.81}$$

With these dimensionless parameters, the reflection coefficient r is expressed as:

$$\begin{aligned} r &= \frac{1 + p - (1 + 1/k^2)\bar{\omega}\bar{Z}_m - i(k^2 - p)/k}{1 + p + (1 + 1/k^2)\bar{\omega}\bar{Z}_m + i(k^2 - p)/k} e^{-i2k_1 l} \\ &= \{1 - \frac{2[(1 + 1/k^2)\bar{\omega}\bar{Z}_m + i(k^2 - p)/k]}{1 + p + (1 + 1/k^2)\bar{\omega}\bar{Z}_m + i(k^2 - p)/k}\} e^{-i2k_1 l}. \end{aligned} \tag{7.82}$$

When $\bar{\omega} = 1$, the device is operating at the optimum frequency. Hence the input impedance of the termination is chosen as:

$$\begin{aligned} \bar{Z}_{mo} &= \bar{R}_{ro} + i\bar{R}_{io}, \\ \bar{R}_{ro} &= \frac{1+p}{1+1/k^2}\,|_{\bar{\omega}=1}, \\ \bar{R}_{io} &= \frac{kp-k^3}{1+k^2}\,|_{\bar{\omega}=1}\,. \end{aligned} \tag{7.83}$$

The 1400-ft riser is again finally employed as an example. It is assumed to be subject to constant tension equal to the average value, $T_{av} = 2.224 \times 10^5$ N. SHEAR7 found that the 6th frequency is one of the important frequencies. We set optimum frequency $\Omega = \omega_6 = 1.8275$ rad/s for this analysis. The parameters are designed to satisfy Eqs. (7.76), (7.79) and (7.83). Figure 7-17 shows the reflection coefficient modulus at the termination. At $\bar{\omega} = 1$, the reflection coefficient is zero, and hence no energy is reflected. Figure 7-17 also indicates that much energy around $\omega = \Omega$ is absorbed. The effects of the parameters on the bandwidth can be evaluated numerically.

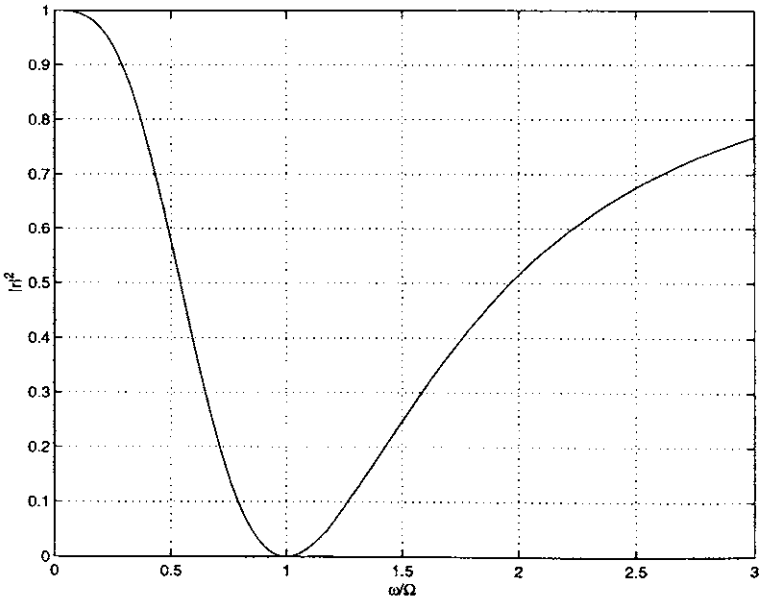

Figure 7-17: Wave reflection coefficient at the termination

Chapter 8

Vibration Analysis of a Coupled Fluid/ Riser System

8.1 Introduction

One of the major components in offshore petroleum production is a production riser. A production riser system often consists of external casing and an internal liner, which are separated by an incompressible viscous fluid. In addition, there may be intermediate guides or supports (centralizers) distributed between the two parallel pipes. The objective of this chapter is to mathematically model this coupled system, to establish the theoretical formulation systematically, to solve for undamped or damped natural frequencies, to investigate effects of coupling factors on forced vibration, and to explore new means of vibration suppression by designing the parameters of coupling components.

A double-uniform beam system coupled by longitudinally distributed springs or an ideal fluid or the combination of both is studied. The beams are assumed to be classical Bernoulli-Euler ones. Approximate closed-form solutions to natural frequencies and mode amplitude ratios are first found for a coupled double-beam system. A beam-type dynamic vibration absorber is presented and an optimal tuning design is found. The similar research is done for the coupled system in which both beams are uniform ones under constant tension. We introduce an additional coupling factor, an

ideal fluid between two beams, for the coupled system. The effects of the fluid on natural frequencies and mode shapes are discussed.

One of the difficulties in vibration analysis of a general coupled fluid/riser system is the mathematical models of the coupling components including viscous fluid and centralizers. The risers are general ones with variable properties and subjected to spatially varying tension. Hydrodynamic forces act on the external riser. It is noted that dynamic stiffness analysis converts the dynamic problem into a pseudo-static one with frequency as a parameter. That is, time no longer appears explicitly but is replaced by phase relationships among all variables. An approximate scheme combining a variational principle with the Ritz method is developed to establish the theoretical formulation systematically. The WKB-based frequency-dependent shape function is employed as a Ritz vector. The implicit expression of dynamic stiffness is found for the complex coupled system. The WKB-based Dynamic Stiffness Method (DSM) with the Wittrick-Williams (W-W) algorithm is extended for the analysis of the coupled system. Natural frequencies and mode shapes are found with good accuracy. Effects of coupling factors, including viscosity of fluid, damping and rigidity of centralizers on forced vibration, are investigated.

8.2 Free vibration of a spring connected double-beam system and optimal design of a dynamic absorbing beam

8.2.1 Analytical solutions

For simplification, the coupled system is assumed to be composed of double uniform Bernoulli-Euler beams. Coupling springs are evenly distributed in the longitudinal direction. Both beams have the same length and are simply supported at their ends. An illustration is shown in Figure 8-2.

Free vibration equations of motion of a spring coupled double-beam system are

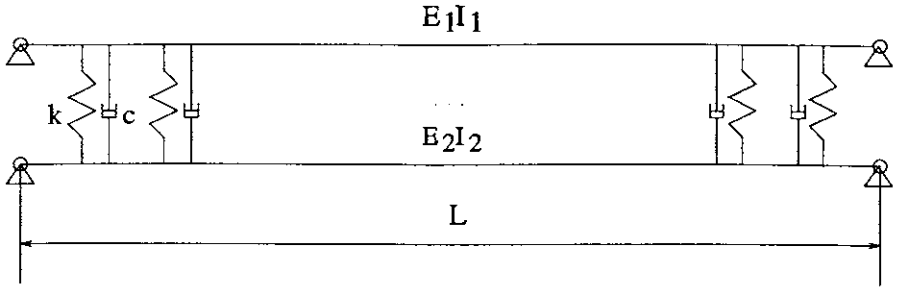

Figure 8-1: A double-beam system coupled by springs and dampers

described by the following equations:

$$E_1 I_1 w_1^{(IV)} + m_1 \ddot{w}_1 + \sum_{m=1}^{M} k[w_1(x) - w_2(x)]\delta(x - x_m) = 0,$$
$$E_2 I_2 w_2^{(IV)} + m_2 \ddot{w}_2 + \sum_{m=1}^{M} k[w_2(x) - w_1(x)]\delta(x - x_m) = 0, \qquad (8.1)$$

where δ is a Dirac delta function, $w_i = w_i(x,t)$ (i=1, 2) is the transverse beam deflection, E_i is the Young's modulus of elasticity, I_i is the moment of inertia, and k is the stiffness of centralizers. Boundary conditions for simply supported beams are:

$$w_i(0,t) = w_i''(0,t) = w_i(l,t) = w_i''(l,t) = 0, \qquad i = 1, 2. \qquad (8.2)$$

The homogeneous partial differential equations (8.1) with boundary conditions (8.2) are solved by assuming the solutions in the form:

$$w_i(x,t) = \sum_{n=1}^{\infty} X_n(x) q_{in}(t), \qquad i = 1, 2, \qquad (8.3)$$

where $q_{in}(t)$ is the unknown time function, and $X_n(x)$ is the mode shape function for a simply supported beam, namely,

$$X_n(x) = \sin(k_n x), \qquad k_n = n\pi/l, \qquad n = 1, 2, 3, ... \qquad (8.4)$$

Substituting Eqs. (8.3) and (8.4) into (8.1), then using orthogonality of the eigen functions, assuming that the system is weakly coupled and natural frequencies are well separated, and neglecting cross terms lead to:

$$\begin{aligned} \ddot{q}_{1n} + (E_1 I_1 k_n^4 + k^*) m_1^{-1} q_{1n} - k^* m_1^{-1} q_{2n} = 0, \\ \ddot{q}_{2n} + (E_2 I_2 k_n^4 + k^*) m_2^{-1} q_{2n} - k^* m_2^{-1} q_{1n} = 0, \end{aligned} \tag{8.5}$$

where

$$k^* = \frac{2k}{l} \sum_{m=1}^{M} \sin^2(\frac{n\pi x_m}{l}),$$

M is the total number of springs.

Equations (8.5) can then be rewritten as:

$$\begin{aligned} \ddot{q}_{1n} + \Omega_{11n}^2 q_{1n} - \Omega_{10}^2 q_{2n} = 0, \\ \ddot{q}_{2n} + \Omega_{22n}^2 q_{2n} - \Omega_{20}^2 q_{1n} = 0, \end{aligned} \tag{8.6}$$

where

$$\Omega_{iin}^2 = (E_i I_i k_n^4 + k^*) m_i^{-1}, \qquad \Omega_{i0}^2 = k^* m_i^{-1}, \qquad (i = 1, 2).$$

The solutions to Eqs. (8.6) are as follows:

$$q_{1n} = C_n e^{i\omega_n t}, \qquad q_{2n} = D_n e^{i\omega_n t}, \qquad i = \sqrt{-1}, \tag{8.7}$$

where ω_n is the natural frequency of the system. Substituting Eqs. (8.7) into (8.6) results in the homogeneous equations for unknown constants C_n and D_n:

$$\begin{aligned} (\Omega_{11n}^2 - \omega_n^2) C_n - \Omega_{10}^2 D_n = 0, \\ (\Omega_{22n}^2 - \omega_n^2) D_n - \Omega_{20}^2 C_n = 0. \end{aligned} \tag{8.8}$$

Eqs. (8.8) have non-trivial solutions when the determinant of the coefficient matrix is equal to zero, namely:

$$\begin{vmatrix} \Omega_{11n}^2 - \omega_n^2 & -\Omega_{10}^2 \\ -\Omega_{20}^2 & \Omega_{22n}^2 - \omega_n^2 \end{vmatrix} = 0. \tag{8.9}$$

Expanding Eq. (8.9) yields the characteristic equation:

$$\omega_n^4 - (\Omega_{11n}^2 + \Omega_{22n}^2)\omega_n^2 + (\Omega_{11n}^2\Omega_{22n}^2 - \Omega_{10}^2\Omega_{20}^2) = 0. \tag{8.10}$$

There are two different, real, and positive roots $\omega_{1,2n}^2$:

$$\omega_{1,2n}^2 = \frac{1}{2}[(\Omega_{11n}^2 + \Omega_{22n}^2) \mp \sqrt{(\Omega_{11n}^2 - \Omega_{22n}^2) + 4\Omega_{10}^2\Omega_{20}^2}], \qquad \omega_{1n} < \omega_{2n}. \tag{8.11}$$

The solution to Eq. (8.7) can be written as:

$$\begin{aligned} q_{1n} &= C_{1n}e^{i\omega_{1n}t} + C_{2n}e^{-i\omega_{1n}t} + C_{3n}e^{i\omega_{2n}t} + C_{4n}e^{-i\omega_{2n}t}, \\ q_{2n} &= D_{1n}e^{i\omega_{1n}t} + D_{2n}e^{-i\omega_{1n}t} + D_{3n}e^{i\omega_{2n}t} + D_{4n}e^{-i\omega_{2n}t}. \end{aligned} \tag{8.12}$$

Introducing trigonometric functions, Eqs. (8.12) are rewritten as:

$$\begin{aligned} q_{1n} &= \sum_{i=1}^{2}[A_{in}\sin(\omega_{in}t) + B_{in}\cos(\omega_{in}t)], \\ q_{2n} &= \sum_{i=1}^{2}[A_{in}\sin(\omega_{in}t) + B_{in}\cos(\omega_{in}t)]a_{in}, \end{aligned} \tag{8.13}$$

where

$$a_{1,2n} = 0.5\Omega_{10}^{-2}[(\Omega_{11n}^2 - \Omega_{22n}^2) \pm \sqrt{(\Omega_{11n}^2 - \Omega_{22n}^2)^2 + 4\Omega_{10}^2\Omega_{20}^2}]. \tag{8.14}$$

It can be found from this equation that the coefficient a_{1n} is dependent on the lower natural frequency ω_{1n} and is always positive, while a_{2n} is dependent on the higher frequency ω_{2n} and is always negative. The ω_{1n} and ω_{2n} ($\omega_{1n} < \omega_{2n}$) are two infinite sequences of natural frequencies of the coupled system. As shown by Oniszczuk [51, 52, 53] for a continuously and elastically coupled system, the natural mode shapes

of the coupled beam corresponding to two sequences of natural frequencies ω_{in} are:

$$X_{1in} = \sin(k_n x), \qquad X_{2in} = a_{in} \sin(k_n x). \tag{8.15}$$

A spring connected simply-supported double-beam system has two kinds of mode shapes. One is synchronous ($a_{1n} > 0$) with lower natural frequencies ω_{1n} and the other is asynchronous ($a_{2n} < 0$) with higher natural frequencies ω_{2n}.

8.2.2 Optimal design of a dynamic absorbing beam

Now considering dampers located with the springs, the equations of motion of the coupled system are written as:

$$\begin{aligned} E_1 I_1 w_1^{(IV)} + m_1 \ddot{w}_1 + \sum_{m=1}^{M} k[w_1(x) - w_2(x)]\delta(x - x_m) + \sum_{m=1}^{M} c[\dot{w}_1(x) - \dot{w}_2(x)]\delta(x - x_m) &= \\ p e^{i\omega t}\delta(x - a), & \\ E_2 I_2 w_2^{(IV)} + m_2 \ddot{w}_2 + \sum_{m=1}^{M} k[w_2(x) - w_1(x)]\delta(x - x_m) + \sum_{m=1}^{M} c[\dot{w}_2(x) - \dot{w}_1(x)]\delta(x - x_m) &= \\ 0, & \end{aligned} \tag{8.16}$$

where $pe^{i\omega t}$ is a concentrated harmonic force acting on Beam 1, and a is the distance of the exciting force measured from the left end.

Following the same procedure as in obtaining Eqs. (8.5), we obtain the following equations:

$$\begin{aligned} m_1 \ddot{q}_{1n} + (E_1 I_1 k_n^4 + k^*) q_{1n} - k^* q_{2n} + c^*(\dot{q}_{1n} - \dot{q}_{2n}) = 0, \\ m_2 \ddot{q}_{2n} + (E_2 I_2 k_n^4 + k^*) q_{2n} - k^* q_{1n} + c^*(\dot{q}_{2n} - \dot{q}_{1n}) = 0, \end{aligned} \tag{8.17}$$

where $c^* = \frac{2k}{l} \sum_{m=1}^{M} \sin^2(\frac{n\pi x_m}{l})$. Equations (8.17) represent a two-degree-of-freedom system with two masses and three springs, as shown in Figure 8-2 with: $k_1 = E_1 I_1 k_n^4$, $k_2 = k^*$, $k_3 = E_2 I_2 k_n^4$, $c_2 = c^*$.

Using the Den Hartog method, Aida, et al [54] obtained an optimal solution to the case in Figure 8-2. Applying this solution, the procedure of optimal design of a

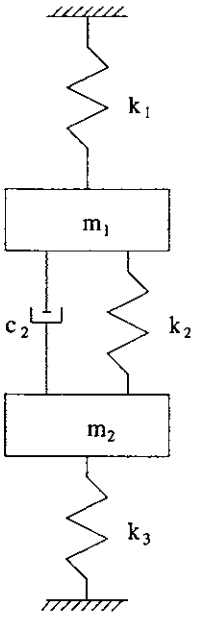

Figure 8-2: Two-degrees-of-freedom system for nth mode

dynamic absorbing beam in this problem is depicted as follows:

1. The mass ratio $\mu = \frac{m_2}{m_1}$ is set at the beginning.

2. The non-dimensional amplitude of a fixed point on the resonance curve of Beam 1, Y_{1p}, is calculated from

$$Y_{1p} = \frac{\sqrt{\frac{2+\mu}{\mu}}}{1 - \frac{E_2 I_2}{E_1 I_1 \mu}}, \tag{8.18}$$

which requires $E_2 I_2 < \mu E_1 I_1$.

3. The equivalent spring constant k^* and damper c^* are given as follows:

$$k^* = E_1 I_1 k_n^4 \frac{\sqrt{\mu(2+\mu)}}{(1+\mu)^2 Y_{1p}}, \tag{8.19}$$

$$c^* = 2\mu\sqrt{m_1 h^2 E_1 I_1 k_n^4}, \tag{8.20}$$

in which

$$h^2 = \frac{h_P^2 + h_Q^2}{2}, \tag{8.21}$$

and

$$\begin{pmatrix} h_P^2 \\ h_Q^2 \end{pmatrix} = \frac{(2+2\mu) \mp 2\sqrt{\mu(2+\mu)}}{4(1+\mu)^3 Y_{1P}[(1+\mu)Y_{1P} - \sqrt{\mu(2+\mu)} \mp 1]}. \tag{8.22}$$

8.2.3 An example: A coupled double-axial cylinder system

The specifications of a spring coupled double - riser system, where tension is neglected, are as follow:

Length $l = 1944$ ft;

Young's modulus $E = 30000$ Ksi;

Mass per unit length of external pipe (added mass of external fluid included with $C_a = 1.0$) $m_1 = 169.2134$ kg/m;

Outer diameter of external pipe $d_{1o} = 13.375$ inches;

Inner diameter of external pipe $d_{1i} = 12.615$ inches;

Area moment of inertia of external pipe $I_1 = 1.3642 \times 10^{-4}\ m^4$;

Mass per length of inner pipe (inside water included) $m_2 = 87.2117$ kg/m;

Outer diameter of inner pipe $d_{2o} = 9.75$ inches;

Inner diameter of inner pipe $d_{2i} = 9.155$ inches;

Area moment of inertia of inner pipe $I_2 = 4.1110 \times 10^{-5}\ m^4$;

spring stiffness ratio $r_{sp} = 1.0$, which is defined as

$$r_{sp} = \frac{k}{EI_2/L^3}, \tag{8.23}$$

where L is spring spacing.

There are 19 connecting springs evenly and longitudinally distributed. Tables 8.1 and 8.2 respectively shows that natural frequencies, obtained by means of Eq. (8.11), of synchronous and asynchronous vibrations. In order to verify the solutions, the WKB-based dynamic stiffness method with the W-W algorithm (error requirement 1.0×10^{-3}) is employed for analyzing the elastically coupled system and the results are included in the tables for comparison. Both Tables 8.1 and 8.2 indicate that solutions by Eq. (8.11) are accurate.

Order	by Eq. (8.11)	WKB-DSM
1	0.0017	0.0017
2	0.0068	0.0068
3	0.0152	0.0151
4	0.0270	0.0270
5	0.0419	0.0419
6	0.0596	0.0596
7	0.0795	0.0794
8	0.1009	0.1009
9	0.1240	0.1238
10	0.1494	0.1494

Table 8.1: Comparison of natural frequencies f_{1n} (Hz) of synchronous vibrations

Order	by Eq. (8.11)	WKB-DSM
1	0.0697	0.0696
2	0.0700	0.0698
3	0.0711	0.0709
4	0.0741	0.0740
5	0.0801	0.0800
6	0.0903	0.0902
7	0.1060	0.1060
8	0.1279	0.1278
9	0.1556	0.1555
10	0.1883	0.1883

Table 8.2: Comparison of natural frequencies f_{2n} (Hz) of asynchronous vibrations

Effects of spring stiffness on natural frequencies are studied by varying the stiffness ratio. Spring stiffness ratios are set to be 1 and then 10. Figure 8-3 depicts the results of synchronous and asynchronous natural frequencies, which correspond to in-phase and out-of phase mode shapes, respectively.

Figure 8-3 shows that there is a general tendency to increase natural frequencies

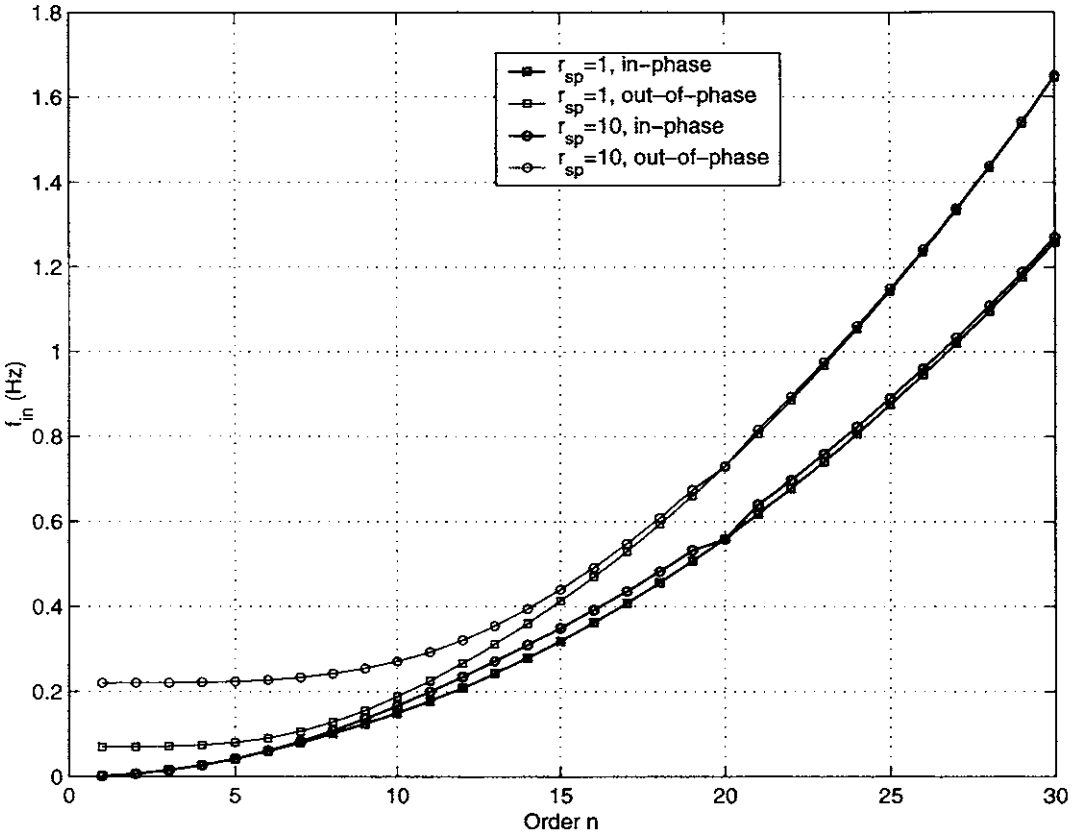

Figure 8-3: Effects of spring stiffness on synchronous and asynchronous natural frequencies

f_{in} with the spring stiffness ratio. The increase for lower asynchronous natural frequencies is greater than for higher ones. The effect of spring stiffness on much higher asynchronous natural frequencies is insignificant. The increase for lower asynchronous natural frequencies is much higher than for lower synchronous natural frequencies. Spring stiffness has almost no effect on much lower synchronous natural frequencies. In addition, for a specific mode where all spring connecting points happen to be its

nodes, spring stiffness then has no effect on the natural frequencies at all. In this example, this specific mode number is 20.

Finally, design an optimal tuning to the 15th mode of Beam 1. Optimal parameters were obtained as: $k^* = 105.2213$, and $c^* = 38.6914$. The unit concentrated harmonic force is acting on $l/4$ away from the left end. Figure 8-4 depicts the numerical results by optimal and un-optimal tunings (by running Matlab code coupfb32c.m), where ω_1 is the 1st circular frequency of Beam 1 (0.0115 rad/s). This figure indicates the benefit of an optimally tuned dynamic absorbing beam (Beam 2).

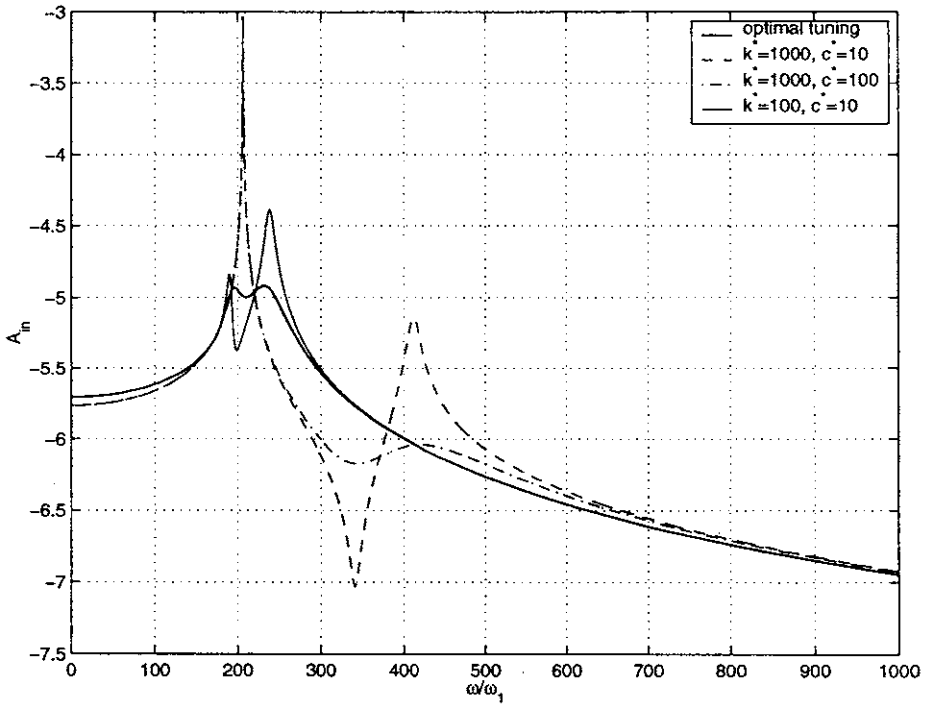

Figure 8-4: Frequency response of the 15th mode due to a concentrated force

8.3 Free vibration of a spring-coupled tensioned beam system and optimal design of a dynamic absorbing beam

8.3.1 Analytical solutions

Both beams in the coupled system discussed in Section 8.2 are now assumed to be subject to constant tension. Other assumptions are the same as previously.

Free vibration equations of motion of a spring-coupled constantly tensioned beam system are described by the following equations:

$$\begin{aligned} E_1 I_1 w_1^{(IV)} + m_1 \ddot{w}_1 - T_1 w_1'' + \sum_{m=1}^{M} k[w_1(x) - w_2(x)]\delta(x - x_m) = 0, \\ E_2 I_2 w_2^{(IV)} + m_2 \ddot{w}_2 - T_2 w_2'' + \sum_{m=1}^{M} k[w_2(x) - w_1(x)]\delta(x - x_m) = 0, \end{aligned} \tag{8.24}$$

where $T_i (i = 1, 2)$ is the constant tension in each beam.

Following the same procedure as in Section 8.2.1, one obtains the following equations:

$$\begin{aligned} \ddot{q}_{1n} + (E_1 I_1 k_n^4 + T_1 k_n^2 + k^*) m_1^{-1} q_{1n} - k^* m_1^{-1} q_{2n} = 0, \\ \ddot{q}_{2n} + (E_2 I_2 k_n^4 + T_2 k_n^2 + k^*) m_2^{-1} q_{2n} - k^* m_2^{-1} q_{1n} = 0. \end{aligned} \tag{8.25}$$

Equations (8.25) can then be rewritten as:

$$\begin{aligned} \ddot{q}_{1n} + \Omega_{11n}^2 q_{1n} - \Omega_{10}^2 q_{2n} = 0, \\ \ddot{q}_{2n} + \Omega_{22n}^2 q_{2n} - \Omega_{20}^2 q_{1n} = 0, \end{aligned} \tag{8.26}$$

where $\Omega_{iin}, (i = 1, 2)$ is defined differently from in Section 8.2.1 as:

$$\Omega_{iin}^2 = (E_i I_i k_n^4 + T_i k_n^2 + k^*) m_i^{-1}. \tag{8.27}$$

With this new definition of Ω_{iin}, natural frequencies and mode ratios have identical formulas to Eqs. (8.11) and (8.14).

8.3.2 Optimal design of a dynamic absorbing beam

Now including damping of spacers, the equations of motion of the coupled system are written as

$$\begin{aligned} E_1 I_1 w_1^{(IV)} + m_1 \ddot{w}_1 - T_1 w_1'' + \sum_{m=1}^{M} k[w_1(x) - w_2(x)]\delta(x - x_m) \\ + \sum_{m=1}^{M} c[\dot{w}_1(x) - \dot{w}_2(x)]\delta(x - x_m) &= e^{i\omega t}\delta(x - a), \\ E_2 I_2 w_2^{(IV)} + m_2 \ddot{w}_2 - T_2 w_2'' + \sum_{m=1}^{M} k[w_2(x) - w_1(x)]\delta(x - x_m) \\ + \sum_{m=1}^{M} c[\dot{w}_2(x) - \dot{w}_1(x)]\delta(x - x_m) &= 0. \end{aligned} \tag{8.28}$$

Again, Eqs. (8.28) represent a two-degree-of-freedom system with two masses and three springs. Now re-define k_1 and k_3 as follows:

$$k_1 = E_1 I_1 k_n^4 + T_1 k_n^2, \qquad k_3 = E_2 I_2 k_n^4 + T_2 k_n^2. \tag{8.29}$$

With the new definitions of k_1 and k_3, the optimal tuning procedure is same as in Section 8.2.2.

8.3.3 An example: A coupled constantly tensioned beam system

On the basis of the example in Section 8.2.3, the beams are now assumed to be subjected to constant tension, which is chosen to be the average values, $T_1 = 3.1442 \times 10^5$ N, $T_2 = 1.7692 \times 10^5$ N, respectively. Assuming $r_{sp} = 0.10$, Tables 8.3 and 8.4 show natural frequencies of synchronous and asynchronous vibrations (obtained by running coupfb32b1.m) and include the results found by the WKB-based DSM with the W-W algorithm. Both tables demonstrate that values, obtained by (8.11) with

the new definition of Ω_{iin} $(i = 1, 2)$, are accurate. Figure 8-5 demonstrates optimal tuning to the 15th mode of Beam 1. Optimal values of parameters are $k^* = 64.2742$ N/m, $c^* = 13.7205$ N.s/m. This figure indicates the benefit of using Beam 2 as an optimally tuned dynamic absorbing beam.

Order	analy. solution	WKB-DSM
1	0.0369	0.0369
2	0.0737	0.0737
3	0.1109	0.1109
4	0.1489	0.1489
5	0.1879	0.1878
6	0.2283	0.2282
7	0.2702	0.2701
8	0.3138	0.3137
9	0.3594	0.3594
10	0.4053	0.4052

Table 8.3: Comparison of natural frequencies f_{1n} (Hz) of synchronous vibrations

Order	analy. solution	WKB-DSM
1	0.0436	0.0435
2	0.0788	0.0788
3	0.1163	0.1163
4	0.1548	0.1548
5	0.1941	0.1941
6	0.2342	0.2342
7	0.2753	0.2754
8	0.3175	0.3174
9	0.3608	0.3608
10	0.4073	0.4073

Table 8.4: Comparison of natural frequencies f_{2n} (Hz) of asynchronous vibrations

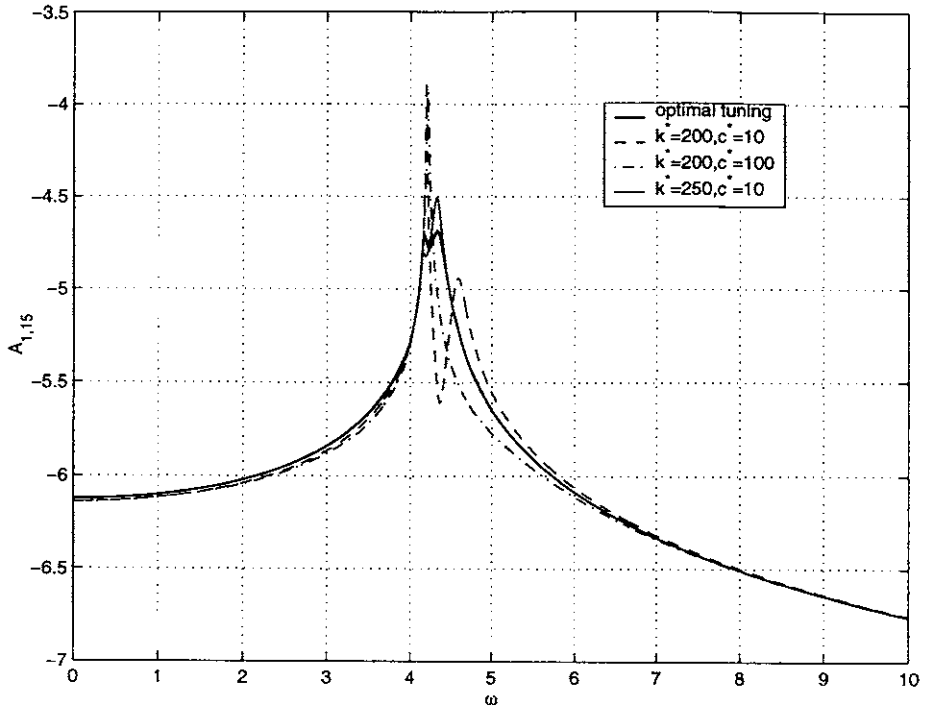

Figure 8-5: Frequency response of the 15th mode due to a concentrated force

8.4 Free vibration of a constantly tensioned beam system coupled by an ideal fluid and springs

8.4.1 Analytical solutions

Consider a coupled fluid/riser system which consists of an external cylinder and internal one located concentrically and connected by evenly distributed springs. The annular region is filled with an ideal fluid (incompressible and frictionless). The beam-like vibration is studied. Two cylinders are modeled as Euler-Bernoulli beams subjected to constant tension. The equations of motion of the coupled system are:

$$\begin{aligned} E_1 I_1 w_1^{(IV)} + (m_1 + m_{11})\ddot{w}_1 - T_1 w_1'' + \sum_{m=1}^{M} k[w_1(x) - w_2(x)]\delta(x - x_m) & \\ +m_{12}\ddot{w}_2 &= 0, \\ E_2 I_2 w_2^{(IV)} + (m_2 + m_{22})\ddot{w}_2 - T_2 w_2'' + \sum_{m=1}^{M} k[w_2(x) - w_1(x)]\delta(x - x_m) & \\ +m_{21}\ddot{w}_1 &= 0, \end{aligned} \quad (8.30)$$

where $m_{il}(i,l=1,2)$ is added mass, which is indicated in Section 8.5.1.

Following the same procedure as in Section 8.2.1 and noting that $m_{12}=m_{21}$, the homogeneous algebraic equations for the unknown constants C_n and D_n are yielded as:

$$\begin{aligned}(k_1k_n^4+T_1k_n^2+k^*-\bar{m}_1\omega_n^2)C_n-(k^*+m_{12}\omega_n^2)D_n &= 0,\\ (k_2k_n^4+T_2k_n^2+k^*-\bar{m}_2\omega_n^2)D_n-(k^*+m_{21}\omega_n^2)C_n &= 0,\end{aligned} \tag{8.31}$$

where the $\bar{m}_1$ and $\bar{m}_2$ are defined as: $\bar{m}_1\equiv m_1+m_{11}$, $\bar{m}_2\equiv m_2+m_{22}$.

Equations (8.31) have non-trivial solutions when the determinant of the coefficient matrix is equal to zero. The frequency (characteristic) equation is obtained as:

$$\begin{aligned}(\bar{m}_1\bar{m}_2-m_{12}^2)\omega_n^4-\omega_n^2[\bar{m}_1(k_2k_n^4+T_2k_n^2+k^*)+\bar{m}_2(k_1k_n^4+T_1k_n^2+k^*)\\ +2m_{12}k^*]+(k_1k_n^4+T_1k_n^2+k^*)(k_2k_n^4+T_2k_n^2+k^*)-(k^*)^2=0.\end{aligned} \tag{8.32}$$

Define the coefficients in this equation as follows:

$$A \equiv \bar{m}_1\bar{m}_2-m_{12}^2, \tag{8.33}$$

$$B \equiv \bar{m}_1(k_2k_n^4+T_2k_n^2+k^*)+\bar{m}_2(k_1k_n^4+T_1k_n^2+k^*)+2m_{12}k^*, \tag{8.34}$$

$$C \equiv (k_1k_n^4+T_1k_n^2+k^*)(k_2k_n^4+T_2k_n^2+k^*)-(k^*)^2. \tag{8.35}$$

Then natural frequencies are:

$$\omega_{in}^2=\frac{B\mp\sqrt{B^2-4AC}}{2A},\qquad (i=1,2), \tag{8.36}$$

where $\omega_{1n}^2<\omega_{2n}^2$.

The mode ratio a_{in} is:

$$a_{in}=\frac{k_1k_n^4+T_1k_n^2+k^*-\bar{m}_1\omega_{in}^2}{k^*+m_{12}\omega_{in}^2}=\frac{k^*+m_{21}\omega_{in}^2}{k_2k_n^4+T_2k_n^2+k^*-\bar{m}_2\omega_{in}^2}. \tag{8.37}$$

In the un-coupled vibrations, one of the cylinders is rigid. The un-coupled natural frequency, $\bar{\omega}_{in}^2$, is

$$\bar{\omega}_{in}^2 = \frac{k_i k_n^4 + T_i k_n^2 + k^*}{\bar{m}_i}, \qquad (i = 1, 2). \tag{8.38}$$

It can also be shown that $\omega_{1n}^2 < \bar{\omega}_{1n}^2 < \bar{\omega}_{2n}^2 < \omega_{2n}^2$ (cf. Chen 1978 [55]).

With the definition of un-coupled natural frequencies in Eq. (8.38), Eq. (8.37) is further rewritten as

$$a_{in} = \frac{\bar{m}_1(\bar{\omega}_{1n}^2 - \omega_{in}^2)}{k^* + m_{12}\omega_{in}^2} = \frac{k^* + m_{21}\omega_{in}^2}{\bar{m}_2(\bar{\omega}_{2n}^2 - \omega_{in}^2)}. \tag{8.39}$$

The following three cases, based on Eq. (8.39), are investigated:

Case 1: only coupled by springs

Without fluid, then $m_{12} = m_{21} = 0$, $\bar{m}_1 = m_1$, and $\bar{m}_2 = m_2$. Eq. (8.39) reduces to:

$$a_{in} = \frac{m_1(\bar{\omega}_{1n}^2 - \omega_{in}^2)}{k^*} = \frac{k^*}{m_2(\bar{\omega}_{2n}^2 - \omega_{in}^2)}. \tag{8.40}$$

As discussed in Section 8.2.1, Eq. (8.40) shows that a_{1n}, corresponding to ω_{1n}, is positive, while a_{2n}, corresponding to ω_{2n}, is negative.

Case 2: only coupled by ideal fluid

Without springs, i.e., $k^* = 0$, then Eq. (8.39) is rewritten as:

$$a_{in} = \frac{\bar{m}_1(\bar{\omega}_{1n}^2 - \omega_{in}^2)}{m_{12}\omega_{in}^2} = \frac{m_{21}\omega_{in}^2}{\bar{m}_2(\bar{\omega}_{2n}^2 - \omega_{in}^2)}. \tag{8.41}$$

Noting that $m_{12} = m_{21} < 0$, Eq. (8.41) shows that a_{1n}, corresponding to ω_{1n}, is negative, while a_{2n}, corresponding to ω_{2n}, is positive. This result is opposite to that in Case 1.

Case 3: coupled by springs and ideal fluid

Whether mode shapes are in-phase and out-of-phase depends on the sign of a_{in}, which is expressed in Eq. (8.39). It is known that $(\bar{\omega}_{2n}^2 - \omega_{1n}^2) > 0$ and $(\bar{\omega}_{2n}^2 - \omega_{2n}^2) < 0$. The sign of $(k^* + m_{12}\omega_{in}^2)$ finally determines that of a_{in}. The sign of $(k^* + m_{12}\omega_{in}^2)$ is employed to predict when the phenomenon occurs that some of out-of-phase modes

disappear while some additional in-phase modes appear.

8.4.2 An example: a constantly tensioned beam system coupled by an ideal fluid and springs

The specifications of both beams are identical to those in the example in Section 8.3.3. Mass density of fluid is $\rho_w = 1000\, kg/m^3$.

Case 1: Only coupled by springs ($r_{sp} = 1.0$)

Table 8.5 shows natural frequencies of asynchronous and synchronous vibrations of the coupled system.

Figure 8-6 depicts the corresponding first four in-phase and out-of-phase mode

Order	asynchronous	synchronous
1	0.0791	0.0370
2	0.1026	0.0741
3	0.1331	0.1117
4	0.1674	0.1499
5	0.2040	0.1890
6	0.2424	0.2293
7	0.2823	0.2711
8	0.3237	0.3145
9	0.3667	0.3596
10	0.4118	0.4061

Table 8.5: Comparison of natural frequencies(Hz) of asynchronous and synchronous vibrations (Case 1)

shapes. The characteristic vibrations of the elastically coupled system are either synchronous or asynchronous. Table 8.5 indicate that the first mode corresponding to the lowest natural frequency is synchronous. Compared with Tables 8.3 and 8.4, Table 8.5 demonstrate that with the stiffness ratio of the springs, the natural frequencies increase, as shown in Figure 8-3. With the stiffness ratio, the coupling between the two beams becomes stronger.

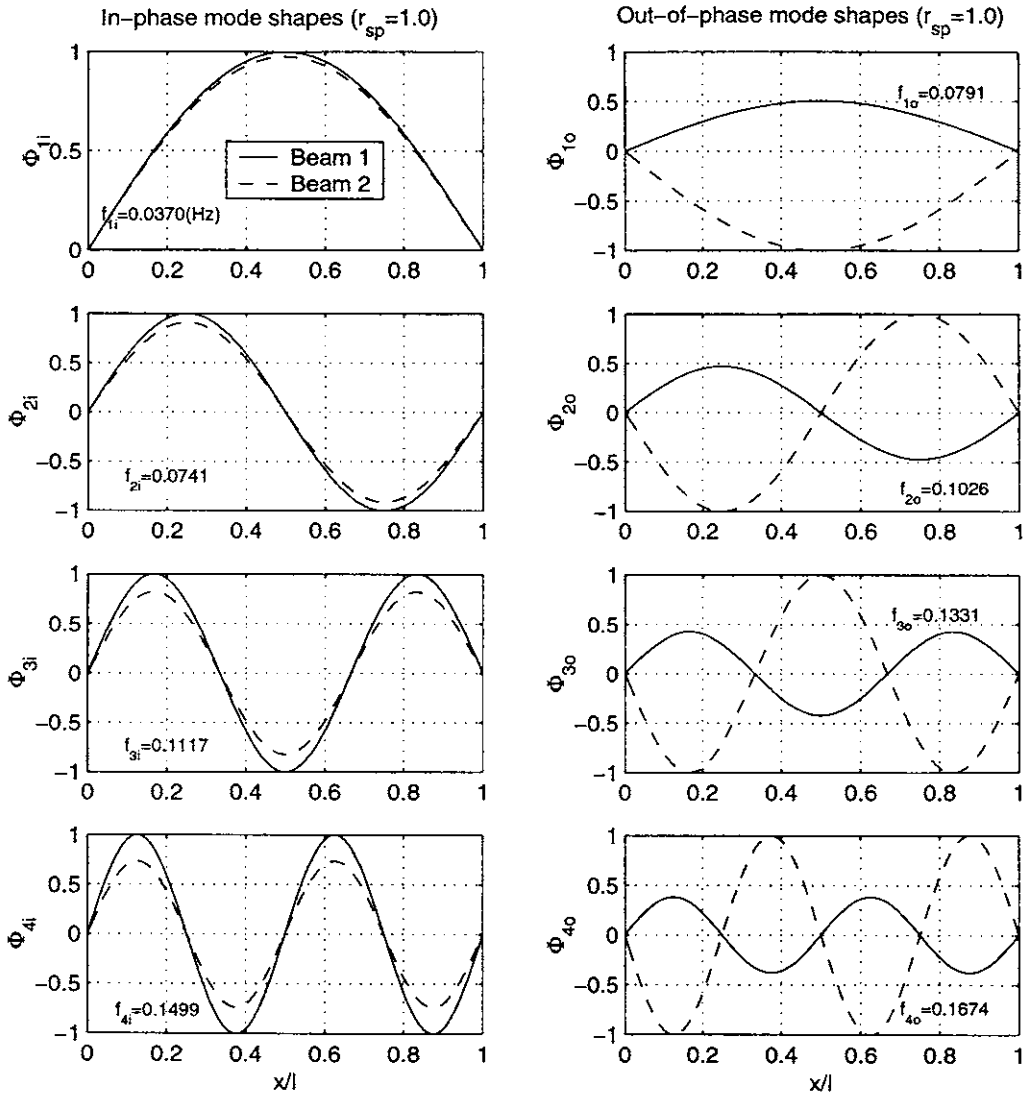

Figure 8-6: The first four synchronous and asynchronous mode shapes (Case 1)

Case 2: Only coupled by fluid ($r_{sp} = 0$)

Table 8.6 shows natural frequencies of asynchronous and synchronous vibrations of the coupled system.

Order	asynchronous	synchronous
1	0.0157	0.0358
2	0.0315	0.0719
3	0.0474	0.1084
4	0.0636	0.1457
5	0.0801	0.1838
6	0.0969	0.2231
7	0.1142	0.2638
8	0.1319	0.3060
9	0.1503	0.3499
10	0.1692	0.3957

Table 8.6: Comparison of natural frequencies(Hz) of asynchronous and synchronous vibrations (Case 2)

Figure 8-7 demonstrates the corresponding first four in-phase and out-of-phase mode shapes. The fluid introduces the coupling between the two beams and reduces the natural frequencies because of the added mass. As predicted in Section 8.4.1, the coupled system has in-phase and out-of-phase characteristic vibrations. When the two beams are out of phase, the fluid in between is displaced and thus the fluid's inertia effect is large. When the two beams are in phase, the effect of the coupling fluid's inertia is reduced. hence, out-of-phase mode shapes are beneficial in suppressing vibration. Table 8.6 in this case indicates that the first mode shape is asynchronous.

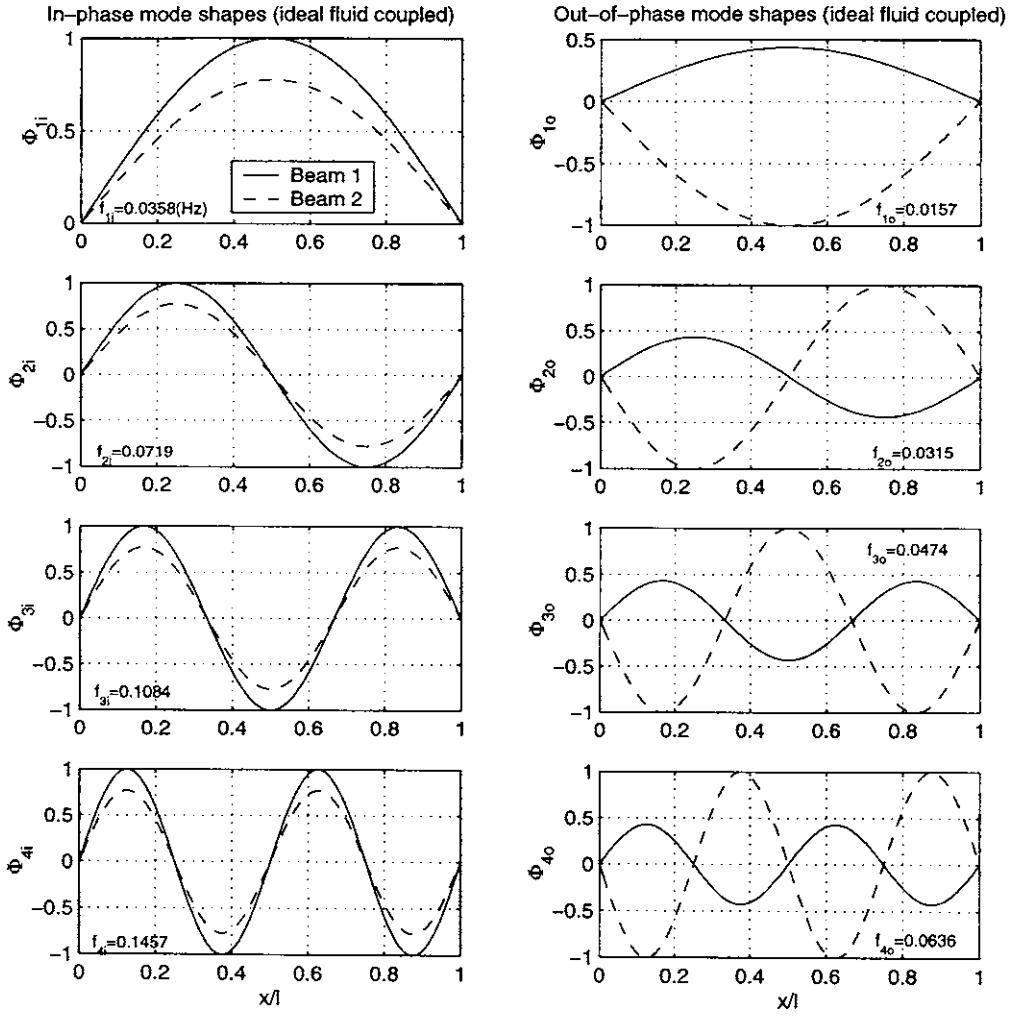

Figure 8-7: The first four synchronous and asynchronous mode shapes (Case 2)

Case 3: Coupled by the fluid and springs ($r_{sp} = 1.0$)

Tables 8.7 and 8.8 show respectively natural frequencies f_{1n} and f_{2n} found by means of (8.36). The results obtained by the WKB-based dynamic stiffness method are also included for comparison. The two tables indicate that solutions by Eq. (8.36) are accurate. Compared with Table 8.5, Both tables indicate that the natural frequencies are lowered due to the fluid.

Figures 8-8 and 8-9 depict the first four in-phase and out-of-phase mode shapes

Order	analy. solution	WKB-DSM
1	0.0309	0.0309
2	0.0426	0.0426
3	0.0555	0.0555
4	0.0699	0.0699
5	0.0851	0.0855
6	0.1011	0.1016
7	0.1178	0.1187
8	0.1351	0.1362
9	0.1530	0.1549
10	0.1716	0.1742

Table 8.7: Comparison of natural frequencies f_{1n} (Hz)

Order	analy. solution	WKB-DSM
1	0.0384	0.0384
2	0.0724	0.0724
3	0.1087	0.1086
4	0.1459	0.1459
5	0.1840	0.1840
6	0.2233	0.2233
7	0.2639	0.2639
8	0.3061	0.3061
9	0.3500	0.3500
10	0.3958	0.3958

Table 8.8: Comparison of natural frequencies f_{2n} (Hz)

obtained by the WKB-based dynamic stiffness method and analytical solutions, re-

spectively. In these figures, subscripts "i" and "o" denote in-phase and out-of-phase modes, respectively. It is found that the first out-of-phase mode in Figures 8-6 and 8-7 disappears while an additional first in-phase mode occurs. This phenomenon can also be observed from the coefficients of natural mode shapes a_{in} shown in Table 8.9. The signs of a_{1n} and a_{2n} are opposite. When the phenomenon occurs, a_{1n} and a_{2n} have the same sign and are both positive in this case.

It is further found by checking the sign of $(k^* + m_{12}\omega_{in}^2)$ that this phenomenon doesn't occur until $r_{sp} \geq 0.65$. When $r_{sp} = 10$, the original 3rd out-of-phase mode disappears while an additional in-phase mode appears, shown in Figure 8-10. The corresponding coefficients of natural frequencies a_{in} are depicted in Table 8.10.

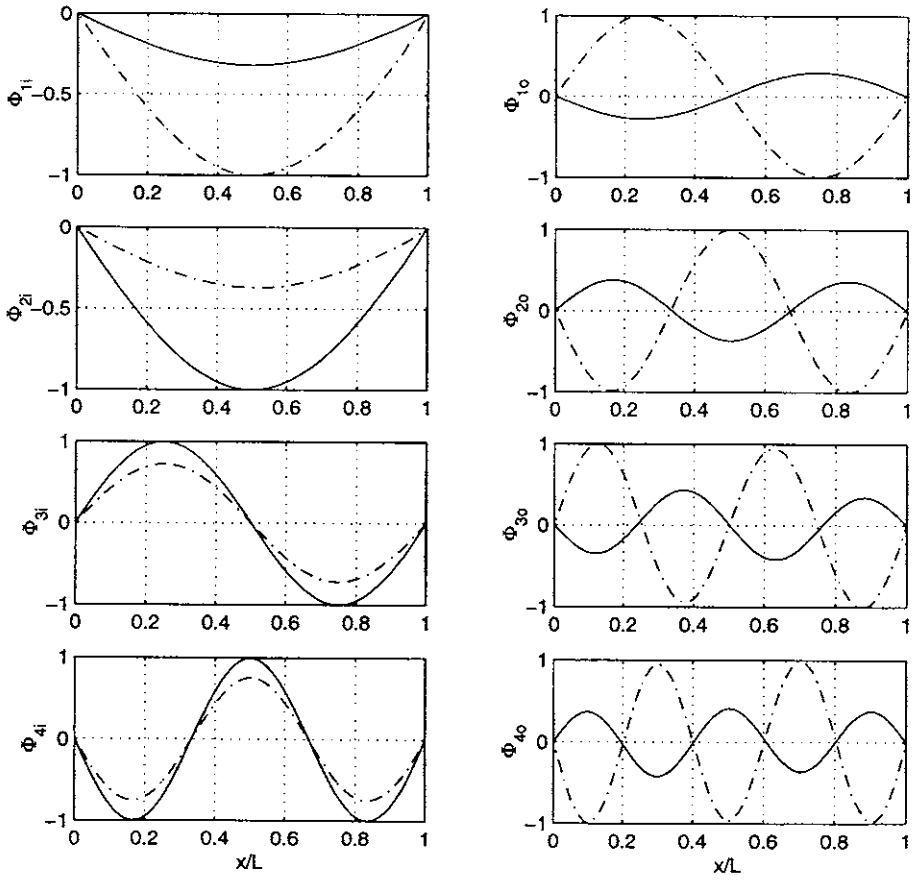

Figure 8-8: First four synchronous and asynchronous mode shapes by the WKB-DSSM (solid line: Beam 1; dash-dot line: Beam 2)

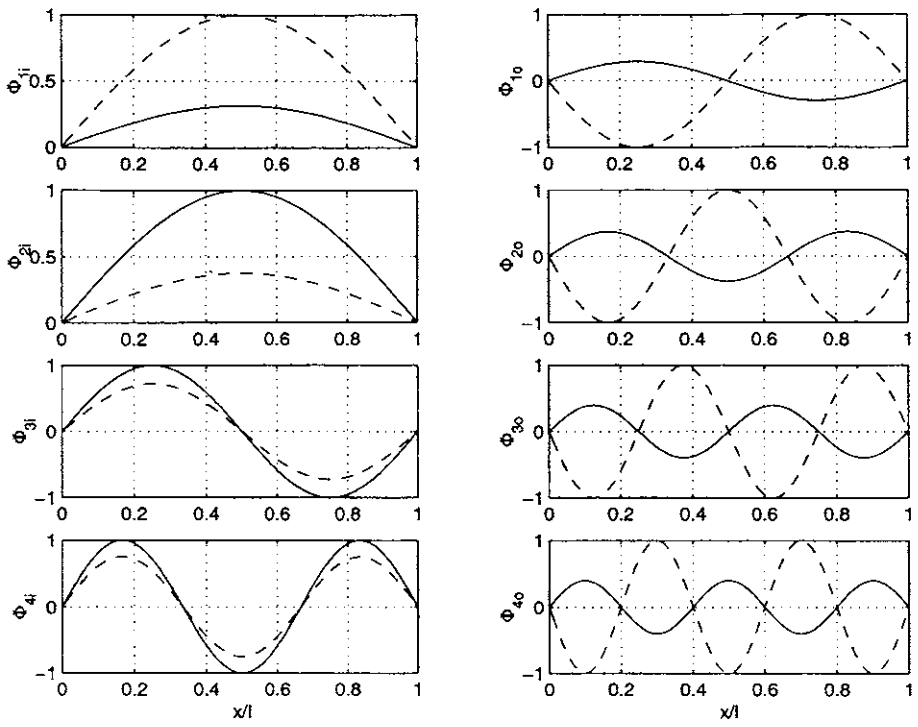

Figure 8-9: First four synchronous and asynchronous mode shapes by using closed form solutions (solid line: Beam 1; dash-dot line: Beam 2)

Order	a_{1n}	a_{2n}
1	3.1468	0.3768
2	-3.3993	0.7231
3	-2.6794	0.7529
4	-2.5294	0.7608
5	-2.4876	0.7632
6	-2.4855	0.7633
7	-2.5034	0.7623
8	-2.5333	0.7606
9	-2.5715	0.7585
10	-2.6157	0.7562

Table 8.9: Coefficients of natural mode shapes $a_{in}(r_{sp} = 1.0)$

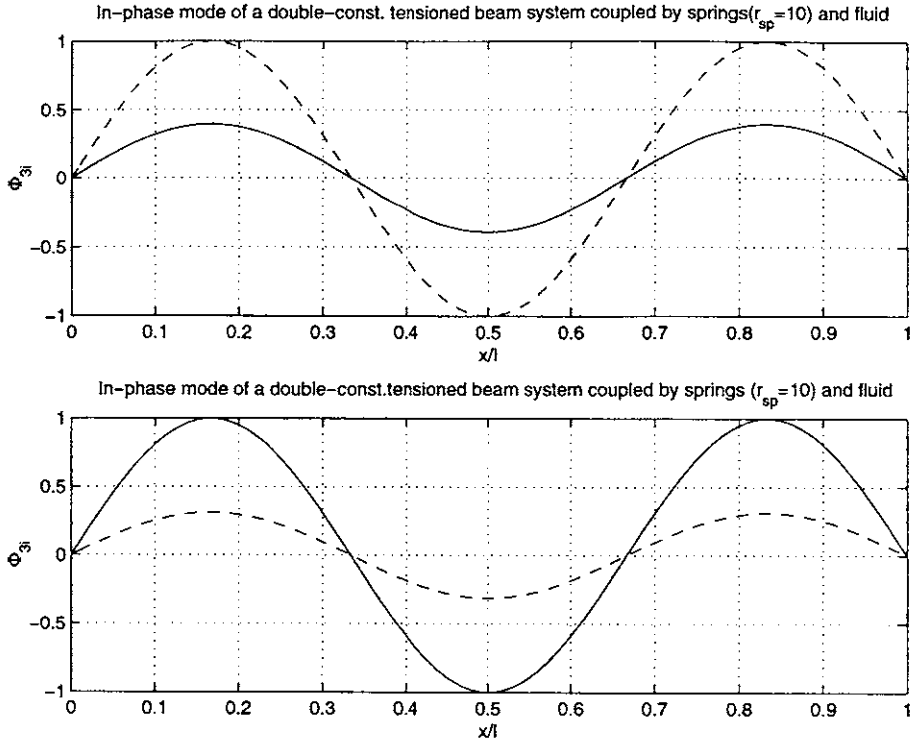

Figure 8-10: The third in-phase mode shapes($r_{sp} = 10$, solid line: Beam 1; dash-dot line: Beam 2)

Order	a_{1n}	a_{2n}
1	1.0313	-0.6287
2	1.2013	-0.2918
3	2.5451	0.3120
4	-39.3288	0.6012
5	-5.1384	0.6820
6	-3.6999	0.7136
7	-3.2415	0.7286
8	-3.0418	0.7364
9	-2.9479	0.7403
10	-2.9076	0.7421

Table 8.10: Coefficients of natural mode shapes a_{in} ($r_{sp} = 10$)

8.5 Theoretical formulation of a general coupled double-riser system

8.5.1 Hydrodynamic forces of viscous fluid in between concentric cylinders

Consider two concentric circular cylinders separated by an incompressible viscous fluid annulus as shown in Figure 8-11, where r_1 and r_2 are the interface radii between fluid and tubes. In application, the length of tubes is much larger than the radii r_i $(i = 1, 2)$. Thus, the fluid field can be two-dimensional; that is, the axial motion of

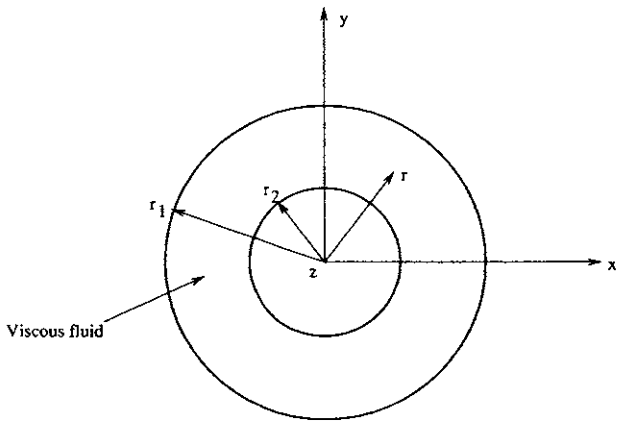

Figure 8-11: Schematic of two concentric tubes containing a viscous fluid

fluid is neglected. It is convenient to express the Navier-Stokes equation in the circular cylindrical coordinate system (r, θ, z), which governs the motion of viscous fluids. For small amplitude oscillations, the equations of motion can be linearized. Chen[56, 57] found that fluid forces acting on cylinders are linear functions of the cylinder motions, and that the forces can be separated into two components: one proportional to the real part of the coefficient α_{il}, $Re(\alpha_{il})$, is in phase with the cylinder acceleration and is related to the added mass effect, while the other proportional to the imaginary part of α_{il}, $Im(\alpha_{il})$, opposes the movement of the cylinder and is related to a damping mechanism. The hydrodynamic forces can also be expressed in terms of cylinder

acceleration and velocity as:

$$X_i = -\sum_{l=1}^{2} m_{il}\ddot{x}_l - \sum_{l=1}^{2} c_{il}\dot{x}_l, \tag{8.42}$$

where $x_l(t)$ is the instantaneous displacement of the lth cylinder, the dot denotes differentiation with respect to time, and

$$\begin{aligned} m_{il} &= \rho\pi r_i r_l R_e(\alpha_{il}), \\ c_{il} &= \rho\pi r_i r_l I_m(\alpha_{il}). \end{aligned} \tag{8.43}$$

m_{il} and c_{il} are the added mass and fluid damping coefficients of the system, respectively.

It is convenient to define an oscillation Reynolds number $N_R = \omega r_2^2/\nu$, where ν is kinematic viscosity, and radius ratio $\gamma = r_2/r_1$. The fluid force coefficient α_{il} depends on the oscillation Reynolds number N_R and radius ratio γ in a very complicated way. Approximate solutions can be obtained in special cases, where the most often used are shown as follows:

(a): $N_R >> 1$ and moderate gap (e.g., $G > 0.01$ and $N_R > 10^4$)

$$\alpha_{11} = \frac{\beta_1(1+\gamma^2)\sin(G\beta_1) - 2(2-\gamma+\gamma^2)\cos(G\beta_1) + 4\gamma\sqrt{\gamma}}{\beta_1(1-\gamma^2)\sin(G\beta_1) + 2\gamma(1+\gamma)\cos(G\beta_1) - 4\gamma\sqrt{\gamma}}, \tag{8.44}$$

where $G = (r_1 - r_2)/r_2 = (1-\gamma)/\gamma$, $\beta_1^2 = -jN_R$

(b): $N_R >> 1$ and $G^2 N_R >> 1$ (e.g., $N_R > 10^4$ and $G^2 N_R > 10^4$)

$$\alpha_{11} = \frac{\beta_1(1+\gamma^2) - j2(2-\gamma+\gamma^2)}{\beta_1(1-\gamma^2) + j2\gamma(1+\gamma)} \tag{8.45}$$

(c): $\nu \to 0$, $N_R \to \infty$

Eqs. (8.44) and (8.45) reduce to that of in-viscid fluid:

$$\alpha_{11} = \frac{1+\gamma^2}{1-\gamma^2}. \tag{8.46}$$

All other coefficients α_{il} are obtained in terms of α_{11}:

$$\begin{aligned} \alpha_{12} &= \alpha_{21} = -\gamma(1+\alpha_{11}), \\ \alpha_{22} &= 1+\gamma^2(1+\alpha_{11}). \end{aligned} \tag{8.47}$$

8.5.2 Formulation of a coupled fluid/riser system

It has been demonstrated that the hydrodynamic force can be calculated for two concentric cylinders separated by an incompressible viscous fluid. The governing equations of motion of external and internal risers in a coupled fluid/riser system are:

$$\frac{\partial^2}{\partial x^2}(EI_1(x)\frac{\partial^2 w_1}{\partial x^2}) - \frac{\partial}{\partial x}(T_1(x)\frac{\partial w_1}{\partial x}) + m_1(x)\frac{\partial^2 w_1}{\partial t^2} = h_1(x,t) + f_1(x,t), \tag{8.48}$$

$$\frac{\partial^2}{\partial x^2}(EI_2(x)\frac{\partial^2 w_2}{\partial x^2}) - \frac{\partial}{\partial x}(T_2(x)\frac{\partial w_2}{\partial x}) + m_2(x)\frac{\partial^2 w_2}{\partial t^2} = h_2(x,t) + f_2(x,t), \tag{8.49}$$

where the subscripts '1' and '2' denote external and internal risers respectively, $f_i(x,t)$ $(i=1,2)$ includes external exciting force and concentrated ones due to centralizers, and $h_i(x,t)$ $(i=1,2)$ is the hydrodynamic force defined in Eq. (8.42).

Substituting Eq. (8.42) into Eqs. (8.48) and (8.49) yields:

$$\begin{aligned} \frac{\partial^2}{\partial x^2}(EI_1(x)\frac{\partial^2 w_1}{\partial x^2}) - \frac{\partial}{\partial x}(T_1(x)\frac{\partial w_1}{\partial x}) &+ (m_1+m_{11})\frac{\partial^2 w_1}{\partial t^2} + m_{12}\frac{\partial^2 w_2}{\partial t^2} \\ &+ c_{11}\frac{\partial w_1}{\partial t} + c_{12}\frac{\partial w_2}{\partial t} = f_1(x,t), \end{aligned} \tag{8.50}$$

$$\begin{aligned} \frac{\partial^2}{\partial x^2}(EI_2(x)\frac{\partial^2 w_2}{\partial x^2}) - \frac{\partial}{\partial x}(T_2(x)\frac{\partial w_2}{\partial x}) &+ (m_2+m_{22})\frac{\partial^2 w_2}{\partial t^2} + m_{21}\frac{\partial^2 w_1}{\partial t^2} \\ &+ c_{21}\frac{\partial w_1}{\partial t} + c_{22}\frac{\partial w_2}{\partial t} = f_2(x,t). \end{aligned} \tag{8.51}$$

Define the following non-dimensioned parameters:

$s = \frac{x}{l}$, $\omega_o = \sqrt{\frac{E_0 I_0}{m_0 l^4}}$, $\tau = \omega_o t$, and $Y_i = \frac{w_i}{D_e}$,

where the subscript 'o' represents the values at a reference cross section, and D_e is an effective diameter. Then Eqs. (8.50) and (8.51) can be written in a non-dimensional

form:

$$\begin{aligned}
\frac{\partial^2}{\partial s^2}(P_1(s)\frac{\partial^2 Y_1}{\partial s^2}) - \frac{\partial}{\partial s}(Q_1(s)\frac{\partial Y_1}{\partial s}) &+ M_{11}(s)\frac{\partial^2 Y_1}{\partial \tau^2} + M_{12}(s)\frac{\partial^2 Y_2}{\partial \tau^2} \\
&+ C_{11}\frac{\partial Y_1}{\partial \tau} + C_{12}\frac{\partial Y_2}{\partial \tau} = f_1(s,\tau), \quad (8.52) \\
\frac{\partial^2}{\partial s^2}(P_2(s)\frac{\partial^2 Y_2}{\partial s^2}) - \frac{\partial}{\partial s}(Q_2(s)\frac{\partial Y_2}{\partial s}) &+ M_{22}(s)\frac{\partial^2 Y_2}{\partial \tau^2} + M_{21}(s)\frac{\partial^2 Y_1}{\partial \tau^2} \\
&+ C_{22}\frac{\partial Y_2}{\partial \tau} + C_{21}\frac{\partial Y_1}{\partial \tau} = f_2(s,\tau), \quad (8.53)
\end{aligned}$$

where,

$$\begin{aligned}
&P_i = \frac{E_i I_i}{E_o I_o}, \qquad Q_i = \frac{T_i l^2}{E_o I_o}, \qquad M_{ii} = \frac{m_i(x)}{m_o}, \\
&M_{ij} = \frac{m_{ij}}{m_o}, \qquad C_{ii} = \frac{c_{ii}}{m_o \omega_o}, \qquad C_{ij} = \frac{c_{ij}}{m_o \omega_o}, \\
&f_i(s,\tau) = \frac{f_i(x,t) l^4}{D_e E_o I_o}, \qquad (i,\, j = 1,2).
\end{aligned}$$

Assuming $Y_i(s,\tau) = R_i(s)e^{i\wedge\tau}$ $(i = 1,2)$ and substituting it into Eqs. (8.52) and (53) result in:

$$\begin{aligned}
\frac{\partial^2}{\partial s^2}(P_1(s)\frac{\partial^2 R_1}{\partial s^2}) - \frac{\partial}{\partial s}(Q_1(s)\frac{\partial R_1}{\partial s}) &- M_{11}(s)\wedge^2 R_1 - M_{12}(s)\wedge^2 R_2 \\
&+ i\wedge C_{11}R_1 + i\wedge C_{12}R_2 = F_1(s), \quad (8.54) \\
\frac{\partial^2}{\partial s^2}(P_2(s)\frac{\partial^2 R_2}{\partial s^2}) - \frac{\partial}{\partial s}(Q_2(s)\frac{\partial R_2}{\partial s}) &- M_{22}(s)\wedge^2 R_2 - M_{21}(s)\wedge^2 R_1 \\
&+ i\wedge C_{22}R_2 + i\wedge C_{21}R_1 = F_2(s), \quad (8.55)
\end{aligned}$$

where $F_1(s) \equiv f_1(s,\tau)e^{-i\wedge\tau}$, $F_2(s) \equiv f_2(s,\tau)e^{-i\wedge\tau}$, and $\wedge$ is a dimensionless frequency, $\wedge = \omega/\omega_o$.

The dynamic stiffness formulation of a coupled fluid/riser system is obtained by establishing a weak form of the equations (8.54) and (8.55) using the Galerkin procedure. Equations (8.54) and (8.55) are weighted with virtual displacements, $\bar{v}_1$ and $\bar{v}_2$, respectively:

$$\int_s \bar{v}_1[\frac{\partial^2}{\partial s^2}(P_1(s)\frac{\partial^2 R_1}{\partial s^2}) \quad - \quad \frac{\partial}{\partial s}(Q_1(s)\frac{\partial R_1}{\partial s}) - M_{11}(s)\wedge^2 R_1 - M_{12}(s)\wedge^2 R_2$$

$$+ \quad i \wedge C_{11}R_1 + i \wedge C_{12}R_2]ds = \int_s \bar{v}_1 F_1(s)ds, \tag{8.56}$$

$$\int_s \bar{v}_2[\frac{\partial^2}{\partial s^2}(P_2(s)\frac{\partial^2 R_2}{\partial s^2}) - \frac{\partial}{\partial s}(Q_2(s)\frac{\partial R_2}{\partial s}) - M_{22}(s) \wedge^2 R_2 - M_{21}(s) \wedge^2 R_1$$
$$+ \quad i \wedge C_{22}R_2 + i \wedge C_{21}R_1]ds = \int_s \bar{v}_2 F_2(s)ds. \tag{8.57}$$

Integrating over the domain of interest s and transforming – to lower the order of the derivatives in the expressions of (8.56) and (8.57) and to incorporate the natural boundary conditions as forcing terms – gives the variational equations to be discretized by finite element interpolations.

The first two terms in the left side of Eq. (8.56) are transformed as follows:

$$\begin{aligned}
&\int_s \bar{v}_1 \frac{\partial^2}{\partial s^2}(P_1(s)\frac{\partial^2 R_1}{\partial s^2})ds \\
&= \bar{v}_1 \frac{\partial}{\partial s}(P_1(s)\frac{\partial^2 R_1}{\partial s^2}) \mid_s - \int_s \frac{\partial \bar{v}_1}{\partial s}\frac{\partial}{\partial s}(P_1(s)\frac{\partial^2 R_1}{\partial s^2})ds, \\
&= \bar{v}_1 \frac{\partial}{\partial s}(P_1(s)\frac{\partial^2 R_1}{\partial s^2}) \mid_s - \frac{\partial \bar{v}_1}{\partial s}P_1(s)\frac{\partial^2 R_1}{\partial s^2} \mid_s + \int_s \frac{\partial^2 \bar{v}_1}{\partial s^2}P_1(s)\frac{\partial^2 R_1}{\partial s^2}ds, \qquad (8.58) \\
&\int_s \bar{v}_1 \frac{\partial}{\partial s}(Q_1(s)\frac{\partial R_1}{\partial s})ds \\
&= \bar{v}_1(Q_1(s)\frac{\partial R_1}{\partial s} \mid_s - \int_s \frac{\partial \bar{v}_1}{\partial s}Q_1(s)\frac{\partial R_1}{\partial s}ds. \qquad (8.59)
\end{aligned}$$

The first two terms in the left side of Eq. (8.57) can be transformed into similar forms with subscript 2 instead of 1. Assuming that both beams are simply supported, we have the displacement boundary conditions S_u : $\bar{v}_i = 0$ and the forcing boundary conditions S_f : $P_i(s)\frac{\partial^2 R_i}{\partial s^2} = 0$, $(i = 1, 2)$ on the ends. Similar formulation for other boundary conditions can be found. Equations (8.56) and (8.57) are then rewritten as:

$$\begin{aligned}
\int_s \frac{\partial^2 \bar{v}_1}{\partial s^2}P_1(s)\frac{\partial^2 R_1}{\partial s^2}ds &+ \int_s \frac{\partial \bar{v}_1}{\partial s}Q_1(s)\frac{\partial R_1}{\partial s}ds - \int_s \bar{v}_1(M_{11}(s) \wedge^2 -i \wedge C_{11})R_1 ds \\
&- \int_s \bar{v}_1(M_{12}(s) \wedge^2 -i \wedge C_{12})R_2 ds = \int_s \bar{v}_1 F_1(s)ds, \\
\int_s \frac{\partial^2 \bar{v}_2}{\partial s^2}P_2(s)\frac{\partial^2 R_2}{\partial s^2}ds &+ \int_s \frac{\partial \bar{v}_2}{\partial s}Q_2(s)\frac{\partial R_2}{\partial s}ds - \int_s \bar{v}_2(M_{22}(s) \wedge^2 -i \wedge C_{22})R_2 ds \\
&- \int_s \bar{v}_2(M_{21}(s) \wedge^2 -i \wedge C_{21})R_1 ds = \int_s \bar{v}_2 F_2(s)ds. \qquad (8.60)
\end{aligned}$$

In the finite element analysis, we approximate the system as an assemblage of discrete finite elements interconnected at nodal points. The above equations are further expressed as:

$$\begin{aligned}
\sum_m \Big(\int_{s(m)} \frac{\partial^2 \bar{v}_1}{\partial s^2} P_1(s) \frac{\partial^2 R_1}{\partial s^2} ds \;+\; & \int_{s(m)} \frac{\partial \bar{v}_1}{\partial s} Q_1(s) \frac{\partial R_1}{\partial s} ds - \int_{s(m)} \bar{v}_1 (M_{11}(s) \wedge^2 - i \wedge C_{11}) R_1 ds \\
- & \int_{s(m)} \bar{v}_1 (M_{12}(s) \wedge^2 - i \wedge C_{12}) R_2 ds\Big) = \sum_m \int_{s(m)} \bar{v}_1 F_1(s) ds, \\
\sum_m \Big(\int_{s(m)} \frac{\partial^2 \bar{v}_2}{\partial s^2} P_2(s) \frac{\partial^2 R_2}{\partial s^2} ds \;+\; & \int_{s(m)} \frac{\partial \bar{v}_2}{\partial s} Q_2(s) \frac{\partial R_2}{\partial s} ds - \int_{s(m)} \bar{v}_2 (M_{22}(s) \wedge^2 - i \wedge C_{22}) R_2 ds \\
- & \int_{s(m)} \bar{v}_2 (M_{21}(s) \wedge^2 - i \wedge C_{21}) R_1 ds\Big) = \sum_m \int_{s(m)} \bar{v}_2 F_2(s) ds.
\end{aligned} \tag{8.61}$$

The forces $f_i(x,t)$ $(i = 1, 2)$ in Eqs. (8.50) and (8.51) include external distributed force $f_i^e(x,t)$ and the concentrated forces $f_i^c(x,t)$ due to centralizers, which are evenly distributed in the longitudinal direction of a riser. Thus:

$$f_i(x,t) = f_i^e(x,t) + f_i^c(x,t). \tag{8.62}$$

The force due to coupling centralizers, which are modeled as spring-dampers, is written as:

$$f_1^c(x,t) = -\sum_{n=1}^{N_m} [k_n(w_1 - w_2) + c_n(\dot{w}_1 - \dot{w}_2)]\delta(x - x_n), \tag{8.63}$$

$$f_2^c(x,t) = -\sum_{n=1}^{N_m} [k_n(w_2 - w_1) + c_n(\dot{w}_2 - \dot{w}_1)]\delta(x - x_n), \tag{8.64}$$

where N_m is the number of centralizers distributed within the m-th element. It is noted that $f_1^c(x,t) = -f_2^c(x,t)$.

$$\begin{aligned}
f_1^c(s,\tau) &= -\frac{l^4}{D_e E_0 I_0} \sum_{n=1}^{N_m} [k_n(w_1 - w_2) + c_n(\dot{w}_1 - \dot{w}_2)]\delta(x - x_n) \\
&= -\frac{l^4}{E_0 I_0} \sum_{n=1}^{N_m} [k_n(Y_1 - Y_2) + c_n(\dot{Y}_1 - \dot{Y}_2)]\delta(x - x_n).
\end{aligned} \tag{8.65}$$

We assume that:

$$R_1^{(m)}(s) = \mathbf{H}_1^{(m)}(s)\hat{\mathbf{U}}_1, \tag{8.66}$$

$$R_2^{(m)}(s) = \mathbf{H}_2^{(m)}(s)\hat{\mathbf{U}}_2, \tag{8.67}$$

where $\mathbf{H}_1^{(m)}(s)$ and $\mathbf{H}_2^{(m)}(s)$ are the m-th elemental interpolation function of an external riser and that of an internal riser, respectively. They are found in this research from the WKB-based frequency-dependent shape functions of risers when they are un-coupled. The $\hat{\mathbf{U}}_1$ and $\hat{\mathbf{U}}_2$ are nodal point displacements of the total element assemblage in external and internal risers, respectively. Likewise, the expressions are obtained for virtual displacements, $\bar{v}_1$ and $\bar{v}_2$,

$$\bar{v}_1^{(m)}(s) = \mathbf{H}_1^{(m)}(s)\bar{\hat{\mathbf{U}}}_1, \tag{8.68}$$

$$\bar{v}_2^{(m)}(s) = \mathbf{H}_2^{(m)}(s)\bar{\hat{\mathbf{U}}}_2. \tag{8.69}$$

The formulation of the spectrum element method for the coupled problem is obtained by means of substituting Eqs. (8.66) to (8.69) into (8.61).
The left-hand side of the first equation of (8.61) is:

$$\begin{aligned} LHS &= \bar{\hat{\mathbf{U}}}_1^T \sum_m [\int_{s^{(m)}} (\mathbf{H}_1^{''(m)}(s))^T P_1(s) \mathbf{H}_1^{''(m)}(s) ds + \int_s (\mathbf{H}_1^{'(m)}(s))^T Q_1(s) \mathbf{H}_1^{'(m)}(s) ds \\ &- \int_{s^{(m)}} \mathbf{H}_1^{(m)T} (M_{11}(s) \wedge^2 - i \wedge C_{11}) \mathbf{H}_1^{(m)}(s) ds] \hat{\mathbf{U}}_1 \\ &- \bar{\hat{\mathbf{U}}}_1^T \sum_m [\int_{s^{(m)}} \mathbf{H}_1^{(m)T}(s) (M_{12}(s) \wedge^2 - i \wedge C_{12}) \mathbf{H}_2^{(m)}(s) ds] \hat{\mathbf{U}}_2. \end{aligned} \tag{8.70}$$

The right-hand side of the first equation of (8.61) is:

$$\begin{aligned} RHS &= \bar{\hat{\mathbf{U}}}_1^T \sum_m \int_{s^{(m)}} \mathbf{H}_1^{(m)T} F_1^e(s) ds \\ &- \underbrace{\bar{\hat{\mathbf{U}}}_1^T \sum_m \int_{s^{(m)}} \mathbf{H}_1^{(m)T} [\frac{l^4}{E_0 I_0} \sum_{n=1}^{N_m} [k_n(Y_1 - Y_2) + c_n(\dot{Y}_1 - \dot{Y}_2)] \delta(x - x_n)] ds e^{-i\wedge\tau}}_{(I)}. \end{aligned} \tag{8.71}$$

The second term (I) in Eq. (8.71) is further expressed as:

$$
\begin{aligned}
(I) &= \bar{\hat{\mathbf{U}}}_1^T \sum_m \int_{s^{(m)}} \mathbf{H}_1^{(m)T} [\frac{l^4}{E_0 I_0} \sum_{n=1}^{N_m} [k_n(Y_1 - Y_2) + c_n(\dot{Y}_1 - \dot{Y}_2)] \delta(x - x_n)] ds e^{-i\wedge\tau}, \\
&= \bar{\hat{\mathbf{U}}}_1^T \sum_m \int_{x^{(m)}} \mathbf{H}_1^{(m)T} [\frac{l^3}{E_0 I_0} \sum_{n=1}^{N_m} [k_n(Y_1 - Y_2) + c_n(\dot{Y}_1 - \dot{Y}_2)] \delta(x - x_n)] dx e^{-i\wedge\tau}, \\
&= \bar{\hat{\mathbf{U}}}_1^T \frac{l^3}{E_0 I_0} \sum_m \sum_{n=1}^{N_m} \mathbf{H}_1^{(m)T} [k_n(Y_1 - Y_2) + c_n(\dot{Y}_1 - \dot{Y}_2)] \mid_{x=x_n} e^{-i\wedge\tau}, \\
&= \bar{\hat{\mathbf{U}}}_1^T \frac{l^3}{E_0 I_0} \sum_m \sum_{n=1}^{N_m} \mathbf{H}_1^{(m)T} [k_n(R_1 - R_2) + i \wedge c_n \omega_0 (R_1 - R_2)] \mid_{s=s_n}, \\
&= \bar{\hat{\mathbf{U}}}_1^T \sum_m \sum_{n=1}^{N_m} \mathbf{H}_1^{(m)T} [48 k_n^* (R_1 - R_2) + i2 \wedge c_n^* (R_1 - R_2)] \mid_{s=s_n}, \\
&= \bar{\hat{\mathbf{U}}}_1^T \sum_m [\sum_{n=1}^{N_m} \mathbf{H}_1^{(m)T} (48 k_n^* + i2 \wedge c_n^*) R_1 \mid_{s=s_n} - \sum_{n=1}^{N_m} \mathbf{H}_1^{(m)T} (48 k_n^* + i2 \wedge c_n^*) R_2 \mid_{s=s_n}],
\end{aligned}
\tag{8.72}
$$

where dimensionless stiffness k_n and damping c_n^* of centralizers are defined as:

$$
k_n^* \equiv \frac{k_n}{\frac{48 E_0 I_0}{l^3}}, \tag{8.73}
$$

$$
c_n^* \equiv \frac{c_n l^3 \omega_0}{2 E_0 I_0} = \frac{c_n}{2(m_0 l)\omega_0}. \tag{8.74}
$$

Substituting Eqs. (8.66) and (8.67) into Eq. (8.72) results in:

$$
\begin{aligned}
(I) &= \bar{\hat{\mathbf{U}}}_1^T \sum_m [\sum_{n=1}^{N_m} \mathbf{H}_1^{(m)T} (48 k_n^* + i2 \wedge c_n^*) \mathbf{H}_1^{(m)}] \mid_{s=s_n} \hat{\mathbf{U}}_1 \\
&- \bar{\hat{\mathbf{U}}}_1^T \sum_m [\sum_{n=1}^{N_m} \mathbf{H}_1^{(m)T} (48 k_n^* + i2 \wedge c_n^*) \mathbf{H}_2^{(m)}] \mid_{s=s_n} \hat{\mathbf{U}}_2.
\end{aligned}
\tag{8.75}
$$

Replacing Eq. (8.75) into (8.71), the first equation in (8.61) is rewritten as:

$$
\mathbf{K}_{11} \hat{\mathbf{U}}_1 + \mathbf{K}_{12} \hat{\mathbf{U}}_2 = \mathbf{F}_1, \tag{8.76}
$$

where,

$$\begin{aligned}
\mathbf{K}_{11} &= \sum_m \{ \int_{s^{(m)}} (\mathbf{H}_1^{''(m)}(s))^T P_1(s) (H)_1^{''(m)}(s) ds + \int_{s^{(m)}} (\mathbf{H}_1^{'(m)}(s))^T Q_1(s) \mathbf{H}_1^{'(m)}(s) ds \\
&- \int_{s^{(m)}} \mathbf{H}_1^{(m)T} (M_{11}(s) \wedge^2 - i \wedge C_{11}) \mathbf{H}_1^{(m)}(s) ds \\
&+ [\sum_{n=1}^{N_m} \mathbf{H}_1^{(m)T} (48 k_n^* + i2 \wedge c_n^*) \mathbf{H}_1^{(m)}] \mid_{s=s_n} \}, \qquad (8.77) \\
\mathbf{K}_{12} &= -\sum_m \int_{s^{(m)}} \mathbf{H}_1^{(m)T}(s) (M_{12}(s) \wedge^2 - i \wedge C_{12}) \mathbf{H}_2^{(m)}(s) ds \\
&- \sum_m [\sum_{n=1}^{N_m} \mathbf{H}_1^{(m)T} (48 k_n^* + i2 \wedge c_n^*) \mathbf{H}_2^{(m)}] \mid_{s=s_n}, \qquad (8.78) \\
\mathbf{F}_1 &= \sum_m \int_{s^{(m)}} \mathbf{H}_1^{(m)T} F_1(s) ds. \qquad (8.79)
\end{aligned}$$

Following the same procedure, the second equation in (8.61) is rewritten as:

$$\mathbf{K}_{21} \hat{\mathbf{U}}_1 + \mathbf{K}_{22} \hat{\mathbf{U}}_2 = \mathbf{F}_2, \qquad (8.80)$$

where,

$$\begin{aligned}
\mathbf{K}_{22} &= \sum_m \{ \int_{s^{(m)}} (\mathbf{H}_2^{''(m)}(s))^T P_2(s) \mathbf{H}_2^{''(m)}(s) ds + \int_{s^{(m)}} (\mathbf{H}_2^{'(m)}(s))^T Q_2(s) \mathbf{H}_2^{'(m)}(s) ds \\
&- \int_{s^{(m)}} \mathbf{H}_2^{(m)T} (M_{22}(s) \wedge^2 - i \wedge C_{22}) \mathbf{H}_2^{(m)}(s) ds \\
&+ [\sum_{n=1}^{N_m} \mathbf{H}_2^{(m)T} (48 k_n^* + i2 \wedge c_n^*) \mathbf{H}_2^{(m)}] \mid_{s=s_n} \}, \qquad (8.81) \\
\mathbf{K}_{21} &= -\sum_m \int_{s^{(m)}} \mathbf{H}_2^{(m)T}(s) (M_{21}(s) \wedge^2 - i \wedge C_{21}) \mathbf{H}_1(s)^{(m)} ds \\
&- \sum_m [\sum_{n=1}^{N_m} \mathbf{H}_2^{(m)T} (48 k_n^* + i2 \wedge c_n^*) \mathbf{H}_1^{(m)}] \mid_{s=s_n}, \qquad (8.82) \\
\mathbf{F}_2 &= \sum_m \int_{s^{(m)}} \mathbf{H}_2^{(m)T} F_2(s) ds. \qquad (8.83)
\end{aligned}$$

Equations (8.76) and (8.80) are written in matrix form:

$$\begin{bmatrix} \mathbf{K}_{11} & \mathbf{K}_{12} \\ \mathbf{K}_{21} & \mathbf{K}_{22} \end{bmatrix} \begin{bmatrix} \hat{\mathbf{U}}_1 \\ \hat{\mathbf{U}}_2 \end{bmatrix} = \begin{bmatrix} \mathbf{F}_1 \\ \mathbf{F}_2 \end{bmatrix}. \qquad (8.84)$$

With one symbol to represent each matrix in Eq. (8.84), it is rewritten in the abbreviated form as:

$$\mathbf{KU} = \mathbf{F}, \tag{8.85}$$

where $\mathbf{K}$ is the global dynamic stiffness matrix of the coupled system:

$$\mathbf{K} = \begin{bmatrix} \mathbf{K}_{11} & \mathbf{K}_{12} \\ \mathbf{K}_{21} & \mathbf{K}_{22} \end{bmatrix},$$

$\mathbf{U}$ is the global nodal displacement vector, and $\mathbf{F}$ is the global nodal force vector.

The construction of the spectrum element matrices, which corresponds to the global assemblage degrees of freedom (used in Eqs. (8.77) to (8.79) and (8.81) to (8.83)), can be directly achieved by identifying the global degrees of freedom that correspond to the local degrees of freedom. However, considering $\mathbf{H}^{(m)}$ corresponding to the global assemblage degrees of freedom, only those columns that correspond to element degrees of freedom have nonzero entries, and the main objective in defining the specific matrix is to be able to express the assemblage process of the element matrices in a theoretically elegant manner. In the practical implementation of the spectrum element method, this elegance is also present, but all element matrices are calculated corresponding only to element degrees of freedom and then directly assembled using the correspondence between the local element and global assemblage degrees of freedom. Hence, the frequency-dependent shape function derived in Chapter 4 is directly employed.

8.6 Undamped and damped natural frequency analysis of a coupled system

Assuming that fluid in between two risers is ideal and that damping in centralizers is neglected, then the coupled system is undamped. Natural frequencies of such an undamped system are found by means of either a determinant plotting method or an iterative root-search technique.

The WKB-based dynamic stiffness method with the W-W algorithm is extended in this research to the analysis of natural frequencies of the coupled system. Each segment with continuous properties in both external and internal risers is regarded as one element. Each mode component at nodal points is obtained easily by Gauss elimination. Mode distribution within each element is obtained as previously through frequency dependent shape functions, as shown in Eqs. (8.66) and (8.67). Hence, natural frequencies and corresponding mode shapes are found with good accuracy by means of fewer elements. This method has been employed in the analysis of a double-uniform beam system discussed in sections 8.2 to 8.4, which is either elastically coupled by discrete springs, or ideal fluid, or the combination of both. Compared with the analytical solutions in the examples, the natural frequencies and mode shapes of the coupled system found by the WKB-based DSM with the W-W algorithm are accurate.

If fluid viscosity and damping in centralizers are considered, a coupled system is a damped one. Natural frequencies of a damped coupled system are complex. Complex frequencies are found in this research by means of the Muller method, which is described in section 3.5. The method requires initial estimation of roots. When a coupled system is not heavily damped, the undamped natural frequencies are good approximate initial values.

The above description is further demonstrated through the following example of a coupled system in which both of the cylinders are simply supported and whose specifications are as follow:

Young's modulus $E = 30000$ Ksi;

Length of both cylinders $L = 1944$ ft;

Mass per unit length of external pipe (added mass of outside water included, $C_a = 1.0$) $m_1 = 169.2134$ kg/m;

Outer diameter of external pipe $d_{1o} = 13.375$ inches;

Inner diameter of external pipe $d_{1i} = 12.615$ inches;

Area moment of inertia of external pipe $I_1 = 1.3642 \times 10^{-4}\ m^4$;

Minimum tension on external pipe $T_{10} = 2.5 \times 10^4$ pounds;

Linearly varying tension factor of external pipe $\alpha_1 = 47.00$ lb/ft;

Mass per length (insider water included) of internal pipe $m_2 = 87.2117$ kg/m;

Outer diameter of internal pipe $d_{2o} = 9.75$ inches;

Inner diameter of internal pipe $d_{2i} = 9.155$ inches;

Area moment of inertia of internal pipe $I_2 = 4.1110 \times 10^{-5}\ m^4$;

Minimum tension on internal pipe $T_{20} = 1.0 \times 10^4$ pounds;

Linearly varying tension factor of internal pipe $\alpha_2 = 30.63$ lb/ft;

Number of evenly distributed identical centralizers $n_{sp} = 19$.

The following four cases are investigated:

Case 1: only coupled by springs

Each riser is discretized into 20 evenly distributed elements. Setting spring stiffness ratio k^* is 1.0/48, 10/48 and 100/48 respectively, undamped natural frequencies are obtained by means of the WKB-based DSM with the W-W algorithm and shown in Table 8.11. This table shows that natural frequencies generally increase with rigidity of centralizers.

Order	$k_* = 1/48$	$k_* = 10/48$	$k_* = 100/48$
1	0.0344	0.0344	0.0344
2	0.0692	0.0693	0.0693
3	0.0778	0.1049	0.1049
4	0.0982	0.1416	0.1416
5	0.1050	0.1795	0.1796
6	0.1259	0.2188	0.2190
7	0.1417	0.2217	0.2603
8	0.1576	0.2297	0.3031
9	0.1796	0.2429	0.3479
10	0.1923	0.2593	0.3945

Table 8.11: Natural frequencies (Hz) of the double-riser system coupled by only springs

Case 2: only coupled by ideal fluid

Natural frequencies of an ideal fluid coupled system are obtained by using the WKB-

based DSM with the W-W algorithm. Each riser is regarded as one element. The first 10 natural frequencies in Hz are found as:
0.0144, 0.0290, 0.0335, 0.0439, 0.0591, 0.0672, 0.0748, 0.0912, 0.1020, and 0.1082, respectively.

Case 3: generally coupled by springs and ideal fluid

The case is the combination of Case 1 ($k^* = 1.0/48$) and Case 2. Natural frequencies are found using 20 elements, as in Case 1. Table 8.12 indicates the results and includes those in Cases 1 and 2 for comparison. This table demonstrates that the fluid lowers the natural frequencies and softens the coupled system.

Order	by springs	by fluid	Case (3)
1	0.0344	0.0144	0.0294
2	0.0692	0.0290	0.0368
3	0.0778	0.0335	0.0408
4	0.0982	0.0439	0.0525
5	0.1050	0.0591	0.0658
6	0.1259	0.0672	0.0681
7	0.1417	0.0748	0.0804
8	0.1576	0.0912	0.0960
9	0.1796	0.1020	0.1023
10	0.1923	0.1082	0.1125

Table 8.12: Natural frequencies (Hz) of a coupled two-riser system

The 11th to 16th natural frequencies in Hz are further found to be:
0.1298, 0.1381, 0.1481, 0.1672, 0.1750, 0.1875.

The corresponding first 16 mode shapes are shown in Figures 8-12 and continued in 8-13. Both figures indicate that when the system is weakly coupled by centralizers, its mode shapes are either in-phase or out-of-phase. As found in section 8.4.2, the original first out-of-phase mode in Figures 8-6 and 8-7 disappears while an additional first in-phase mode occurs. The difference in the first two modes, Φ_1 and Φ_2, is that the deformation of the internal riser is larger in Φ_1 while that of the external riser is larger in Φ_2.

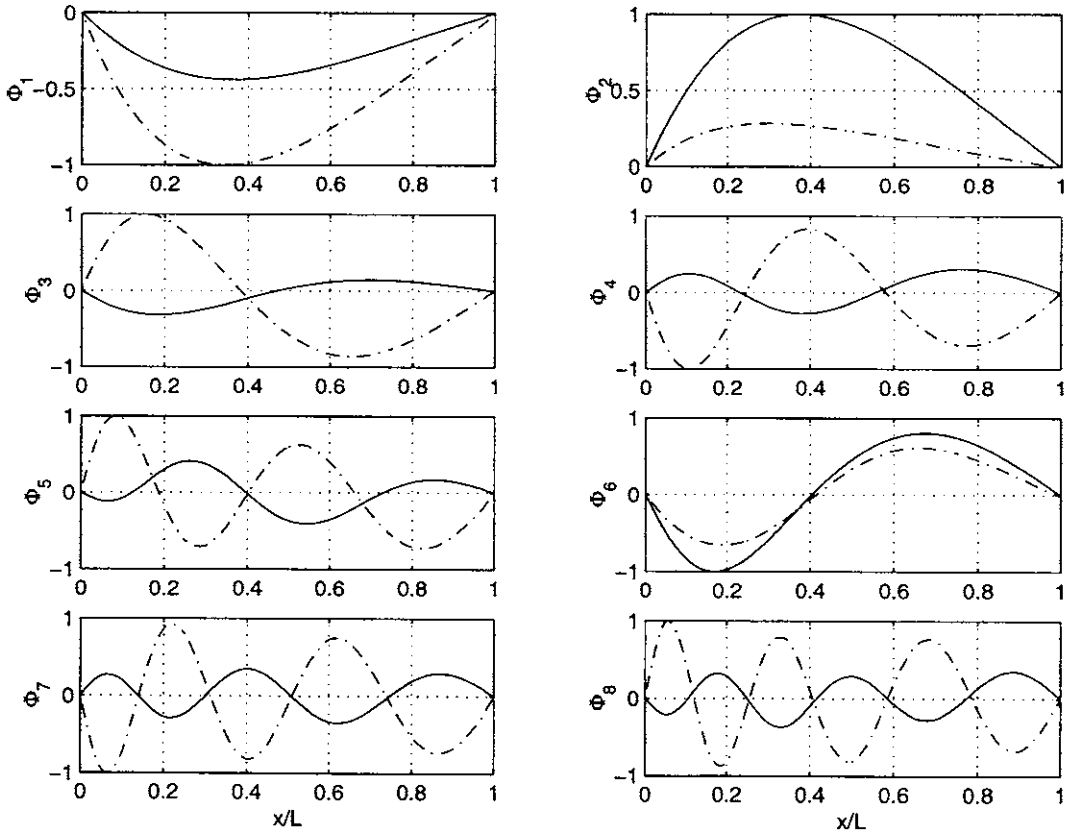

Figure 8-12: The first 8 mode shapes of the coupled system ($k^* = 1/48$, solid line: external riser; dash-dot line: internal riser)

In order to find characteristic vibrations of the coupled system, we further set the stiffness ratio k^* to be 1 and 1000, respectively. Table 8.13 shows the natural

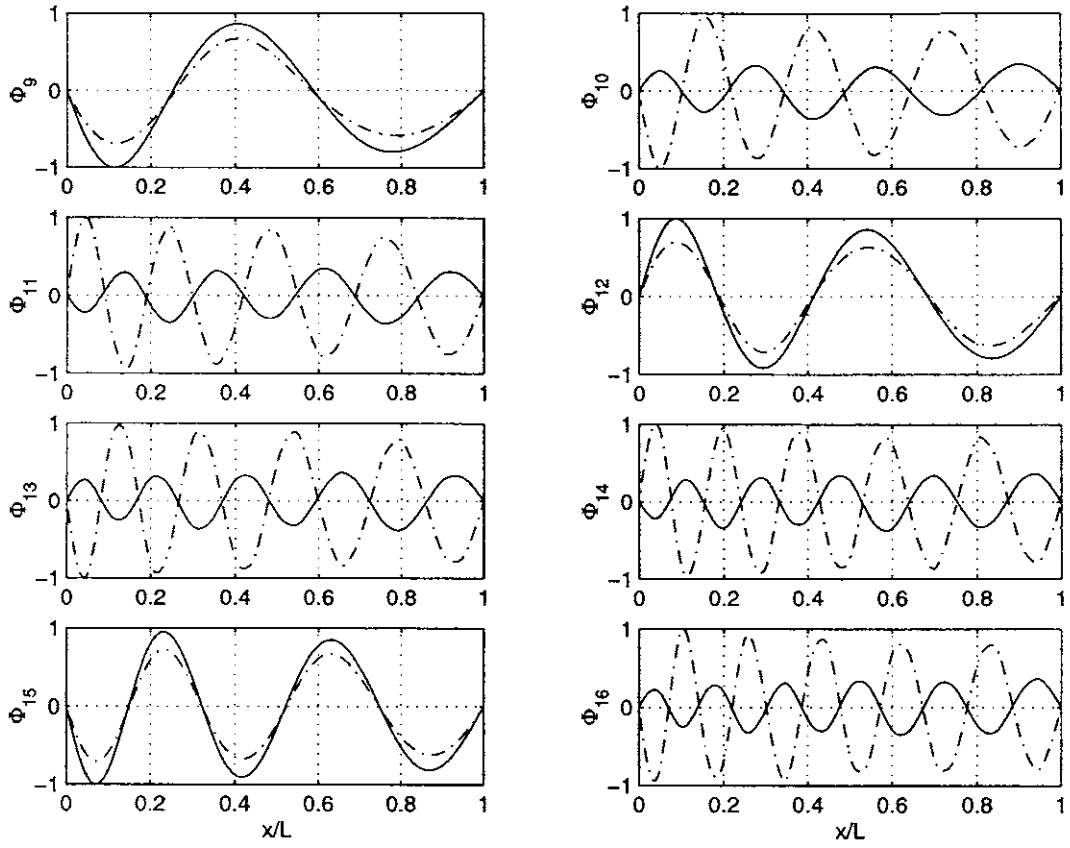

Figure 8-13: The 9th to 16th mode shapes of the coupled system ($k^* = 1/48$, coupled by the fluid and springs)

frequencies and includes the results corresponding to $k^* = 1/48$ for comparison. This table demonstrates that the natural frequencies of the coupled system increase with the stiffness ratio k^* of centralizers.

Figures 8-14 and 8-15 depict the first 16 mode shapes of the coupled system when

Order	$k^* = 1/48$	$k^* = 1$	$k^* = 1000$
1	0.0294	0.0324	0.0324
2	0.0368	0.0651	0.0652
3	0.0408	0.0981	0.0988
4	0.0525	0.1313	0.1334
5	0.0658	0.1636	0.1692
6	0.0681	0.1919	0.2064
7	0.0804	0.2068	0.2450
8	0.0960	0.2089	0.2851
9	0.1023	0.2125	0.3264
10	0.1125	0.2127	0.3481
11	0.1298	0.2186	0.3691
12	0.1381	0.2278	0.4005
13	0.1481	0.2281	0.4160
14	0.1672	0.2412	0.4422
15	0.1750	0.2442	0.4648
16	0.1875	0.2549	0.4877

Table 8.13: Natural frequencies (Hz) of a coupled two-riser system

$k^* = 1$. These two figures indicate that when the system is moderately coupled by centralizers, the first few modes are in-phase while higher mode shapes are roughly either in-phase or out-of-phase but with shifted peaks. Figure 8-14 shows that the system in the first two mode shapes vibrates as a single beam and no relative motion appears between the beams.

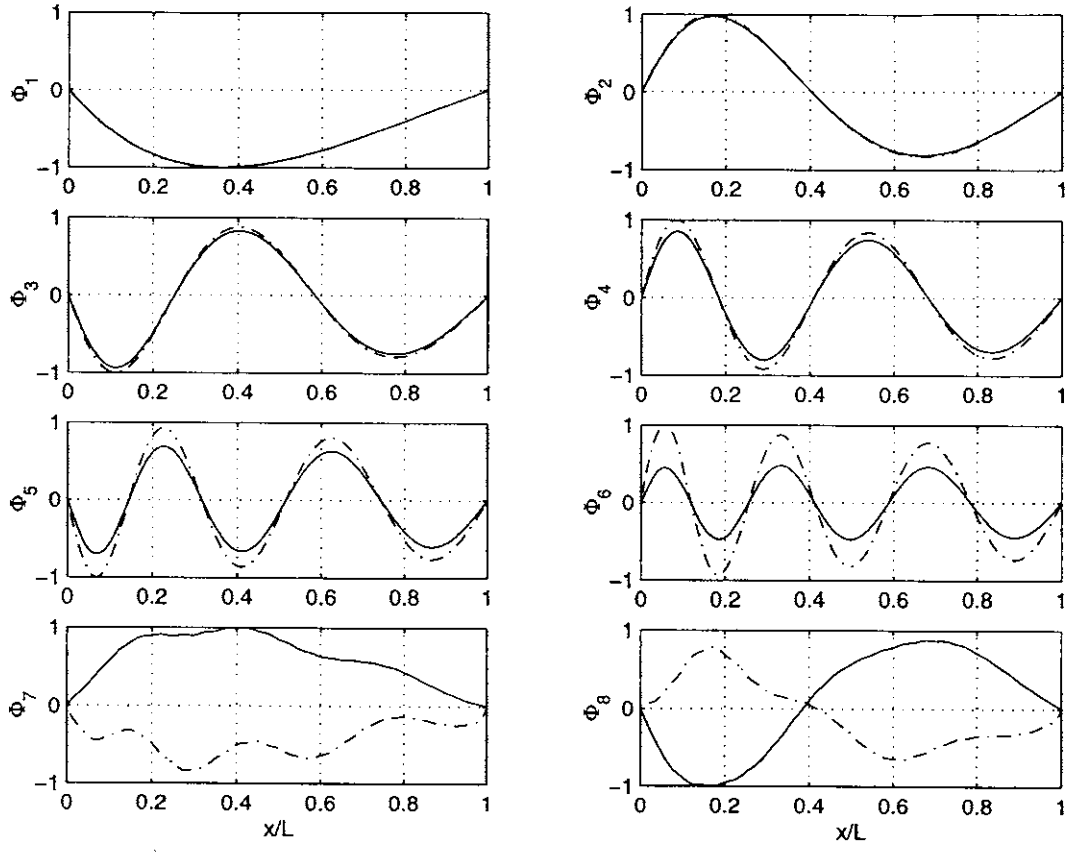

Figure 8-14: The first 8 mode shapes of the coupled system ($k^* = 1$, solid line: external riser; dash-dot line: internal riser)

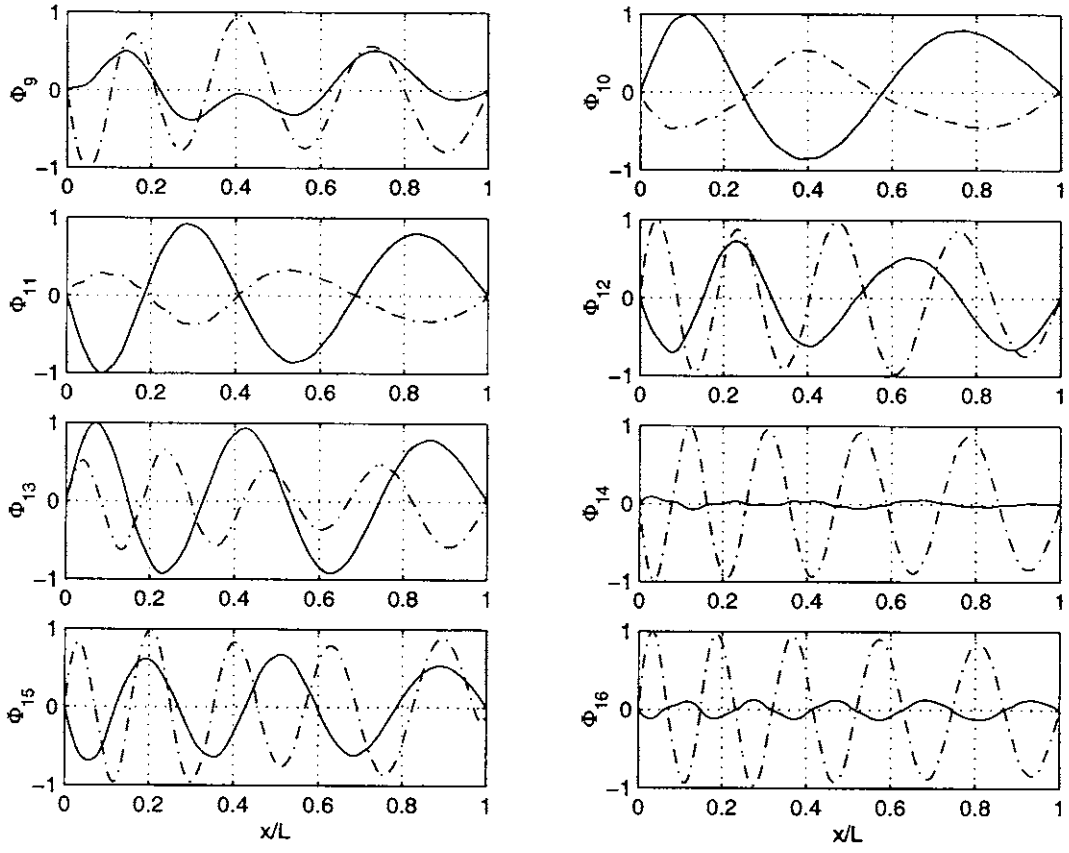

Figure 8-15: The 9th to 16th mode shapes of the coupled system ($k^* = 1$, coupled by the fluid and springs)

Figures 8-16 and 8-17 show the first 16 mode shapes of the coupled system when $k^* = 1000$. These figures indicate that when the system are strongly coupled by centralizers, the system in the low mode shapes vibrates as a single beam and no relative motion occurs between the beams while relative motion between the beams in high mode shapes first appears near the bottom and then spreads towards the top with the mode number. Since the centralizers in this case are very rigid, all the mode shapes demonstrate that no relative motion appears at the connection points.

Figures 8-12 to 8-17 indicate that the stiffness of centralizers has a great influence on the mode shapes of the coupled system.

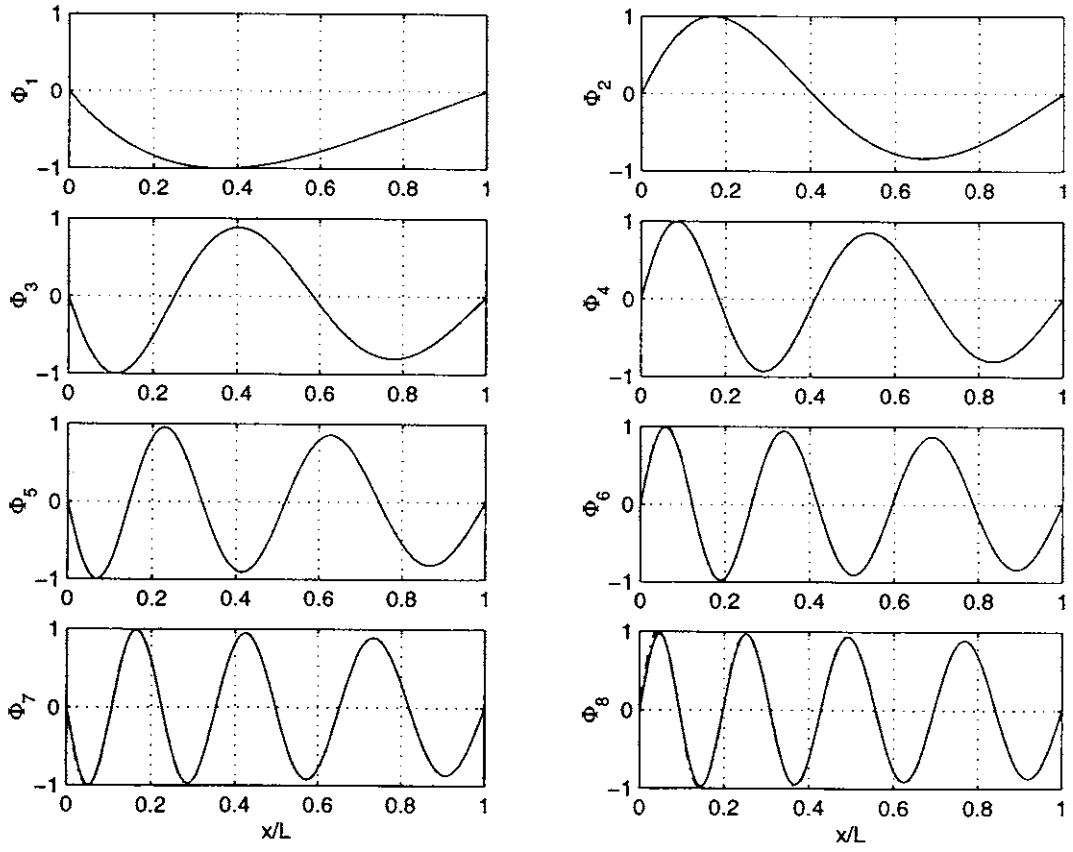

Figure 8-16: The first 8 mode shapes of the coupled system ($k^* = 1000$, solid line: external riser; dash-dot line: internal riser)

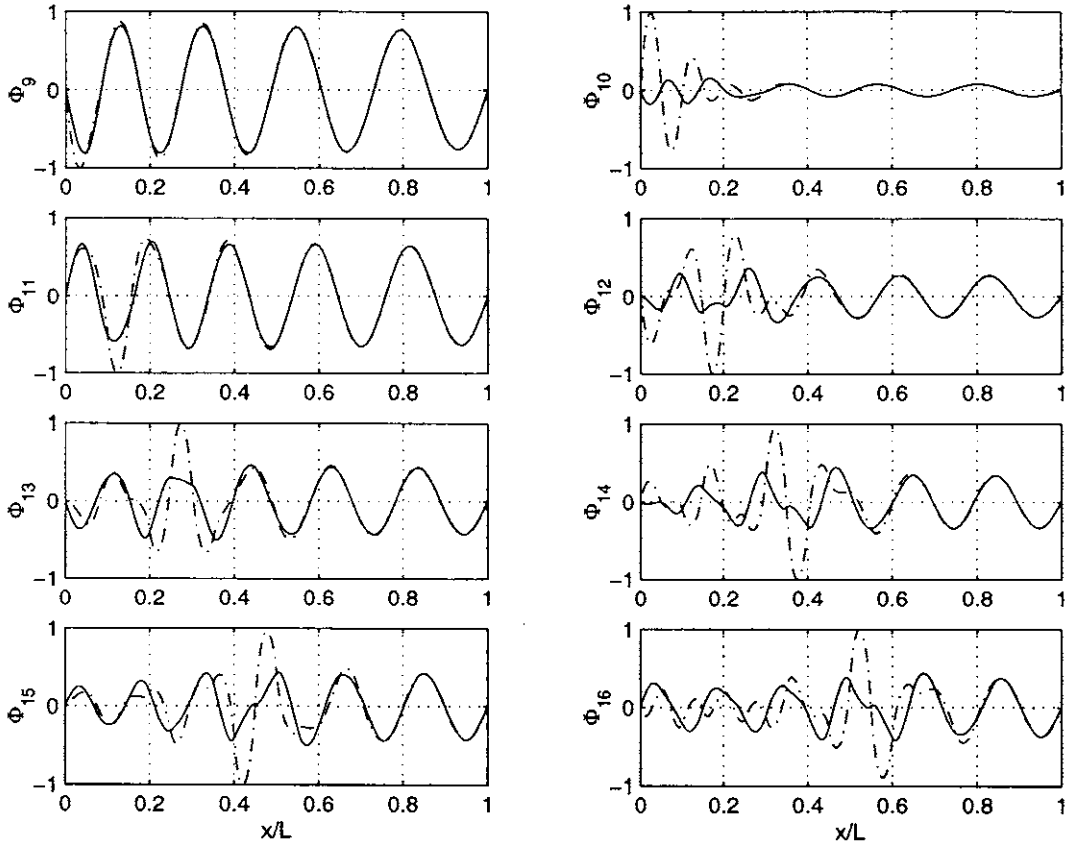

Figure 8-17: The 9th to 16th mode shapes of the coupled system ($k^* = 1000$, coupled by the fluid and springs

Case 4: coupled by dashpot-springs and a viscous fluid

Assuming that the two risers are coupled by dashpot-springs and viscous fluid, complex circular frequencies are found by means of the Muller method. Damping $c^* = 0.5$ and stiffness ratio $k^* = 1.0/48$ are assumed for the centralizers. The oscillation Reynolds number N_R is set to be 1.0×10^6 and 1.0×10^4, respectively. The results by the Muller method are shown in Table 8.13, where modal damping ratios are included in brackets. Modal damping ratio ξ_n is the ratio of the real and imaginary parts of the complex frequency, namely,

$$\xi = \frac{\omega_{ni}}{\omega_{nr}} \tag{8.86}$$

Table 8.14 depicts that modal damping ratios increase with reduction of the oscillation Reynolds number N_R. Hence it is observed from the definition of the oscillation Reynolds number N_R that modal damping increases with kinematic viscosity of the fluid.

Order	$N_R = 1.0 \times 10^6$	$N_R = 1.0 \times 10^4$
1	0.2112+0.0372i (0.1761)	0.2032+0.0394i (0.1937)
2	0.2527+0.0448i (0.1775)	0.2473+0.0478i (0.1932)
3	0.3264+0.0463i (0.1418)	0.3197+0.0504i (0.1577)
4	0.4108+0.0469i (0.1142)	0.4026+0.0525i (0.1304)
5	0.5025+0.0475i (0.0946)	0.4928+0.0547i (0.1110)
6	0.6001+0.0481i (0.0802)	0.5888+0.0570i (0.0967)
7	0.6424+0.0047i (0.0073)	0.6410+0.0052i (0.0082)
8	0.7035+0.0488i (0.0694)	0.6905+0.0594i (0.0861)
9	0.8122+0.0496i (0.0610)	0.7975+0.0621i (0.0778)
10	0.8666+0.0045i (0.0052)	0.8650+0.0054i (0.0063)

Table 8.14: Complex circular frequencies($\omega = \omega_r + i\omega_i$) of a coupled two-riser system

8.7 Effects of coupling factors on the vibration of a coupled system

The dynamic response in the coupled system due to harmonic excitation is found by solving Eq. (8.85). In this section, effects of fluid viscosity (oscillation Reynolds number), damping and rigidity of centralizers, and spacing of centralizers are investigated numerically through the example in Section 8.6. Structural damping of both risers is set to be $\delta_1 = \delta_2 = 0.01$. The harmonic force is assumed to distribute within the range of 10 % the length near the top of the external riser. This range is simulated as a power-in region, in which the exciting distributed force is assumed to be in phase with displacement. As in SHEAR7, a sign function is used to determine the sign of the exciting force, based on the wave number of the external riser under average tension within the power-in region.

The Root-Mean-Square value (RMS) of the dimensionless displacement vector of each riser is employed to measure the global vibration level:

$$u_{irms} = \sqrt{\sum_{j=1}^{N} |u_{ij}|^2}, \qquad (i = 1, 2), \tag{8.87}$$

where N is the number of nodal points in each riser and u_{ij} is the displacement at the j-th point in the i-th riser.

Based on the theoretical formulation of a general coupled double-riser system, a computational program is developed for the analysis. The added mass from the fluid outside of an external riser is considered. The value of $NCOUP$ identifies the type of the coupled system:

(1) $NCOUP = 0$, without coupling only external riser is analyzed and its inside fluid mass included.

(2) $NCOUP = 1$, two risers are coupled by longitudinally distributed discrete springs and dampers due to centralizers.

(3) $NCOUP = 2$, two riser are coupled only by viscous fluid in between.

(4) $NCOUP = 3$, Two risers are generally coupled by viscous fluid in between and

longitudinally distributed discrete springs and dampers due to centralizers.

8.7.1 Fluid viscosity

Assuming that the two risers are coupled by viscous fluid (coupling type NCOUP=2), we investigate the effect of fluid viscosity by running the developed code. In order to observe benefit by increasing fluid viscosity, the RMS frequency response of the external riser when un-coupled is calculated for comparison. In this model, both the mass of internal fluid and the added mass of external fluid are included in its mass density. The oscillation Reynolds number, N_R, is first set to be 1.0×10^4 and 1.0×10^3, respectively. Given the radius ratio γ of two pipes, the fluid force coefficients are functions of N_R.

Figures 8-18 to 8-19 show the results under different values of N_R. Figure 8-18 shows that the RMS displacement response of the external riser when coupled is much less than than that in the un-coupled model. Figures 8-18 and 8-19 depict that the reduction of oscillation Reynolds number results in the reduction of vibration of both external and internal risers.

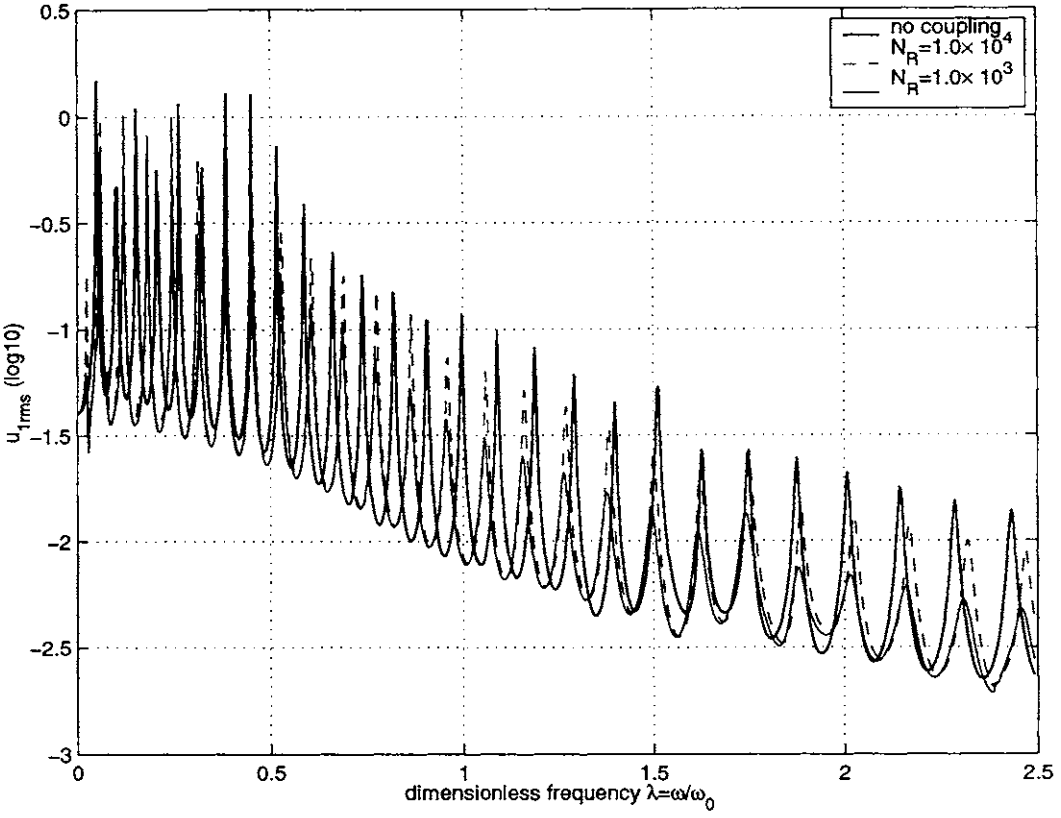

Figure 8-18: The RMS frequency response of the external riser (fluid coupled, NCOUP=2)

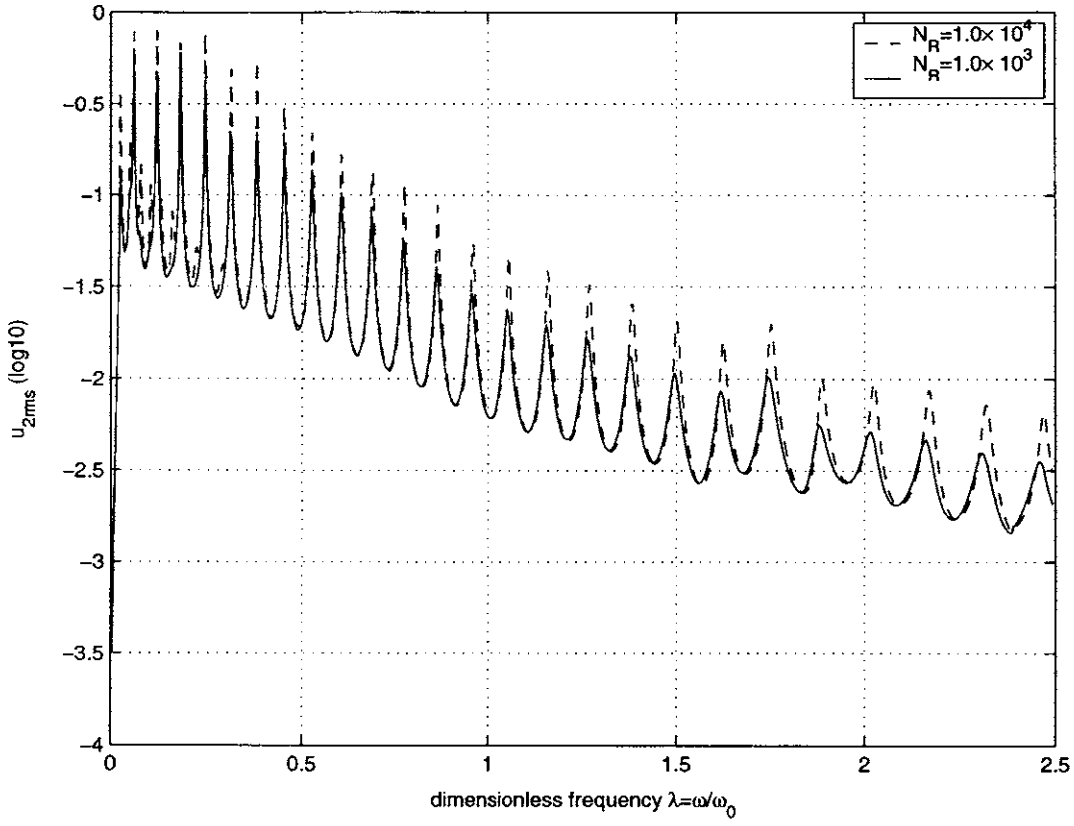

Figure 8-19: The RMS frequency response of the internal riser (fluid coupled, NCOUP=2)

The limit value of oscillation Reynolds number which contributes to vibration suppression of the coupled system is found through continuously reducing its value and observing change of the peaks in the response curves. Figures 8-20 and 8-21 indicate that the limit value of N_R is about 1.0×10^2, at which the vibration of the coupled system is maximally reduced. The deviation from this value results in increase of the RMS displacement response.

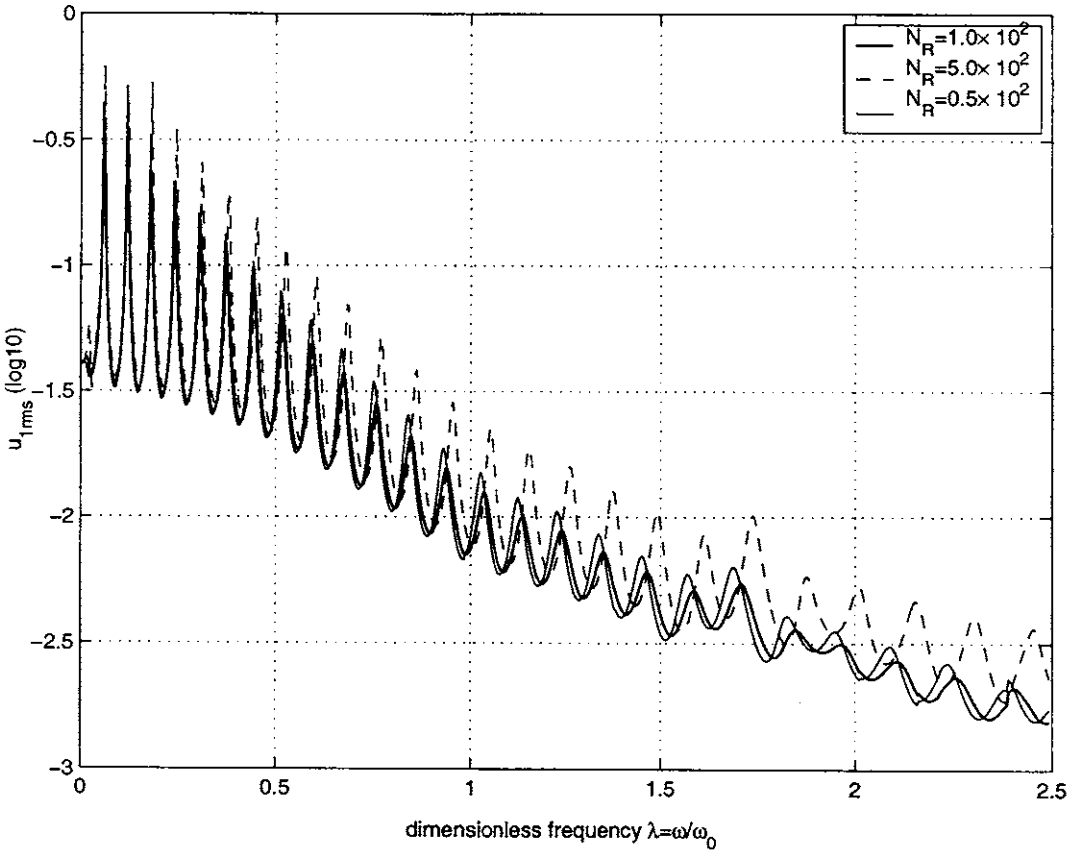

Figure 8-20: The RMS frequency response of the external riser (fluid coupled, NCOUP=2)

We can find an optimum kinematic viscosity ν_o of the fluid in between corresponding to a specific current. If the current speed of interest is $V = 1\,m/s$, we can obtain the corresponding vortex-shedding frequency f_s. The outside diameter of the external riser is $D = 0.3397\,m$. Assuming the Strouhal number $S_t = 0.2$, the vortex-

shedding frequency is $f_s = \frac{S_t V}{D} = 0.5887$ Hz. The circular vortex-shedding frequency $\omega_s = 2 \times \pi \times f_s = 3.6990$ rad/s. The radius of internal riser is $r_2 = 0.1238\,m$. From the definition of N_R, we have: $\nu = \omega_s r_2^2 / N_R$. The optimal kinematic viscosity of the fluid in between in this case is $\nu_o = 5.6715 \times 10^{-4}$.

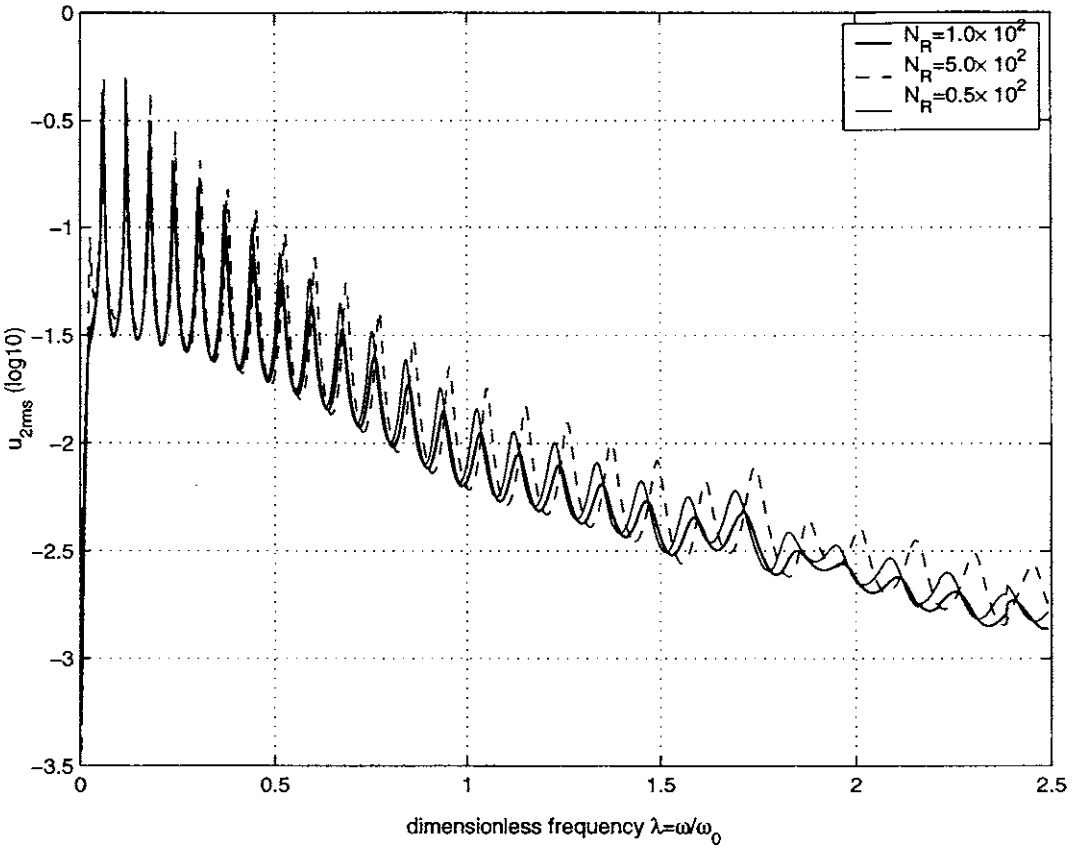

Figure 8-21: The RMS frequency response of the internal riser (fluid coupled, NCOUP=2)

8.7.2 Damping of centralizers

Assuming that the two risers are coupled by both viscous fluid and dashpot-springs (coupling type: NCOUP=3), the effect of damping of centralizers is studied numerically setting kinematic viscosity of the fluid $\nu = 1.0 \times 10^{-4}$ and dimensionless stiffness ratio of springs $k^* = 1$. Figures 8-22 to 8-25 depict the RMS frequency response of the coupled system under different values of k^*. Figures 8-22 and 8-23 show that the damping of centralizers can also contribute to the vibration reduction of the system. Figure 8-22 includes the result of the un-coupled external riser for comparison. Figures 8-24 and 8-25 show the RMS response of the system under large values of dimensionless damping c^*. These figures indicate that the vibration of both external and internal risers is reduced due to the damping of centralizers.

The optimal c^* within the frequency range of interest is found by varying its value and observing the change of the peaks in the response curves.The cross section of the internal riser is employed as an reference one. The reference circular frequency is $\omega_0 = 3.5112$ rad/s. This frequency in Hz is $f_0 = 0.5588$. As shown in Section 8.7.1, the vortex-shedding frequency corresponding to current speed $V = 1.0\,m/s$ is $f_s = 0.5887$ Hz. The dimensionless frequency is then $\lambda_s = f_s/f_0 = 0.5887/0.5588 = 1.0535$. Figures 8-24 and 8-25 show that the optimal damping c^* of centralizers is around 20. Since the mode shapes at lower natural frequencies are in phase, there is no relative motion between the two cylinders. Hence, the damping of centralizers doesn't suppress the vibration of the coupled system at a very low frequency.

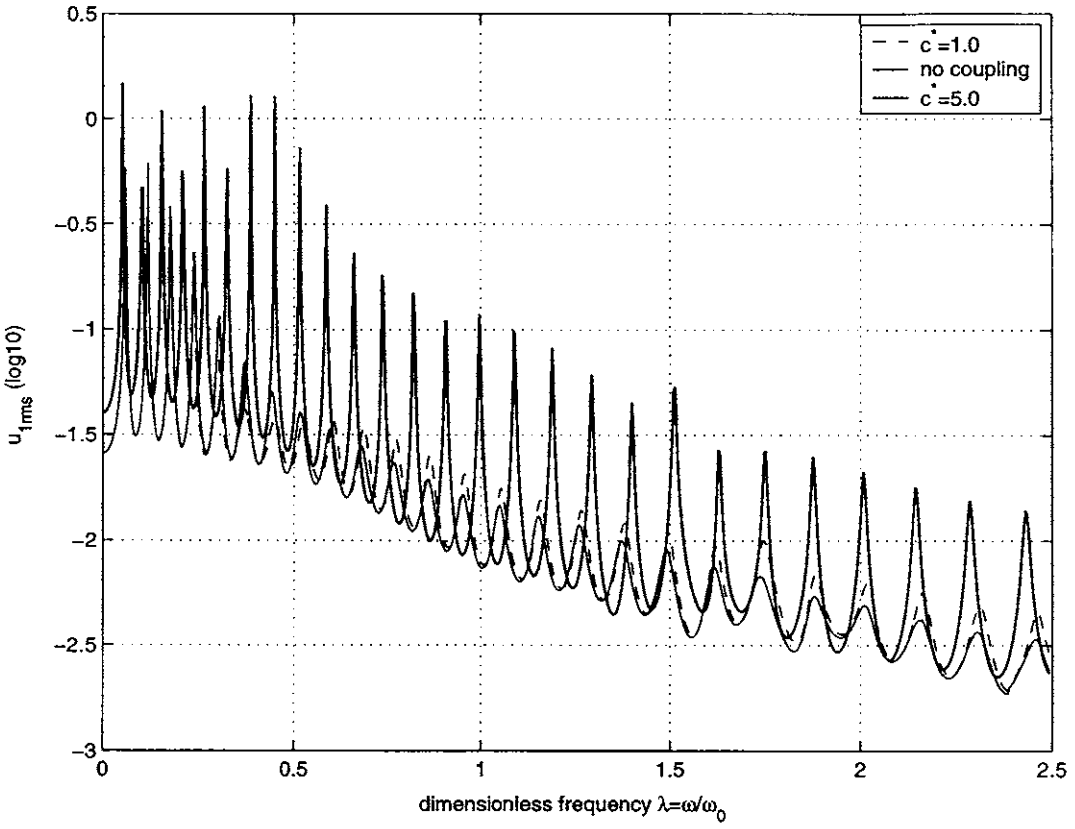

Figure 8-22: The RMS frequency response of the external riser (generally coupled, NCOUP=3)

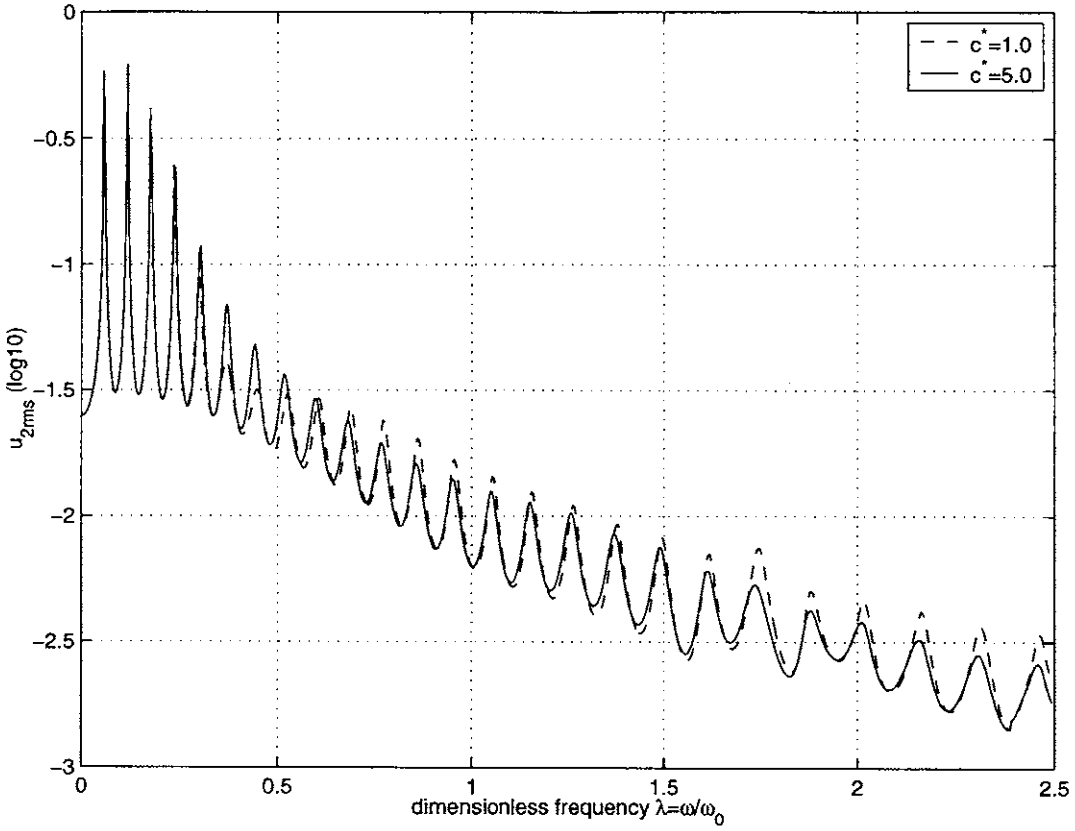

Figure 8-23: The RMS frequency response of the internal riser (generally coupled, NCOUP=3)

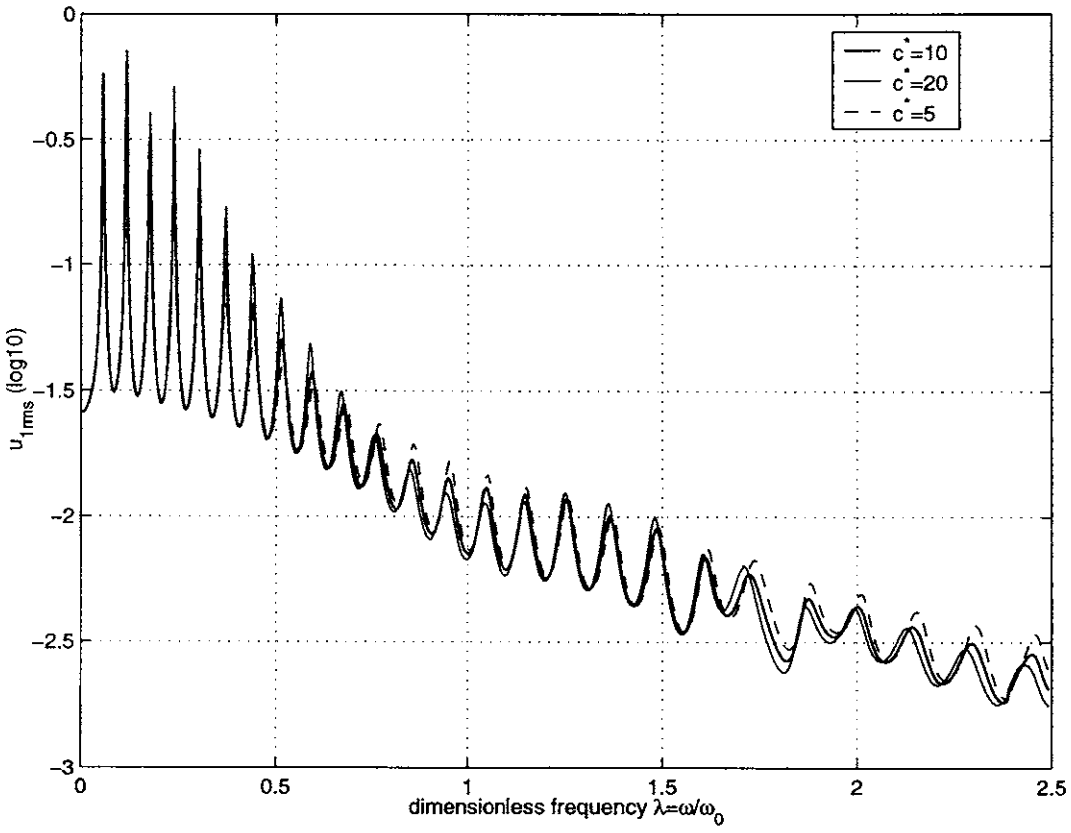

Figure 8-24: The RMS frequency response of the external riser (generally coupled, NCOUP=3)

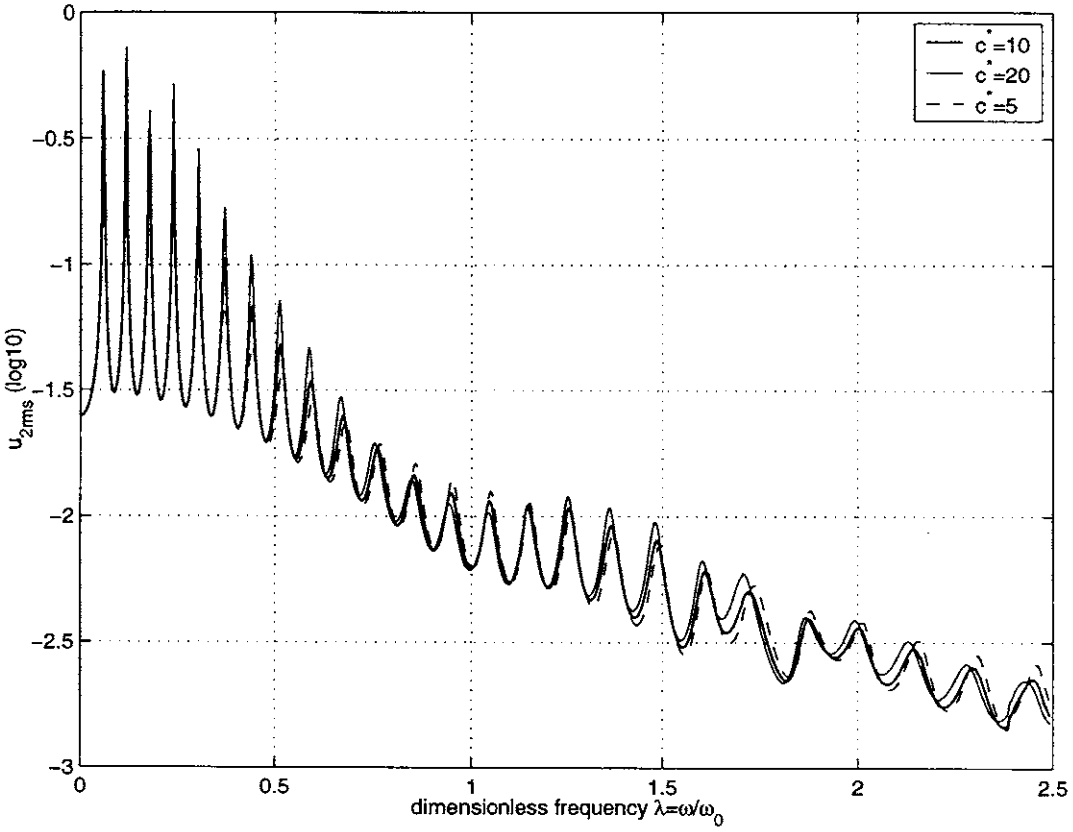

Figure 8-25: The RMS frequency response of the internal riser (generally coupled, NCOUP=3)

8.7.3 Rigidity of centralizers

Section 8.6 discusses the effects of rigidity of centralizers on undamped natural frequencies and mode shapes. With the stiffness ratio k^* of centralizers, natural frequencies of the coupled system increase. The rigidity of centralizers influences the mode shapes of the coupled system. When centralizers are very rigid, the low mode shapes are similar to those of a single beam, namely two risers are linked together and no relative motion appears between them. In this case, high mode shapes first show relative motion near the bottom and the portion having relative motion spreads toward the top with the mode order.

In the generally coupled system (coupling type: NCOUP=3), the fluid in between is viscous and centralizers are modeled as dashpot-springs. Setting the kinematic viscosity of the fluid $\nu = 1.0 \times 10^{-4}\, m^2/s$ and the dimensionless damping $c^* = 1.0$, we evaluate the effect of rigidity of centralizers on the dynamic response. Figures 8-26 to 8-29 depict the RMS frequency response of both external and internal risers. Figures 8-26 to 8-27 show that more vibration is reduced with the rigidity of centralizers. Figure 8-26 includes the result of the external riser when uncoupled for comparison. Figures 8-28 to 8-29 demonstrate the frequency response of the system under large values of k^*. An optimal value of k^* within a frequency range of interest can be similarly found as in Section 8.7.2.

The rigidity of centralizers doesn't contribute to the vibration reduction of the system at low frequencies. With the rigidity of centralizers, more and more low-order mode shapes are in-phase and their behaviors are similar to those of a single beam. In-phase modes don't show the relative motion between beams and are not beneficial to increment of fluid damping forces. Hence in-phase modes suppress the effect of fluid viscosity.

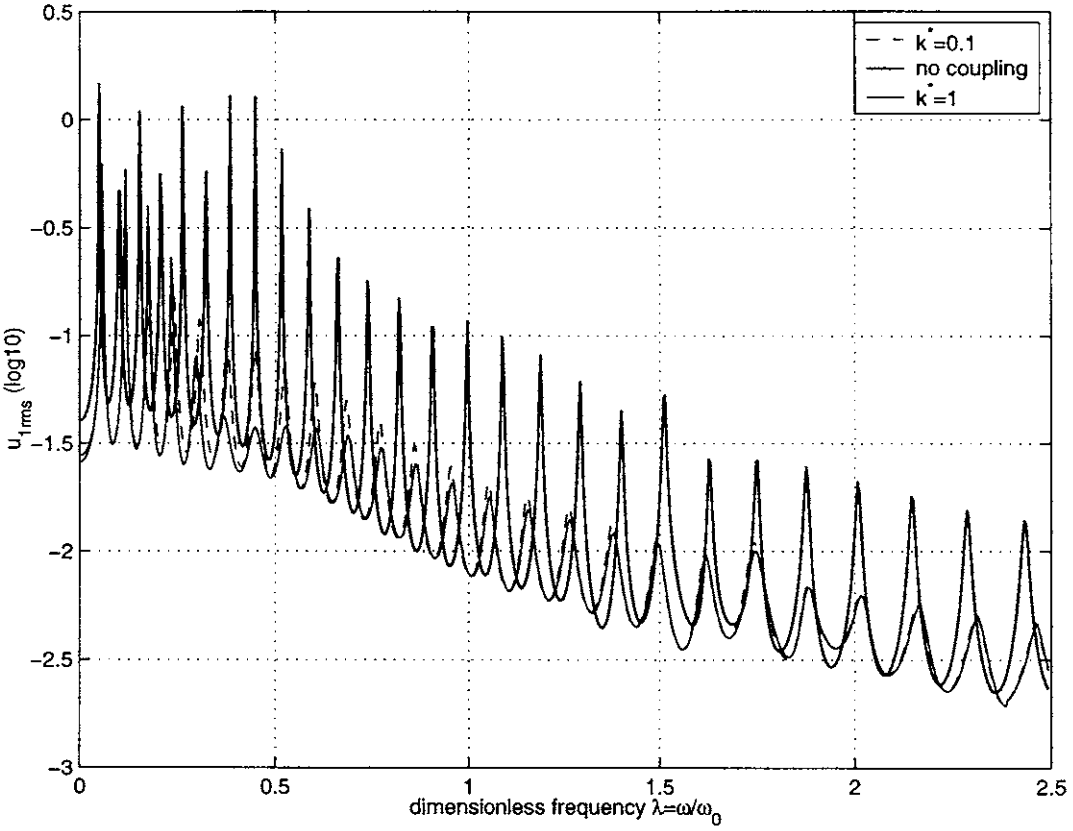

Figure 8-26: The RMS frequency response of the external riser (generally coupled, NCOUP=3)

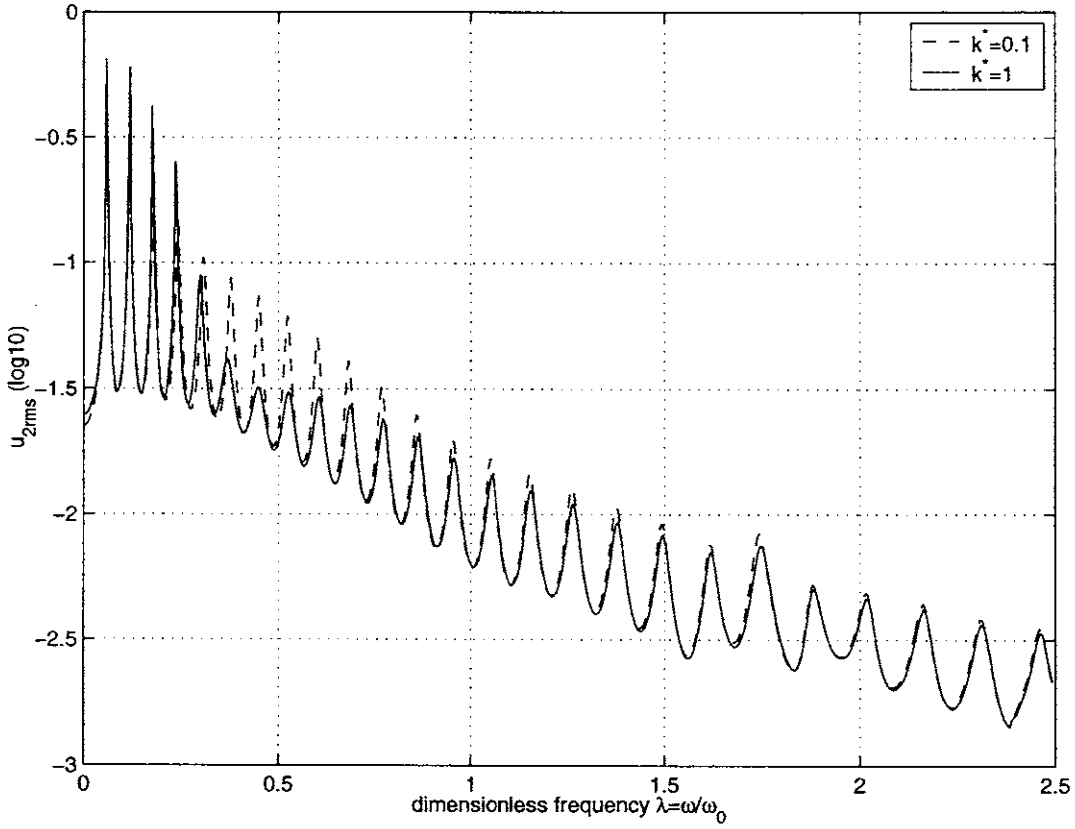

Figure 8-27: The RMS frequency response of the internal riser (generally coupled, NCOUP=3)

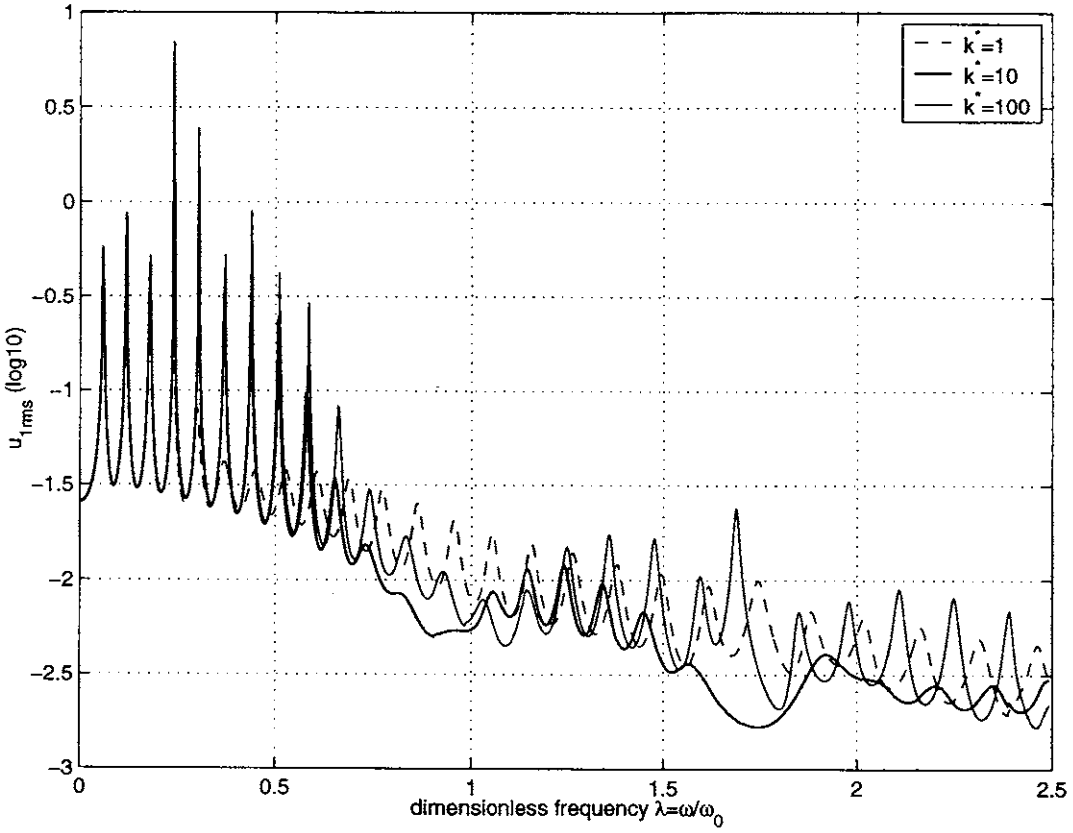

Figure 8-28: The RMS frequency response of the external riser (generally coupled, NCOUP=3)

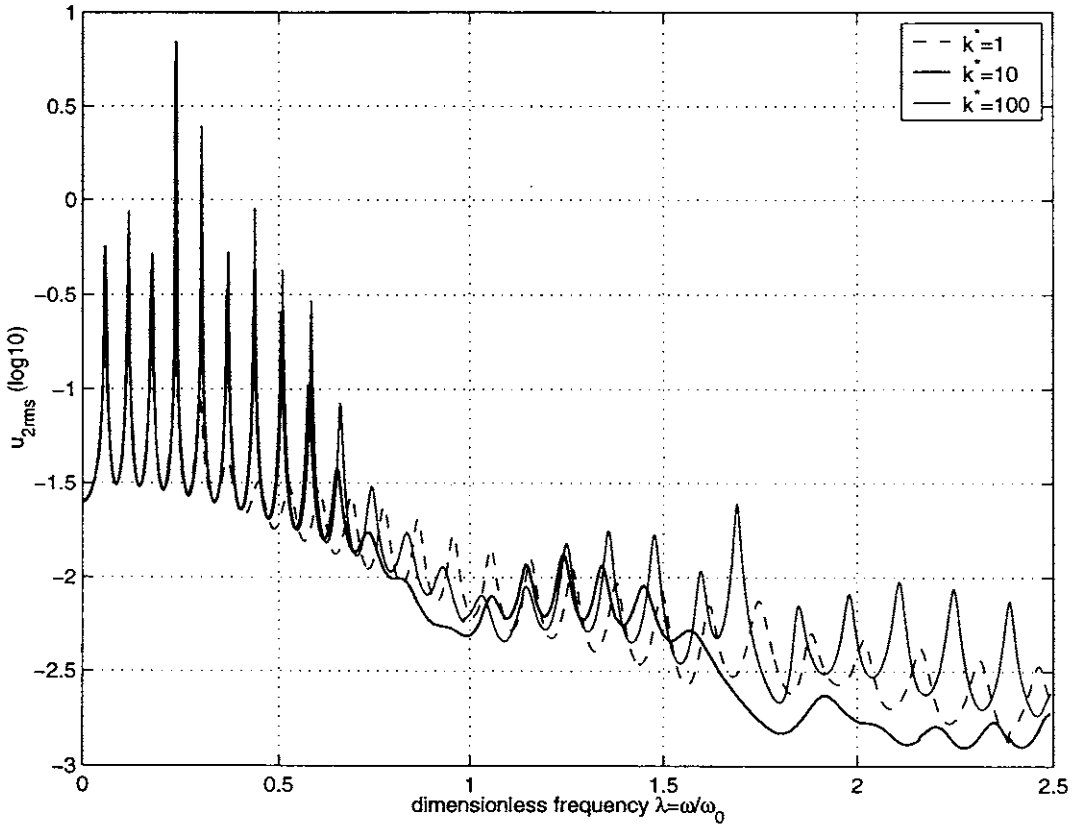

Figure 8-29: The RMS frequency response of the internal riser (generally coupled, NCOUP=3)

8.7.4 Spacing of centralizers

In order to check the effect of spacing of centralizers on the RMS frequency response of the coupled system, we calculate the following two cases:

Case (1): increasing the distribution density of centralizers and setting the spacing of centralizers equal to half of the previous one (namely the spacing is L/40), the total number of centralizers is double the previous one and is equal to 40.

Case (2): The distribution of centralizers is set as previously.

For both cases, the fluid viscosity is $\nu = 1.0 \times 10^{-4} m^2/s$, the dimensionless stiffness k^* is defined with respect to the spacing in **Case (1)** and is equal to 1000, and the dimensionless damping of centralizers are set to be zero, i.e., $c^* = 0.0$. Figures 8-30 and 8-31 show the RMS frequency response of both external and internal risers.

Both figures indicate that with the spacing of centralizers, the vibration of the coupled system is significantly reduced over a large range of frequency. However, the spacing does not result in the vibration suppression at low frequencies. Since the centralizers are very rigid, the modes at low natural frequencies are in-phase and their behavior is similar to those of a single beam. Hence, the effect of the fluid viscosity is suppressed.

We find a vortex-shedding frequency corresponding to a specific value of current velocity. The separation of centralizers is chosen so that within the frequency range of interest the vibration is suppressed. In our experience, the fundamental frequency for an one-span simply-supported internal riser should be slightly less than the vortex-shedding frequency. In the **Case (2)**, the first natural frequency of the one-span simply-supported beam is $f_{span} = 0.56$ Hz. The vortex-shedding frequency corresponding to current velocity $V = 1.0$ m/s is $f_{VIV} = 0.59$ Hz. Since f_{span} is less than f_{VIV}, it is appropriate to choose the span in **Case (2)**. It is noted that the separation of centralizers should not be too large for the wall clearance between the pipes.

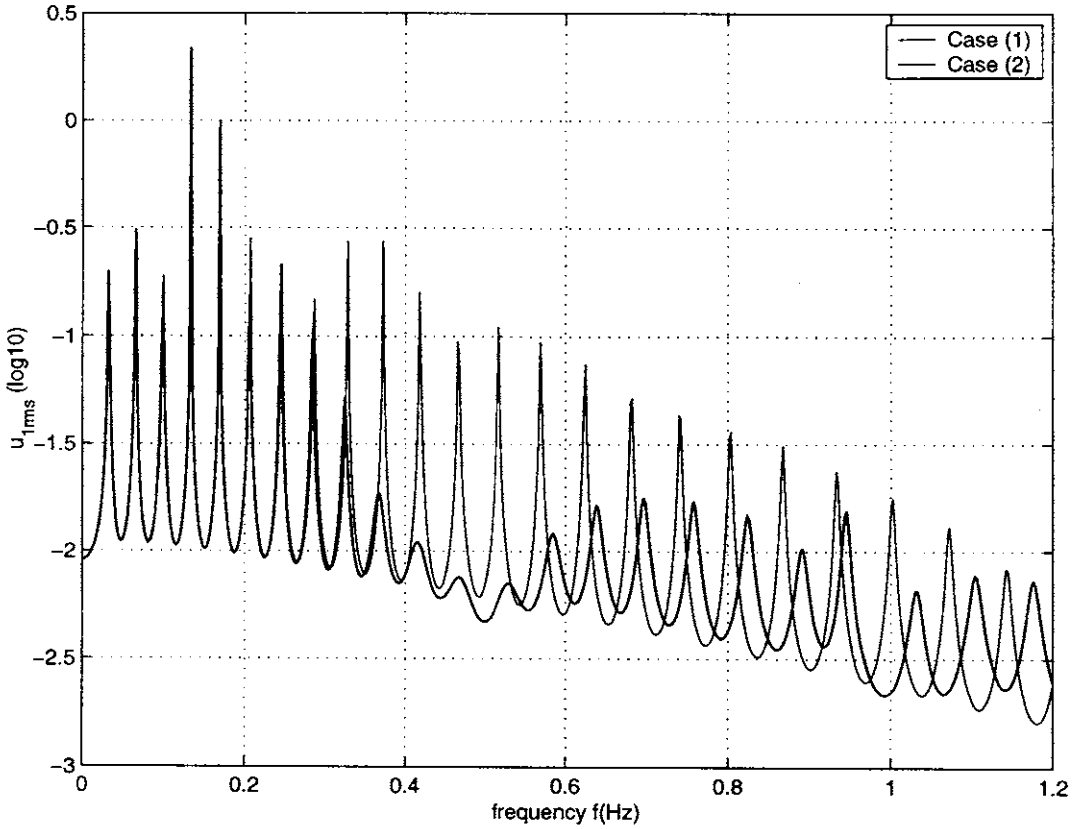

Figure 8-30: The RMS frequency response of the external riser (generally coupled, NCOUP=3)

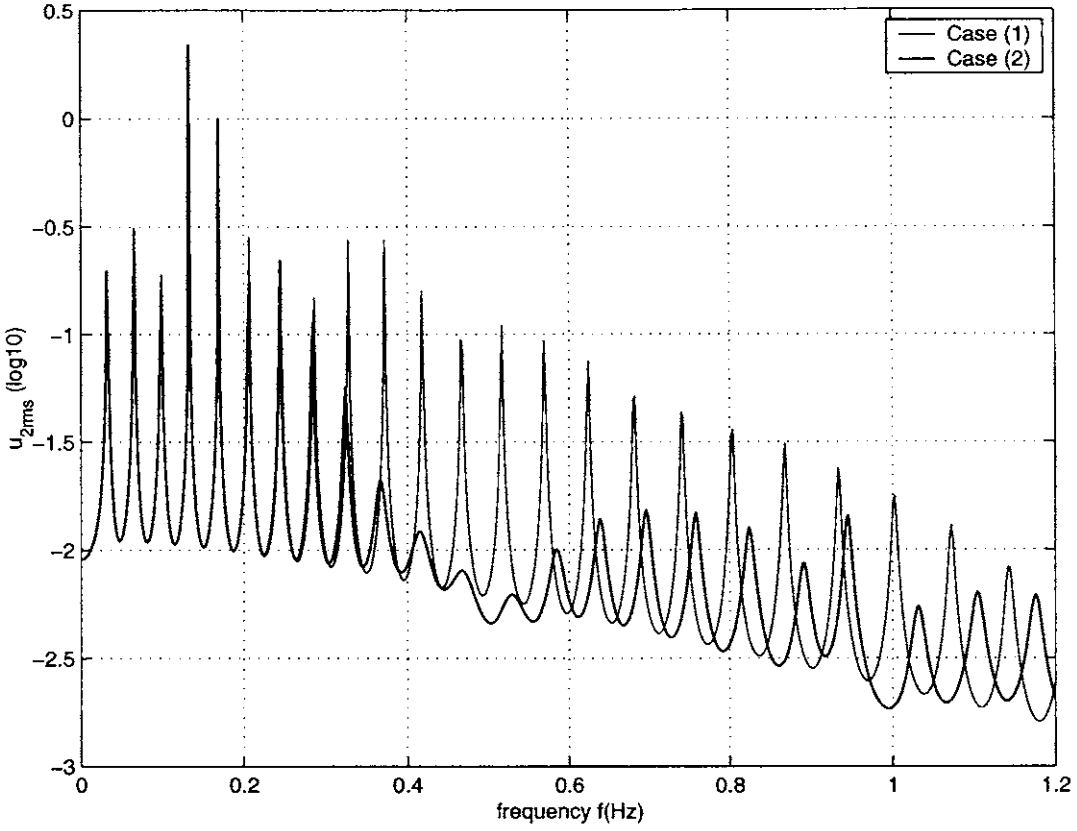

Figure 8-31: The RMS frequency response of the external riser (generally coupled, NCOUP=3)

Chapter 9

Summary

9.1 New contributions

This thesis makes new contributions in the following aspects:

(1) The WKB-based dynamic stiffness method is presented by combining the DSM procedure with the WKB approximation for effectively modeling non-uniform marine risers with variable properties. The WKB-based elemental dynamic stiffness matrix and the frequency-dependent shape function for a general non-uniform beam structure are derived and their implicit forms are given. Natural frequencies are found by equating to zero the determinant of the global dynamic stiffness matrix, which is obtained by following the procedure in the conventional FEM. Compared with the FEM, much fewer elements are needed to solve for low natural frequencies as well as high frequencies. Moreover, mode shapes, slopes and curvatures are important data to predict the VIV of a riser. The formulas for calculating them are derived. With the modal data as an input file (common.mds), SHEAR7 predicts the VIV of a non-uniform riser.

(2) The W-W algorithm for a uniform beam structure is extended to the analysis of a general non-uniform one. This algorithm further improves the WKB-based DSM and provides a foolproof basis for the automatic computation of any and all natural frequencies for a non-uniform beam structure. With this technique, many fewer elements are required for finding natural frequencies. Only one element is needed for the

analysis of a simply-supported uniform riser under variable tension. There potentially exist numerical problems in analyzing marine riser models with complex boundary conditions. The WKB-based DSM with the W-W algorithm effectively overcomes the problems and accurately generates modal data for predicting VIV.

(3) The TMM is employed to discuss the wave propagation in a beam system with discontinuities. Wave reflection and transmission matrices are derived in terms of transfer-matrix elements. When the length of a beam structure is very large and high natural frequencies are desired, the TMM has numerical problems in the analysis. The symbolic operation-based TMM is presented for overcoming the numerical problems. A non-uniform beam structure is often approximated in TMM by a number of stepped uniform beams. Three approximate schemes for a uniform beam under variable tension are specifically investigated and their convergence rates are compared. Based on the relationship between dynamic stiffness and transfer matrices, a new transfer matrix for describing the non-uniformity of a general beam structure is implicitly derived and transformed into the corresponding delta-matrix for overcoming numerical problems.

(4) The internal relationships between the DSM and TMM and between their corresponding matrices are generalized by introducing transformation matrices due to different sign conventions. Using the relationships, this thesis provides a unified approach to the analysis of a non-uniform beam system with discontinuities. The WKB-based DSM is powerful in analyzing a non-uniform beam. For a member element with discontinuities, its overall transfer matrix is found by the TMM and the matrix is then transformed into the corresponding dynamic stiffness matrix. Since unwanted degrees of freedom are eliminated in the TMM, a limited number of degrees of freedom are needed to analyze a general non-uniform beam system with discontinuities. Based on the relationship between transfer and dynamic stiffness matrices, the dynamic stiffness library, shown in Appendix C, is further established.

(5) The means of suppressing vibration of a general beam structure is explored. The optimal tuning of multiple identical DVAs to a uniform beam with general boundary conditions is analytically found. On the basis of the WKB-based DSM, the opti-

mal tuning of multiple identical DVAs to a non-uniform beam system under variable tension is investigated. The effect of structural damping on the optimal tuning is also discussed. In a double-uniform beam system weakly coupled by longitudinally distributed discrete springs and dampers, one beam is used as a dynamic absorbing beam optimally tuned to the other one and the optimal solution is obtained. Moreover, the wave-absorbing termination for a beam system, based on the research by Vandiver and Li, is derived.

(6) The vibration analysis of a coupled double-beam system is systematically investigated from the simple to the complicated. This thesis discusses the vibration analysis of a double-uniform beam system weakly coupled by discrete springs and dampers distributed longitudinally. Similar research is done for the coupled system where both uniform beams are under constant tension. When both beams are additionally ideal fluid-coupled, the effects of fluid on natural frequencies and mode shapes are studied. A practical composite riser structure is modeled as a generally coupled double-beam system, where both beams are non-uniform ones under variable tension, fluid is viscous, and stiffness and damping from centralizers are longitudinally distributed. The theoretical formulation of such a complicated system is derived. The effects on frequency response of coupling factors are numerically evaluated. Natural frequencies of the coupled system are effectively found by means of the WKB-based DSM with the W-W algorithm. In order to check damping effects, complex natural frequencies of the system are obtained by using the Muller method.

9.2 Further work

Further research is recommended as follows:

(1) to implement the improved numerical models in a VIV prediction program such as Shear7 so that potential numerical problems in the analysis of marine risers with complex boundary conditions will be overcome;

(2) to generate a guideline to an optimal design of coupling components for suppressing vibration of a coupled system;

(3) to extend the mathematical formulation of a coupled double-riser system to analyzing a more complicated system; for example, there is the third pipe inside of an internal riser; and

(4) to apply the improved methods to the analysis of a submerged floating pipeline in deep water. There are discrete buoyancy elements and tethers distributed along a pipeline. Each span part can be regarded as one element. The TMM is first employed to obtain the overall transfer matrix and then the matrix is transformed into the corresponding dynamic stiffness matrix. In this way, all intermediate degrees of freedom within a span are eliminated. Hence, a non-uniform pipeline system with discontinuities is effectively analyzed by means of a limited number of degrees of freedom. With the modal data found by the improved approaches, the VIV and fatigue life are predicted by using Shear7. We have conducted some preliminary work in this aspect.

Appendix A

Vibration Analysis of a Riser Under Linearly Varying Tension Using FEM

A.1 Derivation of geometric stiffness matrix

In this section, it is of main interest that FEM is used to analyze vibration analysis of a beam under linearly varying tension. The work due to axial load is :

$$W = -\frac{1}{2}\int_0^l N(x)(\frac{\partial v}{\partial x})^2 dx, \tag{A.1}$$

where tension $N(x) = T_0 + \alpha x$, and α is the proportional factor.
Eq. (A.1) is rewritten as:

$$W = -\frac{1}{2}\int_0^l (T_0 + \alpha x)(\frac{\partial v}{\partial x})^2 dx = \underbrace{-\frac{1}{2}\int_0^l T_0(\frac{\partial v}{\partial x})^2 dx}_{(I)} \underbrace{-\frac{\alpha}{2}\int_0^l x(\frac{\partial v}{\partial x})^2 dx}_{(II)} \tag{A.2}$$

From Eq. (A.2), the corresponding geometric stiffness induced by linearly varying tension consists of two parts, (I) and (II). Part (I) is that due to constant minimum tension T_0 while Part (II) is that due to the linear increment of tension.

We first consider Part (II):

$$\frac{\alpha}{2}\int_0^l x(\frac{\partial v}{\partial x})^2 dx = \frac{\alpha}{2l} q_e^T [\int_0^1 (x_0 + l\xi)(\frac{dN_e}{d\xi})^T \frac{dN_e}{d\xi}] q_e. \tag{A.3}$$

The corresponding geometric stiffness K_{II} induced by linear increment of tension is:

$$K_{II} = \frac{\alpha}{l}\int_0^1 (x_0 + l\xi)(\frac{dN_e}{d\xi})^T \frac{dN_e}{d\xi} d\xi. \tag{A.4}$$

K_{II} is further expressed as:

$$\begin{aligned} K_{II} &= \frac{\alpha}{l}[x_0 \int_0^1 (\frac{dN_e}{d\xi})^T \frac{dN_e}{d\xi} d\xi + l\int_0^1 \xi(\frac{dN_e}{d\xi})^T \frac{dN_e}{d\xi} d\xi] \\ &= \frac{\alpha x_0}{l}\int_0^1 (\frac{dN_e}{d\xi})^T \frac{dN_e}{d\xi} d\xi + \alpha\int_0^1 \xi(\frac{dN_e}{d\xi}) d\xi \\ &\equiv \frac{\alpha x_0}{T_0} K_I + \alpha\int_0^1 \xi(\frac{dN_e}{d\xi})^T \frac{dN_e}{d\xi} d\xi, \end{aligned} \tag{A.5}$$

in which $K_I \equiv \frac{T_0}{l}\int_0^1 (\frac{dN_e}{d\xi})^T \frac{dN_e}{d\xi} d\xi$ is the stiffness matrix induced by constant tension T_0.

Maple V is used to derive the following integral:

$$K_G{}'' = \int_0^1 \xi(\frac{dN_e}{d\xi})^T \frac{dN_e}{d\xi} d\xi, \tag{A.6}$$

where $(\frac{dN_e}{d\xi})^T = \begin{pmatrix} 6\xi(\xi-1) \\ l(1-4\xi+3\xi^2) \\ 6\xi(1-\xi) \\ l(3\xi^2-2\xi) \end{pmatrix}$.

We thus obtain:

$$K_G{}'' = \int_0^1 \xi(\frac{dN_e}{d\xi})^T \frac{dN_e}{d\xi} d\xi = \begin{pmatrix} \frac{3}{5} & \frac{1}{10}l & -\frac{3}{5} & 0 \\ \frac{1}{10}l & \frac{1}{30}l^2 & -\frac{1}{10}l & -\frac{1}{60}l^2 \\ -\frac{3}{5} & -\frac{1}{10}l & \frac{3}{5} & 0 \\ 0 & -\frac{1}{60}l^2 & 0 & \frac{1}{10}l^2 \end{pmatrix}. \tag{A.7}$$

Equation (A.5) leads to:

$$K_{II} = \frac{\alpha x_0}{T_0} K_I + \alpha K_G''. \tag{A.8}$$

Similarity, the stiffness K_I is found by using Maple V:

$$K_I = \frac{T_0}{l} \begin{pmatrix} \frac{6}{5} & \frac{1}{10}l & -\frac{6}{5} & \frac{1}{10}l \\ \frac{1}{10}l & \frac{2}{15}l^2 & -\frac{1}{10}l & -\frac{1}{30}l^2 \\ -\frac{6}{5} & -\frac{1}{10}l & \frac{6}{5} & -\frac{1}{10}l \\ \frac{1}{10}l & -\frac{1}{30}l^2 & -\frac{1}{10}l & \frac{2}{15}l^2 \end{pmatrix}. \tag{A.9}$$

Finally, with Eqs. (A.8) and (A.9), we can find that the geometric stiffness matrix due to the linearly varying tension is:

$$K = K_I + K_{II} \tag{A.10}$$

$$= \frac{T_0 + \alpha x_0}{l} K_G' + \alpha K_G'', \tag{A.11}$$

in which, K_G'' is shown in (A.7) and K_G' is:

$$K_G' = \begin{pmatrix} \frac{6}{5} & \frac{1}{10}l & -\frac{6}{5} & \frac{1}{10}l \\ \frac{1}{10}l & \frac{2}{15}l^2 & -\frac{1}{10}l & -\frac{1}{30}l^2 \\ -\frac{6}{5} & -\frac{1}{10}l & \frac{6}{5} & -\frac{1}{10}l \\ \frac{1}{10}l & -\frac{1}{30}l^2 & -\frac{1}{10}l & \frac{2}{15}l^2 \end{pmatrix}. \tag{A.12}$$

A.2 Example

Example 1 a 1400-ft Long Riser Under a Linearly Varying Tension

Length $l = 1400\, ft$;

Young's modulus $E = 29000$ Ksi;

Moment of inertia $I = 0.02074\, ft^4$;

Total mass per length including added mass effects $m = 7.45789\, Slugs/ft$;

Minimum tension $T_0 = 50000.0$ Pounds;

Linearly varying tension $\alpha = 115.25\, lb/ft$.

A FEM code, which incorporates the new type element, is developed by using Matlab. Figure A-1 shows the results. This figure shows that much fewer elements is needed

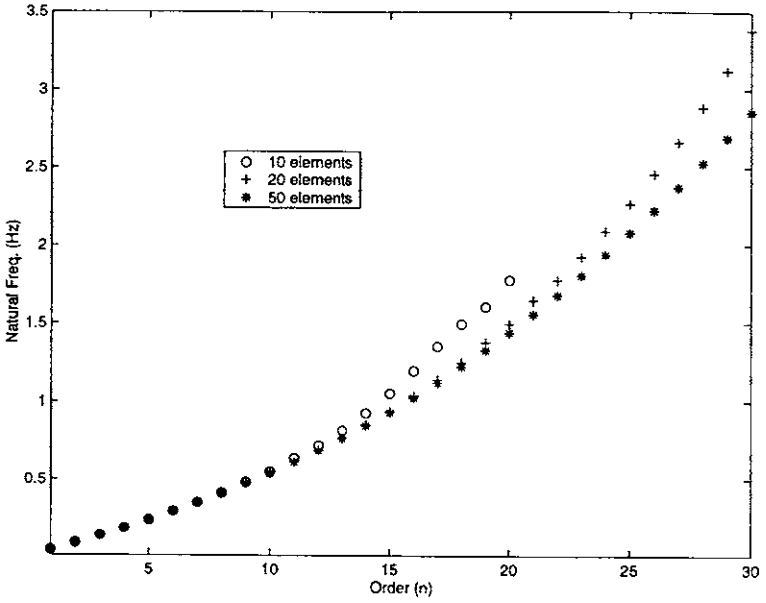

Figure A-1: Natural frequencies of the 1400-ft riser

to obtain lower-order natural frequencies. Table A-1 also shows Shear7's result for comparison. In this table, the new FEM uses 50 elements to solve this problem. Figure A-2 depicts the first three mode shapes.

Further, in order to check the validness of using the new geometric stiffness matrix induced by linear varying tension, use the approximation method for comparison, i.e. assume each element under its average tension. Table A-2 shows the results and indicates that tension has higher influence on lower natural frequencies than on higher frequencies. In Table A-2, the exact values are the converged ones obtained by using more elements . It can be seen that the new geometric stiffness matrix is more efficient.

Increasing the linearly varying tension factor α up to be $1152.5 lb/ft$, the result comparison is shown in Table A-3. With higher value of α, the derived matrix works much better, especially for lower natural frequencies.

Hence, the advantages of the new geometric stiffness matrix induced by linearly

Order	shear7	New FEM
1	0.0447	0.0446
2	0.0902	0.0903
3	0.1370	0.1372
4	0.1857	0.1861
5	0.2368	0.2372
6	0.2904	0.2909
7	0.3470	0.3475
8	0.4067	0.4073
9	0.4699	0.4705
10	0.5367	0.5374
11	0.6073	0.6080
12	0.6819	0.6827
13	0.7607	0.7616

Table A.1: Comparison of natural frequencies (Hz)

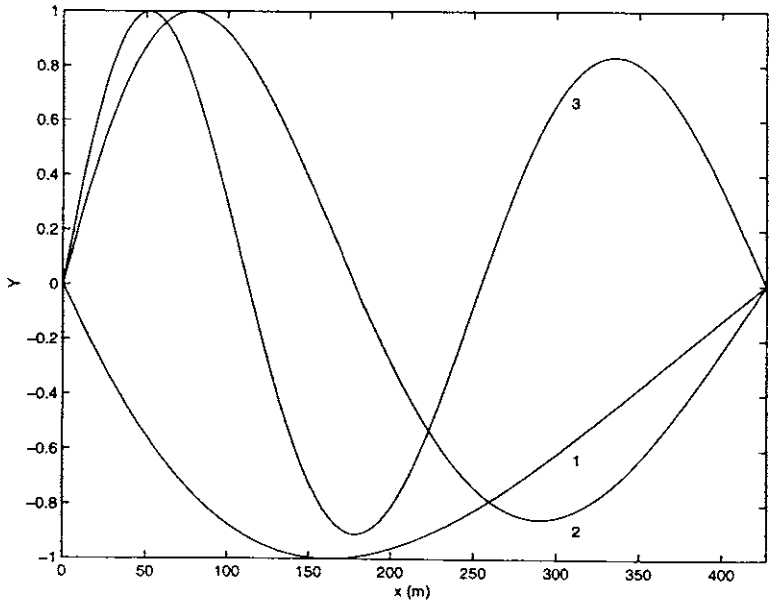

Figure A-2: The first three mode shapes of the 1400-ft riser

Order	Exact	FEM	Approx.
1	0.0446	0.0446	0.0447
2	0.0903	0.0903	0.0905
3	0.1372	0.1373	0.1376
4	0.1861	0.1861	0.1865
5	0.2372	0.2374	0.2379
6	0.2909	0.2916	0.2922
7	0.3475	0.3494	0.3501
8	0.4073	0.4120	0.4129
9	0.4705	0.4811	0.4812
10	0.5374	0.5479	0.5455

Table A.2: Comparison of natural frequencies (Hz)

Order	Exact	FEM	Approx.
1	0.0969	0.0970	0.0996
2	0.1993	0.1996	0.2043
3	0.3033	0.3038	0.3105
4	0.4095	0.4109	0.4191
5	0.5183	0.5214	0.5302
6	0.6300	0.6355	0.6415
7	0.7444	0.7525	0.7509
8	0.8618	0.8722	0.8701
9	0.9820	1.0003	1.0099
10	1.1052	1.1368	1.1421

Table A.3: Comparison of natural frequencies (Hz)

varying tension lie in:

(1) The element can describe the case that tension is not of slowly varying.

(2) Compared with using a conventional FEM, the new geometric stiffness matrix requires fewer elements for solving natural frequencies and mode shapes of a beam under a linearly varying tension.

Appendix B

The frequency dependent shape function

With the Maple V, Chapter 4 derives the frequency dependent shape function Φ in Eq.(4.13) as follows:

$$
\begin{aligned}
\varphi(1) &= -\frac{1}{\delta_1}(T_2(s)B_1(s)T_2(1)T_1(0)h_1(0)T_1(1)B_2B_3h_1(1) \\
&+ T_2(s)B_1(s)T_2(1)T_1(0)h_1(0)T_1(1)B_1h_2(1)B_4 \\
&+ T_2(s)B_2(s)T_1^2(1)T_2(0)h_2(0)h_1(1)B_3^2 \\
&- T_2(s)B_2(s)T_1^2(1)T_2(0)h_2(0)h_1(1)B_4^2 \\
&- T_2(s)B_2(s)T_1(1)B_1T_2(1)T_1(0)h_1(0)B_3h_1(1) \\
&+ T_2(s)B_2(s)T_1(1)B_2T_2(1)h_2(1)T_1(0)h_1(0)B_4 \\
&- T_1(s)B_3(s)T_2(0)h_2(0)T_2(1)T_1(1)B_2B_3h_1(1) \\
&- T_1(s)B_3(s)T_2(0)h_2(0)T_2(1)T_1(1)B_1h_2(1)B_4 \\
&+ T_1(s)B_4(s)T_2(1)T_2(0)h_2(0)T_1(1)B_2B_4h_1(1) \\
&+ T_1(s)B_4(s)T_2(1)T_2(0)h_2(0)T_1(1)B_3B_1h_2(1) \\
&- T_1(s)B_4(s)T_2^2(1)B_1^2T_1(0)h_1(0)h_2(1) \\
&- T_1(s)B_4(s)T_2^2(1)B_2^2h_2(1)T_1(0)h_1(0)) \\
\varphi(2) &= \frac{l}{\delta_1}(-T_2(s)B_1(s)T_1^2(1)T_2(0)h_1(1)B_3^2
\end{aligned}
$$

$$
\begin{aligned}
&+ T_2(s)B_1(s)T_1^2(1)T_2(0)h_1(1)B_4^2 \\
&- T_2(s)B_1(s)T_1(1)B_2T_2(1)T_1(0)B_4h_1(1) \\
&- T_2(s)B_1(s)T_1(1)B_1T_2(1)h_2(1)T_1(0)B_3 \\
&+ T_2(s)B_2(s)T_2(1)T_1(0)T_1(1)B_1B_4h_1(1) \\
&- T_2(s)B_2(s)T_2(1)T_1(0)T_1(1)B_2h_2(1)B_3 \\
&+ T_1(s)B_3(s)T_2(1)B_1T_2(0)B_3T_1(1)h_1(1) \\
&+ T_1(s)B_3(s)T_2^2(1)B_1^2h_2(1)T_1(0) \\
&- T_1(s)B_3(s)T_2(1)B_2h_2(1)T_2(0)B_4T_1(1) \\
&+ T_1(s)B_3(s)T_2^2(1)B_2^2h_2(1)T_1(0) \\
&- T_1(s)B_4(s)T_2(1)T_2(0)T_1(1)B_1B_4h_1(1) \\
&+ T_1(s)B_4(s)T_2(1)T_2(0)T_1(1)B_2h_2(1)B_3) \\
\varphi(3) &= \frac{1}{\delta_1}(T_2(s)B_1(s)T_1(0)h_1(0)T_2(0)B_3T_1(1)h_1(1) \\
&+ T_2(s)B_1(s)T_1^2(0)h_1(0)B_1T_2(1)h_2(1) \\
&- T_2(s)B_2(s)T_1(0)T_2(0)h_2(0)B_4T_1(1)h_1(1) \\
&+ T_2(s)B_2(s)T_1^2(0)B_2T_2(1)h_2(1)h_1(0) \\
&- T_1(s)B_3(s)T_2^2(0)h_2(0)B_3T_1(1)h_1(1) \\
&- T_1(s)B_3(s)T_2(0)h_2(0)B_1T_2(1)h_2(1)T_1(0) \\
&+ T_1(s)B_4(s)T_2^2(0)h_2(0)B_4T_1(1)h_1(1) \\
&- T_1(s)B_4(s)T_2(0)B_2T_2(1)h_2(1)T_1(0)h_1(0)) \\
\varphi(4) &= -\frac{l}{\delta_1}(T_2(s)B_1(s)T_1(0)h_1(0)T_2(0)B_4T_1(1) \\
&- T_2(s)B_1(s)T_1^2(0)h_1(0)B_2T_2(1) \\
&- T_2(s)B_2(s)T_1(0)T_2(0)h_2(0)B_3T_1(1) \\
&+ T_2(s)B_2(s)T_1^2(0)B_1T_2(1)h_1(0) \\
&- T_1(s)B_3(s)T_2^2(0)h_2(0)B_4T_1(1) \\
&+ T_1(s)B_3(s)T_2(0)h_2(0)B_2T_2(1)T_1(0) \\
&+ T_1(s)B_4(s)T_2^2(0)h_2(0)B_3T_1(1)
\end{aligned}
$$

$$
\begin{aligned}
& - T_1(s)B_4(s)T_2(0)B_1T_2(1)T_1(0)h_1(0)) \\
\delta_1 \;=\; & -T_2^2(0)h_2(0)T_1^2(1)h_1(1)B_3^2 \\
& + T_2^2(0)h_2(0)T_1^2(1)h_1(1)B_4^2 \\
& - T_2(0)h_2(0)T_1(1)B_2T_2(1)T_1(0)B_4h_1(1) \\
& - T_2(0)h_2(0)T_1(1)B_1T_2(1)h_2(1)T_1(0)B_3 \\
& + B_1T_2(1)T_1(0)h_1(0)T_2(0)B_3T_1(1)h_1(1) \\
& + B_1^2T_2^2(1)T_1^2(0)h_1(0)h_2(1) \\
& - B_2T_2(1)h_2(1)T_1(0)h_1(0)T_2(0)B_4T_1(1) \\
& + B_2^2T_2^2(1)h_2(1)T_1^2(0)h_1(0). \qquad \text{(B.1)}
\end{aligned}
$$

Appendix C

Dynamic Stiffness Library

C.1 A general non-uniform beam under variable tension

Chapter 4 derives the dynamic stiffness matrix of a general non-uniform beam under variable tension by using the WKB approximation. With the aid of the mathematical software Maple V, we find the upper triangular elements of the WKB-based dynamic stiffness matrix $\mathbf{k}$ as follows:

$$
\begin{aligned}
\mathbf{k}(1,1) &= \frac{-E_0 I_0}{l^3 \delta} h_2(0) T_2(0) T_2(1) T_1(0) h_1(0) T_1(1) (B_2 B_3 h_1(1) \\
&+ B_1 h_2(1) B_4) P(0) (h_2^2(0) + h_1^2(0)) \\
\mathbf{k}(1,2) &= \frac{-E_0 I_0}{l^2 \delta} (T_2^2(0) h_2^3(0) T_1^2(1) P(0) h_1(1) B_3^2 \\
&- T_2^2(0) h_2^3(0) T_1^2(1) P(0) h_1(1) B_4^2 \\
&+ T_2(0) h_2^3(0) T_1(1) P(0) B_2 T_2(1) T_1(0) B_4 h_1(1) \\
&+ T_2(0) h_2^3(0) T_1(1) P(0) h_1(1) B_4^2 \\
&+ T_2(0) h_2^3(0) T_1(1) P(0) B_2 T_2(1) T_1(0) B_4 h_1(1) \\
&+ T_2(0) h_2^3(0) T_1(1) P(0) B_1 T_2(1) h_2(1) T_1(0) B_3 \\
&+ T_2^2(0) h_2(0) T_1^2(1) Q(0) h_1(1) B_3^2
\end{aligned}
$$

$$
\begin{aligned}
&- T_2^2(0)h_2(0)T_1^2(1)Q(0)h_1(1)B_4^2 \\
&+ T_2(0)h_2(0)T_1(1)Q(0)B_2T_2(1)T_1(0)B_4h_1(1) \\
&+ T_2(0)h_2(0)T_1(1)Q(0)B_1T_2(1)h_2(1)T_1(0)B_3 \\
&+ h_1^3(0)T_1(0)T_2(1)P(0)B_1T_2(0)B_3T_1(1)h_1(1) \\
&+ h_1^3(0)T_1^2(0)T_2^2(1)P(0)B_1^2h_2(1) \\
&- h_1^3(0)T_1(0)T_2(1)P(0)B_2h_2(1)B_4T_1(1)T_2(0) \\
&+ h_1^3(0)T_1^2(0)T_2^2(1)P(0)B_2^2h_2(1) \\
&- h_1(0)T_1(0)T_2(1)Q(0)B_1T_2(0)B_3T_1(1)h_1(1) \\
&- h_1(0)T_1^2(0)T_2^2(1)Q(0)B_1^2h_2(1) \\
&+ h_1(0)T_1(0)T_2(1)Q(0)B_2h_2(1)B_4T_2(0)T_1(1) \\
&- h_1(0)T_1^2(0)T_2^2(1)Q(0)B_2^2h_2(1))
\end{aligned}
$$

$$
\begin{aligned}
\mathbf{k}(1,3) &= \frac{E_0I_0}{l^3\delta}h_2(0)T_2(0)T_1(0)h_1(0)(T_2(0)B_3T_1(1)h_1(1) \\
&+ B_1T_2(1)h_2(1)T_1(0))P(0)(h_2^2(0)+h_1^2(0)) \\
\mathbf{k}(1,4) &= \frac{-E_0I_0}{l^2}h_2(0)T_2(0)T_1(0)h_1(0)(T_2(0)B_4T_1(1) \\
&- B_2T_2(1)T_1(0))P(0)(h_2^2(0)+h_1^2(0)) \\
\mathbf{k}(2,2) &= -\frac{E_0I_0}{l\delta}P(0)T_2(0)T_2(1)T_1(0)T_1(1)(B_1B_4h_1(1) \\
&- B_2h_2(1)B_3)(h_2^2(0)+h_1^2(0)) \\
\mathbf{k}(2,3) &= \frac{E_0I_0}{l^2\delta}P(0)T_2(0)T_1(0)(T_2(0)h_2(0)(B_4T_1(1)h_1(1) \\
&- B_2T_2(1)h_2(1)T_1(0)h_1(0))(h_2^2(0)+h_1^2(0)) \\
\mathbf{k}(2,4) &= -\frac{E_0I_0}{l\delta}P(0)T_2(0)T_1(0)(T_2(0)h_2(0)B_3T_1(1) \\
&- B_1T_2(1)T_1(0)h_1(0))(h_2^2(0)+h_1^2(0)) \\
\mathbf{k}(3,3) &= -\frac{E_0I_0}{l^3\delta}T_2(1)h_2(1)T_1(0)T_2(0)T_1(1)h_1(1)(B_2h_2^2(1)h_1(0)P(1)B_3 \\
&+ 2B_2h_1(0)Q(1)B_3 + B(1)h_2^2(1)P(1)h_2(0)B_4 \\
&+ 2B_1Q(1)h_2(0)B_4 + h_2(0)B_4h_1^2(1)P(1)B_1 \\
&+ B_3h_1^2(1)P(1)B_2h_1(0)) \\
\mathbf{k}(3,4) &= -\frac{E_0I_0}{l^2\delta}(-B_2T_2(1)h_2^3(1)T_1(0)h_1(0)P(1)T_2(0)B_4T_1(1)
\end{aligned}
$$

$$
\begin{aligned}
&+ B_2^2T_2^2(1)h_2^2(1)T_1^2(0)h_1(0)P(1)\\
&- B_2T_2(1)h_2(1)T_1(0)h_1(0)Q(1)T_2(0)B_4T_1(1)\\
&+ B_2^2T_2^2(1)h_2(1)T_1^2(0)h_1(0)Q(1)\\
&- B_1T_2(1)h_2^3(1)T_1(0)P(1)T_2(0)h_2(0)B_3T_1(1)\\
&+ B_1^2T_2^2(1)h_2^3(1)T_1^2(0)P(1)h_1(0)\\
&- B_1T_2(1)h_2(1)T_1(0)Q(1)T_2(0)h_2(0)B_3T_1(1)\\
&+ B_1^2T_2^2(1)h_2(1)T_1^2(0)Q(1)h_1(0)\\
&- T_2^2(0)h_2(0)B_4^2T_1^2(1)h_1^3(1)P(1)\\
&+ T_2(0)h_2(0)B_4T_1(1)h_1^3(1)P(1)B_2T_2(1)T_1(0)\\
&- T_2^2(0)h_2(0)B_4^2T_1^2(1)h_1(1)Q(1)\\
&+ T_2(0)h_2(0)B_4T_1(1)h_1(1)Q(1)B_2T_2(1)T_1(0)\\
&+ T_2^2(0)B_3^2T_1^2(1)h_1^3(1)P(1)h_2(0)\\
&- T_2(0)B_3T_1(1)h_1^3(1)P(1)B_1T_2(1)T_1(0)h_1(0)\\
&+ T_2^2(0)B_3^2T_1^2(1)h_1(1)Q(1)h_2(0)\\
&- T_2(0)B_3T_1(1)h_1(1)Q(1)B_1T_2(1)T_1(0)h_1(0)\\
\mathbf{k}(4,4) &= \frac{E_0I_0}{l\delta}P(1)T_2(1)T_1(0)T_2(0)T_1(1)(-B_1h_2^2(1)h_1(0)B_4\\
&+ B_2h_2^2(1)h_2(0)B_3 + B_3h_1^2(1)h_2(0)B_2 - B_4h_1^2(1)B_1h_1(0))\\
\delta &= T_2^2(0)h_2(0)T_1^2(1)h_1(1)B_3^2 - T_2^2(0)h_2(0)T_1^2(1)h_1(1)B_4^2\\
&+ T_2(0)h_2(0)T_1(1)B_2T_2(1)T_1(0)B_4h_1(1)\\
&+ T_2(0)h_2(0)T_1(1)B_1T_2(1)h_2(1)T_1(0)B_3\\
&- B_1T_2(1)T_1(0)h_1(0)T_2(0)B_3T_1(1)h_1(1)\\
&+ B_2T_2(1)h_2(1)T_1(0)h_1)(0)T_2(0)B_4T_1(1)\\
&- B_2^2T_2^2(1)h_2(1)T_1^2(0)h_1(0). \qquad \text{(C.1)}
\end{aligned}
$$

C.2 A uniform Bernoulli-Euler beam

Eq. (6.30) shows the upper triangular elements of the dynamic stiffness matrix of a uniform beam. It is rewritten in the abbreviated form:

$$\mathbf{k} = \frac{EI}{l^3}\begin{bmatrix} F_6 & -F_4 l & F_5 & F_3 l \\ -F_4 l & F_2 l^2 & -F_3 l & F_1 l^2 \\ F_5 & -F_3 l & F_6 & F_4 l \\ F_3 l & F_1 l^2 & F_4 l & F_2 l^2 \end{bmatrix}, \tag{C.2}$$

where the frequency functions F_i (i=1-6) are defined as:

$F_1 = -\lambda(\sinh\lambda - \sin\lambda)/\delta$

$F_2 = -\lambda(\cosh\lambda\sin\lambda - \sinh\lambda\cos\lambda)/\delta$

$F_3 = -\lambda^2(\cosh\lambda - \cos\lambda)/\delta$

$F_4 = \lambda^2(\sinh\lambda\sin\lambda)/\delta$

$F_5 = \lambda^3(\sinh\lambda + \sin\lambda)/\delta$

$F_6 = -\lambda^3(\cosh\lambda\sin\lambda + \sinh\lambda\cos\lambda)/\delta$

$\delta = \cosh\lambda\cos\lambda - 1$

C.3 A Beam Subjected a Constant Tension

If the effects of the constant axial force P (tension is positive), shear deformation and written inertia are all included, the resulting dynamic stiffness matrix can still be written in the form as in Eq.(1), i.e.,

$$\mathbf{k} = \frac{EI}{l^3}\begin{bmatrix} F_6 & -F_4 l & F_5 & F_3 l \\ -F_4 l & F_2 l^2 & -F_3 l & F_1 l^2 \\ F_5 & -F_3 l & F_6 & F_4 l \\ F_3 l & F_1 l^2 & F_4 l & F_2 l^2 \end{bmatrix}, \tag{C.3}$$

where the frequency functions are:

$F_1 = (\alpha + \eta\beta)(\eta \sinh \alpha - \sin \beta)/\delta$

$F_2 = (\alpha + \eta\beta)(\sin \beta \cosh \alpha - \eta \cos \beta \sinh \alpha)/\delta$

$F_3 = \eta(1 - s^2p^2)(\alpha^2 + \beta^2)(cosh\alpha - \cos \beta)/\delta$

$F_4 = el[(\alpha - \eta\beta)(1 - \cosh \alpha \cos \beta) - (\beta + \eta\alpha) \sin \beta \sinh \alpha]/\delta$

$F_5 = -b^2(\alpha + \eta\beta)(\sinh \alpha + \eta \sin \beta)/\alpha\beta\delta$

$F_6 = b^2(\alpha + \eta\beta)(\sinh \alpha \cos \beta + \eta \sin \beta \cosh \alpha)/\alpha\beta\delta$

where,

$b^2 = \frac{\rho A l^4 \omega^2}{EI}$

$r^2 = \frac{I_o}{Al^2}$

$s^2 = \frac{EI}{GA_s l^2}$

$p^2 = -\frac{Pl^2}{EI}$

$\Delta = \frac{p^2}{b^2} + r^2(1 - s^2p^2) + s^2$

$h = \frac{(1-s^2p^2)\alpha^2 + b^2s^2}{\alpha l}$

$e = \frac{1-s^2p^2)\beta^2 - b^2s^2}{\beta l}$

$\eta = e/h$

$\delta = 2\eta(1 - \cosh \alpha \cos \beta) + (1 - \eta^2) \sin \beta \sinh \alpha$

C.4 Combination of a uniform beam with point mass

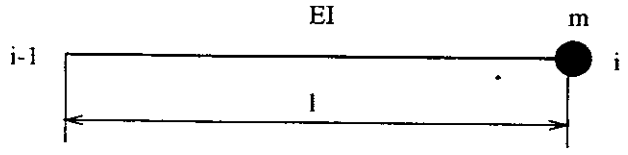

Figure C-1: Combination of beam with point mass

Figure C-1 shows the combination of a uniform beam with a point mass on its right end. The upper triangular elements of dynamic stiffness matrix **k** are:

$$
\begin{aligned}
\mathbf{k}(1,1) &= -\frac{EI\,k^3\,(\cos(kl)\sinh(kl)+\cosh(kl)\sin(kl))}{\cosh(kl)\cos(kl)-1};\\
\mathbf{k}(1,2) &= -\frac{EI\,k^2\sinh(kl)\sin(kl)}{\cosh(kl)\cos(kl)-1};\\
\mathbf{k}(1,3) &= \frac{EI\,k^3\,(\sinh(kl)+\sin(kl))}{\cosh(kl)\cos(kl)-1};\\
\mathbf{k}(1,4) &= \frac{EI\,k^2\,(-\cosh(kl)+\cos(kl))}{\cosh(kl)\cos(kl)-1};\\
\mathbf{k}(2,2) &= \frac{EI\,k\,(-\cosh(kl)\sin(kl)+\cos(kl)\sinh(kl))}{\cosh(kl)\cos(kl)-1};\\
\mathbf{k}(2,3) &= -\frac{EI\,k^2\,(-\cosh(kl)+\cos(kl))}{\cosh(kl)\cos(kl)-1};\\
\mathbf{k}(2,4) &= -\frac{EI\,k\,(\sinh(kl)-\sin(kl))}{\cosh(kl)\cos(kl)-1};\\
\mathbf{k}(3,3) &= -\frac{m\,\omega^2\cosh(kl)\cos(kl)+k^3EI\,\sinh(kl)\cos(kl)+k^3EI\,\sin(kl)\cosh(kl)-m\,\omega^2}{\cosh(kl)\cos(kl)-1};\\
\mathbf{k}(3,4) &= \frac{EI\,k^2\sinh(kl)\sin(kl)}{\cosh(kl)\cos(kl)-1};\\
\mathbf{k}(4,4) &= \frac{EI\,k\,(-\cosh(kl)\sin(kl)+\cos(kl)\sinh(kl))}{\cosh(kl)\cos(kl)-1}.
\end{aligned}
\tag{C.4}
$$

C.5 Combination of a uniform tensioned beam with point mass

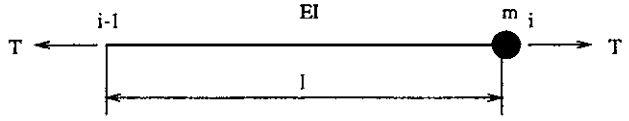

Figure C-2: Combination of tensioned beam with point mass

Figure C-2 shows the combination of a uniform tensioned beam with a point mass on its right end. The upper triangular elements of $\mathbf{k}$ are found as:

$$
\begin{aligned}
\mathrm{k}(1,1) &= [{\lambda_1}^3 \sin(\lambda_1 l)\cosh(\lambda_2 l) + {\lambda_2}^3 \sinh(\lambda_2 l)\cos(\lambda_1 l) \\
&\quad + {\lambda_1}^2 \lambda_2 \cos(\lambda_1 l)\sinh(\lambda_2 l) + \lambda_1 {\lambda_2}^2 \cosh(\lambda_2 l)\sin(\lambda_1 l)]\lambda_1 EI \lambda_2/\delta; \\
\mathrm{k}(1,2) &= [\lambda_1 EI {\lambda_2}^3 - 2\lambda_1 T\lambda_2 + {\lambda_1}^4 \sin(\lambda_1 l)\sinh(\lambda_2 l)EI \\
&\quad + {\lambda_1}^2 \sin(\lambda_1 l)\sinh(\lambda_2 l)T + {\lambda_2}^4 \sinh(\lambda_2 l)\sin(\lambda_1 l)EI \\
&\quad - {\lambda_2}^2 \sinh(\lambda_2 l)\sin(\lambda_1 l)T - \lambda_2 EI {\lambda_1}^3 \\
&\quad + {\lambda_1}^3 \lambda_2 \cos(\lambda_1 l)\cosh(\lambda_2 l)EI + 2\lambda_1 \lambda_2 \cos(\lambda_1 l)\cosh(\lambda_2 l)T \\
&\quad - \lambda_1 {\lambda_2}^3 \cosh(\lambda_2 l)\cos(\lambda_1 l)EI]/\delta; \\
\mathrm{k}(1,3) &= -[\lambda_1 EI \lambda_2 \left({\lambda_2}^2 + {\lambda_1}^2\right)(\lambda_1 \sin(\lambda_1 l) + \lambda_2 \sinh(\lambda_2 l))]/\delta; \\
\mathrm{k}(1,4) &= -[\lambda_1 EI \lambda_2 \left({\lambda_2}^2 + {\lambda_1}^2\right)(\cos(\lambda_1 l) - \cosh(\lambda_2 l))]/\delta; \\
\mathrm{k}(2,2) &= -EI\,[\cos(\lambda_1 l)\sinh(\lambda_2 l){\lambda_1}^3 - \cosh(\lambda_2 l)\sin(\lambda_1 l){\lambda_2}^3 \\
&\quad - \sin(\lambda_1 l)\lambda_2 \cosh(\lambda_2 l){\lambda_1}^2 + \sinh(\lambda_2 l)\lambda_1 \cos(\lambda_1 l){\lambda_2}^2]/\delta; \\
\mathrm{k}(2,3) &= \lambda_1 EI \lambda_2 \left({\lambda_2}^2 + {\lambda_1}^2\right)(\cos(\lambda_1 l) - \cosh(\lambda_2 l))/\delta; \\
\mathrm{k}(2,4) &= -EI \left({\lambda_2}^2 + {\lambda_1}^2\right)(\sin(\lambda_1 l)\lambda_2 - \sinh(\lambda_2 l)\lambda_1)/\delta; \\
\mathrm{k}(3,3) &= -[-2\lambda_1 \lambda_2 m\omega^2 \cos(\lambda_1 l)\cosh(\lambda_2 l) - {\lambda_1}^4 \lambda_2 \sin(\lambda_1 l)EI \cosh(\lambda_2 l) \\
&\quad - \lambda_1 {\lambda_2}^4 \sinh(\lambda_2 l)EI \cos(\lambda_1 l) + 2m\omega^2 \lambda_2 \lambda_1 \\
&\quad + m\omega^2 \sin(\lambda_1 l){\lambda_2}^2 \sinh(\lambda_2 l) - m\omega^2 \sinh(\lambda_2 l){\lambda_1}^2 \sin(\lambda_1 l) \\
&\quad - \cos(\lambda_1 l){\lambda_1}^3 {\lambda_2}^2 EI \sinh(\lambda_2 l) - {\lambda_1}^2 {\lambda_2}^3 \cosh(\lambda_2 l)EI \sin(\lambda_1 l)]/\delta; \\
\mathrm{k}(3,4) &= -[\lambda_1 EI {\lambda_2}^3 - 2\lambda_1 T\lambda_2 \\
&\quad + {\lambda_1}^4 \sin(\lambda_1 l)\sinh(\lambda_2 l)EI + {\lambda_1}^2 \sin(\lambda_1 l)\sinh(\lambda_2 l)T \\
&\quad + {\lambda_2}^4 \sinh(\lambda_2 l)\sin(\lambda_1 l)EI - {\lambda_2}^2 \sinh(\lambda_2 l)\sin(\lambda_1 l)T \\
&\quad - \lambda_2 EI {\lambda_1}^3 + {\lambda_1}^3 \lambda_2 \cos(\lambda_1 l)\cosh(\lambda_2 l)EI \\
&\quad + 2\lambda_1 \lambda_2 \cos(\lambda_1 l)\cosh(\lambda_2 l)T - \lambda_1 {\lambda_2}^3 \cosh(\lambda_2 l)\cos(\lambda_1 l)EI]/\delta \\
\mathrm{k}(4,4) &= -EI\,[\cos(\lambda_1 l)\sinh(\lambda_2 l){\lambda_1}^3 - \cosh(\lambda_2 l)\sin(\lambda_1 l){\lambda_2}^3 \\
&\quad - \sin(\lambda_1 l)\lambda_2 \cosh(\lambda_2 l){\lambda_1}^2 + \sinh(\lambda_2 l)\lambda_1 \cos(\lambda_1 l){\lambda_2}^2]/\delta; \\
\delta &= 2\lambda_1 \lambda_2 - \sinh(\lambda_2 l){\lambda_1}^2 \sin(\lambda_1 l) + \sin(\lambda_1 l){\lambda_2}^2 \sinh(\lambda_2 l)
\end{aligned}
$$

$$-2\,\lambda_1\,\lambda_2\,\cos(\lambda_1\,l)\cosh(\lambda_2\,l). \tag{C.5}$$

C.6 Combination of a tensioned beam with spring-dashpot support

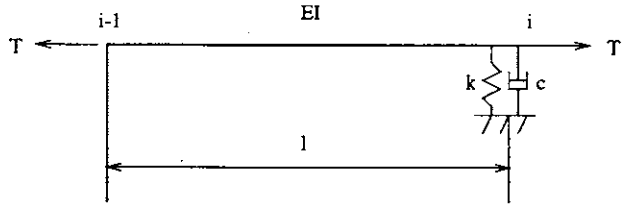

Figure C-3: Combination of tensioned beam with spring-dashpot support

The upper triangular elements of dynamic stiffness matrix of a uniform tensioned beam with spring-dashpot support, shown in Figure C-3, are:

$$\begin{aligned}
\mathbf{k}(1,1) &= -[\sin(\lambda_1 l)\lambda_1{}^3\cosh(\lambda_2 l) + \sinh(\lambda_2 l)\lambda_2{}^3\cos(\lambda_1 l) \\
&\quad +\lambda_1{}^2\lambda_2\sinh(\lambda_2 l)\cos(\lambda_1 l) + \lambda_1\lambda_2{}^2\cosh(\lambda_2 l)\sin(\lambda_1 l)]EI\;\lambda_1\lambda_2/\delta; \\
\mathbf{k}(1,2) &= -[\lambda_1 EI\;\lambda_2{}^3 - 2\,\lambda_2\lambda_1 T \\
&\quad +\lambda_1{}^4\sin(\lambda_1 l)\sinh(\lambda_2 l)EI + \lambda_1{}^2\sin(\lambda_1 l)\sinh(\lambda_2 l)T \\
&\quad +\lambda_2{}^4\sinh(\lambda_2 l)\sin(\lambda_1 l)EI - \lambda_2{}^2\sinh(\lambda_2 l)\sin(\lambda_1 l)T \\
&\quad -\lambda_2 EI\;\lambda_1{}^3 + \lambda_1{}^3\lambda_2\cos(\lambda_1 l)\cosh(\lambda_2 l)EI \\
&\quad +2\,\lambda_1\lambda_2\cos(\lambda_1 l)\cosh(\lambda_2 l)T - \lambda_1\lambda_2{}^3\cosh(\lambda_2 l)\cos(\lambda_1 l)EI]/\delta; \\
\mathbf{k}(1,3) &= [\lambda_1\lambda_2\left(\lambda_2{}^2 + \lambda_1{}^2\right)EI\;(\lambda_1\sin(\lambda_1 l) + \lambda_2\sinh(\lambda_2 l))]/\delta; \\
\mathbf{k}(1,4) &= -\lambda_1\lambda_2(\lambda_2{}^2 + \lambda_1{}^2)EI\;(-\cos(\lambda_1 l) + \cosh(\lambda_2 l))/\delta; \\
\mathbf{k}(2,2) &= -[-\cos(\lambda_1 l)\sinh(\lambda_2 l)\lambda_1{}^3 + \cosh(\lambda_2 l)\sin(\lambda_1 l)\lambda_2{}^3 \\
&\quad +\sin(\lambda_1 l)\lambda_2\cosh(\lambda_2 l)\lambda_1{}^2 - \sinh(\lambda_2 l)\lambda_1\cos(\lambda_1 l)\lambda_2{}^2]EI/\delta; \\
\mathbf{k}(2,3) &= \lambda_1\lambda_2\left(\lambda_2{}^2 + \lambda_1{}^2\right)EI\;(-\cos(\lambda_1 l) + \cosh(\lambda_2 l))/\delta;
\end{aligned}$$

$$
\begin{aligned}
\mathbf{k}(2,4) &= \left(\lambda_2{}^2 + \lambda_1{}^2\right) EI\ (\sin(\lambda_1 l)\lambda_2 - \sinh(\lambda_2 l)\lambda_1)\ /\delta; \\
\mathbf{k}(3,3) &= -[-2\,\lambda_1\lambda_2 k\cos(\lambda_1 l)\cosh(\lambda_2 l) - 2\,\lambda_1\lambda_2 i\omega\, c\cos(\lambda_1 l)\cosh(\lambda_2 l) \\
&\quad +\lambda_1{}^4\lambda_2\sin(\lambda_1 l)EI\ \cosh(\lambda_2 l) + \lambda_1\lambda_2{}^4\sinh(\lambda_2 l)EI\ \cos(\lambda_1 l) + 2\,k\lambda_2\lambda_1 \\
&\quad +k\sin(\lambda_1 l)\lambda_2{}^2\sinh(\lambda_2 l) - k\sinh(\lambda_2 l)\lambda_1{}^2\sin(\lambda_1 l) \\
&\quad +2\,i\omega\, c\lambda_2\lambda_1 + i\omega\, c\sin(\lambda_1 l)\lambda_2{}^2\sinh(\lambda_2 l) \\
&\quad -i\omega\, c\sinh(\lambda_2 l)\lambda_1{}^2\sin(\lambda_1 l) + \lambda_1{}^3\lambda_2{}^2\cos(\lambda_1 l)EI\ \sinh(\lambda_2 l) \\
&\quad +\cosh(\lambda_2 l)\lambda_1{}^2\lambda_2{}^3 EI\ \sin(\lambda_1 l)]/\delta; \\
\mathbf{k}(3,4) &= [\lambda_1 EI\,\lambda_2{}^3 - 2\,\lambda_2\lambda_1 T + \lambda_1{}^4\sin(\lambda_1 l)\sinh(\lambda_2 l)EI \\
&\quad +\lambda_1{}^2\sin(\lambda_1 l)\sinh(\lambda_2 l)T + \lambda_2{}^4\sinh(\lambda_2 l)\sin(\lambda_1 l)EI \\
&\quad -\lambda_2{}^2\sinh(\lambda_2 l)\sin(\lambda_1 l)T - \lambda_2 EI\,\lambda_1{}^3 \\
&\quad +\lambda_1{}^3\lambda_2\cos(\lambda_1 l)\cosh(\lambda_2 l)EI + 2\,\lambda_1\lambda_2\cos(\lambda_1 l)\cosh(\lambda_2 l)T \\
&\quad -\lambda_1\lambda_2{}^3\cosh(\lambda_2 l)\cos(\lambda_1 l)EI]/\delta; \\
\mathbf{k}(4,4) &= [\cos(\lambda_1 l)\sinh(\lambda_2 l)\lambda_1{}^3 - \cosh(\lambda_2 l)\sin(\lambda_1 l)\lambda_2{}^3 \\
&\quad -\sin(\lambda_1 l)\lambda_2\cosh(\lambda_2 l)\lambda_1{}^2 \\
&\quad +\sinh(\lambda_2 l)\lambda_1\cos(\lambda_1 l)\lambda_2{}^2]EI/\delta; \\
\delta &= 2\,\lambda_1\lambda_2\cos(\lambda_1 l)\cosh(\lambda_2 l) - 2\,\lambda_1\lambda_2 \\
&\quad -\sin(\lambda_1 l)\lambda_2{}^2\sinh(\lambda_2 l) + \sinh(\lambda_2 l)\lambda_1{}^2\sin(\lambda_1 l).
\end{aligned}
\tag{C.6}
$$

C.7 A uniform tensioned beam with an abosrber on the right end

Figure C-4 shows a uniform tensioned beam with an absorber on its right end. The upper triangular elements of $\mathbf{k}$, derived in Section 6.5, are:

$$
\begin{aligned}
\mathbf{k}(1,1) &= [\lambda_1{}^3\sin(\lambda_1 l)\cosh(\lambda_2 l) + \lambda_2{}^3\sinh(\lambda_2 l)\cos(\lambda_1 l) \\
&\quad +\lambda_1{}^2\lambda_2\cos(\lambda_1 l)\sinh(\lambda_2 l) + \lambda_1\lambda_2{}^2\cosh(\lambda_2 l)\sin(\lambda_1 l)]\lambda_1 EI\,\lambda_2/\delta;
\end{aligned}
$$

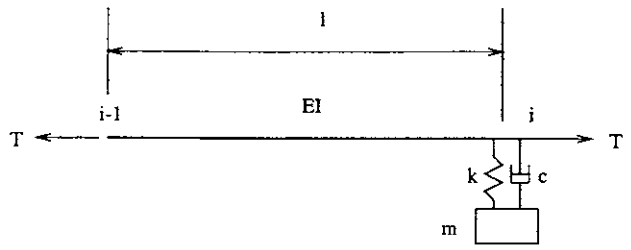

Figure C-4: Combination of tensioned beam with an absorber

$$
\begin{aligned}
\mathbf{k}(1,2) &= [\lambda_1 EI\,{\lambda_2}^3 - 2\,\lambda_1\,\lambda_2\,T + {\lambda_1}^4 \sin(\lambda_1 l)\sinh(\lambda_2 l)EI \\
&\quad + {\lambda_1}^2 \sin(\lambda_1 l)\sinh(\lambda_2 l)T + {\lambda_2}^4 \sinh(\lambda_2 l)\sin(\lambda_1 l)EI \\
&\quad - {\lambda_2}^2 \sinh(\lambda_2 l)\sin(\lambda_1 l)T - \lambda_2 EI\,{\lambda_1}^3 \\
&\quad + {\lambda_1}^3\lambda_2 \cos(\lambda_1 l)\cosh(\lambda_2 l)EI + 2\,\lambda_1\,\lambda_2 \cos(\lambda_1 l)\cosh(\lambda_2 l)T \\
&\quad - \lambda_1\,{\lambda_2}^3 \cosh(\lambda_2 l)\cos(\lambda_1 l)EI]/\delta; \\
\mathbf{k}(1,3) &= -[EI\left({\lambda_2}^2 + {\lambda_1}^2\right)\lambda_1\,\lambda_2\,(\lambda_1 \sin(\lambda_1 l) + \lambda_2 \sinh(\lambda_2 l))]/\delta; \\
\mathbf{k}(1,4) &= -[EI\left({\lambda_2}^2 + {\lambda_1}^2\right)\lambda_1\,\lambda_2\,(\cos(\lambda_1 l) - \cosh(\lambda_2 l))]/\delta; \\
\mathbf{k}(2,2) &= -EI\,[\cos(\lambda_1 l){\lambda_1}^3 \sinh(\lambda_2 l) - \cosh(\lambda_2 l){\lambda_2}^3 \sin(\lambda_1 l) \\
&\quad - \lambda_2 \sin(\lambda_1 l)\cosh(\lambda_2 l){\lambda_1}^2 + \lambda_1 \sinh(\lambda_2 l)\cos(\lambda_1 l){\lambda_2}^2]/\delta; \\
\mathbf{k}(2,3) &= [EI\left({\lambda_2}^2 + {\lambda_1}^2\right)\lambda_1\,\lambda_2\,(\cos(\lambda_1 l) - \cosh(\lambda_2 l))]/\delta; \\
\mathbf{k}(2,4) &= [EI\left({\lambda_2}^2 + {\lambda_1}^2\right)(-\sin(\lambda_1 l)\lambda_2 + \sinh(\lambda_2 l)\lambda_1)]/\delta; \\
\mathbf{k}(3,3) &= [2\,\lambda_1\,\lambda_2\,m\omega^3 jc - \lambda_1\,{\lambda_2}^4 \sinh(\lambda_2 l)EI\,k\cos(\lambda_1 l) \\
&\quad - 2\,\lambda_1\,\lambda_2\,m\omega^2 k\cos(\lambda_1 l)\cosh(\lambda_2 l) - {\lambda_1}^4\lambda_2 \sin(\lambda_1 l)EI\,j\omega\,c\cosh(\lambda_2 l) \\
&\quad + {\lambda_1}^4\lambda_2 \sin(\lambda_1 l)EI\,m\omega^2\cosh(\lambda_2 l) - \lambda_1\,{\lambda_2}^4 \sinh(\lambda_2 l)EI\,j\omega\,c\cos(\lambda_1 l) \\
&\quad + \lambda_1\,{\lambda_2}^4 \sinh(\lambda_2 l)EI\,m\omega^2\cos(\lambda_1 l) - 2\,\lambda_1\,\lambda_2\,m\omega^3 jc\cos(\lambda_1 l)\cosh(\lambda_2 l) \\
&\quad + \cosh(\lambda_2 l){\lambda_1}^2{\lambda_2}^3 EI\,m\omega^2\sin(\lambda_1 l) + \cos(\lambda_1 l){\lambda_1}^3{\lambda_2}^2 EI\,m\omega^2\sinh(\lambda_2 l) \\
&\quad - {\lambda_1}^4\lambda_2 \sin(\lambda_1 l)EI\,k\cosh(\lambda_2 l) - m\omega^3 jc\sinh(\lambda_2 l){\lambda_1}^2\sin(\lambda_1 l) \\
&\quad + m\omega^3 jc\sin(\lambda_1 l){\lambda_2}^2\sinh(\lambda_2 l) - \cos(\lambda_1 l){\lambda_1}^3{\lambda_2}^2 EI\,j\omega\,c\sinh(\lambda_2 l) \\
&\quad - \cos(\lambda_1 l){\lambda_1}^3{\lambda_2}^2 EI\,k\sinh(\lambda_2 l) - m\omega^2 k\sinh(\lambda_2 l){\lambda_1}^2\sin(\lambda_1 l) \\
&\quad + m\omega^2 k\sin(\lambda_1 l){\lambda_2}^2\sinh(\lambda_2 l) - \cosh(\lambda_2 l){\lambda_1}^2{\lambda_2}^3 EI\,k\sin(\lambda_1 l)
\end{aligned}
$$

$$
\begin{aligned}
&+2\,\lambda_1\,\lambda_2\,m\omega^2 k - \cosh(\lambda_2\,l)\lambda_1{}^2\lambda_2{}^3 EI\,j\omega\,c\sin(\lambda_1\,l)] \\
&/[\delta(-k + m\omega^2 - j\omega\,c)]; \\
\mathbf{k}(3,4) &= -[\lambda_1\,EI\,\lambda_2{}^3 - 2\,\lambda_1\,\lambda_2\,T + \lambda_1{}^4\sin(\lambda_1\,l)\sinh(\lambda_2\,l)EI \\
&+\lambda_1{}^2\sin(\lambda_1\,l)\sinh(\lambda_2\,l)T + \lambda_2{}^4\sinh(\lambda_2\,l)\sin(\lambda_1\,l)EI \\
&-\lambda_2{}^2\sinh(\lambda_2\,l)\sin(\lambda_1\,l)T - \lambda_2\,EI\,\lambda_1{}^3 \\
&+\lambda_1{}^3\lambda_2\,\cos(\lambda_1\,l)\cosh(\lambda_2\,l)EI + 2\,\lambda_1\,\lambda_2\,\cos(\lambda_1\,l)\cosh(\lambda_2\,l)T \\
&-\lambda_1\,\lambda_2{}^3\cosh(\lambda_2\,l)\cos(\lambda_1\,l)EI]/\delta; \\
\mathbf{k}(4,4) &= -EI\,[\cos(\lambda_1\,l)\lambda_1{}^3\sinh(\lambda_2\,l) - \cosh(\lambda_2\,l)\lambda_2{}^3\sin(\lambda_1\,l) \\
&-\lambda_2\,\sin(\lambda_1\,l)\cosh(\lambda_2\,l)\lambda_1{}^2 + \lambda_1\,\sinh(\lambda_2\,l)\cos(\lambda_1\,l)\lambda_2{}^2]/\delta; \\
\delta &= -2\,\lambda_1\,\lambda_2\,\cos(\lambda_1\,l)\cosh(\lambda_2\,l) + 2\,\lambda_1\,\lambda_2 \\
&+\sin(\lambda_1\,l)\lambda_2{}^2\sinh(\lambda_2\,l) - \sinh(\lambda_2\,l)\lambda_1{}^2\sin(\lambda_1\,l). \qquad \text{(C.7)}
\end{aligned}
$$

C.8 Combination of a tensioned beam with concentrated mass and rotary inertia

The upper triangular elements of dynamic stiffness matrix $\mathbf{k}$ of a uniform tensioned beam with concentrated mass and rotary inertia, shown in Figure C-5, are:

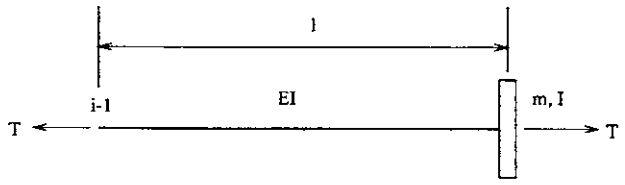

Figure C-5: Combination of tensioned beam with concentrated mass and rotary inertia

$$
\begin{aligned}
\mathbf{k}(1,1) &= -[\sin(\lambda_1 l)\lambda_1{}^3\cosh(\lambda_2 l) + \lambda_2{}^3\sinh(\lambda_2 l)\cos(\lambda_1 l) \\
&+\lambda_1{}^2\lambda_2\cos(\lambda_1 l)\sinh(\lambda_2 l) + \lambda_1\lambda_2{}^2\cosh(\lambda_2 l)\sin(\lambda_1 l)]EI\,\lambda_1\lambda_2/\delta;
\end{aligned}
$$

$$
\begin{aligned}
\mathbf{k}(1,2) &= -[\lambda_1 EI\ {\lambda_2}^3 - 2\,\lambda_1\lambda_2 T + \sin(\lambda_1 l){\lambda_1}^4 \sinh(\lambda_2 l) EI \\
&\quad + \sin(\lambda_1 l){\lambda_1}^2 \sinh(\lambda_2 l) T + {\lambda_2}^4 \sinh(\lambda_2 l) \sin(\lambda_1 l) EI \\
&\quad - {\lambda_2}^2 \sinh(\lambda_2 l) \sin(\lambda_1 l) T - \lambda_2 EI\ {\lambda_1}^3 \\
&\quad + {\lambda_1}^3 \lambda_2 \cos(\lambda_1 l) \cosh(\lambda_2 l) EI + 2\,\lambda_1\lambda_2 \cos(\lambda_1 l) \cosh(\lambda_2 l) T \\
&\quad - \lambda_1 {\lambda_2}^3 \cosh(\lambda_2 l) \cos(\lambda_1 l) EI]/\delta; \\
\mathbf{k}(1,3) &= \lambda_1\lambda_2 \left({\lambda_2}^2 + {\lambda_1}^2\right) EI\ (\lambda_1 \sin(\lambda_1 l) + \lambda_2 \sinh(\lambda_2 l))/\delta; \\
\mathbf{k}(1,4) &= -\lambda_1\lambda_2 \left({\lambda_2}^2 + {\lambda_1}^2\right) EI\ (-\cos(\lambda_1 l) + \cosh(\lambda_2 l))/\delta; \\
\mathbf{k}(2,2) &= -EI\ (-\cos(\lambda_1 l) \sinh(\lambda_2 l){\lambda_1}^3 + \cosh(\lambda_2 l) \sin(\lambda_1 l){\lambda_2}^3 \\
&\quad + \sin(\lambda_1 l)\lambda_2 \cosh(\lambda_2 l){\lambda_1}^2 - \sinh(\lambda_2 l)\lambda_1 \cos(\lambda_1 l){\lambda_2}^2)/\delta; \\
\mathbf{k}(2,3) &= \lambda_1\lambda_2 \left({\lambda_2}^2 + {\lambda_1}^2\right) EI\ (-\cos(\lambda_1 l) + \cosh(\lambda_2 l))/\delta; \\
\mathbf{k}(2,4) &= \left({\lambda_2}^2 + {\lambda_1}^2\right) EI\ (\sin(\lambda_1 l)\lambda_2 - \sinh(\lambda_2 l)\lambda_1)/\delta; \\
\mathbf{k}(3,3) &= -[2\,\lambda_1\lambda_2 m_c\omega^2 \cos(\lambda_1 l) \cosh(\lambda_2 l) + {\lambda_1}^4\lambda_2 \sin(\lambda_1 l) EI\ \cosh(\lambda_2 l) \\
&\quad + \lambda_1 {\lambda_2}^4 \sinh(\lambda_2 l) EI\ \cos(\lambda_1 l) - 2\,\lambda_1\lambda_2 m_c\omega^2 \\
&\quad - m_c\omega^2 \sin(\lambda_1 l){\lambda_2}^2 \sinh(\lambda_2 l) + m_c\omega^2 \sinh(\lambda_2 l){\lambda_1}^2 \sin(\lambda_1 l) \\
&\quad + {\lambda_1}^3{\lambda_2}^2 \cos(\lambda_1 l) EI\ \sinh(\lambda_2 l) + \cosh(\lambda_2 l){\lambda_1}^2{\lambda_2}^3 EI\ \sin(\lambda_1 l)]/\delta; \\
\mathbf{k}(3,4) &= [\lambda_1 EI\ {\lambda_2}^3 - 2\,\lambda_1\lambda_2 T + \sin(\lambda_1 l){\lambda_1}^4 \sinh(\lambda_2 l) EI \\
&\quad + \sin(\lambda_1 l){\lambda_1}^2 \sinh(\lambda_2 l) T + {\lambda_2}^4 \sinh(\lambda_2 l) \sin(\lambda_1 l) EI \\
&\quad - {\lambda_2}^2 \sinh(\lambda_2 l) \sin(\lambda_1 l) T - \lambda_2 EI\ {\lambda_1}^3 + {\lambda_1}^3\lambda_2 \cos(\lambda_1 l) \cosh(\lambda_2 l) EI \\
&\quad + 2\,\lambda_1\lambda_2 \cos(\lambda_1 l) \cosh(\lambda_2 l) T - \lambda_1 {\lambda_2}^3 \cosh(\lambda_2 l) \cos(\lambda_1 l) EI]/\delta; \\
\mathbf{k}(4,4) &= -[-2\,\lambda_1\lambda_2 i_c\omega^2 + i_c\omega^2{\lambda_1}^2 \sin(\lambda_1 l) \sinh(\lambda_2 l) - i_c\omega^2{\lambda_2}^2 \sinh(\lambda_2 l) \sin(\lambda_1 l) \\
&\quad - {\lambda_1}^3 \cos(\lambda_1 l) EI\ \sinh(\lambda_2 l) + {\lambda_2}^3 \cosh(\lambda_2 l) EI\ \sin(\lambda_1 l) \\
&\quad + 2\,\lambda_1\lambda_2 i_c\omega^2 \cos(\lambda_1 l) \cosh(\lambda_2 l) + {\lambda_1}^2\lambda_2 \sin(\lambda_1 l) EI\ \cosh(\lambda_2 l) \\
&\quad - \lambda_1 {\lambda_2}^2 \sinh(\lambda_2 l) EI\ \cos(\lambda_1 l)]/\delta; \\
\delta &= 2\,\lambda_1\lambda_2 \cos(\lambda_1 l) \cosh(\lambda_2 l) - 2\,\lambda_1\lambda_2 \\
&\quad - \sin(\lambda_1 l){\lambda_2}^2 \sinh(\lambda_2 l) + \sinh(\lambda_2 l){\lambda_1}^2 \sin(\lambda_1 l)
\end{aligned}
\tag{C.8}
$$

C.9 Combination of a tensioned beam with concentrated mass and spring support

Figure C-6 shows a uniform tensioned beam with concentrated mass and linear spring support on its right end. The upper triangular elements of its dynamic stiffness matrix **k** are:

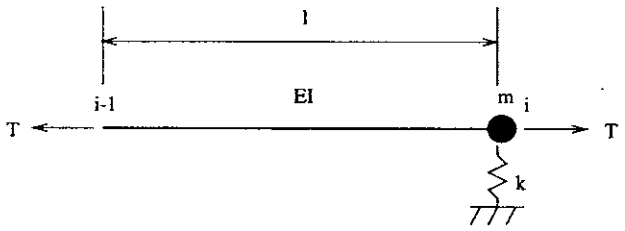

Figure C-6: Combination of tensioned beam with concentrated mass and spring support

$$
\begin{aligned}
\mathbf{k}(1,1) &= -[{\lambda_1}^3 \sin(\lambda_1 l)\cosh(\lambda_2 l) + {\lambda_2}^3 \sinh(\lambda_2 l)\cos(\lambda_1 l) \\
&\quad + {\lambda_1}^2 \lambda_2 \cos(\lambda_1 l)\sinh(\lambda_2 l) + \lambda_1 {\lambda_2}^2 \cosh(\lambda_2 l)\sin(\lambda_1 l)] EI\ \lambda_1 \lambda_2 / \delta; \\
\mathbf{k}(1,2) &= -[\lambda_1 EI\ {\lambda_2}^3 - 2\,\lambda_1 \lambda_2 T + {\lambda_1}^4 \sin(\lambda_1 l)\sinh(\lambda_2 l) EI \\
&\quad + {\lambda_1}^2 \sin(\lambda_1 l)\sinh(\lambda_2 l) T + {\lambda_2}^4 \sinh(\lambda_2 l)\sin(\lambda_1 l) EI \\
&\quad - {\lambda_2}^2 \sinh(\lambda_2 l)\sin(\lambda_1 l) T - \lambda_2 EI\ {\lambda_1}^3 + {\lambda_1}^3 \lambda_2 \cos(\lambda_1 l)\cosh(\lambda_2 l) EI \\
&\quad + 2\,\lambda_1 \lambda_2 \cos(\lambda_1 l)\cosh(\lambda_2 l) T - \lambda_1 {\lambda_2}^3 \cosh(\lambda_2 l)\cos(\lambda_1 l) EI]/\delta; \\
\mathbf{k}(1,3) &= [\lambda_1 \lambda_2 \left({\lambda_1}^2 + {\lambda_2}^2\right) EI\ (\lambda_1 \sin(\lambda_1 l) + \lambda_2 \sinh(\lambda_2 l))]/\delta; \\
\mathbf{k}(1,4) &= -\lambda_1 \lambda_2 \left({\lambda_1}^2 + {\lambda_2}^2\right) EI\ (-\cos(\lambda_1 l) + \cosh(\lambda_2 l))/\delta; \\
\mathbf{k}(2,2) &= [\cos(\lambda_1 l)\sinh(\lambda_2 l){\lambda_1}^3 - \cosh(\lambda_2 l)\sin(\lambda_1 l){\lambda_2}^3 \\
&\quad - \sin(\lambda_1 l)\lambda_2 \cosh(\lambda_2 l){\lambda_1}^2 + \sinh(\lambda_2 l)\lambda_1 \cos(\lambda_1 l){\lambda_2}^2] EI/\delta; \\
\mathbf{k}(2,3) &= \lambda_1 \lambda_2 \left({\lambda_1}^2 + {\lambda_2}^2\right) EI\ (-\cos(\lambda_1 l) + \cosh(\lambda_2 l))/\delta; \\
\mathbf{k}(2,4) &= -({\lambda_1}^2 + {\lambda_2}^2) EI\ [-\sin(\lambda_1 l)\lambda_2 + \sinh(\lambda_2 l)\lambda_1]/\delta;
\end{aligned}
$$

$$
\begin{aligned}
\mathbf{k}(3,3) &= -[-m\,\omega^2 \sin(\lambda_1 l)\lambda_2{}^2 \sinh(\lambda_2 l) + m\,\omega^2 \sinh(\lambda_2 l)\lambda_1{}^2 \sin(\lambda_1 l) \\
&\quad -2\,\lambda_1\lambda_2 m\,\omega^2 + \lambda_1{}^3\lambda_2{}^2 \cos(\lambda_1 l) EI\ \sinh(\lambda_2 l) \\
&\quad + \cosh(\lambda_2 l)\lambda_2{}^3\lambda_1{}^2 EI\ \sin(\lambda_1 l) + 2\,\lambda_1\lambda_2 k \\
&\quad + k\ \sin(\lambda_1 l)\lambda_2{}^2 \sinh(\lambda_2 l) - k\ \sinh(\lambda_2 l)\lambda_1{}^2 \sin(\lambda_1 l) \\
&\quad + 2\,\lambda_1\lambda_2 m\,\omega^2 \cos(\lambda_1 l)\cosh(\lambda_2 l) - 2\,\lambda_1\lambda_2 k\ \cos(\lambda_1 l)\cosh(\lambda_2 l) \\
&\quad + \lambda_1{}^4\lambda_2 \sin(\lambda_1 l) EI\ \cosh(\lambda_2 l) + \lambda_1\lambda_2{}^4 \sinh(\lambda_2 l) EI\ \cos(\lambda_1 l)]/\delta; \\
\mathbf{k}(3,4) &= [\lambda_1 EI\ \lambda_2{}^3 - 2\,\lambda_1\lambda_2 T + \lambda_1{}^4 \sin(\lambda_1 l)\sinh(\lambda_2 l) EI \\
&\quad + \lambda_1{}^2 \sin(\lambda_1 l)\sinh(\lambda_2 l) T + \lambda_2{}^4 \sinh(\lambda_2 l)\sin(\lambda_1 l) EI \\
&\quad - \lambda_2{}^2 \sinh(\lambda_2 l)\sin(\lambda_1 l) T - \lambda_2 EI\ \lambda_1{}^3 \\
&\quad + \lambda_1{}^3\lambda_2 \cos(\lambda_1 l)\cosh(\lambda_2 l) EI + 2\,\lambda_1\lambda_2 \cos(\lambda_1 l)\cosh(\lambda_2 l) T \\
&\quad - \lambda_1\lambda_2{}^3 \cosh(\lambda_2 l)\cos(\lambda_1 l) EI]/\delta; \\
\mathbf{k}(4,4) &= -\sin(\lambda_1 l)\lambda_2 \cosh(\lambda_2 l)\lambda_1{}^2 + \sinh(\lambda_2 l)\lambda_1 \cos(\lambda_1 l)\lambda_2{}^2] EI/\delta; \\
\delta &= 2\,\lambda_1\lambda_2 \cos(\lambda_1 l)\cosh(\lambda_2 l) - 2\,\lambda_1\lambda_2 \\
&\quad - \sin(\lambda_1 l)\lambda_2{}^2 \sinh(\lambda_2 l) + \sinh(\lambda_2 l)\lambda_1{}^2 \sin(\lambda_1 l).
\end{aligned}
\tag{C.9}
$$

Appendix D

The VIV Prediction of the Helland-Hansen riser

In the second example of Section 5.4.2, we stated the method of predicting VIV of the Helland-Hansen riser. The SHEAR7 input data file is as follows:

1	structural model, nmodel
0	flag To choose SI (0) or English (1) Units.
226	number of segments in the structure
688.	beam Length, meters or feet
1.1303	Drag diameter, meters , type 2 buoyancy
0.5334, 0.5017	beam strength diameters(OD and ID), meters
1025.	fluid density, kg/m**3 or Lbf/Ft**3
$1.3E-6$	kinematic viscosity of the fluid, m**2/s or ft**2/s
908.	970.4 kg/m on buoyancy, averaged with slick portion, mass/m in Air, inc mud
1.0	added Mass Coefficient
1942892.	minimum Tension, newton or Pounds, this value could be off
$2.107E11$	Young'S Modulus, N/m**2 or Ksi

0.0008637	inertia Of Strength Material, m**4 or Ft**4
1087.	fix this aver of buoyant and non-bu sections,linearly Varying Tension, N/m
0.23	Strouhal No.
8, 1, 1	Number of vel points, probability, profile ID
0.0000, 0.00	location (x/l), velocity (m/s) for first point
0.1650, 0.63	location and velocity for each succeeding point
0.2520, 0.72	
0.3820, 0.85	
0.5130, 0.91	
0.6440, 0.96	
0.7740, 0.98	
0.9370, 0.98	
.002	structural modal damping (fraction of critical damping)
0	flag 1 for controlling damping computation (0=program decides)
0	flag 2 for controlling damping computation (0=program decides)
0.4	RMS lift coefficient (if lift flag set to 0 not used)
0.0, 1.0, 0.125	RMS response locations (begin, end, step-size), x/L (OUTPUT File Format)
1	number of SN-curve line segments
0.	cutoff stress range (N/m**2 or KSI)
$1.24E8, 2.E6$	stress range(N/m**2 or ksi), cycles to failure point 1- C curve
$2.92E8, 1.E5$	stress range(N/m**2 or ksi), cycles to failure point 2
1.3	global stress concentration factor
0	number of local stress concentration positions
0.4	reduced velocities bandwidth
0	open .cat file? 0 = no, 1 = yes
0	flag to choose lift coefficient (0=program decides)

0	No. of VIV suppresion regions (0=off)
5	calculation option, NCAL =1, full response calc
0.20, 0	a cutoff to control the No. of excited modes
1.00, 0	multi-mode reduction factor.

Figures D-1 to D-4 show the displacement, acceleration, stress, and damage rate along the riser, respectively. These figures include for comparison the results by using the simple approximation described in Chapter 4.

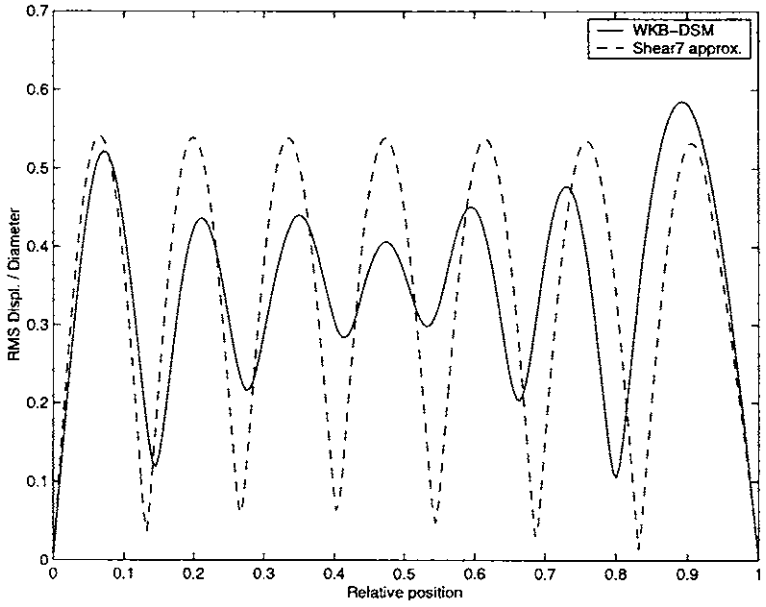

Figure D-1: The displacement along the riser

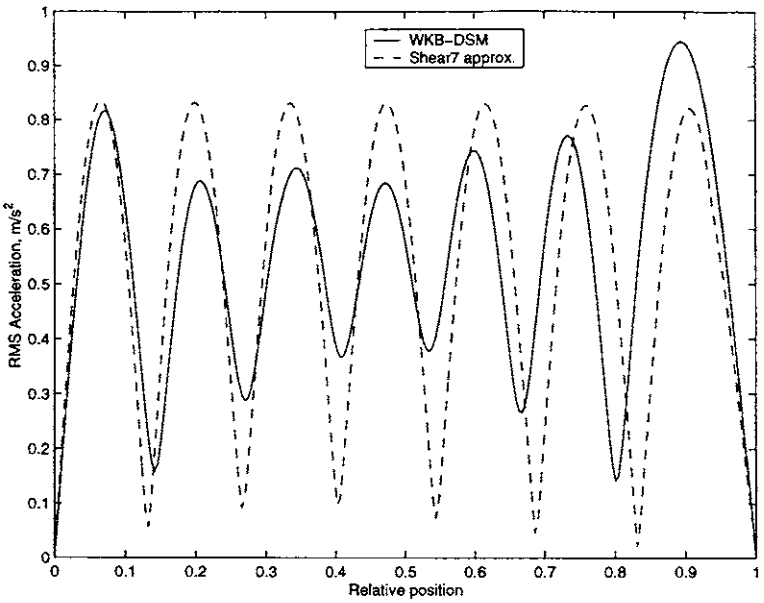

Figure D-2: The acceleration along the riser

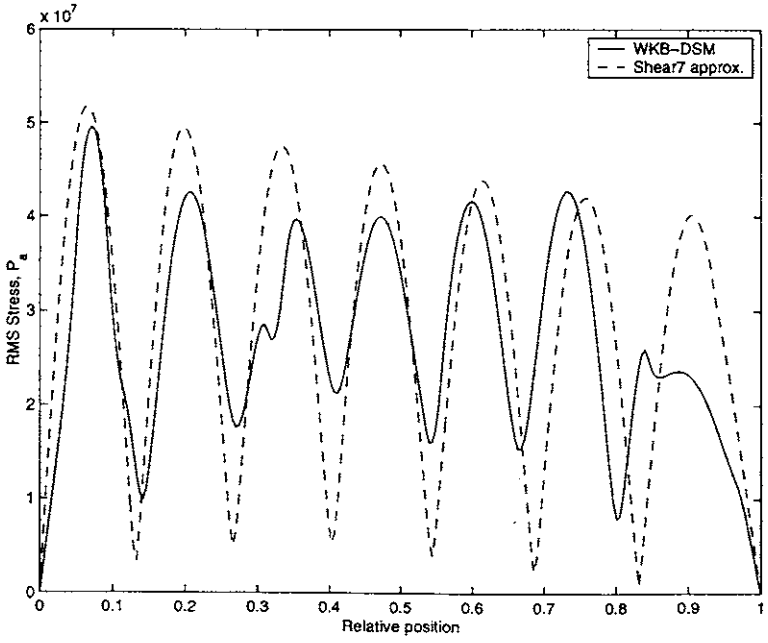

Figure D-3: The stress along the riser

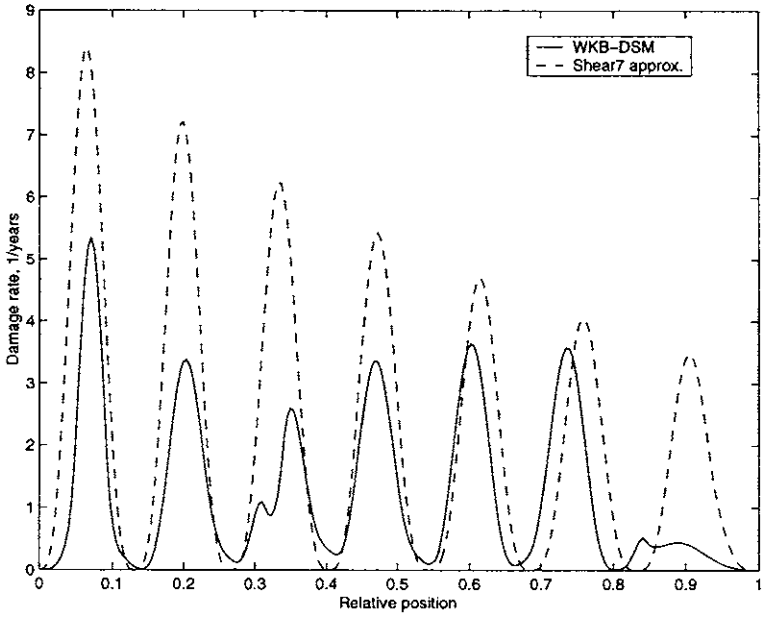

Figure D-4: The damage rate along the riser

Bibliography

[1] D. W. Dareing and T. Huang. Natural frequencies of marine drilling risers, pp. 813-818. *Journal of Petroleum Technology*, 1976.

[2] R. King. A review of vortex shedding research and its application, 4 (46). *Ocean Engineering*, 1977.

[3] T. Sarpakaya. Vortex-induced oscillations, a selective review, 46. *ASME Journal of Applied Mechanics*, 1979.

[4] O. M. Griffin and S. E. Ramberg. Some recent studies of vortex shedding with application to marine tubulars and risers, vol. 104. *Journal of Energy Resources Technology*, 1982.

[5] J. K. Vandiver. Dimensionless parameters important to the prediction of vortex-induced vibration of long, flexible cylinders in ocean currents, 7, 423 - 455. *Journal of Fluids and Structures*, 1993.

[6] J. K. Vandiver, D. Allen, and L. Li. The occurrence of lock-in under highly sheared conditions, 10, 555 - 561. *Journal of Fluids and Structures*, 1996.

[7] Y. C. Kim. *Nonlinear Vibration of Long Slender Beams.* (PhD thesis), MIT, Cambridge, 1983.

[8] N. M. Patrikalakis and C. Chryssostomidis. Linear dynamics of compliant risers. *MIT Sea Grant College Program*, 1985.

[9] N. M. Patrikalakis and G. A. Kriezis. Three-dimensional non-linear dynamics of compliant risers. *MIT Sea Grant College Program*, 1987.

[10] M. S. Triantafyllou, A. Bliek, J. Burgess, and H. Shin. Mooring dynamics for offshore applications (part i: Theory; part ii: Applications). *MIT Sea Grant College Program*, 1986.

[11] Li Li. *The Dynamics of Strings With Rigid Lumps.* (PhD thesis), MIT, Cambridge, 1993.

[12] J. Kim Vandiver and Li Li. *Vibration suppression of tension-dominated structures.* MIT, Cambridge, 1994.

[13] C. R. Levesque. *Vibration Suppression in Finite Length Marine Cable System.* (Ms. thesis), MIT, Cambridge, 1997.

[14] A. A. Tjavaras. *The Dynamics of Highly Extensible Cables.* (PhD thesis), MIT, Cambridge, 1996.

[15] M. A. S. Reis. *Wave Propagation in Elastic Beams and Rods.* (PhD thesis), MIT, Cambridge, 1978.

[16] Mark A. Hayner. *Wave-based finite element method applied to thick, in-vacuo, cylindrical shells with keel or bulkhead plate attachments at middle to high frequency.* (PhD thesis), MIT, Cambridge, 1998.

[17] K. H. Halse. Norwegian deepwater program: improved predictions of vortex-induced vibrations. *Offshore Technology Conference, Houston*, 2000.

[18] D. W. Allen. Vortex-induced vibration of deepwater risers. *Offshore Technology Conference, Houston*, 1998.

[19] T. Huang, D. W. Dareing, and W. T. Beran. Bending of tubular bundles attached to marine risers, vol. 102. *Journal of Energy Resources Technology*, 1980.

[20] L. Li and J. K. Vandiver. Wave propagation in strings with rigid bodies, vol. 117, 493-500. *Journal of Vibration and Acoustics*, 1995.

[21] E. C. Pestel and F. A. Leckie. *Matrix Methods in Elastomechanics.* McGraw-Hill Book Company, Inc., New York, 1963.

[22] R. Uhrig. The transfer matrix method seen as one method of structural analysis among others, 4 (2), pp. 813-818. *Journal of Sound and Vibration*, 1966.

[23] W. C. Hurty and M. F. Rubinstein. *Dynamics of Structures.* Prentice-Hall, Inc., New Jersey, 1964.

[24] F. Leckie and E. Pestel. Transfer-matrix fundamentals. *Int. J. Mech. Sci., Vol. 2, 137-167*, 1960.

[25] J. P. Den Hartog. *Mechanical Vibrations.* McGraw-Hill, New York, 1956.

[26] B. R. Mace. Wave reflection and transmission in beams, 97 (2), 237-246. *Journal of Sound and Vibration*, 1984.

[27] W. D. Pilkey and P. Y. Chang. *Modern Formulas for Statics and Dynamics.* McGraw-Hill Book Company, New York, 1978.

[28] W. H. Wittrick and F. W. Williams. A general algorithm for computing natural frequencies of elastic structures, vol. xx iv, pt.3, 264-284. *Quart. Journ. Mech. and Applied Math.*, 1971.

[29] A. Simpson. On the solution of $s(\omega)x = 0$ by a newtonian procedure. *J. of Sound and Vibration, 97 (1), 153-164*, 1984.

[30] T. H. Richards and Y. T. Leung. An accurate method in structural vibration analysis. *J. of Sound and Vibration 55 (3), 363-376*, 1977.

[31] P. Swannell. The automatic computation of the natural frequencies of structural frames using an exact matrix technique,pp. 289-301. *Theory and Practice in Finite Element Structural Analysis, University of Tokyo Press*, 1973.

[32] A. Y. T. Leung. *Dynamic Stiffness and Substructures.* Springer-Verlag, New York, 1993.

[33] F. W. Williams and W. H. Wittrick. Exact buckling and frequency calculations surveyed. *Journal of Structural Engineering, Vol. 109, No. 1, 169-187*, 1983.

[34] S. D. Conte. *Elementary Numerical Analysis.* McGraw-Hill Book Company, New Jersey, 1972.

[35] R. D. Blevin. *Formulas for Natural Frequency and Mode Shape.* Robert E. Krieger Publishing Company, Florida, 1990.

[36] W. P. Howson and F. W. Williams. Natural frequencies of frames with axially loaded timoshenko members, 26 (4), 503-515. *Journal of Sound and Vibration,* 1973.

[37] W. M. Laird and G. F. Auconead. Upper and lower bounds for the eigenvalues of vibrating beams with linearly varying axial load. *National Aeronautics and Space Administration Report NASA-CR-653,* 1966.

[38] T. Huang and W. D. Dareing. Buckling and frequencies of long vertical pipes, 95 (em1), 503-515. *Journal of the Engineering Mechanics Division, Proceedings of the American Society of Civil Engineers,* 1969.

[39] Ray W. Clough and Joseph Penzien. *Dynamics of Structures.* McGraw-Hill Book Company, Inc., New York, 1975.

[40] C. M. Bender and S. A. Orszag. *Advanced Mathematical Methods for Scientists and Engineers.* McGraw-Hill Book Company, New York, 1978.

[41] K. J. Bathe. *Finite Element Procedures.* Prentice-Hall International Inc., New Jersey, 1996.

[42] J. R. Banerjee and F. W. Williams. Exact bernoulli-euler dynamic stiffness matrix for a range of tapered beams, vol. 21, pp. 2289-2302. *International Journal for Numerical Methods in Engineering,* 1985.

[43] J. K. Vandiver and L. Li. *Shear7 Program Theoretical Manual.* MIT, Cambridge, 1997.

[44] W. D. Pilkey. *Manual for the Response of Structural Members, Vol. I and II.* Clearinghpouse, Chicago, 1969.

[45] S. H. Crandall. *Engineering Analysis.* McGraw-Hill, New York, 1956.

[46] J. E. Brock. A note on the damped vibration absorber. *Transactions of the American Society of Mechanical Engineers: Journal of Applied mechanics 49, A9-22*, 1946.

[47] D. Young. Theory of dynamic vibration absorbers for beams. *Proceedings of the First U. S. National Congress of Applied Mechanics, 91-96*, 1952.

[48] J. Kim Vandiver and L. Li. Suppression of cable vibration by means of wave absorbing terminations. *Proc. of Behavior of Offshore Structures Conference, MIT Vol. 2, 633-643*, 1994.

[49] A. G. Thompson. Optimum tuning and damping of a dynamic vibration absorber applied to a force excited and damped primary system. *J. of Sound and Vibration 77 (3), 403-415*, 1981.

[50] J. Kim Vandiver and S. Mitome. Effect of liquid storage tanks on the dynamic response of offshore platforms. *Applied Ocean Research Vol. 1, No. 2, 67-74*, 1979.

[51] O. Oniszczuk. Transverse vibration of elastically connected double-string complex system, part i: Free vibrations. *J. of Sound and Vibration 232 (2), 355-366*, 2000.

[52] O. Oniszczuk. Transverse vibration of elastically connected double-string complex system, part ii: Forced vibrations. *J. of Sound and Vibration 232 (2), 367-386*, 2000.

[53] O. Oniszczuk. Transverse vibration of elastically connected simply supported double-beam complex system. *J. of Sound and Vibration 232 (2), 387-403*, 2000.

[54] T. Aida, S. Toda, Ogawa N., and Y. Imada. Vibration control of beams by beam-type dynamic vibration absorbers. *J. of Engineering Mechanics Vol. 118, No. 2, 248-258*, 1992.

[55] T. T. Yeh and S. S. Chen. The effect of fluid viscosity on coupled tube/fluid vibrations. *J. of Sound and Vibration 59 (3), 453-467*, 1978.

[56] S. S. Chen. *Flow-Induced Vibration of Circular Cylindrical Structures.* Hemisphere Publishing Corporation, New York, 1987.

[57] S. S. Chen. Free vibration of a coupled fluid/structural system. *J. of Sound and Vibration 21 (4), 387-398*, 1972.